

**Forschungsbericht 2021-23**

**Reduction of Aircraft Noise  
by Wing Design  
and Add-On Technologies**

Heinrich Marc Koch

Deutsches Zentrum für Luft- und Raumfahrt  
Institut für Aerodynamik und  
Strömungstechnik  
Göttingen



DLR

Deutsches Zentrum  
für Luft- und Raumfahrt

Heinrich Marc KOCH

Institut für Aerodynamik und Strömungstechnik des DLR, Göttingen

### **Reduktion von Fluglärm durch Flügelplanform-Änderungen und Lärmindernde Technologien**

*Dissertation Technische Universität Braunschweig*

*DLR-Forschungsbericht 2021-23, 2021, 130 Seiten, 116 Bilder, 21 Tabellen, 231 Literaturstellen, 47,00 € zzgl. MwSt.*

Für Bewohner um Flughäfen, welche von Fluglärm betroffen sind, ist dieser ein ernstzunehmendes Problem. Daher wird in dieser Arbeit das Lärminderungs-Potential auf Basis der Boeing 747-400 mit Hilfe von Simulationen ermittelt. *Dabei wird zum einen die Flügel-Planform in einer Parameterstudie geändert, und zum anderen werden sukzessive lärmindernde Technologien verbaut.* Die Flügel-Planform und jede lärmindernde Technologie beeinflusst die Flugeigenschaften des Flugzeugs und wird in einer Parameterstudie untersucht. Der Bodenlärm wird anhand eines Indexes auf Basis eines Aufwachkriteriums des Deutschen Zentrums für Luft- und Raumfahrt e.V. ermittelt. Die Anflugprozedur nutzt die jeweils individuellen Flugeigenschaften eines jeden einzelnen Flugzeugs aus, um die Bevölkerung möglichst gering mit Lärm zu belasten. Werden diese zwei Flugverfahren genutzt, so verursachen die Flugzeuge die geringste Anzahl Aufwachreaktionen, die innerhalb der kürzesten Strecke eine vorher definierte Flughöhe erreichen und die mit einer möglichst geringen Anfluggeschwindigkeit in Reiseflugkonfiguration anfliegen. Lärmindernden Technologien beeinflussen die Flugeigenschaften so sehr, dass die Flügel-Planform optimiert werden sollte.

*Aircraft noise prediction, low-noise aircraft, climb performance, awakening reactions, B747-400, four-engine aircraft, long-range aircraft*

Heinrich Marc KOCH

Institute of Aerodynamics and Flow Technology, DLR Göttingen

### **Reduction of Aircraft Noise by Wing Design and Add-On Technologies**

*Doctoral Thesis University of Technology Braunschweig*

*DLR-Forschungsbericht 2021-23, 2021, 130 pages, 116 figs., 21 tabs., 231 refs., 47.00 €*

As aircraft noise is a major concern for residents living in the vicinity of airports, this thesis investigates the noise reduction capability of a large and heavy tube-and-wing airliner through design modifications employing a simulation study. The planform parameters determine the airplane's flight mechanics and influence the ground noise impact. The planform and low-noise techniques are changed in a parameter study. Their ground noise is evaluated based on the DLR's awakening criterion. Absent of low-noise technologies, the approach speed and the ground track length between the point of break release and the point at which the airplane reached a height of 1200 m are found to be the most important criteria to lower the approach and departure-induced ground noise, respectively. The application of low-noise technologies influences the airplane's flight performance, which shifts the set of the planform parameter values to achieve the optimal airplane design. In summary, it is shown that the collective consideration of various planform parameters while designing airplanes has been found to be more effective than just the sole application of low-noise technologies to existing airplanes.

# **Forschungsbericht 2021-23**

## **Reduction of Aircraft Noise by Wing Design and Add-On Technologies**

Heinrich Marc Koch

Deutsches Zentrum für Luft- und Raumfahrt  
Institut für Aerodynamik und  
Strömungstechnik  
Göttingen

130 Seiten  
116 Bilder  
21 Tabellen  
231 Literaturstellen



Deutsches Zentrum  
DLR für Luft- und Raumfahrt

# Reduction of Aircraft Noise by Wing Design and Add-On Technologies

Von der Fakultät für Maschinenbau  
der Technischen Universität Carolo-Wilhelmina zu Braunschweig

zur Erlangung der Würde  
eines Doktor-Ingenieurs (Dr.-Ing.)  
genehmigte Dissertation

|                       |  |
|-----------------------|--|
| von:                  | Heinrich Marc Koch, M.Sc.  |
| aus (Geburtsort):     | Lüdinghausen   |
| eingereicht am:       | 18. März 2021  |
| mündliche Prüfung am: | 01. Oktober 2021   |
| Gutachter:            | Prof. Dr.-Ing. Jan Werner Delfs<br>Prof. Dr.-Ing. Sabine Christine Langer<br>Prof. Dr.-Ing. Andreas Strohmayer |





# License

## Title

“Reduction of Aircraft Noise by Wing Design and Add-On Technologies”

## Author

Heinrich Marc Koch

## Publisher

© Deutsches Zentrum für Luft- und Raumfahrt e.V.  
Wissenschaftliche Information  
D-51170 Köln  
Portz-Wahnheide  
Linder Höhe  
D-51147 Köln

ISSN 1434-8454

## Publisher Statement

This work is made available according to the conditions of the Creative Commons Attribution-ShareAlike 3.0 Germany ( CC BY-SA 3.0 DE) license. This work contains images with special rights. These images are marked separately, and are not covered by CC BY-SA 3.0 DE. Full details of this license are available at: <https://creativecommons.org/licenses/by-sa/3.0/de>

## License

 Creative Commons Attribution-ShareAlike 3.0 Germany (CC BY-SA 3.0 DE) license

# Abstract

As aircraft noise is a major concern for residents living in the vicinity of airports, this thesis investigates the noise reduction capability of a large and heavy tube-and-wing airliner through design modifications employing a simulation study. The planform parameters determine the airplane's flight mechanics and, in turn, influence the ground noise impact. The planform is changed in a parameter study, and low-noise techniques, namely fan sound shielding, ultra-high bypass ratio engine, droop nose, trailing-edge brush, and landing gear fairing, are sequentially applied to the airplanes. Their ground noise is evaluated based on the DLR's awakening criterion. Absent of low-noise technologies, the approach speed and the ground track length between the point of break release and the point at which the airplane reached a height of 1200 m are found to be the most important criteria to lower the approach and departure-induced ground noise, respectively. Since the departure-induced ground noise causes the majority of the overall awakening reactions, it dominates the selection process of the optimal airplane design. The application of low-noise technologies influences the airplane's flight performance, which shifts the set of the planform parameter values to achieve the optimal airplane design. In summary, it is shown that the collective consideration of various planform parameters while designing airplanes has been found to be more effective than just the sole application of low-noise technologies to existing airplanes.

**Keywords:** Aircraft noise prediction, low-noise aircraft, low-noise characteristics, low-noise flight path, conceptual aircraft design, stall speed, climb performance, awakening reactions, FlipNA, PANAM, PrADO, SHADOW, B747-400, four-engine aircraft, long-range aircraft, low drag minimum power, ICAO-A procedure

## Zusammenfassung

Für Bewohner um Flughäfen, welche von Fluglärm betroffen sind, ist dieser ein ernstzunehmendes Problem. Daher wird in dieser Arbeit das Lärminderungs-Potential auf Basis der Boeing 747-400, einem großen Langstreckenflugzeug, mit Hilfe von Simulationen ermittelt. Dabei wird zum einen die Flügel-Planform in einer Parameterstudie geändert, und zum anderen werden sukzessive lärmmindernde Technologien verbaut. Die Flügel-Planform beeinflusst die Flugeigenschaften des Flugzeugs. Jede angewandte lärmmindernde Technologie jedoch auch. Daher wird für jede lärmmindernde Technologie eine neue Parameterstudie durchgeführt, um das letztendliche Lärminderungs-Potential für jede Technologiestufe zu ermitteln. Bei den gewählten Flügel-Planform-Parametern handelt es sich um die Vorderkantenpfeilung, die Flügelfläche und die Flügelstreckung. Die lärmmindernden Technologien umfassen die Abschattung des Fan-Schalls durch den Flügel, ein Triebwerks-Typ mit sehr hohem Nebenstromverhältnis, eine formvariable Flügel-Vorderkante, Borsten an der Flügelhinterkante und Fahrwerksverkleidungen.

Der Bodenlärm wird anhand eines Indexes auf Basis eines Aufwachkriteriums des Deutschen Zentrums für Luft- und Raumfahrt e.V. ermittelt. Die Flugzeuge starten entlang einer Standard-Abflugprozedur, dem ICAO-A Abflug. Während des Landeanflugs hingegen wurde auf eine Anflugprozedur zurück gegriffen, welche die jeweils individuellen Flugeigenschaften eines jeden einzelnen Flugzeugs ausnutzt, um die Bevölkerung möglichst gering mit Lärm zu belasten. Werden diese zwei Flugverfahren genutzt, so verursachen die Flugzeuge die geringste Anzahl Aufwachreaktionen, die:

- innerhalb der kürzesten Strecke eine vorher definierte Flughöhe erreichen (hier 1200 m)
- mit einer möglichst geringen Anfluggeschwindigkeit in Reiseflugkonfiguration anfliegen.

Darüber hinaus verändern die lärmindernden Technologien die Flugeigenschaften so sehr, dass die Flügel-Planform geändert werden sollte, um ein optimales Flugzeug zu erhalten. “Optimal” bedeutet hierbei eine Kombination aus Bodenlärm und Kosten.

Zusammenfassend zeigt sich, dass es Vorteile bringt die Flügel-Planform zu überarbeiten, sobald angebaute Technologien die Flugeigenschaften ändern.

## Acknowledgements

Time is a precious commodity of which some people have given me particularly generous amounts. I would like to take the opportunity to recognize a few of these people. First, I would like to thank my adviser and colleague Dr. **Lothar Bertsch**. I owe him much gratitude for his continuous support and encouragement. His enthusiasm, motivation, and patience are an inspiration to his colleagues, including me. Importantly, he also advocated for the funding of this study. And for the ultimate funding of this study, I would like to express my appreciation to Prof. **Andreas Dillmann** from DLR.

I thank my doctoral supervisor, Prof. **Jan Delfs**, for his valuable comments during our meetings. His ability to explain complicated contexts vividly, enabling everybody to stay on top of any topic. My thanks also go to my supervisors Prof. **Sabine Langer** and Prof. **Andreas Strohmayer** for providing valuable feedback and guidance.

This study would not have been possible without the many helpful discussions with my colleagues at DLR. Next to Dr. Lothar Bertsch I want also recognize Dr. **Ullrich Isermann**, Dr. **Rainer Schmid**, Dr. **Till Raitor**, Dr. **Jason Blinstrub**, **Vincent Domogalla**, and Dr. **Florian Wolters**. Additionally, Dr. **Wolfgang Heinze** provided support and an important basis for this work: PrADO. Prof. **Dick Simons** and Assoc. Prof. **Mirjam Snellen** supported me during my visit at TUDelft.

**Ankur Vats** taught me how to put my thoughts into writing. She helped describing figures and complex contexts in a way that allows other people to understand my research. For her unlimited patience I am grateful. **Beatrice Carter** proofread parts of this thesis. I thank her for her insights into English grammar. **Wilhelm Koch** carefully listened to my thoughts, which was very valuable support. Finally, I thank my family and friends, who got me through this process and, without their unwavering support, crossing the finish line would not have been possible.



# Contents

|   |            |
|---|------------|
| <b>Contents</b>   | <b>x</b>   |
| <b>List of Figures</b>                                    | <b>xiv</b> |
| <b>List of Tables</b>                                     | <b>xix</b> |
| <b>Nomenclature</b>                                       | <b>xxi</b> |
| List of Symbols . . . . .                                 | xxi        |
| List of Abbreviations . . . . .                           | xxiv       |
| List of Software . . . . .                                | xxvi       |
| <b>1 Introduction</b>                                     | <b>1</b>   |
| 1.1 Research Scope and Objective . . . . .                | 3          |
| 1.2 Outline of this Thesis . . . . .                      | 5          |
| <b>2 Noise Source Modeling and Planform Parameters</b>    | <b>7</b>   |
| 2.1 Airframe Noise Sources . . . . .                      | 8          |
| 2.1.1 Clean Wing . . . . .                                | 8          |
| 2.1.2 High-Lift Devices . . . . .                         | 9          |
| 2.1.3 Landing Gear . . . . .                              | 11         |
| 2.2 Propulsion Unit . . . . .                             | 13         |
| 2.2.1 Fan . . . . .                                       | 13         |
| 2.2.2 Jet . . . . .                                       | 15         |
| 2.3 Interaction Noise . . . . .                           | 16         |
| 2.4 Departure and Approach Procedures . . . . .           | 17         |
| 2.5 Planform Parameters . . . . .                         | 18         |
| <b>3 Software</b>   | <b>19</b>  |
| 3.1 Conceptual Airplane Design Software . . . . .         | 20         |
| 3.2 Trajectory Calculation for Noise Assessment . . . . . | 21         |
| 3.3 Airplane Ground Noise Prediction . . . . .            | 23         |
| 3.4 Fan Sound Shielding Prediction . . . . .              | 24         |
| 3.5 Modifications . . . . .                               | 24         |
| <b>4 Reference Airplane and Validation</b>                | <b>27</b>  |
| 4.1 Reference Airplane . . . . .                          | 28         |
| 4.2 Flyover Noise Measurements . . . . .                  | 33         |
| 4.3 Simulations . . . . .                                 | 37         |
| 4.4 Comparison . . . . .                                  | 38         |

|          |  |            |
|----------|--|------------|
| 4.4.1    | Approaches at Idle Thrust . . . . .                                      | 40         |
| 4.4.2    | Approaches at Medium Thrust . . . . .                                    | 41         |
| 4.4.3    | Departures at Full Thrust . . . . .                                      | 44         |
| 4.5      | Summary of the Chapter . . . . .   | 48         |
| <b>5</b> | <b>Target Function and Flight Procedures</b>                             | <b>49</b>  |
| 5.1      | Area Under Investigation . . . . .                                       | 49         |
| 5.2      | Noise Assessment Index . . . . .   | 50         |
| 5.3      | Direct Operating Cost Index . . . . .                                    | 52         |
| 5.4      | Target Function . . . . .  | 53         |
| 5.5      | Procedures for Noise Assessment . . . . .                                | 54         |
| 5.5.1    | Departure . . . . .  | 54         |
| 5.5.2    | Approach . . . . .   | 56         |
| 5.6      | Design Mission . . . . .   | 60         |
| <b>6</b> | <b>How Planform Parameters Affect Ground Noise</b>                       | <b>61</b>  |
| 6.1      | Departure Situation . . . . .  | 62         |
| 6.2      | Approach Situation . . . . .   | 66         |
| 6.3      | Effects of Planform Parameters on the Awakening Index . . . . .          | 69         |
| 6.3.1    | Aspect Ratio . . . . .   | 70         |
| 6.3.2    | Wing Area . . . . .  | 73         |
| 6.3.3    | Sweep . . . . .  | 76         |
| 6.4      | Airplane Selection . . . . .   | 78         |
| 6.5      | Awakening Distribution Caused by the Basic Airplane . . . . .            | 80         |
| 6.6      | Awakening Distribution Caused by the Reference Airplane . . . . .        | 83         |
| 6.7      | Chapter Conclusion . . . . .   | 86         |
| <b>7</b> | <b>Ground Noise Reduction by Low-Noise Technologies</b>                  | <b>89</b>  |
| 7.1      | Fan Noise Shielding . . . . .  | 92         |
| 7.2      | Jet Noise Reduction . . . . .  | 100        |
| 7.3      | Wing Noise Reduction . . . . .   | 105        |
| 7.4      | Landing Gear Noise Reduction . . . . .                                   | 110        |
| 7.5      | Quietest Airplane Designs . . . . .                                      | 115        |
| 7.6      | Chapter Conclusion . . . . .   | 116        |
| <b>8</b> | <b>Discussion</b>  | <b>119</b> |
| 8.1      | Main Findings . . . . .  | 119        |
| 8.2      | Outlook . . . . .  | 123        |
| <b>9</b> | <b>Conclusion</b>  | <b>129</b> |
|          | <b>Index</b>   | <b>131</b> |
|          | <b>References</b>  | <b>133</b> |
| <b>A</b> | <b>Additional Figures</b>  | <b>151</b> |
| <b>B</b> | <b>Error Estimation</b>  | <b>177</b> |
| B.1      | Error Estimation: Single Sound Source Compared with Four Sound Sources . | 177        |

**C Additional Data and Information Describing the Airplane Designs 179**  
C.1 Center of Gravity of the B747-400 . . . . . 179  
C.2 Data of All Airplanes . . . . . 179



# List of Figures

- 1.1 Outline of the thesis . . . . . 6
- 2.1 Sound emission angles ( $\alpha^*$  and  $\beta^*$ ). . . . . 7
- 2.2 Flap side-edge noise-reduction device. . . . . 11
- 2.3 Main landing gear of a B747-400 . . . . . 12
- 3.1 PrADO process chain . . . . . 19
- 3.2 Application of PrADO to the different steps of airplane calculation. . . 21
- 3.3 Typical approach procedures: LDLP, CDA, and SCDA. . . . . 23
- 3.4 Engine sound source splitting. . . . . 25
- 4.1 Airplane location relative to the microphone on the ground. . . . . 27
- 4.2 Reference airplane . . . . . 28
- 4.3 Fixed and variable camber Kruger flap . . . . . 29
- 4.4 Payload range chart of B747-400 original and PrADO model . . . . . 31
- 4.5 B747-400 approaching at Parchim International Airport, Germany . . . 33
- 4.6 Principle of a spectrum recorded by a surface, a 1.2 m, and a free-field microphone . . . . . 34
- 4.7 Microphone locations . . . . . 35
- 4.8 Categories of the investigated events. . . . . 39
- 4.9 Measured SPL spectra at microphone and reverse-calculated up to the airplane’s location . . . . . 39
- 4.10 Level time histories for idle-thrust approach events: 073-23 and 089-23 . 40
- 4.11 Reverse-calculated sound emission spectra and PANAM-calculated sound emission spectra for idle-thrust events: 073-23 and 089-23. . . . . 41
- 4.12 Level time histories for medium-thrust approach events: 071-21 and 053-21. . . . . 42
- 4.13 Fan broadband noise spectrum for event 086-21 in 60° direction and A-weighting function. . . . . 42
- 4.14 Reverse-calculated sound emission spectra and PANAM-calculated sound emission spectra for five events at medium thrust. . . . . 43
- 4.15 Level time histories for the two full-thrust departure events: 072-21 and 086-21. . . . . 44
- 4.16 Reverse-calculated sound emission spectra and PANAM-calculated sound emission spectra at full thrust during departure for 30° prior to the overhead position (prior to noise model modification) . . . . . 45
- 4.17 Old and new coefficients for the buzz-saw component of the fan noise model. . . . . 46
- 4.18 Level time histories for the two full-thrust departure events, 072-21 and 086-21, applying the buzz-saw noise update. . . . . 47
- 4.19 Reverse-calculated sound emission spectra and PANAM-calculated sound emission spectra at full thrust during departure for 30° prior to the overhead position (after noise model modification) . . . . . 47
- 4.20 Reverse-calculated sound emission spectra and PANAM-calculated sound emission spectra for the overhead position (after noise model modification) . . . . . 48

|      |  |    |
|------|--|----|
| 5.1  | Area under investigation. . . . .  | 50 |
| 5.2  | Segments of the ICAO-A departure procedure . . . . .   | 55 |
| 5.3  | Reference departure procedure compared to other thrust settings . . . . .  | 56 |
| 5.4  | Low drag minimum power procedure . . . . .   | 58 |
| 5.5  | Reference approach procedure compared to other approach procedures . . . . .   | 59 |
| 6.1  | Correlation coefficients of various variables with Departure Awakening Index . . . . .   | 63 |
| 6.2  | Trajectories of all airplanes from the basic airplane study flying the ICAO-A procedure. . . . .   | 64 |
| 6.3  | Correlation coefficients of various variables with the Approach Awakening Index . . . . .  | 67 |
| 6.4  | Overall Awakening Index over the aspect ratio for $\varphi_{LE} = 36^\circ$ . . . . .  | 70 |
| 6.5  | Ground track length up to a flight height of 1200 m over the aspect ratio for $\varphi_{LE} = 36^\circ$ and all the wing areas. . . . .                  | 71 |
| 6.6  | Cruise configuration approach velocity over the aspect ratio for $\varphi_{LE} = 36^\circ$ . . . . .   | 72 |
| 6.7  | Overall Awakening Index over the wing area for $\varphi_{LE} = 36^\circ$ . . . . .   | 73 |
| 6.8  | Maximum takeoff weight over the aspect ratio for $\varphi_{LE} = 36^\circ$ . . . . .   | 74 |
| 6.9  | Velocity at the end of the cruise configuration segment over the wing areas for the leading-edge sweep angle $\varphi_{LE} = 36^\circ$ . . . . .         | 74 |
| 6.10 | Overall Awakening Index over the leading-edge sweep angle for $A_W = 520 \text{ m}^2$ . . . . .  | 76 |
| 6.11 | Maximum takeoff weight over the leading-edge sweep angle for $A_W = 520 \text{ m}^2$ . . . . .   | 77 |
| 6.12 | Velocity at the end of the cruise configuration segment over the leading-edge sweep angle for $A_W = 520 \text{ m}^2$ and all the aspect ratios. . . . . | 78 |
| 6.13 | Direct Operating Cost Index and Overall Awakening Index for the various airplane designs including the reference B747-400. . . . .                       | 79 |
| 6.14 | Manual: How to read the legend showing the dominating noise sources. . . . .   | 81 |
| 6.15 | Dominating noise sources during departure of the basic airplane . . . . .  | 82 |
| 6.16 | Dominating noise sources during approach of the selected basic airplane . . . . .  | 83 |
| 6.17 | Comparison of the departure trajectories of the basic airplane to the reference airplane. . . . .  | 83 |
| 6.18 | Dominating noise sources during departure of the reference airplane . . . . .  | 84 |
| 6.19 | Difference in the A-weighted maximum SPL during departure of the basic airplane compared to the reference airplane. . . . .                              | 85 |
| 6.20 | Dominating noise sources during approach of the reference airplane. . . . .  | 85 |
| 6.21 | Difference in the A-weighted maximum SPL during approach of the basic airplane compared to the reference airplane. . . . .                               | 86 |
| 7.1  | Engine-over-wing airplane . . . . .  | 92 |
| 7.2  | Pylon mounted perpendicular to the wing's chord plane . . . . .  | 93 |
| 7.3  | Awakening Index over x-position of the fan disc center of the engine-over-wing airplane . . . . .  | 94 |
| 7.4  | Direct Operating Cost Index over Awakening Index of the engine-over-wing airplane . . . . .  | 95 |
| 7.5  | Departure and approach trajectories of the engine-over-wing airplane and the basic airplane. . . . .   | 97 |
| 7.6  | Dominating noise sources of the engine-over-wing airplane during departure . . . . .   | 98 |
| 7.7  | Difference in the A-weighted maximum SPL during departure of the engine-over-wing airplane compared to the basic airplane. . . . .                       | 98 |
| 7.8  | Dominating noise sources of the engine-over-wing airplane during approach . . . . .  | 99 |
| 7.9  | Difference in the A-weighted maximum SPL during approach of the engine-over-wing airplane compared to the basic airplane. . . . .                        | 99 |

|          |  |     |
|----------|--|-----|
| 7.10     | Departure and approach trajectory of the new-engine-option airplane and the engine-over-wing airplane. . . . .   | 102 |
| 7.11     | Dominating noise sources of the new-engine-option airplane during departure . . . . .  | 102 |
| 7.12     | Difference in the A-weighted maximum SPL during departure of the new-engine-option airplane compared to the engine-over-wing airplane. . . . .             | 103 |
| 7.13     | Dominating noise sources of the new-engine-option airplane during the approach . . . . .   | 103 |
| 7.14     | Difference in the A-weighted maximum SPL during approach of the new-engine-option airplane compared to the engine-over-wing airplane. . . . .              | 104 |
| 7.15     | A-weighted SPL at 30 km before approach threshold on the ground track of the new-engine-option airplane compared to the engine-over-wing airplane. . . . . | 104 |
| 7.16     | Departure and approach trajectories of the low-noise-wing airplane and the new-engine-option airplane. . . . .   | 107 |
| 7.17     | Dominating noise sources of the low-noise-wing airplane during departure   | 108 |
| 7.18     | Difference in the A-weighted maximum SPL during the departure of the low-noise-wing airplane compared to the new-engine-option airplane. . . . .           | 108 |
| 7.19     | Dominating noise sources of the low-noise-wing airplane during the approach . . . . .  | 109 |
| 7.20     | Difference in the A-weighted maximum SPL during approach of the low-noise-wing airplane compared to the new-engine-option airplane. . . . .                | 110 |
| 7.21     | Landing gear fairing of the landing-gear-fairing airplane . . . . .  | 111 |
| 7.22     | Departure and approach trajectory of the landing-gear-fairing airplane and the low-noise-wing airplane. . . . .  | 113 |
| 7.23     | Dominating noise sources of the landing-gear-fairing airplane during approach . . . . .  | 113 |
| 7.24     | Difference in the A-weighted maximum SPL during approach of the landing-gear-fairing airplane compared to the low-noise-wing airplane. . . . .             | 114 |
| A.5.0.1  | Departure Awakening Index as in Figure 5.3 with unmodified Kontos fan sound model. . . . .   | 151 |
| A.6.0.2  | Correlation coefficients of various variables with the Overall Awakening Index . . . . .   | 152 |
| A.6.1.3  | Max. climb angle over the Departure Awakening Index of the basic airplane  | 153 |
| A.6.1.4  | Distance until a height of 1200 m is reached over the Departure Awakening Index . . . . .  | 154 |
| A.6.1.5  | Sketch explaining that a steep averaged climb response lowers the ground noise . . . . .   | 155 |
| A.6.2.6  | Velocity at the end of the cruise configuration segment over the Approach Awakening Index of the basic airplane. . . . .                                   | 156 |
| A.6.3.7  | Leading-edge sweep angle and Overall Awakening Index for the various airplane designs of the basic airplane study. . . . .                                 | 157 |
| A.6.3.8  | Overall Awakening Index over the aspect ratio for $\varphi_{LE} = 36^\circ$ . . . . .  | 158 |
| A.6.3.9  | Departure Awakening Index over the aspect ratio for $\varphi_{LE} = 36^\circ$ . . . . .  | 159 |
| A.6.3.10 | Approach Awakening Index over the aspect ratio for $\varphi_{LE} = 36^\circ$ . . . . .   | 159 |
| A.6.3.11 | Ground track length up to a flight height of 1200 m over the aspect ratio for $\varphi_{LE} = 28^\circ$ . . . . .  | 160 |
| A.6.3.12 | Ground track length up to a flight height of 1200 m over the aspect ratio for $\varphi_{LE} = 44^\circ$ . . . . .  | 160 |
| A.6.3.13 | Glide ratio in cruise configuration ( $E_{cr,e}$ ) over the aspect ratio for $\varphi_{LE} = 36^\circ$ . . . . .   | 161 |
| A.6.3.14 | Maximum takeoff weight over the aspect ratio for $\varphi_{LE} = 36^\circ$ . . . . .   | 161 |
| A.6.3.15 | Overall Awakening Index over the wing area and over the aspect ratios for $\varphi_{LE} = 36^\circ$ . . . . .  | 162 |
| A.6.3.16 | Fuel mass for the design mission over the wing area for $\varphi_{LE} = 36^\circ$ . . . . .  | 162 |

|          |   |     |
|----------|---|-----|
| A.6.3.17 | Overall Awakening Index over the leading-edge sweep angle for $A_W = 520 \text{ m}^2$ . . . . .   | 163 |
| A.6.3.18 | Approach Awakening Index over the leading-edge sweep angle for $A_W = 520 \text{ m}^2$ . . . . .  | 164 |
| A.6.3.19 | Operating empty weight over the leading-edge sweep angle for $A_W = 520 \text{ m}^2$ . . . . .  | 164 |
| A.6.3.20 | Trip fuel mass for design mission over the leading-edge sweep angle for $A_W = 520 \text{ m}^2$ . . . . .                               | 165 |
| A.6.4.21 | Direct Operating Cost Index and Awakening Index for the <b>basic airplane</b> study, colored by leading-edge sweep angle . . . . .      | 166 |
| A.6.4.22 | Direct Operating Cost Index and Awakening Index for the <b>basic airplane</b> study, colored by wing area . . . . .                     | 167 |
| A.6.5.23 | Dominating airframe noise sources during approach of the selected basic airplane. . . . .   | 167 |
| A.6.6.24 | Dominating airframe noise sources during approach of the reference airplane. . . . .  | 168 |
| A.7.1.25 | Direct Operating Cost Index over Awakening Index of the engine-over-wing airplane study, colored by wing area . . . . .                 | 169 |
| A.7.1.26 | Direct Operating Cost Index over Awakening Index of the engine-over-wing airplane study, colored by leading-edge sweep angle . . . . .  | 170 |
| A.7.1.27 | Dominating airframe sound sources of the engine-over-wing airplane during approach . . . . .  | 170 |
| A.7.2.28 | Direct Operating Cost Index over Awakening Index of the new-engine-option airplane . . . . .  | 171 |
| A.7.2.29 | Direct Operating Cost Index over Awakening Index of the new-engine-option airplane study, colored by wing area . . . . .                | 171 |
| A.7.2.30 | Direct Operating Cost Index over Awakening Index of the new-engine-option airplane study, colored by leading-edge sweep angle . . . . . | 172 |
| A.7.2.31 | Dominating airframe noise sources of the new-engine-option airplane during approach . . . . .   | 172 |
| A.7.3.32 | Direct Operating Cost Index over Awakening Index of the low-noise-wing airplane . . . . .   | 173 |
| A.7.3.33 | Direct Operating Cost Index over Awakening Index of the low-noise-wing airplane study, colored by wing area . . . . .                   | 173 |
| A.7.3.34 | Direct Operating Cost Index over Awakening Index of the low-noise-wing airplane study, colored by leading-edge sweep angle . . . . .    | 174 |
| A.7.3.35 | Dominating airframe noise sources of the low-noise-wing airplane during approach . . . . .  | 174 |
| A.7.4.36 | Dominating airframe noise sources of the landing-gear-fairing airplane during approach . . . . .  | 175 |
| B.1.0.1  | Observer location relative to the airplane's center of gravity (COG) and engine locations . . . . .                                     | 177 |
| B.1.0.2  | Estimated noise prediction error due to considering the engine location in the airplane's COG . . . . .                                 | 178 |

# List of Tables

- 4.1 B747-400 data [13] . . . . . 29
- 4.2 Approach and departure procedures flown during measurements at Parchim International Airport. . . . . 35
- 4.3 Selected events to compare measurements with simulations. . . . . 36
- 4.4 Weather conditions during flyover measurements on Sep. 09<sup>th</sup> 2008 . . . . . 36
- 4.5 Data available from Flight Management Computer . . . . . 37
- 4.6 Noise sources and models used to predict airplane noise emission; and damping models to consider atmospheric attenuation and ground effect. . . . . 38
- 4.7 Old and new coefficients of the buzz-saw component of the fan noise model . . . . . 46
  
- 6.1 Parameters that have been varied and their respective range for the parameter study of the basic airplane . . . . . 61
- 6.2 Effects of the planform parameters on the averaged climb response. . . . . 65
- 6.3 Effects of the planform parameters on the velocity at the end of the cruise configuration segment. . . . . 69
- 6.4 List of sound sources regarding the legend of the plots showing the awakening probability and respective sound sources . . . . . 81
  
- 7.1 List and description of the investigated noise-reducing technologies . . . . . 90
- 7.2 List of the design parameters and their ranges . . . . . 91
- 7.3 Airplane data of the engine-over-wing airplane design (eow) compared to the basic airplane and reference airplane (ref). . . . . 96
- 7.4 Airplane data of the new-engine-option airplane (neo) compared to the engine-over-wing airplane (eow) and reference airplane (ref). . . . . 101
- 7.5 Airplane data of the low-noise-wing airplane (lnw) compared to the new-engine-option airplane (neo) and reference airplane (ref). . . . . 106
- 7.6 Airplane data of the landing-gear-fairing airplane (lgf) compared to the low-noise-wing airplane (lnw) and reference airplane (ref). . . . . 112
- 7.7 List with the values of the planform parameter for the quietest airplane designs 115
- 7.8 List with the values of the planform parameters of the selected airplane designs 116
  
- 9.1 List of the reduction of additional awakening reactions for the selected airplane designs relative to the respective previous technology level . . . . . 129
  
- C.1 Airplane data of this thesis' concepts. . . . . 180



# Nomenclature

## List of Symbols

| Symbol                          | Unit                            | Meaning  |
|---------------------------------|---------------------------------|--|
| $f$                             | [Hz]                            | frequency  |
| $f_{\text{bpf}}$                | [Hz]                            | blade passing frequency  |
| $g$                             | $[\frac{\text{m}}{\text{s}^2}]$ | acceleration due to gravity, standard value: $9.807 [\frac{\text{m}}{\text{s}^2}]$             |
| $h$                             | [m]                             | flight height  |
| $h_{\text{cb}}$                 | [m]                             | cutback height   |
| $l$                             | [m]                             | length   |
| $l_{\text{dep}}$                | [m]                             | ground track length from the brake release point   |
| $l_{\text{dep},h=1200\text{m}}$ | [m]                             | ground track length from the brake release point up to a flight height of 1200 m               |
| $m$                             | [kg]                            | mass   |
| $m$                             | [–]                             | mode   |
| $m_{\text{fuel,des}}$           | [kg]                            | trip fuel mass for design mission  |
| $m_{\text{man,empty}}$          | [kg]                            | manufacturer empty weight  |
| $m_{\text{op,empty}}$           | [kg]                            | operating empty weight   |
| $\dot{m}$                       | $[\frac{\text{kg}}{\text{s}}]$  | mass flow  |
| $\dot{m}_{\text{ref}}$          | $[\frac{\text{kg}}{\text{s}}]$  | reference mass flow  |
| $n$                             | [–]                             | counter, $n \in \mathbb{Z}$  |
| $p$                             | [Pa]                            | pressure   |
| $p_{\text{corr}}$               | [–]                             | p-value to prove statistical significance  |
| $r$                             | [–]                             | Pearson's correlation coefficient  |
| $r$                             | [m]                             | observer distance to the sound source  |
| $s_W$                           | [m]                             | wing span  |
| $v$                             | $[\frac{\text{m}}{\text{s}}]$   | velocity   |
| $v_{\text{amb}}$                | $[\frac{\text{m}}{\text{s}}]$   | ambient flow velocity  |
| $v_{\text{gse}}$                | $[\frac{\text{m}}{\text{s}}]$   | velocity at the end of the cruise configuration segment of the low drag minimum power approach |
| $v_{\text{stall}}$              | $[\frac{\text{m}}{\text{s}}]$   | stall speed  |
| $v_{\text{stall,gse}}$          | $[\frac{\text{m}}{\text{s}}]$   | stall speed at the end of the cruise configuration approach segment                            |
| $v_2$                           | $[\frac{\text{m}}{\text{s}}]$   | takeoff safety speed   |
| $\dot{v}$                       | $[\frac{\text{m}}{\text{s}^2}]$ | acceleration   |
| $x$                             | [m]                             | x direction  |
| $x_{\text{ac,cog}}$             | [m]                             | x-position of the airplane's center of gravity, measured from A/C nose                         |

|                      |   |   |
|----------------------|---|---|
| $x_{ac,FDC}$         | [m]   | x-position of the fan disc center, measured from A/C nose       |
| $y$                  | [m]   | y direction   |
| $y_{eng}$            | [m]   | engine spanwise distance from the airplane's x-z plane          |
| $A_i$                | [m <sup>2</sup> ]                                 | area element  |
| $A_W$                | [m <sup>2</sup> ]                                 | wing area   |
| AWI                  | [%]   | Awakening Index   |
| AWI <sub>app</sub>   | [%]   | Approach Awakening Index  |
| AWI <sub>dep</sub>   | [%]   | Departure Awakening Index                                       |
| $C_L$                | [-]   | wing or whole airplane lift coefficient                         |
| $C_{L,cr,e}$         | [-]   | wing or whole airplane lift coefficient at end of cruise flight |
| DOC                  | $[\frac{\text{cost}}{\text{seat}\cdot\text{km}}]$ | direct operating cost   |
| DOC <sub>ref</sub>   | $[\frac{\text{cost}}{\text{seat}\cdot\text{km}}]$ | direct operating cost of the reference airplane                 |
| DOCI                 | [%]   | Direct Operating Cost Index, B747-400 as reference              |
| $E$                  | [-]   | glide ratio   |
| $E_{cr,e}$           | [-]   | glide ratio at end of cruise flight                             |
| $E_{tot}$            | [J]   | total energy  |
| $L_p$                | [dB]  | sound pressure level (SPL)                                      |
| $L_{pA}$             | [dB]  | A-weighted SPL  |
| $L_{pA}(t)$          | [dB]  | A-weighted SPL time history                                     |
| $L_{pA,max}$         | [dB]  | A-weighted maximum SPL  |
| $L_{p,fan}$          | [dB]  | SPL of fan sound  |
| $\Delta L_{p,sweep}$ | [dB]  | delta SPL due to sweep  |
| $Ma$                 | [-]   | Mach number   |
| $Ma_{cr}$            | [-]   | cruise Mach number  |
| $Ma_{T,rel}$         | [-]   | relative fan blade tip Mach number                              |
| $Ma_{T,rel,des}$     | [-]   | relative design fan blade tip Mach number                       |
| $N$                  | [-]   | number of pair of scores  |
| $N_1$                | $[\frac{1}{min} \vee \%]$                         | fan rotational speed  |
| $N_{1,cb}$           | [%]   | cutback engine speed  |
| $N_{1,ne}$           | [%]   | never-exceed engine speed                                       |
| $N_{1,to}$           | [%]   | takeoff engine speed  |
| $N_{AWR}$            | [-]   | number of awakening reactions                                   |
| $N_{AWR,ref}$        | [-]   | number of awakening reactions of the reference scenario         |
| $N_{AWR,i}$          | [-]   | awakenings per area element                                     |
| $N_R$                | [-]   | number of rotor blades of the engine                            |
| $N_S$                | [-]   | number of stator vanes of the engine                            |
| $P_{AWR}$            | [%]   | probability of awakening response                               |
| $P_{AWR,i}$          | [%]   | probability of awakening response in the area element i         |
| $T$                  | [kN]  | thrust  |
| $\frac{MLW}{A_W}$    | $[\frac{N}{m^2}]$                                 | wing loading at maximum landing weight                          |
| $\frac{MTOW}{A_W}$   | $[\frac{N}{m^2}]$                                 | wing loading at maximum takeoff weight                          |
| $\alpha$             | [°]   | angle of attack   |
| $\alpha_{max}$       | [°]   | maximum angle of attack   |
| $\alpha^*$           | [°]   | polar sound emission angle                                      |
| $\beta^*$            | [°]   | sideline sound emission angle                                   |
| $\gamma$             | [°]   | descent or climb angle  |
| $\gamma_{max}$       | [°]   | max. climb angle along departure using maximum engine           |
|                      | thrust  |   |

|                       |  |  |
|-----------------------|--|--|
| $\gamma_1$            | [°]  | slope of the first approach segment  |
| $\gamma_2$            | [°]  | slope of the second approach segment   |
| $\eta_{\text{fan}}$   | [-]  | fan stage isentropic efficiency  |
| $\kappa$              | [-]  | heat capacity ratio  |
| $\lambda$             | [m]  | wavelength   |
| $\varphi$             | [°]  | 25%-chord sweep angle  |
| $\varphi$             | [rad]  | directivity angle = $\text{radian}(\beta^*) + \pi$                           |
| $\varphi_{\text{LE}}$ | [°]  | leading-edge sweep angle   |
| $\pi$                 | [-]  | ratio of the circle's circumference to its diameter, standard value: 3.14159 |
| $\pi_{\text{t,fan}}$  | [-]  | fan total pressure ratio   |
| $\rho_{\text{corr}}$  | [-]  | Spearman's correlation coefficient   |
| $\rho_{\text{pop},i}$ | $\left[\frac{\text{people}}{\text{km}^2}\right]$ | population density   |
| $\Lambda_{\text{W}}$  | [-]  | aspect ratio of the wing   |

## List of Indices

### Subscripts

|              |  |
|--------------|--|
| <i>ac</i>    | aircraft, airplane                                     |
| <i>amb</i>   | ambient  |
| <i>app</i>   | approach   |
| <i>ax</i>    | axial  |
| <i>bp</i>    | bypass   |
| <i>bpf</i>   | blade passing frequency                                |
| <i>cb</i>    | cutback  |
| <i>cog</i>   | center of gravity                                      |
| <i>cr</i>    | cruise flight  |
| <i>des</i>   | design point/design mission                            |
| <i>dep</i>   | departure  |
| <i>e</i>     | end  |
| <i>empty</i> | empty  |
| <i>fan</i>   | fan  |
| <i>flap</i>  | flap = trailing-edge HLD                               |
| <i>fuel</i>  | fuel   |
| <i>gse</i>   | end of the glide segment (low drag minimum power app.) |
| <i>h</i>     | flight height  |
| <i>i</i>     | counter, $i \in \mathbb{N}$                            |
| <i>kin</i>   | kinetic  |
| <i>man</i>   | manufacturer   |
| <i>max</i>   | maximum  |
| <i>ne</i>    | never exceed   |
| <i>op</i>    | operating  |

| <b>Subscripts (continued)</b> | <b>Meaning</b>                 |
|-------------------------------|--------------------------------|
| <i>p</i>                      | pressure                       |
| <i>pop</i>                    | population                     |
| <i>pot</i>                    | potential                      |
| <i>ref</i>                    | reference                      |
| <i>rel</i>                    | relative                       |
| <i>slat</i>                   | slat, Kruger flap              |
| <i>stall</i>                  | stall                          |
| <i>sweep</i>                  | sweep                          |
| <i>t</i>                      | total                          |
| <i>to</i>                     | takeoff                        |
| <i>tot</i>                    | total                          |
| <i>x</i>                      | x direction                    |
| <i>y</i>                      | y direction                    |
| <i>z</i>                      | z direction                    |
| <i>A</i>                      | A-weighted                     |
| <i>AWR</i>                    | additional awakening reactions |
| <i>D</i>                      | drag, overall airplane         |
| <i>FDC</i>                    | fan disk center                |
| <i>I</i>                      | Inlet                          |
| <i>L</i>                      | lift, overall airplane         |
| <i>LE</i>                     | leading edge                   |
| <i>R</i>                      | rotor                          |
| <i>S</i>                      | stator                         |
| <i>T</i>                      | fan tip                        |
| <i>TE</i>                     | trailing edge                  |
| <i>W</i>                      | wing                           |
| <i>1,2</i>                    | counter; in engine for shafts  |

| <b>Superscripts</b> | <b>Meaning</b>            |
|---------------------|---------------------------|
| *                   | directivity from airplane |

## List of Abbreviations

|              |   |
|--------------|---|
| <b>A/C</b>   | aircraft  |
| <b>ACDA</b>  | advanced continuous descent approach  |
| <b>AGL</b>   | above ground level  |
| <b>ALDLP</b> | advanced low drag low power approach  |
| <b>ANP</b>   | Aircraft Noise and Performance Database, Eurocontrol                              |
| <b>ANOPO</b> | Aircraft Noise Prediction Office, NASA  |
| <b>AzB</b>   | Anleitung zur Berechnung von Lärmschutzbereichen (ground noise prediction method) |
| <b>BPF</b>   | blade passing frequency   |
| <b>BWB</b>   | blended wing body   |
| <b>CAA</b>   | computational aeroacoustics   |
| <b>CAS</b>   | calibrated airspeed   |
| <b>CDA</b>   | continuous descent approach   |

|                |  |
|----------------|--|
| <b>CFD</b>     | computational fluid dynamics   |
| <b>COG</b>     | center of gravity  |
| <b>DLR</b>     | German Aerospace Center (Deutsches Zentrum für Luft- und Raumfahrt), Germany |
| <b>EASA</b>    | European Union Aviation Safety Agency  |
| <b>EPNdB</b>   | effective perceived noise decibel  |
| <b>FAA</b>     | Federal Aviation Administration, USA   |
| <b>FDC</b>     | fan disc center  |
| <b>FEM</b>     | finite element method  |
| <b>FFI 2.0</b> | Frankfurter Fluglaermindex 2.0   |
| <b>FMC</b>     | Flight Management Computer   |
| <b>GPS</b>     | global positioning system  |
| <b>HeNAP</b>   | helical noise abatement procedure  |
| <b>HLD</b>     | high-lift device   |
| <b>IATA</b>    | International Air Transport Association                                      |
| <b>ICAO</b>    | International Civil Aviation Organization                                    |
| <b>IFL</b>     | Institute of Aircraft Design and Lightweight Structures, TU Braunschweig     |
| <b>IRU</b>     | inertial reference unit  |
| <b>l.e.</b>    | leading edge   |
| <b>LDLP</b>    | low drag low power approach  |
| <b>LNA</b>     | DLR-Low Noise Aircraft   |
| <b>LNAS</b>    | Low Noise Augmentation System  |
| <b>LW</b>      | landing weight   |
| <b>MCDA</b>    | modified continuous descent approach   |
| <b>MLW</b>     | maximum landing weight   |
| <b>MSL</b>     | main sea level   |
| <b>LW</b>      | landing weight   |
| <b>MODATA</b>  | modified IATA procedure  |
| <b>MSL</b>     | main sea level   |
| <b>MTOW</b>    | maximum takeoff weight   |
| <b>NASA</b>    | National Aeronautics and Space Administration, USA                           |
| <b>OEI</b>     | one engine inoperative   |
| <b>ONERA</b>   | Office national d'études et de recherches aérospatiales, France              |
| <b>PAX</b>     | passenger  |
| <b>PDF</b>     | Portable Document Format   |
| <b>QFF</b>     | Q-Code: pressure at MSL at the present weather conditions                    |
| <b>RSS</b>     | rotor-stator spacing   |
| <b>SCDA</b>    | segmented continuous descent approach  |
| <b>SEL</b>     | sound exposure level [dB]  |
| <b>SFC</b>     | specific fuel consumption [ $\frac{kg}{N \cdot s}$ ]                         |
| <b>SLDLP</b>   | step low drag low power approach   |
| <b>SPL</b>     | sound pressure level   |
| <b>TAS</b>     | true airspeed  |
| <b>TAT</b>     | total air temperature  |
| <b>TOB</b>     | third-octave band  |
| <b>TOBL</b>    | third-octave band level  |
| <b>TOW</b>     | takeoff weight   |

**TU Braunschweig** University of Technology Braunschweig, Germany  
**UHBR** ultra-high bypass ratio  
**USA** United States of America  
**UTC** coordinated universal time

## List of Software

**ANOPP** Aircraft Noise Prediction Program, NASA  
**BCOP** Boeing Climb Out Program  
**FLIPNA** Flightpaths for Noise Analyses, DLR, Version 1  
**FRIDA** Framework for Innovative Design in Aeronautics, Università degli Studi Roma Tre  
**GTLab** Gas Turbine Laboratory, DLR, Cologne  
**LIFTINGLINE** LIFTINGLINE V2.5, DLR  
**PANAM** Parametric Aircraft Noise Analysis Module, DLR, Version VS2010\_1-1-26  
**PrADO** Preliminary Aircraft Design and Optimization Tool, IFL, TU Braunschweig, Verion 11-2015  
**PROFAN** Prediction Model For Airframe Noise, DLR  
**SHADOW** ray-tracing program to calculate shielding effects, DLR

# 1 | Introduction

Aircraft noise is linked with numerous health issues, such as high risk of cardiac ailments, high blood pressure, irritation, and even mental and psychological disorders. Furthermore, humans affected by aircraft noise rate their health as weak and their quality of life as low [91, 94, 132, 216]. These aforementioned health issues are associated with sleep deprivation or even insomnia caused by noise disturbance due to night flyovers [19, 109]. An uninterrupted sleep is crucial to relax as well as recharge the body and mind [18, 156, 219], since it maintains brain functions and also retains and improves memory as well as its plasticity [220, 221].

The total count of passengers per year who traveled by means of airplane has doubled from about 2.25 billion to 4.50 billion from 2006 to 2019 [148]. The two leading airplane manufacturers, Boeing and Airbus, estimated the annual growth rate of European air traffic to be 3.2% and 3.1%, respectively [4, 36]. These estimates refer to passenger kilometers between 2016 and 2036. Although these forecasts exclude the *Covid-19* lockdown impacts, air traffic is still expected to grow further, as was observed after the oil and financial crisis in the past [182]. In the future, aircraft noise resulting from air traffic growth is likely to become a more prevalent concern for residents near airfields. It is an even greater issue in developing countries, which hold a majority of the world's population. Therefore, all the challenges accompanying this trend become significant and need to be studied as well as resolved in order to improve the human well-being and quality of life. Thus, large airplanes are suitable to manage this increasing air traffic. Their associated noise pollution in the future needs to be reduced as much as possible.

As per recommendations by the International Civil Aviation Organization (ICAO), the so-called *Balanced Approach* constituting of the following pillars should be considered for airplane noise reduction [119]:

1. *Reduction of Noise at Source:*

This measure focuses on the application of low-noise technologies on-board to reduce the sound generated by the airplane. Sound sources can be removed, replaced, or their respective emitted sound can be reduced. Also, moving and shielding these sound sources might lower their relevance on the ground.

2. *Land-use Planning and Management:*

Appropriate planning and organization of airfields, cities, and areas vulnerable to airplane induced noise pollution is a significant measure to moderate this issue. For example, new airports shall be constructed away from noise sensitive regions, and noise sensitive institutions should be built away from noise exposed areas.

3. *Noise Abatement Operational Procedures:*

Another method would be to operate the airplanes on noise abatement procedures. Such strategies can be comprised of noise preferential runways, routes, and adjusted procedures for takeoff and landing. Selecting certain trajectories and routes helps to redistribute the

airplane noise impact away from sensitive areas. Ongoing research [155] is dedicated to investigate such routing of air traffic around cities and to minimize its effects on the population.

#### 4. *Operating Restrictions:*

Apart from the above-mentioned methods, another approach to curb noise pollution by airplanes are restrictions. For instance, banning very noisy aircraft or flight operations during nighttime is feasible.

Plenty of efforts have been directed to attain a reduction of sound emissions that are related to specific parts or sound sources of airplanes, which correspond to measure number 1 of the ICAO Balanced Approach. Research advancements in past decades have already achieved the drastic noise reduction by increasing the engine's bypass ratio. This lowered the jet sound emission, although the increase in the bypass ratio is mainly owed to the reduced fuel consumption [161, 207].

To effectively reduce noise on the ground, a holistic approach is required. This involves incorporating the noise-reducing technologies integrated into the overall "airplane" system and examining the consequential effects [105].

Diedrich et al. [54] described such a multidisciplinary design and optimization process for airplane concepts that also predicts their environmental impact. The airplane data of this optimization has been stored in a database. This project had been continued by Hileman et al. [105], who investigated the airplane database.

Later, Hileman et al. [104] researched their database for interesting correlations. However, they kept the takeoff weight constant for their noise study [104, Section VI.I]. They found airplanes with a low leading-edge sweep angle and large wing area were quieter, whereas more fuel-efficient airplanes with smaller wing area and greater sweep angle were louder.

Research work being done at Cranfield University, United Kingdom, focuses on investigating unconventional architectures like blended wing body, broad deltas, and joined wing concepts. They further investigated solutions such as low-speed airplanes, and architectures with specifications as per the Silent Aircraft Initiative [151]. The aim is to achieve a reformed airplane design that simultaneously reduces overall transport cost, effects on global warming, and ground noise.

Werner-Westphal et al. [222, 223] applied a software called Preliminary Aircraft Design and Optimization Tool (PrADO) and coupled it with ground noise predictions to assess the DLR-Low Noise Aircraft (LNA) as well as other airplanes. The ground noise has been predicted using an early stage noise prediction module as a version implemented in PrADO before switching to a noise prediction module called Parametric Aircraft Noise Analysis Module (PANAM).

Bertsch [24] replaced PrADO's aforementioned early stage noise module with PANAM, a more flexible and enhanced noise prediction module, that is continuously upgraded [24, 25, 27, 28]. In 2008, PANAM has been validated using flyover measurements of an A320 [24, 30].

This PrADO-PANAM process chain, also used in this work, has been upgraded by Blinstrub [32]. He implemented a trajectory prediction module called Flightpaths for Noise Analyses (FLIPNA). This module enables fast trajectory prediction within the preliminary design phase for noise analysis.

Researchers at Stanford University [8] built an airplane optimization process and applied it to a 280-passenger airliner. They studied the influence of design parameters with the

ultimate aim to lower the airplane's fuel consumption and ground noise at the certification points [9].

Researchers at Università degli Studi Roma Tre [120, 121], Italy, also studied conventional and unconventional airplane concepts. They developed the software called Framework for Innovative Design in Aeronautics (FRIDA) to investigate airplane designs under the consideration of cost, ground noise at the ICAO certification points, and the size of selected sound exposure level contour areas.

## 1.1 Research Scope and Objective

This thesis aims to analyze the effect of value changes of three selected planform parameters and sequentially applied low-noise technologies on the ground noise. The planform parameters, whose values are changed, are the leading-edge sweep, the aspect ratio, and the wing area. The applied noise-reduction technologies are fan sound shielding, ultra-high bypass ratio engine, droop nose at the wing's leading edge, brush at the wing's trailing edge, and landing gear fairing. Each planform parameter forms a dimension of a matrix. The noise reduction technologies are an additional dimension. Further possible dimensions, such as population distribution, payload factor, and departure and approach procedures, are held constant. In total, therefore, a four-dimensional matrix will be filled with data. This data will be researched for correlations with the ground noise. The ground noise is calculated in terms of the Awakening Index that is calculated from the additional awakening reactions. A combination of the Direct Operating Cost Index and the Awakening Index shall be minimized.

All modifications affect the airplane's mass and its aerodynamics, and hence its flight performance. Airplane design and flight path are mutually linked by the flight performance and affect the ground noise [32, 106]. The individual flight performances have been considered while calculating the approach and the departure trajectories. Thus, each trajectory of an airplane differs from the trajectory of another airplane. The approach procedure has been selected, in order that each airplane utilizes its respective flight performance to minimize its approach-induced ground noise, although a parameter variation is avoided. The ICAO-A departure procedure has been held constant within the whole investigation.

The consideration of the whole system of airplane design, low-noise technologies, and departure as well as approach trajectories is hereby carried out to lower the overall ground noise. As low-noise technologies are likely to affect the flight performance, the lowering of one sound source might increase another one. For example, when a specific low-noise technology eliminates the respective sound source, simultaneously lowering the maximum lift, this leads to an increased approach speed. Then, other sound sources might even surpass the original sound pressure level.

Much previous noise research has been conducted on small- and medium-sized airplanes [24, 32]. But to meet the challenge of air traffic growth, this noise research should also be conducted on large airplanes, such as the LNA [222] or even the B747-400.

The large airliner B747-400 has been chosen for the following reasons:

- large airplanes are an assumed solution to manage the expected air traffic growth
- large airplanes dominate the size of noise protection zones at grand hub airports [123, page 15/16]
- there are available synchronized noise measurements and flight recorder data
- PANAM shall be validated for large airplanes within this thesis

The noise source mechanisms of the airframe components of large long-haul airplanes are the same as for mid-sized airplanes. Thus, also noise-reducing measures, at a first glance, are expected to have a comparable impact on the ground noise for both mid-size and large airplanes. However, a changed drag affects the fuel consumption and might have a stronger economic impact on long distances than on short ones. Therefore, any change might influence more the takeoff weight of long-range than of short- and mid-range airplanes. The takeoff weight also conditions the takeoff performance and its respective ground noise. Hence, it is crucial to investigate the effects of noise-reducing technologies on long-range airplanes and their respective ground noise apart from the mid-range airplanes.

Furthermore, the four-engine airplane provides an excess 33 % of thrust to meet the safety standards in the one-engine-inoperative case. This leads to flatter climb trajectories compared to two-engine airplanes, which feature 100 % excess of thrust. Therefore, various noise reduction measures might have a different impact on four-engine airplanes because the noise along departure of such airplanes impacts over a larger area on the ground. Consequently, measures and technologies, which lower the ground noise caused by the departure, acquire greater significance for four-engine airplanes.

Finding solutions for shielding the fan sound becomes challenging with four-engine tube-and-wing airplanes because always two engines will be more shielded than the remaining two engines. This is due to the shape of the wing, as chord length continues to decrease with increasing spanwise position. In this case, the optimal engine placement in longitudinal direction has been determined to curb the ground noise.

The aforementioned input leads to the main research question:

**To what extent can the ground noise for redesigned large and heavy, long-range tube-and-wing airplanes be reduced, both with and without low-noise technologies?**

Further objectives of this thesis are to answer the following sub-questions:

1. Which characteristics offer the potential to reduce the ground noise of an airplane, and how will an alteration of the planform contribute to that?
2. What are the effects of selected and sequentially applied low-noise technologies on the ground noise?
3. What are the consequences of the sequentially applied low-noise technologies to the airplane design?

To answer these questions, this thesis is based on three previously published works from Heinze, Bertsch, and Blinstrub. Heinze [99] developed PrADO to calculate the airplanes. Bertsch [24] focused on programming and validating PANAM and implementing it into the PrADO. In addition, he redesigned commercially successful mid-sized airplanes of A319/A320 series in PrADO and predicted their ground noise with PANAM. The focus of redesigning these airplanes was to reduce their ground noise by fan sound shielding. Blinstrub [32] developed the trajectory software FLIPNA to rapidly investigate approaches and departures in terms of their ground noise, and included this software in the PrADO-PANAM process chain. FLIPNA calculates the trajectories, which are described by a few parameters, at low computational cost. This makes FLIPNA suitable for the application in the early conceptual airplane design phase.

Compared to Bertsch's and Blinstrub's works [24, 32], this study differs in the type of the reference airplane investigated, the applied assessment method, and the approach to the parameter study.

In this thesis, this PrADO-PANAM process chain is applied to build a database for advanced research of noise reducing characteristics. Bertsch's, Blinstrub's, and Heinze's works<sup>1</sup> enable to consider many effects at once. Subsequently, selected low-noise technologies have been exploited to further research the noise reduction capabilities. The created database will be used to identify the characteristics featuring low-noise airplane designs.

This study aims to consider as many impacts as possible. Particular attention is paid ensuring that as much noise-relevant effects as possible are considered, such as the impact of over-the-wing mounted engines on the takeoff weight or the required horizontal stabilizer size for each wing planform including its impact on the flight mechanics.

This means that the ICAO Balanced Approach measures 1 and 3, which are the noise-reducing technologies and the noise-reducing procedures, have been combined and used. The effects, which result from the noise-reducing technologies, such as changed aerodynamics<sup>2</sup>, structure masses, flight mechanics, as well as stall speeds at different high-lift configurations, have been considered in the whole study. The resulting fuel masses have been reflected in the direct operating cost. The payload mass and design range have been kept constant, in order to keep the airplanes comparable. Payload and range are economic key factors to the airlines. However, the cruise speed<sup>3</sup> has been kept constant for the engine-under-wing airplanes, but has been neglected from the top-level aircraft requirements for the engine-over-wing airplanes, as reduced cruise speeds are required when the wing sweep is lowered. This is important because the cruise speed has an impact on the direct operating cost and the fuel consumption.

The scope of this investigation has been limited to the noisiest operating conditions, i.e., maximum takeoff weight and maximum landing weight, to keep the number of varying parameters low. This means that the payload factor has been set to 100 % and has been kept constant. However, the payload factor is assumed to have an additional impact on the selection process for the optimal airplane, as the quotient of payload to empty operating weight varies for each airplane design.

Available flyover measurements and synchronized flight recorder data has been utilized in order to validate PANAM for the B747-400. Therefore, the ground noise of the precisely flown trajectories has been simulated and compared to the flyover measurements.

## 1.2 Outline of this Thesis

The airplane noise source models and noise reduction technologies, as well as common approach and departure procedures, are outlined in Chapter 2. The outline of the most important chapters of this thesis is depicted in Figure 1.1. It starts with the selected software tools also inclusive of the software modifications, which are described in Chapter 3. In Chapter 4, the employed software is validated by comparing the simulated airplane payload range chart with available manufacturer data, and predicted ground noise with noise measurements. Chapter 5 addresses the metrics to assess the airplane designs, with focus on noise pollution of the residents living around an airport. All the stated methods have been

---

<sup>1</sup>Based on the work of numerous researchers.

<sup>2</sup>Sweep, wetted area, shock induced drag by over-the-wing mounted engines

<sup>3</sup>Further details are provided in Section 7.1.

applied in Chapters 6 and 7. Chapter 6 focuses on the basic effects of the wing design on the Awakening Index, and identifies the **approach speed** and **averaged climb response**<sup>4</sup> as the driving criteria for low-noise airplane design within a constant technology level. Chapter 7 focuses on the sequential implementation of low-noise technologies under consideration of the findings from the previous chapter. At every technology level, the prevailing noise source is identified that is reduced in the next step. The only exception is Section 7.1. In this section, the fan sound is shielded first before the dominant jet sound is reduced. The second to last chapter discusses the findings and, as discussions often result in new ideas, the outlook is directly integrated here. This chapter is followed by a short chapter containing a conclusive summary.

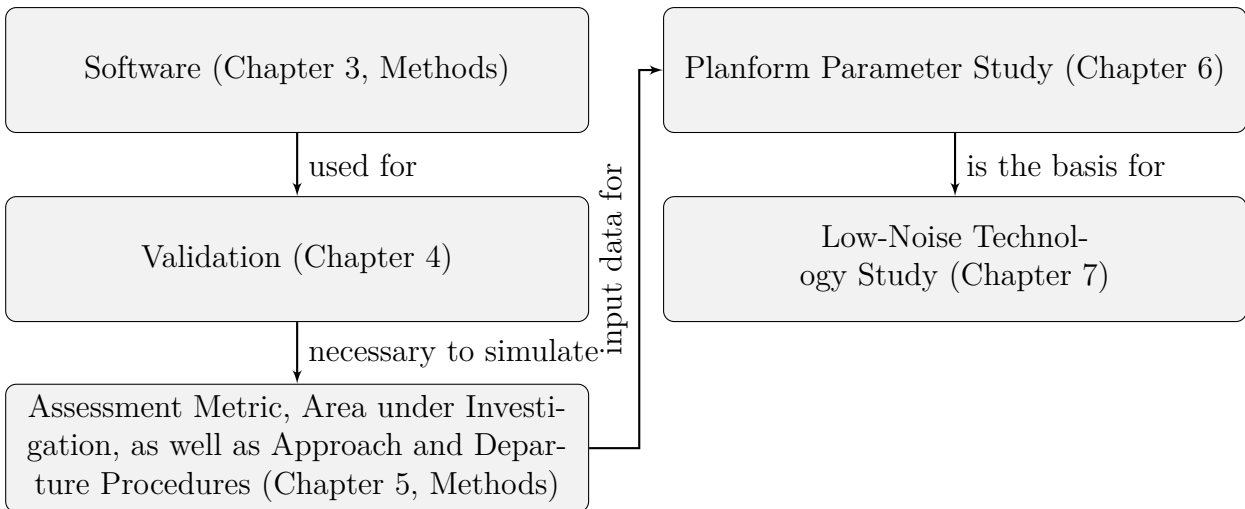


**Figure 1.1:** Outline of the thesis. The main part starts with the software, that has been validated. The assessment metrics presented in Chapter 5 have been used to evaluate the airplanes investigated in Chapters 6 and 7.

---

<sup>4</sup>Definition in Section 6.1.

## 2 | Noise Source Modeling and Planform Parameters

The airplane sound is a combination of airframe, engine sound, and interaction sound. Airframe sound consists of sound generated by wings, high-lift devices, empennage, and landing gears. Engine sound comprises jet sound as well as sound emitting from all engine components. The interaction of any two or more components generates interaction sound. The airplane emits sound and the audience on the ground perceives it as noise. As these models of the sound sources serve to predict the perceived noise, they are named as *noise source models*.

The noise source models, which are implemented in PANAM, are semi-empirical and, most of them, directional. The sound emission direction (red line) is relative to the airplane-fixed coordinate system, as sketched in Figure 2.1. In this figure,  $\beta^*$  is the sideline angle and  $\alpha^*$  is the polar angle.

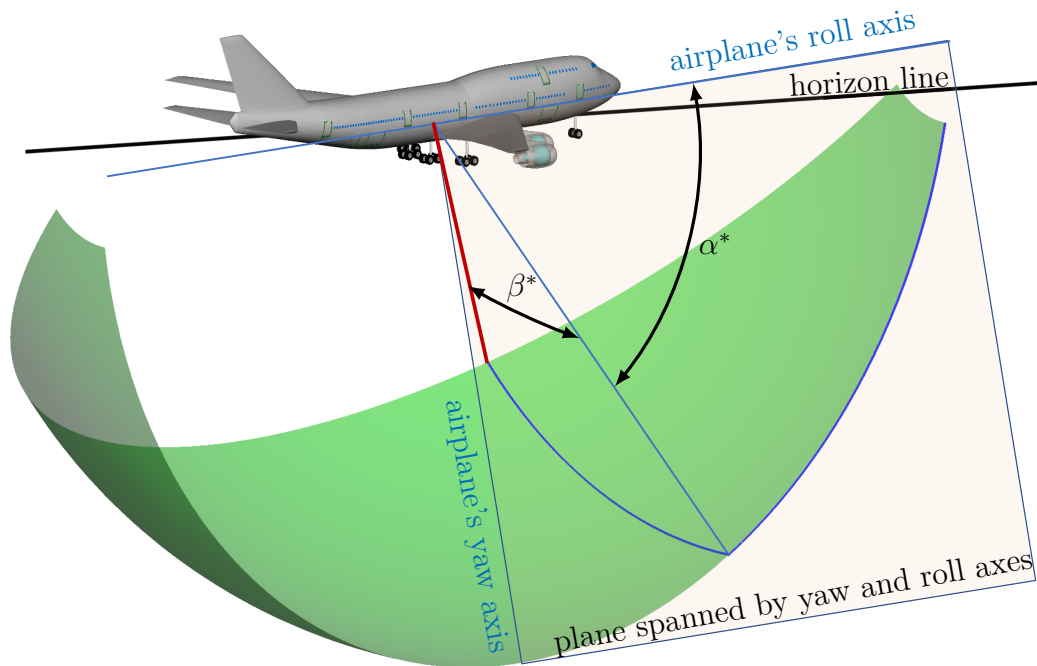


**Figure 2.1:** Sound emission angles ( $\alpha^*$  and  $\beta^*$ ). The sound emission angle to the sideline ( $\beta^*$ ) is measured between the sound emission direction (red line) and the plane spanned by the airplane's roll and yaw axis. When projecting the sound ray on this plane, the polar sound emission angle ( $\alpha^*$ ) is measured starting from the airplane's roll axis to this projected ray. The green sphere is centered in the airplane's center of gravity.

The following Sections 2.1 to 2.3 describe the mechanisms of airframe, engine, and interaction sound. While airframe and engine sound sources are an essential part of this thesis, the interaction sound sources have not been considered. Additionally, the Section 2.4 gives a short overview about the two flight phases departure and approach, which are crucial for the ground noise. Section 2.5 describes the three planform parameters that have been modified within the study.

## 2.1 Airframe Noise Sources

In July 1973, aircraft noise activities at National Aeronautics and Space Administration (NASA) have been consolidated in Aircraft Noise Prediction Office (ANOPO). The goal was to develop a comprehensive Aircraft Noise Prediction Program (ANOPP), which was one of the first combinations of different noise source models [177]. As engine sound dominated the overall airplane sound, ANOPO focused mainly on engine sound research. However, more and more effort was spent on reducing engine noise. Airframe noise levels were only 10 to 15 EPNdB below engine noise levels. Hence, when the engine noise reduction methods, which had been expected for the 1980s, would be successfully implemented then airframe noise would become significant. Fink concluded that the fundamental process of airframe noise radiation has to be understood [77]. He upgraded ANOPP by implementing different airframe noise source models to estimate the overall airframe sound [231]. These airframe noise models describe wing trailing-edge sound [78] in cruise configuration, trailing-edge flap sound [93], leading-edge flap and slat sound [74, 198], and landing gear sound [100].

A lot of effort was put into understanding the airframe sound generating mechanisms [58, 174] and, subsequently, to reduce the associated noise emission of its parts like the slat [46, 61, 63], flap [41, 187, 213], and landing gear [60, 178, 179]. Also, the German Aerospace Center (DLR) has developed noise prediction software to assess the ground noise of airplanes. These software are Prediction Model For Airframe Noise (PROFAN) and PANAM. As PANAM is used to assess the airplanes' ground noise, the noise models used in this thesis will be mentioned in the following sections. A short list of these models and their references is given in Table 4.6 on page 38.

### 2.1.1 Clean Wing

While the wing's leading edge is not a sound source at low turbulence inflow, the trailing edge is. At cruise configuration, the trailing edge dominates the airframe sound [143, Section 5.2]. This sound is generated by the interaction of the trailing edge with the turbulence within the boundary layer and the model is valid for moderate lift coefficient ( $C_L$ ) of  $C_L \leq 0.5$ . A broad overview of the wing sound study has been given by Lockard and Lilley [143]. The trailing-edge far-field sound intensity scales with the 5<sup>th</sup> power of the inflow velocity, originally discovered by Ffowcs-Williams and Hall [226]. Later, this has been confirmed theoretically by Howe [111] and experimentally by Brooks and Hodgson [40]. Perennes found a similar correlation of the sound intensity with the flow velocity, i.e., an exponent of 5.3, through experiments performed on a wing in cruise configuration [163]. In studies about noise reduction potential of trailing-edge sound, Herr [103] confirmed the 5<sup>th</sup> power scaling of the sound intensity with the inflow velocity. In her thesis, she provided a fundamental literature review. Also, she found that the trailing-edge thickness shifts (frequency-wise) the blunt trailing-edge noise humps, which appear at respective vortex-shedding frequencies. However, the trailing-edge thickness does not determine the overall sound pressure level.

## 2.1.2 High-Lift Devices

High-lift devices are required to enable slow flight during departure and approach. High-lift device sound is produced by the leading and trailing-edge high-lift devices, namely the slat or Kruger flap and the Fowler flap, respectively. Wind tunnel tests showed that the slotted slats and flap side edges are the most prominent sound sources [7, 63, 170]. Dobrzynski et al. [63] also investigated flap and slat sound together and found the slat drive tracks to be relevant sound sources.

### Leading-Edge High-Lift Device

Slat sound dominates between 200 Hz to 400 Hz and its sound intensity scales with approximately 4<sup>th</sup> to 5<sup>th</sup> power of the flow velocity in the relevant emission directions [63, 90, 141, 142, 170]. The scaling seems to depend on the direction of sound emission. In this investigation, the PROFAN slat noise model has been used, which features dependency of the sound intensity on the 5.0<sup>th</sup> power of the ambient flow velocity [56]. A conventional slat has two main sound sources, the trailing edge and the shear layer. The slat's trailing edge is blunt, generating high frequency sound through vortex shedding, and the shear layer instabilities generate low-frequency broadband sound [130]. Dobrzynski found that the slat drive tracks are very present locations of sound emission, as their localized sound pressure levels were 8 dB above pure slat noise [63]. This holds true for the whole frequency range of 2 to 40 kHz of a 1 : 10 scale model measured in a wind tunnel.

The Kruger flap is the leading-edge high-lift device mounted on the B747-400. Kruger flap noise is generated by the following mechanisms and parts:

- Cove Flow,
- Cavity,
- Brackets, and
- Gap Flow

ordered by their relevance according to Guo [90]. As per Almonit and Pott-Pollenske [5], the Kruger flap sound is likely to be caused by the drive arm. Dobrzynski et al. adjusted the coefficients of the PROFAN slat noise model to also predict the Kruger flap noise [56]. Hence, the PROFAN slat and Kruger flap noise source model is implemented in PANAM and has been utilized in this thesis to predict the noise generation of the leading-edge high-lift devices: the Kruger flaps.

Influence of leading-edge sweep angle on slat sound pressure level can be estimated by Eq. (2.1) from reference [56].

$$\Delta L_{p,\text{sweep}} = 20 \cdot \log(\cos(\varphi_{\text{LE}})) \quad (2.1)$$

The sweep-dependent sound emission is calculated from the leading-edge sweep angle ( $\varphi_{\text{LE}}$ ). A reduction of the leading-edge sweep angle from 42° to 30° would result in an increase in the sound pressure level of the leading-edge high-lift device. This increase is about 1.3 dB in case of a constant flight speed. The overall effect of sweep, considering mass and flight mechanics, will be investigated later in Section 6.3.3.

### Trailing-Edge High-Lift Device

The B747-400 uses triple-slotted flaps as trailing-edge high-lift devices. Their sound emission is modeled using the PROFAN trailing-edge noise model, which is a semi-empirical

prediction method provided in the references [24, 56]. As shown in the technical report [56], the flap noise model predicts the flap’s sound emission well. The worst-case deviation is an under-prediction of 2 dB OASPL for the departure flap setting [56, figure 28]. Dobrzynski discovered that flap trailing-edge sound of fully extended high-lift devices is low compared to slat and flap side-edge sound [63].

### Flap Side Edge

According to Khorrami et al. and Radeztsky et al. [131, 176], the cross flow at the flap ending determines the sound generation of the flap side edges. This has also been confirmed by Rossignol [187]. This cross flow is caused by the pressure difference between the lower and the upper side of the flap. At the sharp vertices at the flap endings, this flow detaches, forms vortices, and generates sound. Flap side-edge sound consists of two mechanisms. The flow separation at the sharp corners results in high frequency sound, mainly on the first half of the flap chord, whereas the interactions between the large-scale vortex and the flap corners result in low frequency sound [89]. Dobrzynski confirmed that the flap side edge dominates the flap sound and strongly contributes to the overall high-lift device sound within the frequency range of 1 kHz to 2 kHz [63].

Guo [87] provided a semi-empirical model to calculate flap side-edge sound. One decade later, Rossignol measured the flap side-edge sound in a wind tunnel [186] and developed a simple semi-empirical noise source model from the results. A first version of his model [187] was implemented in PANAM and is used in this investigation. This model depends only on flap deflection angle, chord length, and ambient flow speed. For this model, the knowledge of the peak frequency of the flap side-edge sound and its decay are sufficient to describe this sound source. Due to these few dependencies, this model is very fast and suitable for the noise predictions within the preliminary design stage.

Note, that only free flap side edges can experience cross flow. When the flap ending is bounded by, e.g., a fuselage or engine pylon, then no cross flow occurs, such that the flap ending is not considered in the calculation of the sound emission [56].

### Noise Reduction of High-Lift Devices

An overview about reduction of high-lift device sound was provided by Dobrzynski [58]. A very long chord slat, for example, could reduce the ground noise by two mechanisms: relocating the slat trailing edge further above the wing suction side, which reduces the local flow velocity at the slat’s trailing edge; and by flying slower due to an increased maximum lift coefficient [225].

Pott-Pollenske et al. were able to reduce the slat noise by 10 dB by diminishing the slat gap compared to the reference gap [166]. The sound source “slat” can be fully eliminated by replacing it with a droop nose, i.e., a wing leading-edge deformation device. A droop nose has the advantage to be an integral part of the wing, generating no additional noise. One disadvantage is that no new boundary layer is built on the non-deformed section of the suction side, as it would have done using a conventional slat. A new boundary layer would be more stable. Hence, the droop nose reduces the maximum angle of attack ( $\alpha_{\max}$ ) compared to a conventional slat. Within this study, a reduction of  $6.5^\circ$  has been assumed, which was derived from reference [169, Fig. 10]. When the maximum angle of attack is lower it leads to a decreased maximum lift coefficient compared to the higher angle of attack achieved with a conventional slat [7, 44, 169]. This results in a higher flight speed in the respective landing and approach configuration.

Few of the trailing-edge noise-reduction techniques consist of serrations, porous materials, and comb-type or bristle-like design [103]. In 1976, Filler published experimental results that demonstrated the effectiveness of a trailing-edge sweep angle to reduce noise [76]. When a low-swept trailing edge is furnished with serrations, each tooth creates short sections of high sweep. Such serrations have been theoretically investigated by Howe, who stated the noise reduction potential of saw tooth and sinusoidal shaped trailing-edge serrations [112, 113]. The application of porous material softens the impedance transition from the surface downstream to the free flow, as examined by Fink [79]. This treatment applied to a flap and slat trailing edge offered a noise reduction of 2 dB to 3 dB [80]. Furthermore, comb-type trailing edges have been investigated regarding noise reduction [101, 102]. They are easy to manufacture. These studies also provided design criteria for slit and comb-type trailing edges.

Figure 2.2 shows rubber endings closing the gap between two flap segments as applied on an A320 airplane. This rubber sealing obstructs the air flowing around the flap side edge along a major portion of its chord. The rubber filler hinders the flap side-edge sound mechanism where it bridges the gap from one flap segment to the neighboring one.



**Figure 2.2:** Flap side-edge noise-reduction device on an Airbus A320 NEO. The whole wing with the deflected inboard and outboard flap segment is depicted in the left picture. The gap between the two flap segments is sealed with a rubber filler avoiding the airflow from the pressure to the suction side. These rubber fillers are shown in detail in the right picture. Both photographs by Marc Koch © ⓘ ⊕.

The Coanda flap is a potential low-noise technology due to the increased lift coefficient, which lowers the approach speed [33]. Rossian et al. [185] studied the acoustic and aerodynamic effects of an active blown Coanda flap in combination with a droop nose. The Coanda flap sound comprises the following four major sound sources: The first sound source lies within the jet flow above the curvature of the junction between the main airfoil and the deflected flap; the second one is caused by the jet mixing noise; the third one is due to the interaction between the flap trailing edge and the turbulence in the flow that is passing the trailing edge; and the fourth one is flow separation noise. The flap trailing-edge sound becomes predominant when the flow on the flap's suction side detaches.

### 2.1.3 Landing Gear

The deployed landing gear, as depicted in Figure 2.3, is a significant sound source. The main strut, various tubes and pipes, wheels, brakes, and attached parts interact with the

airflow. This generates vortices and therefore sound. Landing gear sound intensity is proportional to the 6<sup>th</sup> power of the local flow velocity measured at the landing gear bogie [170, 203, 205]. The local flow velocity at the main landing gear, when mounted under the wing, is reduced compared to the ambient flow velocity because the flow circulation around the wing profile leads to a reduction of the velocity underneath the wing. The front landing gear encounters the ambient flow velocity ( $v_{\text{amb}}$ ) [88, 170, 206]. In the case of wide-body airplanes such as the B747-400 compared to narrow body aircraft, DLR investigations [59] observed a 2 dB higher sound pressure level of the front landing gear. The increased sound emission is due to a more complex construction compared to a simpler construction of smaller airplanes. This additional sound pressure level (SPL) has been considered in the whole study.



(a) right-bottom view. Photography by Adrian Pingstone [164], published under Public domain (a) front-bottom view. Photography by Ilias N. Diakoumakos, who kindly permitted its usage.

**Figure 2.3:** Main landing gear of the B747-400. The left picture shows the cables, open doors, cavities, retraction actuators, side stays, and struts. All parts cause turbulence in the passing airflow, and hence noise. Moreover, the right picture shows the deployed flaps downstream of the wing mounted landing gear.

Thomas et al. shortened and podded landing gears for evaluated airplanes to reduce their noise generation [217]. Only short fuselages allow such a modification, as the airplane has to pitch up to  $\approx 15^\circ$  during takeoff. Hence, the B747-400 fuselage length does not allow to shorten its landing gears. Podded landing gears might be disadvantageous on long-range flights due to the fairings, which possibly increase fuel consumption caused by higher drag. This would lead to more takeoff weight, which in turn amplifies the ground noise.

Li et al. [138] achieved a noise reduction of about 1.2 dB OASPL by applying perforated landing gear fairings. Within ranges of higher frequencies, the noise might slightly increase,

but does not affect the OASPL. Molin et al. [152] simulated the landing gear sound during the European SILENCER project and validated it using a flight test campaign conducted with an Airbus A340. An overall reduction of 1.8 EPNdB of the landing gear sound can be achieved at the approach certification point by mounting landing gear fairings. The wind tunnel test conducted during the SILENCER project demonstrated that the nose and main landing gear sound could be reduced by 5.4 EPNdB and 3.6 EPNdB, respectively.

Dobrzynski et al. [57] investigated fairings to reduce landing gear sound. Overall, a maximum reduction of 8 dB A-weighted sound pressure level of the landing gear was achieved compared to the SILENCER reference landing gear. This reduction is achieved assuming an optimal toe down bogie angle.

## 2.2 Propulsion Unit

The turbofan engine considered in this study consists of two prevailing noise sources, namely the fan and the jet. Compressor, combustor, and turbine sound are assumed to not determine the sound pressure level on the ground during the approach and departure and, hence, are neglected in PANAM. Especially the turbine sound occurs at high frequencies [137] and does not play a role at relevant distances between airplane and ground because it is attenuated by the atmosphere.

Hence, the following two subsections describe the two prevailing engine noise sources fan and jet. Noise reduction techniques are attached to each of the subsections.

### 2.2.1 Fan

The first versions of ANOPP focused on engine noise prediction. The first fan noise model, which was implemented in ANOPP, was originally developed by Dunn and Peart [65]. This has been enhanced by Heidmann [98]. Kontos et al. [136] improved this Heidmann fan noise model. This model has been continuously upgraded, particularly by NASA [43, 201].

The fan sound is mainly composed of two mechanisms, (a) the blade tip sound and (b) the rotor-stator interaction sound. A third mechanism occurs at supersonic flow relative to the fan blade and is called (c) combination tones. The tip region of the fan blades is a major contributor to the broadband sound emission (a) [197].

The rotor-stator interaction sound (b) is generated by (b.1) the interaction of the potential flow fields of rotor and stator [128] and (b.2) the fan blade wake creating a fluctuating flow field impinging on the stator blades as fixed boundaries, leading to pressure fluctuations [129, 197]. The combination tones (c), also known as buzz-saw noise, are the compression shocks forming at the fan blade leading edge, when its relative velocity is supersonic. These compression shocks radiate in the direction of flight that is at subsonic speed [154].

The fan noise model [136], which is implemented in PANAM, describes these three sound mechanisms, the blade tip sound, buzz-saw noise, and the rotor-stator interaction, by five separate components, namely: (d) inlet tones, (e) inlet broadband sound, (f) inlet combination tones, (g) aft tones, and (h) aft broadband sound. Each component (d-h) is described parametrically by strength, directivity, and spectra for each engine operating condition. According to the model by Heidmann [98] and Kontos [136], the SPL of fan sound ( $L_{p,\text{fan}}$ ) of the model components (d-h) scales with

$$L_{p,\text{fan}} \sim 20 \log \left( \frac{1}{\eta_{\text{fan}}} \left( \pi_{\text{t,fan}}^{\frac{\kappa-1}{\kappa}} \right) \right) + 10 \log \left( \frac{\dot{m}}{\dot{m}_{\text{ref}}} \right) \quad (2.2)$$

This equation shows that a high fan stage isentropic efficiency ( $\eta_{\text{fan}}$ ) and a low fan total pressure ratio ( $\pi_{\text{t, fan}}$ ) lower the sound emission. The heat capacity ratio ( $\kappa$ ) varies with temperature and pressure, and the increase in the mass flow ( $\dot{m}$ ) would increase the predicted fan sound. Further contributors are the relative fan blade tip Mach number ( $Ma_{\text{T,rel}}$ ), relative design fan blade tip Mach number ( $Ma_{\text{T,rel,des}}$ ), rotor-stator spacing, and the respective directivity of each component (d-h). The whole fan sound is predicted by these few parameters, such that the model is very fast at acceptable accuracy. Hence, it is suitable to predict the engine sound within this study.

## Fan Noise Reduction Techniques

Fan ground noise can be reduced by weakening the sound source or shielding the engine, performed individually or together. Weakening would mean to redesign the fan, the stator, or both, while shielding would hide the engine inlet or aft nozzle behind a surface.

Shielding seems to be a promising technique to reduce the engine ground noise by deflecting the fan sound up into the sky. The blended wing body is a beneficial architecture with a large shielding surface [64]. Within this thesis, the large wing of the B747-400 is used to shield the fan sound.

Also, Berton performed ground noise calculations of a four-engine airplane whose engines are shielded by the wing [23]. Berton predicted a significant reduction of the 90 EPNdB and 95 EPNdB contour areas close to the airport.

When the rotor's pressure field interacts with the stator's one, rotating pressure patterns occur called spinning modes. The fan and stator can be designed in such a way that the pressure field of these spinning modes exponentially decreases along the duct. For this purpose, the *Tyler and Sofrin selection rule*, as follows, is commonly applied to aero engines [218].

$$N_S > 1.1 \cdot (1 + Ma_{\text{T,rel}}) \cdot m \cdot N_R \quad (2.3)$$

In case of the relative fan blade tip Mach number ( $Ma_{\text{T,rel}}$ ) being close to one, the required number of stator vanes ( $N_S$ ) to be mounted is more than double the number of number of rotor blades ( $N_R$ ), but not in multiples of each other. At this ratio, the tone resulting from the rotating pressure pattern of the first circumferential mode ( $m = 1$ ) decreases exponentially along the duct. This is called cut-off mode. If the duct is long enough, this tone is so far reduced that it does not contribute to the sound pressure level on ground. For such a decrease in the second circumferential mode ( $m = 2$ ), Eq. (2.3) implies that more than four times as many stator vanes than rotor blades are required [207].

Increasing the chord of the stator vanes distributes their load, reduces their fluctuating local pressure coefficient, and thus leads to less sound generation [55]. The fan blade wake levels out better when the rotor-stator distance is increased. However, such designs require a longer engine and, therefore, increases the engine mass. Trailing-edge blowing could be utilized to 'fill in the wake' [215], but causes a more complex engine design. Furthermore, leaned and swept stator vanes are noise reducing techniques. Both modifications avoid that the rotor wake impinges simultaneously on the whole span of the stator's leading edge. Also fan casing design can contribute to reduce the broadband sound pressure level [12].

Liners are a very effective technology to lower the sound emission from an engine [38, 153, 184, 194]. Liners reduce the sound in the engine intake and in the discharge ducts by about 5 PNdB and 10 PNdB, respectively [207]. The majority of liners applied to engines comprise a perforated sheet, a solid sheet, and a supporting honeycomb structure which ensures the distance between these two sheets. Such a sandwich structure forms chambers with lengths

of about the one-fourth of the wavelength to be reduced. The sound wave going through the hole in the perforated sheet is reflected after one-fourth of its wavelength. The reflected wave released back into the duct after one additional fourth of its wavelength, leading to a  $180^\circ$  shift in its phase. This reflected wave lowers the amplitude of the sound wave within, a process called *reactive cancellation*. Other frequencies are damped by friction of oscillating air molecules in the small holes of the perforated plate, that is called *resistive damping*. The effectiveness of the liner scales with the engine's length-to-diameter ratio [204, 207], such that the sound propagating through the longer, narrower bypass duct is more reduced than the sound propagating through the shorter intake duct.

The aforementioned perforated sheet could be any sheet with holes or a tightly woven wire cloth. Such liners may also be manufactured as a double perforated layer, aiming to attenuate two frequencies and their harmonics [207]. In PANAM, the liner's effect on the sound pressure level is modeled using the description by Moreau et al. [153].

## 2.2.2 Jet

Stone originally published a jet noise model [208] and improved it a few years later [209]. This model has been continuously updated and refined by Stone et al. [210–212], considering suggestions by Low [144]. The version from reference [209] is implemented in PANAM and has been used in this thesis.

When the jet mixes with the ambient flow, it generates mixing sound, which is the sound source dominating the jet induced ground noise along the departure. The relative velocity between jet and ambient flow can be modeled as toroidal vortices, which is a vivid model to describe the mechanism [85, 114]. These toroidal vortices can be modeled as parallel circles, staggered along the jet axis in perpendicular planes. These vortices become larger as the distance to the nozzle increases and interact with each other. Hence, sound generation occurs in the whole jet area and most of the sound is emitted beyond the nozzle exit at a distance of about five to ten times the nozzle diameter. The generated frequency decreases with increased size of the interacting, toroidal vortices, implying that the jet emits higher frequency sound close to the nozzle and lower-frequency sound further away from it. Medium and high bypass turbofan engines create jets with their peak frequencies within 100 Hz to 500 Hz [210, figures 5 - 96]. Such engines have been mounted on the investigated airplanes within this study.

The jet sound emission strongly depends on the jet velocity. The radiated sound power rises with the increase in jet velocity. At low jet velocities, the jet sound becomes recessive compared to the other sound sources. Additionally, the jet sound also depends on the flight speed. The relative jet speed decreases when increasing the flight speed and keeping the jet velocity constant, leading to lower sound pressure levels in the far field. On the contrary, higher flight speeds increase the sound source volume in cubic meters [150], leading to unexpected higher sound pressure levels in the far field during cruise [149]. Jet sound at cruise conditions is a crucial topic for cabin comfort but is out of the scope of this thesis, as the focus is on ground noise affecting the residents around airports.

Stone's jet noise model [209] is confirmed to be reliable by Bridges, Bertsch and Guerin. Bridges et al. [39] compared multiple jet sound prediction methods and found that the Stone model results in a maximum deviation of roughly 2 dB with respect to experimental data. In conversations with Bertsch<sup>1</sup> and Guerin<sup>2</sup>, it was confirmed that the jet noise model is

---

<sup>1</sup>Verbal conversation with Lothar Bertsch, DLR AS, on Jan. 08<sup>th</sup>, 2019

<sup>2</sup>Verbal conversation with Sebastien Guerin, DLR AT, on Dec. 19<sup>th</sup>, 2018

robust and reliable for ground noise prediction within the preliminary airplane design phase. Hence, Stone’s jet noise model [209] has been utilized within this thesis.

## Jet Noise Reduction Techniques

Serrations in the nozzle exit lead to faster mixing of jet and free stream [158, 190]. This decreases the peak turbulence in the shear layer, which lowers the sound generation at low frequencies at the expense of level increase at higher frequencies. During early jet research, corrugated nozzles have been tested [86] and applied to supersonic jet velocities. The objective of such nozzles is the faster mixing of the jet with the ambient flow, leading to low scale vortices and higher frequencies. The sound source volume in cubic meters is reduced, which reduces the far-field sound.

The reduction of the jet velocity is the most effective noise reduction technique [191, 228]. Jet noise strongly depends on its velocity relative to the ambient flow. In the past, it was lowered by reducing the exit flow velocity. The thrust was maintained by increasing the mass flow, which raised the bypass ratio [190, 209]. However, an increased bypass ratio leads to a less effective, passive, acoustic treatment, namely reduced serration and liner efficiency. This drawback of a lowered efficiency of acoustic liners when increasing the bypass ratio is due to a relatively shorter liner length. The ratio of emitted fan sound to generated fan sound would thus increase [204, 207].

## 2.3 Interaction Noise

Interaction noise is an additional noise source that appears only due to the collaboration of two or more components. If one of these components is missing, the noise source disappears. Interaction noise occurs when the disturbed flow or its pressure field interacts with a component, e.g., landing gear wake interacting with the hard surface of the high-lift devices or, with reference to Rego’s literature review [181], the jet pressure field interacting with the hard flap surface. In 1982, Sengupta and Kipersztok [133, 196] investigated the jet-flap interaction noise. They pointed out that jet-flap interaction noise was present for the B707 with a CFM56 engine, but could not be identified for the B747-100 equipped with a JT9D engine. However, an interaction between the jet and flap surface could be expected for the B747, since the thrust gap of the B707 wing is larger than the one of the B747.

This jet-flap sound source is an interaction between the jet and a hard surface, with the shear layer between jet and free flow forming toroidal vortices. Each of these toroidal vortices possesses a pressure field, which passes fast under the deflected flaps or close to the flap endings. These pressure fields interact with the hard surfaces and, hence, generate sound, even without the jet plume brushing the surface [48, 226].

Jente et al. [125] investigated a wide range of values of selected parameters such as flap deflection angle, flap gap and overlap, and jet distance to flap trailing edge. They proved that the noise strongly depends on the distance between the trailing edge of the flap and the jet plume (center line). The sound emission of this interaction is dominant towards the forward direction.

When the landing gear wake impinges on the flap, a new low-frequency noise source occurs. It’s intensity scales with the 6<sup>th</sup> power of the ambient flow velocity ( $v_{amb}$ ) and depends on the vortex strength hitting the flap, which depends on the gear-flap-distance and exhibits no pronounced radiation directivity [115, 159].

It should be noted, that the state-of-the-art in sound source modeling is only weakly developed for interaction sound sources. Moreover, a proper quantification of the isolated interaction sound source is sometimes very difficult experimentally, since installation, engine, and airframe sound sources are very close to one another in both location and sound pressure levels. Yet, these interaction noise sources are not considered by PANAM, as they are usually avoided while designing low-noise airplanes.

## 2.4 Departure and Approach Procedures

Sound sources as mentioned in the previous sections are moved along trajectories to predict their ground noise. Departure and approach are of particular interest because during these flight phases, the airplane flies at low heights, the distance to the population is short, and hence the geometric and atmospheric attenuation is low. Therefore, it is important to keep sound emissions as low as possible during these flight phases. In the following paragraphs, a brief overview of relevant standardized procedures is given.

### Departure

General noise abatement departure procedures, NADP1 and NADP2, are described in reference [117]. The main difference between the two procedures is that while flying the NADP1 the airplane first gains height and then accelerates, while flying the NADP2 the airplane, after reaching the necessary minimum height, first accelerates, and then gains height. The departure noise can be reduced by optimizing the flight routes and their vertical trajectory profiles to lower the noise pollution of the population. In a vertical flight path optimization, parameters such as altitude, engine speed, and velocity are considered [96, 97]. The latter one might also affect the runway capacity. In 1972, Lufthansa launched a steep departure. The takeoff thrust was used to reach height up to 914m without acceleration after lift-off to increase the distance between the sound source and the ground as fast as possible. Before that, common procedures suggested climbing at 304m and then change over to an acceleration segment. Such departure procedure modifications usually relocate the ground noise impact, in order to downsize areas affected by high sound pressure levels. This expands, however, the ones affected by lower sound pressure levels.

By optimizing the flight routes, the ground tracks are planned to minimize the affected population [95]. Prats et al. investigated flight routes and considered fairness in their investigations [171, 172], which includes the weighing of the different noise-sensitive areas such as unpopulated, populated, and industrial areas.

### Approach

Horizontal and vertical optimization also works for approach procedures and their measures have already been listed in the *Balanced Approach* by the ICAO [119]. For safety reasons, horizontal optimization is only possible at greater heights, but not on the final approach segment. In Frankfurt, e.g., more than 20km before the runway the direction is maintained and the airplanes head straight for the runway. Populated areas aligned with the runway direction cannot be avoided. Additionally, airframe and engine noise are dominant during approach, making it complex to improve approaches.

Various procedures have been considered to be low-noise ones, which are comparatively quieter than free approaches conducted by pilots, employing high-lift devices and alternating airbrakes as well as engine thrust. Hence, low-noise procedures compare with this “free” behavior by letting pilots fly slow and high. Low drag low power (LDLP), continuous descent approach (CDA), segmented continuous descent approach (SCDA), and steep low drag low power (SLDLP) are examples of such procedures. The goal of all approach procedures is to fly as follows: the engine set close to approach idle, delayed high-lift devices deployment, at slow approach speed, and at great height [37, 53, 134, 157].

The further development of these standardized procedures leads to the helical noise abatement procedure (HeNAP). Along this procedure the airplane flies the descent section as a helical part to concentrate most of the ground noise within noise insensitive areas [29].

As per Boeing [36], most accidents occur during the approach flight phase. The pilot’s workload and experience are crucial and have to be considered during the planning of any procedure to ensure that flight tasks can sequentially performed by any pilot [68, 69].

## 2.5 Planform Parameters

Three planform parameters that describe the outline of airplane wing projected upon a horizontal plane have been studied with their effect on ground noise and operating cost of airplanes. These three planform parameters are described in the following paragraphs.

The aspect ratio determines if a wing is long and narrow (high aspect ratio) or short and wide (low aspect ratio). It is defined by

$$\Lambda_W = \frac{s_W^2}{A_W} \quad (2.4)$$

with the aspect ratio ( $\Lambda_W$ ) depending on the wing span ( $s_W$ ) and the wing area ( $A_W$ ). Increasing the wing span while keeping the wing area constant, raises the aspect ratio. Wings with high values of the aspect ratio experience less lift-induced drag because of reduced cross flow around the wing tips from the pressure to the suction side, thus forming a weaker wake turbulence. As per Raymer, the optimal aspect ratio should be determined by a trade study [180].

The wing area is relevant for the resulting wing loading and affects climb rate, stall speed, takeoff distance, and landing distance. Moreover, it influences the lift coefficient during cruise, the airplane’s wetted area, and, hence, the drag. The drag affects the required trip fuel mass. Additionally, the wing area conditions the required amount of material, which determines the empty weight. Both fuel mass and wing weight influence the takeoff weight and, hence, the takeoff performance [180].

Higher wing sweep lowers the wave drag during transonic cruise flight, as only the velocity perpendicular to the line connecting the airfoil’s thickest points<sup>3</sup> is significant for the critical Mach number. The higher the sweep angle, the weaker are the shocks formed at a constant transonic cruise speed. Increasing the wing sweep also raises the wing mass and lowers its lift by the cosine of the sweep angle [180]. A wing without sweep would require a reduced cruise speed, which would also lead to a less efficient engine operation. The wave drag also depends on airfoil, thickness ratio and taper ratio, but in this study their respective values have been kept constant.

---

<sup>3</sup>The line connecting the chord positions of maximum airfoil thickness of each section is, in a good approximation, the 25% chord.

### 3 | Software

Software to model airplane design, calculate trajectory, and assess ground noise has been collectively utilized to achieve the optimal airplane design with focus on ground noise and cost. The process chain visualized in Figure 3.1 has been used in this investigation and starts with designing the airplane in PrADO. PrADO uses the engine map, which is externally calculated with GTLab. SHADOW utilizes the airplane design to predict its fan sound shielding capability. PrADO also provides the flight performance. Together with the engine map, the flight performance map is the base for FLIPNA to calculate the trajectory. PANAM utilizes the trajectory, the airplane design, the engine map, and the shielding performance to predict the ground noise. Subsequently, this ground noise and the cost are used to assess the airplane designs by selected metrics that are described in Chapter 5.

The following sections in this Chapter 3 describe these software modules. Whereas, the last section lists modifications and upgrades of these software tools.

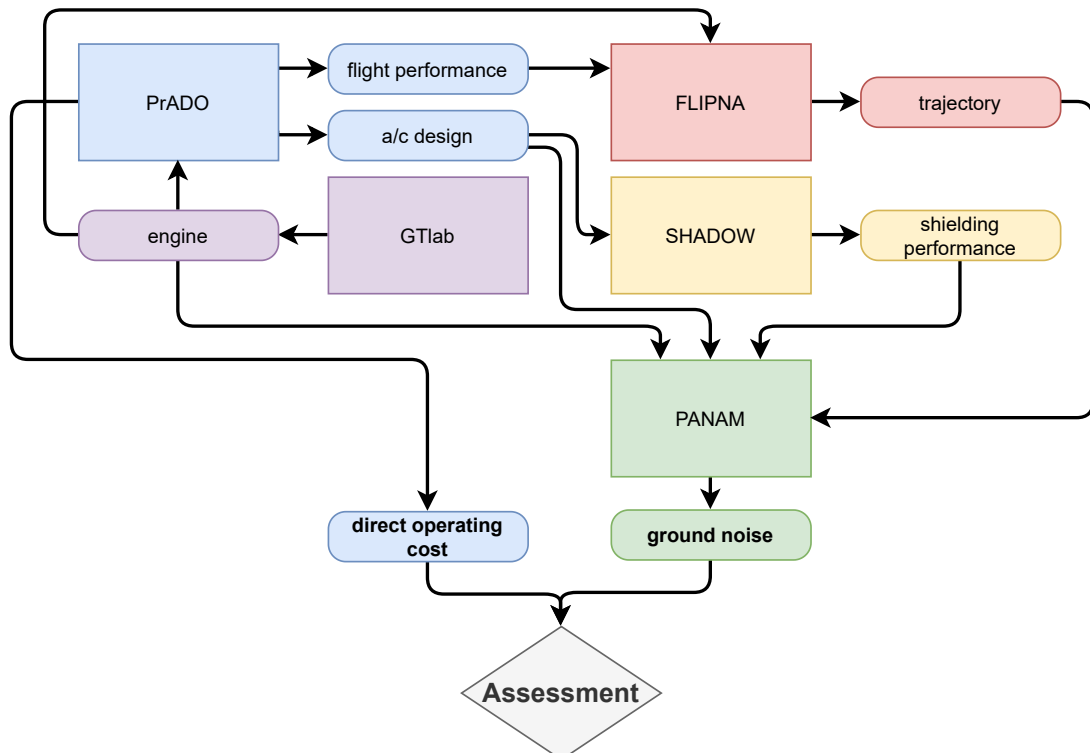


**Figure 3.1:** Applied process chain. Included are PrADO, FLIPNA, PANAM, and SHADOW.

## 3.1 Conceptual Airplane Design Software

PrADO [99] is a software program for the conceptual airplane design. This program combines multiple analytical and statistical analysis into an iterative working software package. It has been developed at TU Braunschweig by Wolfgang Heinze and is still being updated. PrADO provides the full physical flight mechanics, inclusive of aerodynamics and mass of each component and system mounted on and in the airplane [223]. The prediction of the fuselage and wing mass is based on the amount of material that is used to fulfill the airplane's structural requirements. The wing, for example, is sized using a beam model derived from finite-element simulations. Hence, this model is reliable and also applicable to unconventional airplane designs. Moreover, the software considers material's aging in terms of fatigue that leads to greater material thickness when parts are more strained. This design strain comprises the payload factor, the number of flights, and the fuel mass, which is used for the design range. The design range is derived from the mission specifications of the airplane. PrADO has been applied to about 50 different existing and conceptual airplane types such as the DLR *Low Noise Aircraft* [222], a *Blended Wing Body* [92], and the airplane design studies by Bertsch [24]. PrADO results show a good agreement with literature data [222] when applied to existing airplane designs.

Additionally, its available source code allows great flexibility, and thus supports this research. The airplane aerodynamics is calculated by the software called LIFTINGLINE [110], developed by DLR to determine lift distribution and lift-induced drag of any wing geometry. This is done by dividing the wing in a set number of panels, for which the lift is calculated individually. The drag of the airfoil and fuselage is calculated within PrADO to allow more flexibility in the choice of airfoil. For example, the B747-400 has been simulated with supercritical airfoils, which shift the onset of wave drag to higher Mach numbers. PrADO's modular structure enables to exchange modules and databases, such as the engine map replacement by the one calculated using GTLab [20, 183].

The parameter study investigates the influence of leading-edge sweep, aspect ratio, and wing area. For each value combination of the planform parameters, PrADO was applied up to four times from the initial design to the calculated airplane because the wing position, the size of the horizontal stabilizer, and the aerodynamics had to be adjusted. This is outlined in Figure 3.2. Before each additional calculation step, data was re-set by an external module that PrADO cannot automatically re-set within the internal iteration. After the first calculation, the wing position has been adjusted according to keep the wing's aerodynamic center at the same x-position measured from the nose. Between the second and third calculation, the horizontal and vertical stabilizer area, which have been suggested by PrADO, have been corrected and re-set using factors from Section 4.1. After the third calculation, airplanes with engines mounted under the wings are completely calculated. If the engines are mounted above the wings, then the aerodynamics must also be adjusted to account for the change in (wave) drag due to the pylons and engines causing the displacement effect. Hence, the total number of carried out simulations are the number of airplane designs given in Table 7.2 multiplied by three or four, respectively, depending on the engine location.

This procedure in Figure 3.2 should be adapted for future calculations. For example, it would be advantageous, if the simulations of critical flight conditions, which suggest too large horizontal stabilizer and vertical stabilizer areas in the current PrADO version, provide more accurate results in future calculations. This would have the great advantage of using PrADO's internal automatic tailplane area adjustment. More details about the tailplane sizes

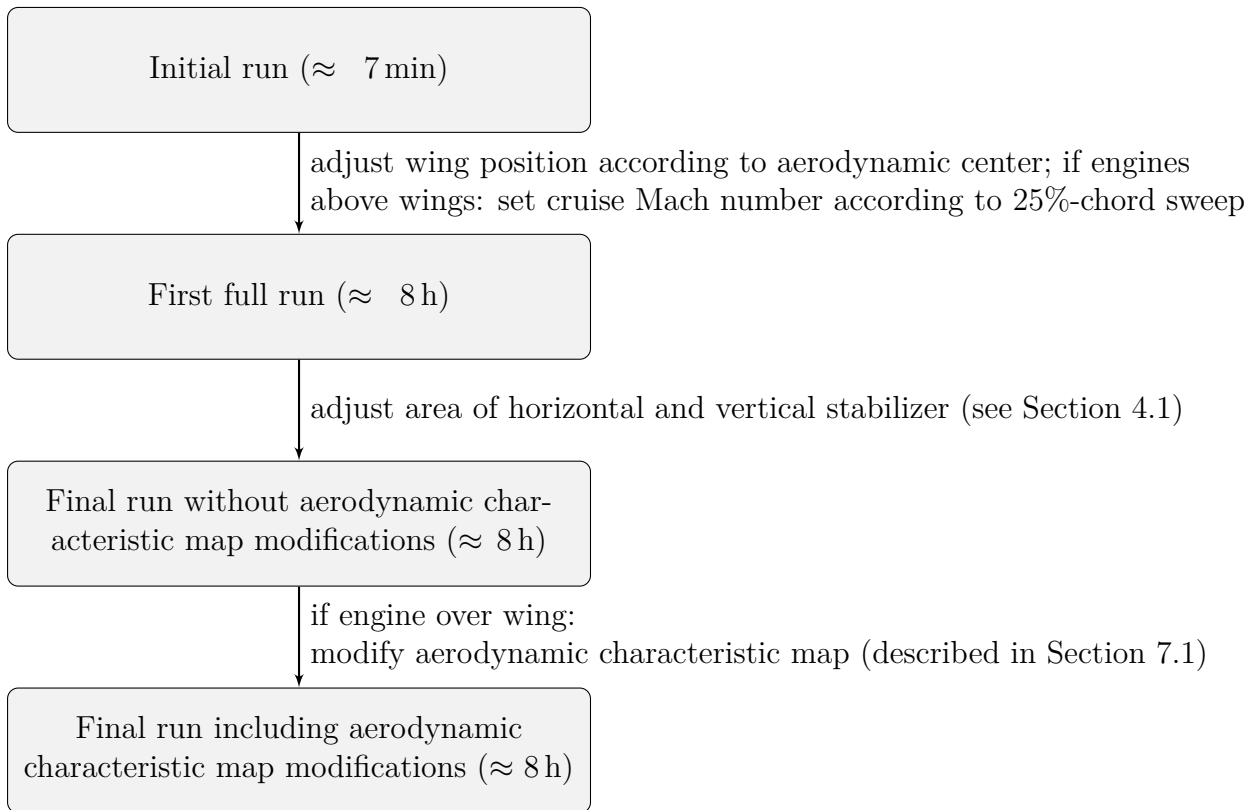


**Figure 3.2:** Application of PrADO to the different steps of airplane calculation. Each step represents a full calculation. Before each calculation, the input data was adjusted.

and why they were corrected are given in Section 4.1 on page 32. In the entire calculation process, the airplane is then already designed for the corresponding fuel consumption.

Furthermore, the procedure in Figure 3.2 can be simplified, if the adjustment of the aerodynamics is not done by an external module, as it has been done in this study, but the aerodynamics are already adjusted within PrADO. This can save a lot of computational time, since the aerodynamics, which condition the required fuel mass, are already considered in the first iteration steps of the calculation of an airplane.

In addition, the results showed that one should keep the quantities such as the stability margin constant in the airplane design software. The constant x-position of the aerodynamic center is disadvantageous because differently sized horizontal stabilizers result in different aerodynamically stable airplanes. This is, in a first approximation, acceptable. However, PrADO provides such a detailed resolution of individual effects that in the future it would be better to aim for a constant stability margin or at least a constant distance between the wing's aerodynamic center and the center of gravity of the airplane.

## 3.2 Trajectory Calculation for Noise Assessment

The approach and departure trajectories are calculated within a few seconds by a tool called FLIPNA [32]. As the aerodynamics and flight performance is individual for each airplane design, these calculations are performed for each airplane design. FLIPNA also

considers the engine map. This software is based on the Eq. (3.1)

$$\sin(\gamma) = \frac{T}{m} - \frac{1}{E} - \frac{\dot{v}}{g} \quad (3.1)$$

employing just a few parameters such as the trajectory descent or climb angle ( $\gamma$ ), thrust ( $T$ ), mass ( $m$ ), glide ratio ( $E$ ), acceleration ( $\dot{v}$ ), and acceleration due to gravity ( $g$ ). Such few dependencies make FLIPNA very fast and, hence, suitable for application in airplane preliminary design studies. FLIPNA calculates reliable, yet preliminary, trajectories for approach and departure. It should be noted that the calculation within FLIPNA is much more complex than Eq. (3.1). For example, the glide ratio depends on the pitching-moment equilibrium. In the pitching moment of the airplane, the engine thrust and the corresponding lever arm are also considered, as well as the lift and the pitching moment of the horizontal stabilizer and the wing. From this it is obvious that even a shift of the center of gravity is considered. The study presented in Chapter 6 has shown that a shift of the center of gravity has a moderate influence on the sound pressure level on the ground, but in direct comparison with other airplanes it is very much responsible for unexpectedly higher noise levels. This means that a change in the center of gravity position can also influence the rank order of airplanes.

Three different approach procedures, for example, are depicted in Figure 3.3. The segment slopes ( $\gamma_1$  and  $\gamma_2$ ) exist for segmented approach procedures, or with the workaround  $\gamma_1 = 0^\circ$  and  $\gamma_2 = \gamma < 0^\circ$  to describe a continuous descent approach (CDA) one. Before the airplane enters any segment along which it would accelerate, the high-lift devices are deployed to the approach configuration to prevent the airplane from accelerating and stalling. At a height of 914 m, the airplane intercepts the final approach segment and deploys its landing gears at 457 m. The high-lift devices have been fully deployed to landing configuration before the stabilization point, where the exact location depends on the flight performance of each airplane. At 305 m, the airplane stabilizes by increasing the engine thrust.

The most important parameters to define the departure are the takeoff engine speed ( $N_{1,to}$ ), the cutback engine speed ( $N_{1,cb}$ ), and the cutback height ( $h_{cb}$ ).

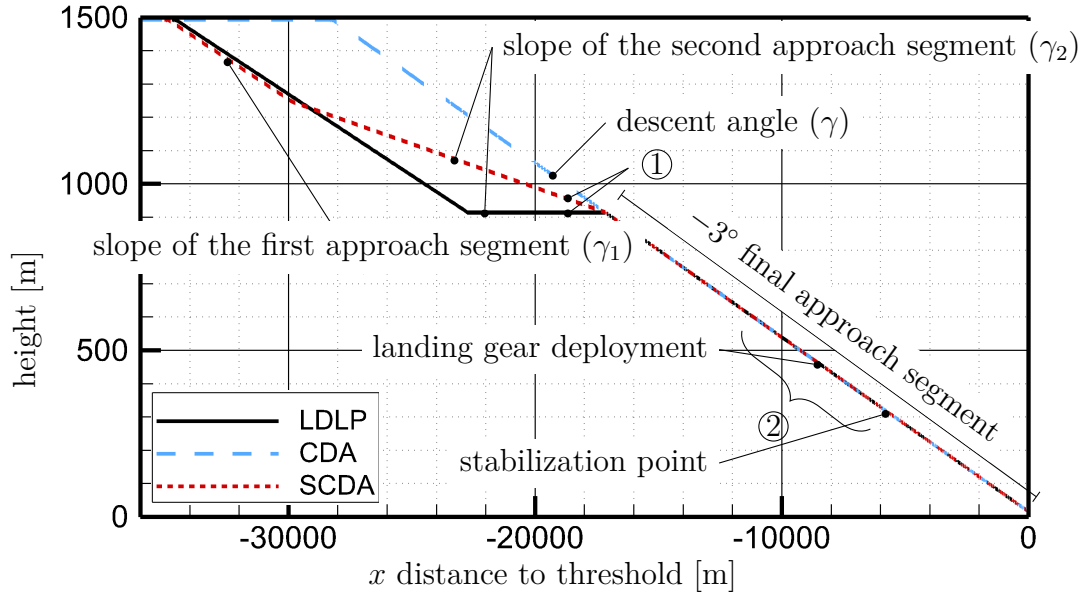


**Figure 3.3:** Typical approach procedures: low drag low power approach (LDLP), continuous descent approach (CDA), and segmented continuous descent approach (SCDA). The slope angles of the segments are used as input parameters for FLIPNA to describe the approach procedure and are marked within the figure. FLIPNA calculates the flap setting, speed, thrust, height, and the resulting interceptions of the segments from the aerodynamic characteristic map, engine performance map, and airplane mass.

- ①: high-lift devices deployment to approach configuration
- ②: high-lift devices deployment to landing configuration

### 3.3 Airplane Ground Noise Prediction

The airplane design, engine characteristic map, and trajectory are used by PANAM [24, 25] to predict the ground noise. PANAM consists of far-field noise source models pertaining to the airplane’s significant sound sources. These sound sources are the engine, high-lift devices, clean wing, landing gear, and the spoiler. All distances and directions from the sound sources to the receiver on ground are calculated from the center of gravity of the airplane. This leads to a small error in the prediction, whose extent depends on the location of the noise source and the airplane’s height, as visualized and comprehended in Appendix B.1. The figure shows that the engine noise prediction of the large B747-400 exhibits an error of a maximum of 0.1 dB at a height of 100 m only due to the spanwise position of the engines. Further uncertainties would be added on top, e.g., the uncertainty of the noise source models, the uncertainty from the propagation through the atmosphere, and the uncertainty from the ground effects. Such uncertainties have not been considered within this thesis. The engine noise itself is predicted by the fan and the jet noise models. Near-field sound is neglected. The predicted sound is propagated through the atmosphere [124] and influenced by the ground surface such as grass or concrete, before it is perceived by receivers. In case of this thesis, a sound-hard ground has been simulated by using the Anleitung zur Berechnung von Lärmschutzbereichen (AzB)-ground noise model from 2006 [42]. This ground effect corresponds to what would be measured with 10-meter microphones, although in these simulations all microphones are placed on the ground. The sound scattering in the atmosphere

due to turbulence [50] has been neglected, because only the noise level differences of the various airplane designs are of interest. This means that PANAM developers do not claim to predict absolute sound pressure values exactly, but to model differences between airplanes well. Human perception of sound is considered in terms of frequency weighing, herein the A-weighing. The noise source models implemented in PANAM are listed in Table 4.6, and have been validated using the medium-range A319 [24, 25, 31]. In the following Chapter 4, PANAM will also be validated for the large and heavy B747-400.

PANAM has been selected as the noise prediction tool as it offers the following advantages:

- high-speed calculation ( $\approx 500 \frac{\mu s}{\text{trajectory point-microphone location}}$  without shielding)
- access to the source code
- well-proved noise source models
- applicable to airplane design and trajectory optimization
- integrated into the PrADO-PANAM process chain
- reliable results, as demonstrated in a tool benchmark test with NASA and ONERA [30]

If the engines are mounted above a large-surface wing, PANAM considers the airplane’s fan sound shielding capability as predicted by SHADOW.

### 3.4 Fan Sound Shielding Prediction

SHADOW is a high-speed ray tracing software developed at DLR [146] to calculate the fan sound shielding capability of airplane geometries – much faster than computational aeroacoustics. It has been designed to be applied in the preliminary aircraft design phase and to model rays radiated from a point sound source to a hemisphere with any given radius. In the PrADO-PANAM workflow, it is applied to the simplified, no flow case. Shielding in a good approximation is a scattering problem at low Mach numbers. This software traces the rays to calculate the shadow zones originating from this point sound source and presents a high-frequency solution as sharp acoustic light and shadow zones, using the linearized Euler equation. The diffracted part is omitted in this calculation and, hence, the diffraction from acoustic-light zone to shadow zone is calculated with the Maggi-Rubinowicz form of the Kirchhoff diffraction theory [145]. The sound intensity along each ray is calculated based on the principle of energy conservation. PANAM uses the pure shielding and reflection by the airplane geometry, which has been provided by SHADOW, and later considers the atmospheric damping. The shielding surfaces are required to be longer and wider than the wavelength  $l \gg \lambda$  to be valid. SHADOW has good accuracy and calculates the results fast, enabling it to predict the shielding capability of an airplane design in the preliminary design phase. PANAM further applies these shielding factors to the fan sound as predicted by the noise models to estimate the fan induced ground noise.

### 3.5 Modifications

The modifications of the software are described in the following paragraphs. These modifications are assumed to support more accurate results.

PANAM has been upgraded in this thesis to also consider large airplanes. The airplane size is determined by the number of aisles set in PANAM’s airplane description, such that

a twin-aisle cabin determines a large one. Noise characteristics of large airplanes consider a 2 dB increase in the sound pressure level of the nose landing gear [56, equation 3.60].

In earlier PANAM versions, the shielding capability of the engine sound sources have been calculated for the fan disc center position [26]. However, this placement in the fan disc center would not consider the two actual locations of sound emission through the engine inlet and bypass nozzle, as visualized in Figure 3.4. Hence, the fan sound sources used in this work have been located at the engine inlet and bypass nozzle center position to calculate the shielding hemisphere [135]. In a first approximation, this is assumed to represent the emission location of fan inlet and fan aft sound, respectively. When the point source is split, each part is placed at a different distance from the leading and trailing edge of the wing. Hence, the split point source method considers different individual shielding capabilities at both locations. This split considers the B747's engine length relative to the chord length in order to increase the accuracy of the prediction. Note, the applied method of shielding the sound sources can affect the selection of the optimal engine position, as the dominance of fan forward and fan aft sound varies. Whereas, the optimal engine position is derived from the minimum ground noise, such that the dominating sound source is wider shielded [135].

For both methods, i.e., splitting the sound sources and combined placement in the fan-disk center, it should be noted that the fan noise models describe far-field sound. However, the shielding of the sound takes place in the near field. This implies that it is by no means guaranteed that splitting the sound source is truly better or more reliable. However, this splitting method does improve many obvious challenges, such as the fact that with placement in the center of the fan disk, fan aft sound was very well shielded when placed above the wing, even though the engine nozzle was already placed one, two or more meters behind the trailing edge of the wing. Thus, more research is needed to further improve the shielding prediction for the requirements of the conceptual design phase of airplanes.

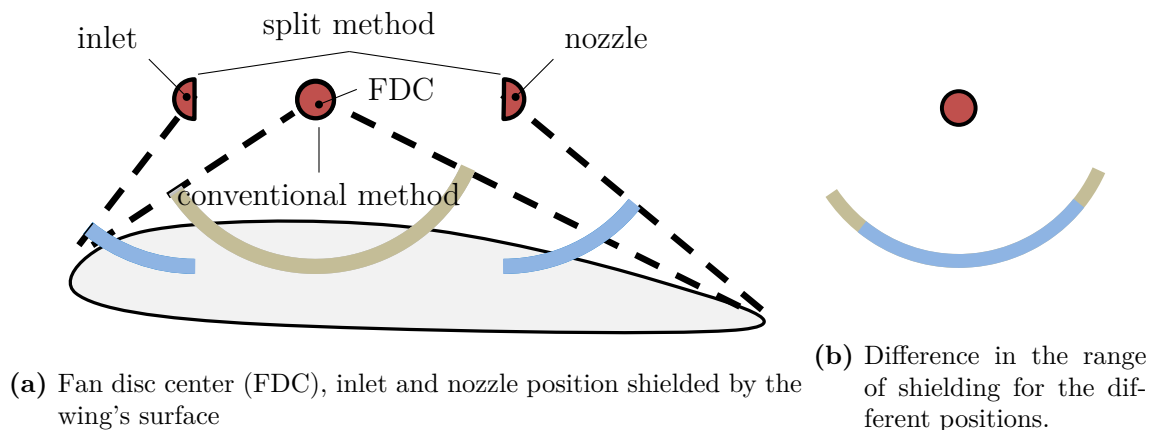


**Figure 3.4:** Engine sound source splitting. Fig. (a) visualizes the angles shielded by the wing. The center circle represents the fan disc center (FDC), while the left and right semicircles represent the engine inlet and bypass nozzle position, respectively. On the right, in Fig. (b), these directions of effective shielding are overlaid to visualize the difference in the shielded directions. This difference strongly depends on the engine's lengthwise position above the wing and the planform.

PANAM has been upgraded to be more flexible and consider various possible individually shielded engine placements and types. If all the engines of one type operate at the same speed, the SHADOW hemispheres of these engines can be respectively summarized in one inlet and one aft sound shielding hemisphere reducing PANAM's simulation time.

A module has been implemented in the PrADO-PANAM process chain, to specifically account for engine-over-wing aerodynamics for the airplane designs under investigation. This module modifies the drag data, which is predicted by PrADO. By default, the aerodynamics are predicted for the forward-under-wing engine location, that is the conventional case. This drag data is based on Fujino and Kawamura's work [83], which supports engines mounted at forward, centered, and aft of over-the-wing location; and fuselage positions. For more details, please refer to Section 7.1 on page 93.

FLIPNA has been upgraded to support open descends at minimum approach speeds, e.g., 1.3 times the stall speed ( $v_{\text{stall}}$ ). This upgrade enables the simulation of the *low drag minimum power* procedure, which utilizes each airplane's slow approach capabilities. This procedure will be described in Section 5.5.2 on page 56.

## 4 | Reference Airplane and Validation

This chapter focuses on describing the reference airplane and validating the applicability of the PANAM-PrADO process chain to model the B747-400. Measured sound events of B747-400 flyovers will be compared with predicted ones. The result of this comparison is that this process chain can be applied to the large airplane under investigation. The focus of this comparison is on the level-time history and on the spectra emitted at the retarded overhead location,  $30^\circ$  prior, and  $30^\circ$  later positions, as sketched in Figure 4.1.

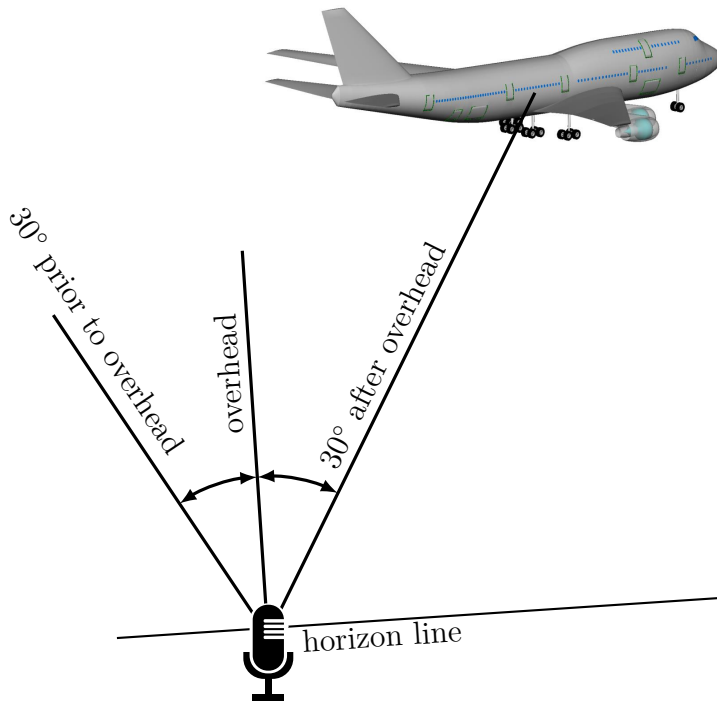


**Figure 4.1:** Airplane location relative to the microphone on the ground. The predicted ground noise has been compared to the measured one, when the airplane emitted the sound at overhead location,  $30^\circ$  prior to, and  $30^\circ$  after overhead position.

The Section 4.1 describes the reference airplane that is the modeled B747-400. The data of this model is compared to official data in terms of mass, required cruise fuel mass, and range. The engine speed-thrust relation of the CF6-80 engine, which was modeled with GTLab, is compared with data from the Boeing Climb Out Program (BCOP). Sections 4.2 and 4.3 describe the measurements and their corresponding simulations. Section 4.4 compares these measurements with the simulations. Section 4.5 summarizes this chapter.

## 4.1 Reference Airplane

The modeled B747-400 using PrADO has been used as the reference airplane in this thesis. The B747-400 is a long-range airplane with 400 seats by default in a three-class seating accessible through two aisles and can transport a maximum payload of 67.3t, see Figure 4.2 and Table 4.1. Within this thesis, a version of the B747-400 with 415 seats has been simulated, to achieve the maximum allowed amount of payload with an average of summer and winter luggage weight of the passengers.

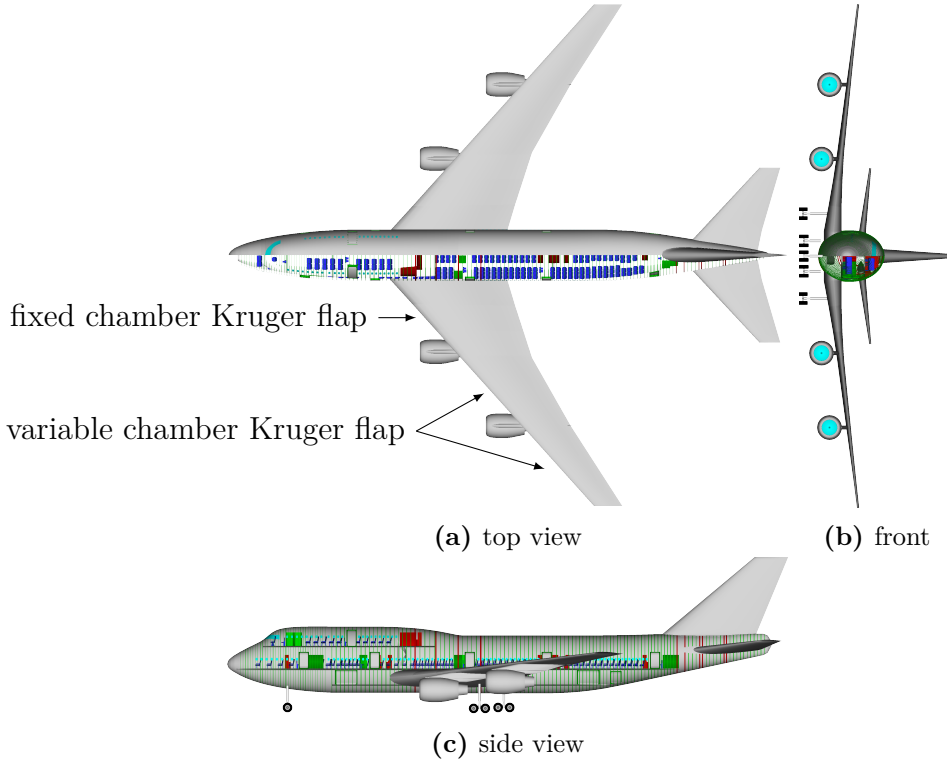


**Figure 4.2:** Reference airplane with its top view, front view, and side view. Half of the fuselage is kept transparent, so that the upper and lower deck are visible. With reference to Figure 4.3, the installation locations of the fixed and variable chamber Kruger flaps are marked.

The B747-400 uses Kruger flaps and triple slotted Fowler flaps as leading- and trailing-edge high-lift devices, respectively. The usage of Kruger flaps is an interesting detail because the slat noise model [56] implemented in the PANAM was originally designed to predict the sound of conventional slats. Later, the coefficients of the slat noise model utilized in PANAM have been updated to predict the sound emission for airplanes equipped with Kruger flaps as well [56]. The types of Kruger flaps mounted on the B747-400 are depicted in Figure 4.3. Rigid Kruger flaps are mounted at inboard position of the inboard engine and sealed up against the wing. This sealing might lower their noise generation. The rest of the Kruger flaps is mounted outboard of the inboard engine and has a variable camber. In the deployed position, the gap between these Kruger flaps and wing remains open.

This work utilizes the DLR flap noise model [56], as mentioned in Section 2.1.2, to calculate the sound emission of the triple-slotted Fowler flaps, which are mounted on the B747-400. The Fowler flaps of the B747-400 are separated by the inboard engine thrust gate,

which has been utilized as a high-speed aileron. According to the flap side edge model, only three of the four flap side edges of a half wing contribute the noise generation, as the fourth flap ending is bounded by the fuselage. In addition, low speed ailerons are placed at the outboard position of the outboard engine [189].

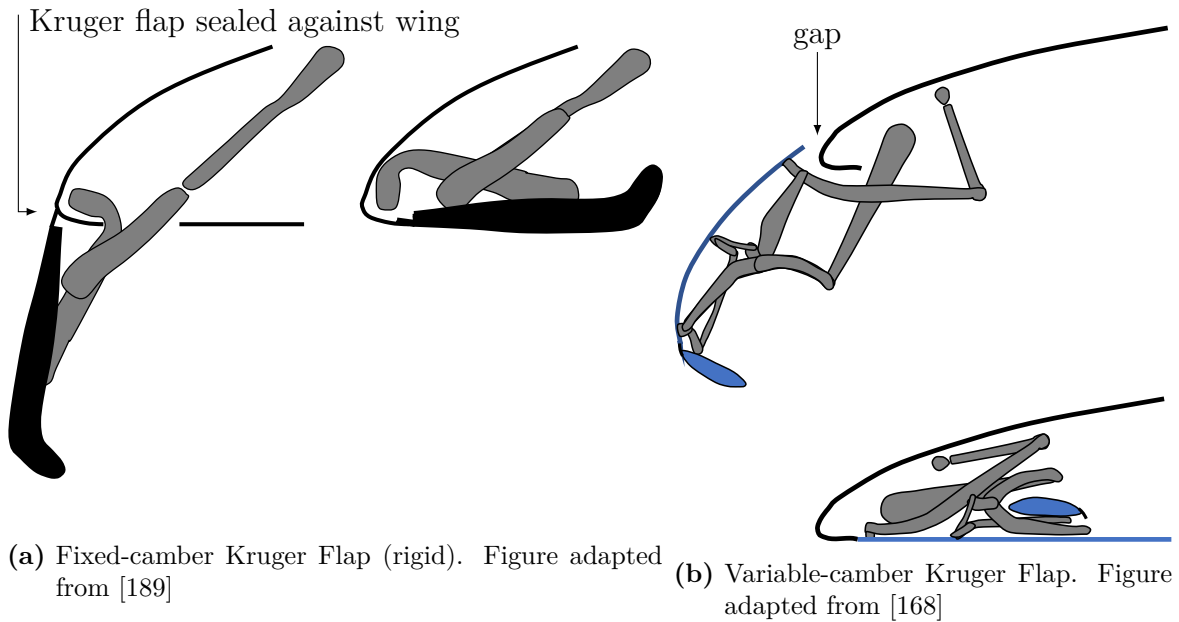


**Figure 4.3:** The picture shows the difference between the fixed and variable camber Kruger flap. The fixed camber Kruger flaps are mounted inboard of the inboard engine, and the variable camber Kruger flaps are mounted outboard of the inboard engine.

**Table 4.1:** B747-400 data [13]

|                     | B747-400                                    |
|---------------------|---|
| length              | 70.67 m                                     |
| span                | 64.92 m                                     |
| height              | 19.51 m                                     |
| leading-edge sweep  | 42.0°                                       |
| 25%-chord sweep     | 38.5°                                       |
| wing area           | 561.93 m <sup>2</sup>                       |
| aspect ratio        | 7.1789                                      |
| MTOW                | 394.6 t                                     |
| MLW                 | 285.8 t                                     |
| engines             | CF6-80 C2B1F with 258 kN thrust each        |
| PAX & payload       | 415 PAX + 26.234 t freight / 67.3 t payload |
| design cruise speed | Mach 0.85                                   |
| max. cruise speed   | Mach 0.92                                   |
| design range        | 10602 km                                    |
| entry into service  | January 1989                                |

The undercarriage system consists of one nose landing gear with two wheels and four main landing gears with four wheels each. Two of the main landing gears are mounted underneath the wings and two underneath the fuselage, as depicted in Figure 2.3. This information is essential for the inflow speed consideration. The inflow velocity for the landing gears mounted underneath the wings is slower than that of the ones mounted under the fuselage, due to the circulation around the wing [59].

An appreciable amount of spadework modeling the B747-400 in PrADO was conducted by Wolfgang Heinze, TU Braunschweig. It consists of the description of the B747-400 in the PrADO data format. This description has been checked, adjusted, and used as input data for PrADO. PrADO calculates the mass of each component of the airplane. For example, for each changed planform, PrADO considers the respective changed wing mass and structural loads to model the wing-fuselage junction. Additionally, the aerodynamics of the airplane changes, such that the required trip fuel mass changes, which, in turn, affects the structural loads. These impacts affect the overall mass of the fuselage. Since the parameter study is based on this reference aircraft, the PrADO model should represent the B747-400 as well as possible.

A first PrADO calculation of the preliminary B747 model delivered deviations in wing and fuselage mass compared to below mentioned FEM and literature data. Hence, for the modeled B747, the fuselage and wing mass have been adjusted by their respective material utilization factor, as described in the following two paragraphs. The material utilization factor describes the ratio of actual fracture stress relative to the fracture stress in the tensile test.

The (a) material utilization factors in PrADO for the fuselage and wing have been tailored to match data available from the PrADO developer Heinze. This data consists of (b) literature data, which estimated the wing mass to be about 44000 kg, and (c) FEM studies conducted by Heinze, who calculated a wing mass of 43132 kg. The calculated wing mass (c) deviates by  $-2\%$  of the literature data (b). The same FEM studies (c) calculated a fuselage mass of 39321 kg. PrADO, by default, predicted deviating masses for fuselage as well as wing in comparison to Heinze's data.

The fuselage and wing mass of the reference airplane, i.e., the PrADO model, have been tailored by adjusting their material utilization factors (a) to 0.221 and 0.510 for the fuselage and wing, respectively. After adjusting these factors (a), the wing and fuselage mass of the reference airplane are 43943 kg and 39341 kg (difference of 1.9% and  $-0.05\%$  to the literature data (b)), respectively. Heinze's FEM simulations (c) calculated material utilization factors of 0.330 and 0.585 for the fuselage and wing, respectively. After adjusting only two factors, the next two paragraphs compare the reference airplane to the data from the Airport Planning Manual. Later on page 32, another correction factor will follow to consider the aerodynamic advantages provided by the winglets.

The B747-400 payload range chart, which is shown in Figure 4.4, had been extracted from the airport planning manual [13, Figure 3.2.1] provided by Boeing company. PrADO's and the official payload range charts show a good agreement to each other.

The B747-400's design range at maximum payload is 10602 km. In order to fly with the maximum possible amount of fuel and to maintain a constant maximum takeoff weight, the payload has to be reduced. At maximum fuel mass, the B747-400 can fly a maximum range of approximately 13,056 km ③. Omitting the payload, the airplane can fly a ferry flight range of 15,060 km ④.

The predicted trip fuel ③ in Figure 4.4 differs by  $-3\%$  and the predicted ferry flight range ④ by  $-1\%$  compared to the Boeing data, respectively. The maximum landing weight

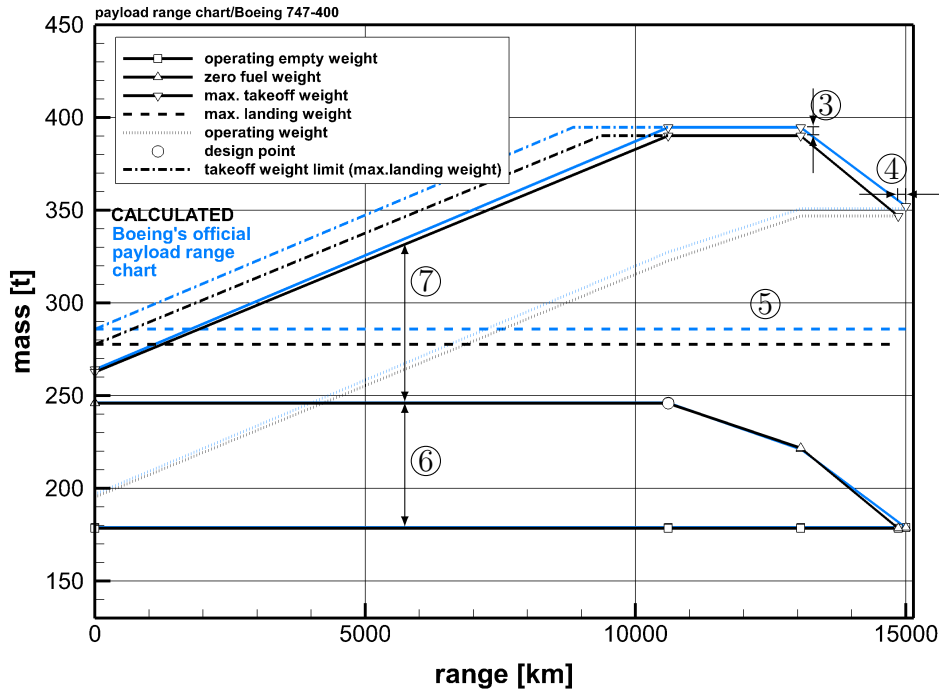


**Figure 4.4:** Comparative payload range chart of the original **B747-400** (blue) and simulated reference airplane (black): ③ difference in trip fuel; ④ difference in ferry flight range; ⑤ maximum landing weight; ⑥ payload; ⑦ trip fuel + reserve fuel.

⑤ differs by 7.8t, which corresponds to a deviation of 2.7%. When PrADO simulates a flight, the whole trip fuel is used. A smaller margin for over-fueling or less fuel consumption on the trip (e.g., due to favorable wind) as compared to the real airplane is considered. By default, PANAM predicts the ground noise at maximum takeoff weight (MTOW) and maximum landing weight (MLW), which are the worst-case conditions for noise prediction. The difference in the MLW at ⑤ in Figure 4.4 will have a minor influence on the ground noise, but no influence on the ranking of the airplanes when ranked by their ground noise at approach.

According to the airport planning manual, the center of gravity at maximum taxi weight lies between  $x_{ac,cog} = 31.337$  m and  $x_{ac,cog} = 31.738$  m, as calculated and indexed in the Appendix C.1 [13, pages 21, 156, and 159]. PrADO calculates the x-position of the airplane's center of gravity  $x_{ac,cog} \approx 33.318$  m at lift-off, shifting towards  $x_{ac,cog} \approx 32.280$  m by the end of the design mission. As the lift-off mass is mostly comparable to the maximum taxi mass, a gap of roughly two meters between the predicted and the official center of gravity is observed. In a real flight, a back shifted center of gravity can lead to an unstable flight condition. Whereas, the simulated flight requires less downforce by the elevator leading to less required wing lift to carry the same mass. This causes a decrease in the overall induced drag, resulting in lowered predicted fuel consumption. As the flight simulations and masses match well, this two-meters gap is acceptable for the following investigations. Additionally, the static margin divided by the mean aerodynamic chord is calculated with a value of  $-20\%$  in average during cruise flight, thus very stable.

PrADO determines the required horizontal and vertical stabilizer area performing stability checks using flight simulations of critical situations. This test checks if the horizontal or vertical stabilizer still steers the airplane in predefined flight situations, such as flight

close to stall speed, rotation at takeoff, approach, one engine inoperative etc.. However, often PrADO recommends deviating area sizes<sup>1</sup> of horizontal and vertical stabilizer than the ones authorized by the Federal Aviation Administration (FAA). As a workaround for this investigation, the factor describing how far the predicted and original area sizes differ is determined. Subsequently, the horizontal and vertical stabilizer areas proposed by PrADO are manually adjusted. In this case, the suggested control surface areas are multiplied by 61.2% for the vertical and 110.2% for the horizontal stabilizer to achieve the actually used sizes.

The wing twist has been adjusted to achieve a nearly elliptical lift distribution in the spanwise direction. It is assumed that also the aircraft manufacturer has designed the wing's lift distribution to be as close as possible to an elliptical one. The aerodynamics have been calculated for a supercritical profile, although the airfoil applied to the B747-400 is unknown [140]. The induced drag is corrected by  $-3\%$  to consider the aerodynamic advantage of the winglets. This value has been determined by Heinze<sup>2</sup>.

The B747-400 is equipped with four CF6-80 C2B1F engines developed by General Electric, each providing a static thrust of 258 kN. The engine map of the CF6-80 has been simulated using GTLab by Florian Wolters, DLR Cologne. This engine map contains relative engine speeds, while the flight recorder data contains absolute engine speeds. Hence, the absolute and relative engine speeds need to be connected to each other. As per the type certificate, the relative fan rotational speed ( $N_1$ ) of  $N_1 = 100\%$  has been set to 3280 rpm and the never-exceed engine speed to  $N_{1,ne} = 117.5\%$  [73]. A comparison of Boeing Climb Out Program data with the DLR's engine performance map shows a good agreement with less than 1% deviation. This comparison contained the correlation of thrust and engine speeds for five flight velocities ranging from  $Ma = 0.0$  to 0.45. The upper half of this velocity range is important for the noise calculation during approach and departure. For confidentiality reasons, further details cannot be furnished.

Additionally, the predicted fuel consumption at the beginning of the cruise leg ( $h = 10.0$  km,  $Ma = 0.85$ ) of the ferry flight has been compared to the data from Heinze, available to him from an undisclosed source. Heinze knows about a specific fuel consumption of  $0.058 \frac{\text{kg}}{\text{N}_s}$  originating from confidential sources and the DLR engine deck provides a specific fuel consumption of  $0.06084 \frac{\text{kg}}{\text{N}_s}$  for the same operating point. So, the herein used model data exhibits an approximately 4% higher predicted specific fuel consumption than Heinze's data point, although the predicted payload range chart shows a slightly lower fuel consumption ④. As clearly evident from Figure 4.4, the predicted fuel consumption is in a closer agreement with the one from Boeing's payload range chart, as compared to the fuel consumption expected from Heinze's specific fuel consumption provided at a particular data point. The comparison of both payload range charts can be concluded as follows:

- fuel consumption is predicted well
- the simulated fuel consumption at full payload and ferry flight is slightly below the official values at marker ③ and ④
- due to the lower fuel consumption, the fuel capacity of the PrADO airplane is lower compared to the original B747-400. This, in combination with lower glide ratios at lower lift coefficients, leads to a reduced ferry flight range ④.
- the simulated design range and masses show good agreement

---

<sup>1</sup>Conversation with Wolfgang Heinze: the predicted required area of the horizontal and vertical stabilizer deviates from the actual area of many authorized airplanes.

<sup>2</sup>Conversation with Wolfgang Heinze on April 03<sup>th</sup>, 2019.

- deviation in maximum landing weight acceptable

## 4.2 Flyover Noise Measurements

In September and October 2008, Lufthansa and DLR conducted a total of 98 flyover noise measurements with four Boeing B747-400, see Figure 4.5, over a span of four days at Parchim International Airport in Germany [62].



**Figure 4.5:** B747-400 approaching at Parchim International Airport, Germany, during the flyover measurement campaign. The data collected with the microphone array at the bottom of the picture has not been used within this comparison. The measurements used within this thesis have been measured with single microphone stations. Photography by Claus Lahiri, DLR.

A full data set for one day, which includes 10 flights with various approach and departure procedure investigations, has been provided for this study. This data set consists of flight recorder data, A-weighted SPLs at five microphone stations, and non-weighted third-octave band spectra. The third-octave band spectra had been recorded within five seconds prior to and after the A-weighted maximum SPL ( $L_{pA,max}$ ) with one second time step resolution.

The employed mobile microphone stations are of a 1.2-meter type and assembled by SINUS GmbH. Unfortunately, unlike surface microphones, 1.2-meter microphones measure the direct and the reflected sound simultaneously, leading to an interference pattern visible in the low-frequency third-octave bands, as shown in Figure 4.6. If the sound wave of any single frequency is fully reflected as by a sound-hard surface, then a phase shift of  $n \cdot 360^\circ + 180^\circ$  of the reflected sound wave would cancel out the direct sound wave at the microphone. A phase shift of  $n \cdot 360^\circ$  due to full reflection amplifies the amplitude at the microphone. Soft ground, as it was under all microphone stations during the measurement campaign, has a different impedance, and damps the reflected sound wave, so that the direct one is not fully canceled out.

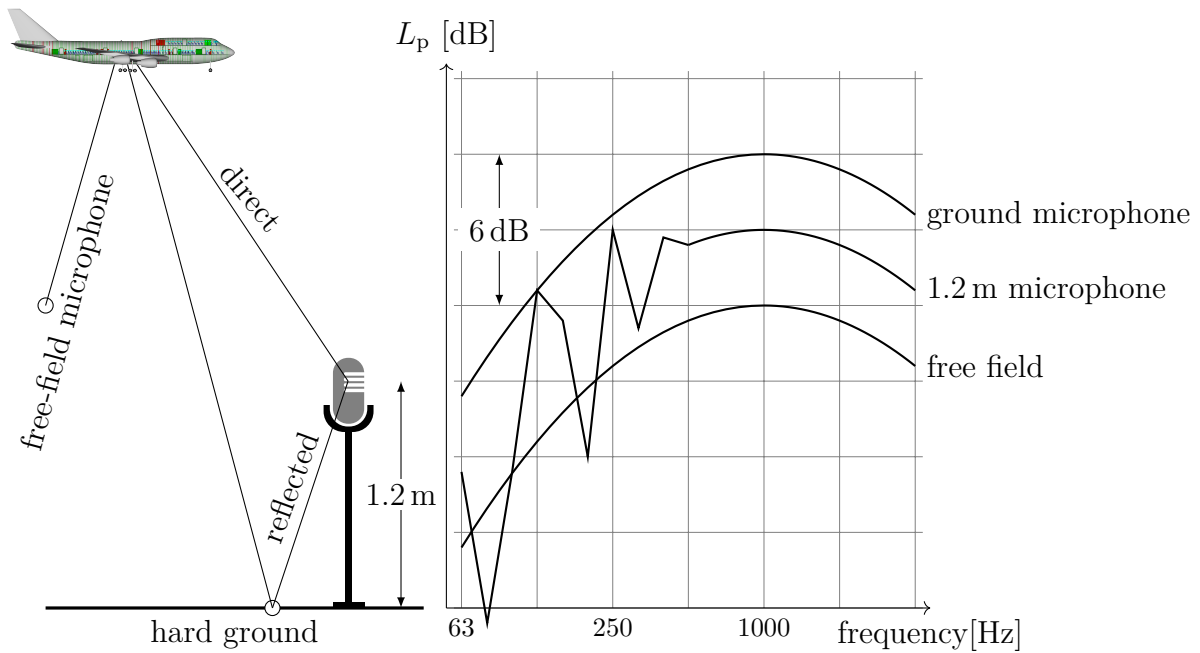


**Figure 4.6:** Principle of spectra as they would be measured with a surface, a 1.2 m, and a free-field microphone. The third-octave band spectrum measured in 1.2-meter height exhibits an interference pattern, mainly at lower frequencies. This is caused by the reflection of the sound wave on ground. For phase shifts of  $n \cdot 360^\circ + 180^\circ$ , the reflected sound wave cancels out the direct sound wave, while for phase shifts of  $n \cdot 360^\circ$  the reflected sound wave amplifies the direct sound wave. Towards higher-frequency third-octave bands, this amplification is not visible any more due to the increasing bandwidth. The free-field microphone measures the sound as emitted by the airplane, but, obviously, affected by the atmosphere. The ground microphone measures the pressure at the boundary condition “hard surface”, thus +6 dB compared to a free-field microphone. Figure adapted from [207].

These microphones were located very close to the ground track as shown in Figure 4.7, with the runway reference point kept one kilometer behind the approach threshold. The approaches and departures were conducted in the west and east direction, respectively. The microphone stations 21 and 22 were generally always crossed by the airplane, as opposed to the other microphone stations that were sometimes crossed because of the loop flown, as illustrated in Figure 4.7. All these microphone locations were on fields or grass and, thus, on soft ground.

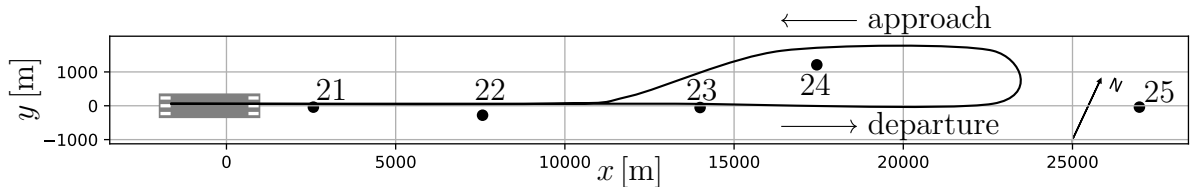


**Figure 4.7:** Microphone locations during recordings on Sep. 9<sup>th</sup> 2008 during measurement campaign in Parchim, Germany. Almost all departures were in the east direction, and all landings in the west direction. The sketched ground track illustrates why the microphones have been overflowed partially, but not always.

The events exhibiting a constant engine speed are of special interest. Such data promises more certainty as it provides constant conditions while comparing with simulated noise data. Hence, the flights are categorized into three groups:

- idle-thrust approach at  $N_1 \leq 50\%$ ,
- medium-thrust approach at  $N_1 \approx 60$  to  $70\%$ , and
- full-thrust takeoff at  $N_1 \approx 100\%$ .

The events matching these criteria and the corresponding labels are listed in Tables 4.2 and 4.3. Hereby, one event is the combination of one flight and one microphone location. An event is labeled with “flight number”-“microphone station”, e.g., 073-21. For example, two flights over three microphones are six events, as there is one recording of each microphone for each flight.

**Table 4.2:** Approach and departure procedures flown during measurements at Parchim International Airport.

| Procedure | Meaning                              |
|-----------|--------------------------------------|
| ACDA      | advanced continuous descent approach |
| ALDLP     | advanced low drag low power approach |
| CDA       | continuous decent approach           |
| ICAO-A    | ICAO-A departure procedure           |
| LDLP      | low drag low power                   |
| MODATA    | modified IATA departure procedure    |

The airplane sound has been measured at weather conditions very close to the ICAO standard atmosphere. Note that the standard atmosphere assumes dry gas. The measurements have been conducted at 70 % humidity at 20° C. As per the conditions given in Table 4.4, the thermals, labeled as ‘turbulence’ by the motorized-aircraft pilots, arising due to the strong sun insolation, are expected. The effects of these thermals on the sound propagation through the atmosphere [227] or on the sound generation at the source have been neglected from the simulations.

The available flight recorder data is listed in Table 4.5. The flight recorder provided all necessary data with a 1 second resolution. This data has been translated into the PANAM format for the ground noise prediction.

**Table 4.3:** Selected events to compare measurements with simulations.

- ✓✓ level time history and one-third-octave band spectra available,  $N_1$  is constant
- ✓ level time history available,  $N_1$  is constant
- ✓ level time history available,  $N_1$  varies or differs

| flight no.  | procedure                   | microphones |    |    |    |    |
|---|-----------------------------|-------------|----|----|----|----|
|   |                             | 21          | 22 | 23 | 24 | 25 |
| idle-thrust approaches with engine speed in idle or below $N_1 \leq 50\%$           |                             |             |    |    |    |    |
| 71  | LDLP Standard Flap schedule | ✓           | ✓  | ✓✓ | ✓  | ✓  |
| 73  | CDA Alternate Flap schedule | ✓           | ✓  | ✓✓ | ✓  | ✓  |
| 74  | CDA Standard                | ✓           | ✓  | ✓✓ | ✓  | ✓  |
| 89  | ALDLP Approach              | ✓           | ✓  | ✓✓ | ✓  | ✓✓ |
| medium-thrust approaches with a constant engine speed of $N_1 \approx 60$ to $70\%$ |                             |             |    |    |    |    |
| 53  | LDLP Standard Flap schedule | ✓✓          | ✓  | ✓  | ✓  | ✓  |
| 71  | LDLP Standard Flap schedule | ✓✓          | ✓  | ✓  | ✓  | ✓✓ |
| 88  | ACDA at approach power      | ✓✓          | ✓  | ✓  | ✓  | ✓  |
| 89  | ALDLP approach              | ✓✓          | ✓  | ✓  | ✓  | ✓  |
| full-thrust takeoffs with a constant engine speed of $N_1 \approx 100\%$            |                             |             |    |    |    |    |
| 72  | MODATA Full Power           | ✓✓          | ✓✓ | ✓  | ✓  | ✓  |
| 85  | MODATA Flex Power           | ✓✓          | ✓✓ | ✓  | ✓  | ✓  |
| 86  | ICAO-A Flex Power           | ✓✓          | ✓✓ | ✓  | ✓  | ✓  |
| 87  | ICAO-A Full Power           | ✓✓          | ✓✓ | ✓  | ✓  | ✓  |

**Table 4.4:** Weather conditions during flyover measurements on Sep. 09<sup>th</sup> 2008 [127]

| Description     | Value                           |
|-----------------|---------------------------------|
| clouds          | $\frac{0}{8} - \frac{1}{8}$     |
| temperature max | $20^\circ C$                    |
| dew point       | $11^\circ C$                    |
| humidity        | 70% at 1400 UTC                 |
| wind            | $3 \frac{m}{s}$ from south west |
| pressure QFF    | 1019 hPa                        |

Data from this flyover measurement campaign have been analyzed previously by various researchers. Henri Siller et al. already investigated the B747-400 engine noise using data from the microphone array visible in the lower part of Figure 4.5 [200]. Almonet presented results of sound measurements of the B747-400 flyovers with focus on the landing gear and the Kruger flaps [6]. The Kruger flaps and flap side edges dominate the high-lift device sound. Rossignol [187] compared data from these flyover measurements with a flap side-edge noise model. He assessed the first version of his model as acceptable, as described in Section 2.1.2 on page 10.

**Table 4.5:** Data available from Flight Management Computer

- GPS positions from Flight Management Computer and inertial reference unit
- calibrated airspeed, true airspeed (TAS), ground speed, and Mach number
- barometric altitude and radio height above ground level
- landing gear status
- angle of attack (indicated, implausible data)
- pitch
- roll angle
- inner and outer aileron deflection angle
- inboard and outboard flap deflection angle
- Kruger flap position
- spoiler deflection angle
- fuel mass flow per engine
- engine speed % rpm per engine,  $N_1$  and  $N_2$
- total air temperature
- wind direction and wind speed

### 4.3 Simulations

PANAM requires a trajectory, an airplane geometry, an engine map and geometry, along with microphone positions as input data. The trajectories have been extracted from flight recorder data listed in Table 4.5 providing the procedures listed in Table 4.3 and translated into the PANAM input format. Since the flight recorder data contains the engine speeds, the engine operating condition is determined via the engine speed in order to calculate the engine sound. Note that PANAM supports engine sound calculation via engine speed and thrust. However, airplanes cannot measure the thrust.

The influence of ground effect is considered by PANAM as described in *AzB* from 2006 [42]. This ground model calculates an approximately 2.9 to 3.01 dB higher sound pressure level compared to free-field conditions for all relevant flight heights above 100 m. The ground, in this case, is simulated as hard surface, although the microphones were placed over grass land and field.

If the ground were sound-hard, the incoming sound wave would be completely reflected. In that case, third-octave band sound pressure levels with mid-frequencies above 200 Hz are measured about 3 dB higher by the 1.2-meter microphones than they would with free-field microphones. In the case of grass, which is softer ground, less sound is reflected and the impedance is unclear. The impedance of the soil is even different for different conditions, such as moisture and compaction. This means that less than 3 dB in addition to the free-field sound pressure level is expected here. According to Smith [202, Fig. 9], one can assume about 1.9 dB lower overall sound pressure levels that are measured by a 1.2-meter microphone over softer ground compared to sound-hard ground. In summary, in PANAM the ground effect as for 10-meter microphones has been simulated. Therefore, the PANAM calculations are expected to predict about 1.9 dB higher sound pressure levels than the measurements because the sound has been measured above grassland and fields. Additionally, this selected ground model does not predict any interference pattern visible in the third-octave bands because it models 10-meter microphones. The visible interference pattern of the 10-meter microphones, however, is shifted towards lower third-octave bands. However, the Rudnik ground model [52, 188], which calculates the ground effect, has been tested as described in the following paragraph.

The modeling of the ground effect with 1.2-meter microphones by the Rudnik ground model [52, 188] had delivered implausible results as this ground model predicted an inter-

ference pattern of the third-octave bands over the whole frequency range beyond 10 kHz. However, an interference pattern, which is visible in the third-octave bands, is expected only for the lower frequency third-octave bands. The implementation of this model needs to be checked.

The data necessary to describe the airplane in PANAM format has been extracted from the detailed PrADO model and comprise the wing shape, high-lift devices, and landing gear. Table 4.6 lists the settings and models being used to predict each individual sound source and the respective ground noise.

**Table 4.6:** Noise sources and models used to predict airplane noise emission; and damping models to consider atmospheric attenuation and ground effect.

| sound source            | model   |
|-------------------------|---|
| fan                     | Kontos fan noise model: buzz-saw <sup>a</sup> , broadband and tones [136] |
| jet                     | Stone jet noise model [209]   |
| clean wing              | DLR wing noise model [56, 170]  |
| Kruger flaps            | DLR leading-edge noise model [56, 170]                                    |
| triple slotted flaps    | DLR flap noise model [56, 170]  |
| flap side edge          | DLR flap side edge model [187]  |
| landing gear            | DLR landing gear noise model [170]  |
| damping model           | model   |
| ground effect           | AzB 2006 [42]   |
| atmospheric attenuation | ISO 9613 [124]  |

<sup>a</sup>The buzz-saw noise model factors have been edited, see Section 4.4.3.

## 4.4 Comparison

This section is dedicated to the comparison of the PANAM simulations with measurements conducted at Parchim International Airport. The A-weighted level time histories are compared with each other. Additionally, the third-octave bands of the sound emitted at the overhead position and in some cases at 30° prior to and at 30° after overhead positions are compared with one another. As only ten single events have been used to compare flyover measurements and simulations, these results might not be representative for the all-year operated airplanes. The noise pollution of an airport vicinity varies with wind, temperature, takeoff weight, and landing weight. However, the advantage of these measurements is that flight recorder data is available to precisely recalculate the flights. The focus of this comparison is laid on the three categories as illustrated in Figure 4.8: approach at idle thrust, approach at medium thrust, and departure at full thrust obtained from Table 4.3. Additionally, the buzz-saw sound model has been adapted to the measurements in conformity with the data provided by Kontos [136].

Figure 4.9a shows two typical spectra of the ground noise measured by a 1.2-meter microphone. The ground reflection at very low frequencies leads to augmentation and cancellation of the measured third-octave bands ⑧, depending on the wave length, band width, microphone height, and ground impedance. Hence, the third-octave bands with mid frequencies

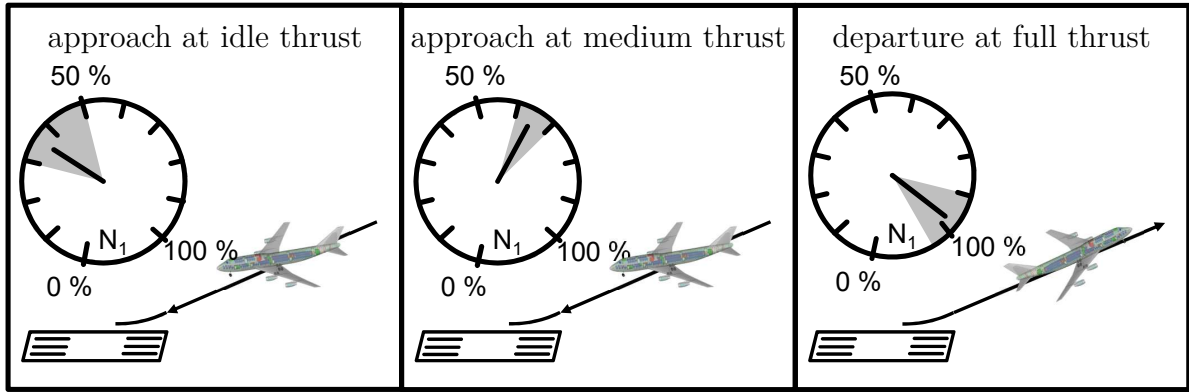


Figure 4.8: Categories of the investigated events.

below 200 Hz have not been considered. To compare the effective sound emissions at different altitudes, the microphone results have been reverse-calculated to the airplane height by adding the atmospheric and geometric attenuation, as shown by an example spectrum in Figure 4.9b. The high atmospheric absorption at high frequencies [124] leads to artificially overestimated sound pressure levels ⑧ when reverse calculated, which are excluded from the comparison. Consequentially, the frequency range from 200 Hz up to 2500 Hz is considered in the reverse-calculated sound emission spectrum.

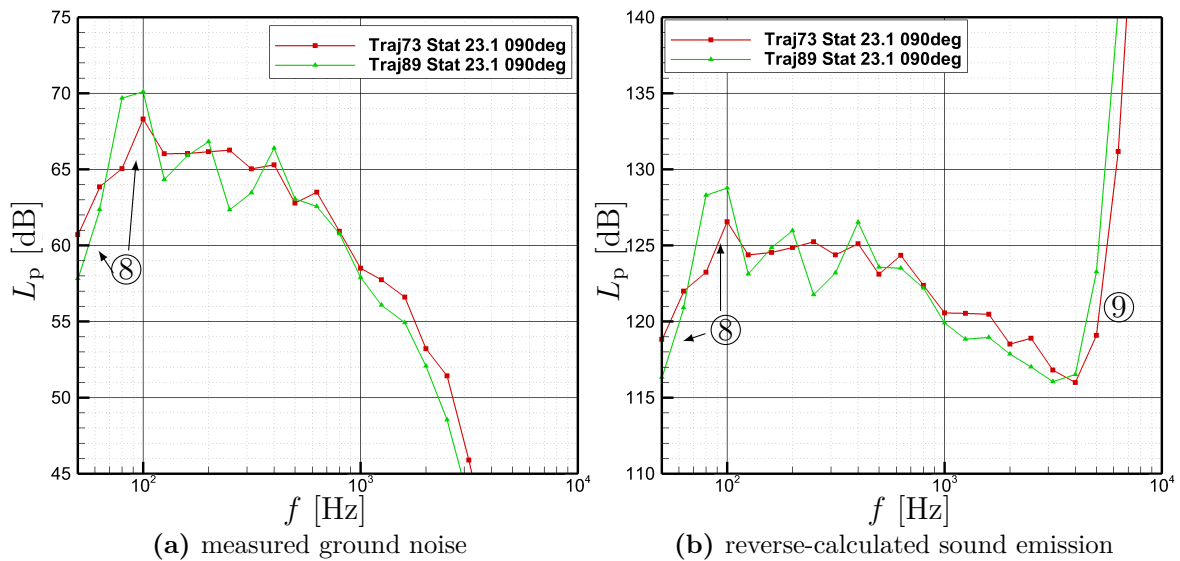
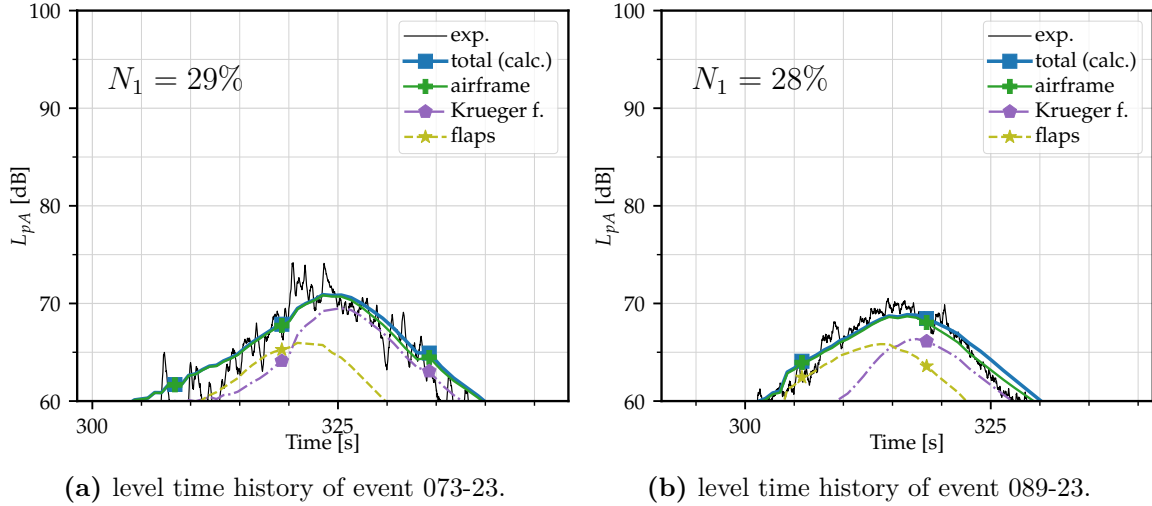


Figure 4.9: Measured SPL spectra (left Fig. (a)) and the reverse-calculated SPL spectra (right Fig. (b)) as it would have been emitted from a fictitious point source at the airplane’s height. An interference pattern occurs at low frequencies. The sound pressure levels reverse-calculated up to the airplane’s altitude become implausible at high frequencies above 4000 Hz due to the great values of added atmospheric absorption. Consequently, the range of third-octave bands between 500 Hz and 2500 Hz has been compared.

#### 4.4.1 Approaches at Idle Thrust

During these events, the engine's contribution to the A-weighted SPL is low compared to the airframe sound. Figure 4.10 shows two representative A-weighted sound pressure level time histories, where the curves show the measured and calculated ones. The predicted A-weighted SPL (—) contains the component-wise individual A-weighted SPLs.



**Figure 4.10:** Measured Parchim and calculated PANAM level time histories for two representative events, 073-23 and 089-23, with engine at idle and, therefore, assumed, dominating airframe sound. Landing gear is retracted. Engine SPL is below 60 dB.

During event 073-23, the airplane flew just above  $100 \frac{m}{s}$ , the Krueger flaps were fully deployed, and the Fowler flaps were deployed at  $10^\circ$ . During event 089-23, the airplane flew at  $95 \frac{m}{s}$ , the Krueger flaps were fully deployed and the Fowler flaps were deployed at  $20^\circ$ . The measured increase, decrease, and A-weighted maximum SPL of the events 073-23 and 089-23 match well with the respective predictions. A slight under-prediction can be observed, although an over-prediction of 1.9 dB has been expected. PANAM does not predict the measured fluctuations of the sound pressure level because the turbulence in the air is neglected.

The third-octave band spectra of these two events 073-23 and 089-23 are depicted in Figure 4.11.

Within the frequency range of 200 Hz to 2.5 kHz, the predicted third-octave band levels match visually well to the measured ones for the overhead and aft direction. Interference pattern can only be identified for the aft emission direction up to 400 Hz. Investigating the forward emission direction, Figure 4.11a, the spectrum of event 073-23 is under-predicted, what can also be found in Figure 4.10a at a time of about 321 seconds. Reasons cannot be identified; however, the turbulence in the atmosphere can affect the sound during the propagation.

Overall, such good match of the airframe noise predictions to the measurements was expected because the airframe noise models were updated to conform with the sound emission of the B747-400 [56, 62]. The Parchim measurement campaign held in 2009 is the data source for this upgrade, during which the data was measured with the large microphone array as depicted in the lower part of Figure 4.5.

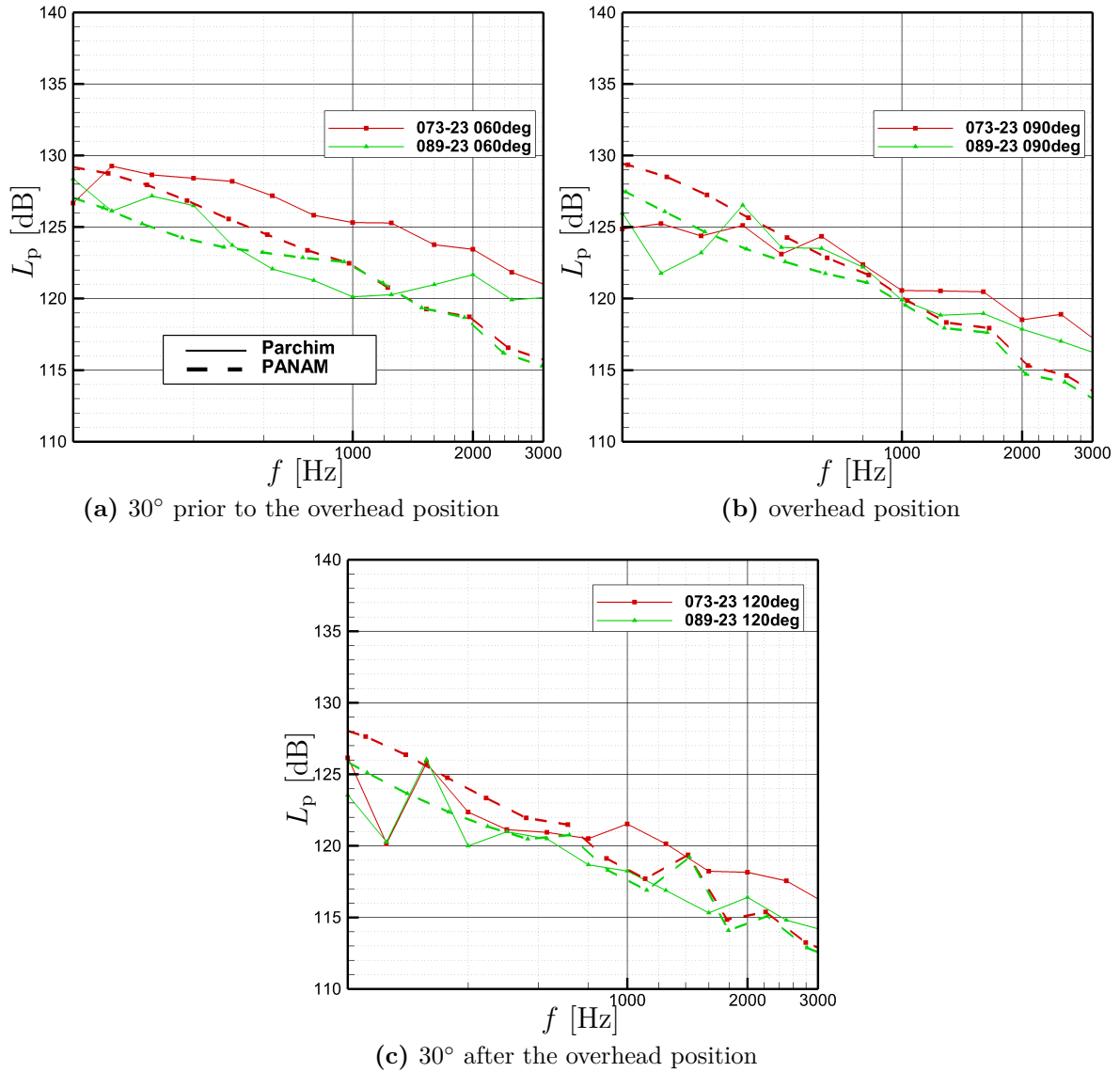


**Figure 4.11:** Measured spectra reverse-calculated to the fictitious point sound source at the airplane's height and PANAM-calculated sound emission spectra for two representative idle-thrust events: 073-23 and 089-23.

#### 4.4.2 Approaches at Medium Thrust

Two approaches have been selected as representative A-weighted SPL time histories for this category, as shown in Figure 4.12, and they agree well with the calculated ground noise.

The engine speed was kept constant and was between 60% and 70%  $N_1$  during the events. This is a typical final approach power setting, which compensates for the drag of the high-lift system and landing gear. The first example, where the A-weighted maximum sound pressure level of the prediction deviates by expected  $\Delta L_{pA} = +2.0$  dB with the measurement (10), is depicted in Figure 4.12a. This good match has been found for all events of these medium-thrust approaches, but it is dominated by the fan broadband noise in the aft direction that is caused by a discontinuity in the liner model at 8 kHz. The liner in the simulations does not attenuate this frequency, see (12) in Figure 4.13. During the 3° final approach segment

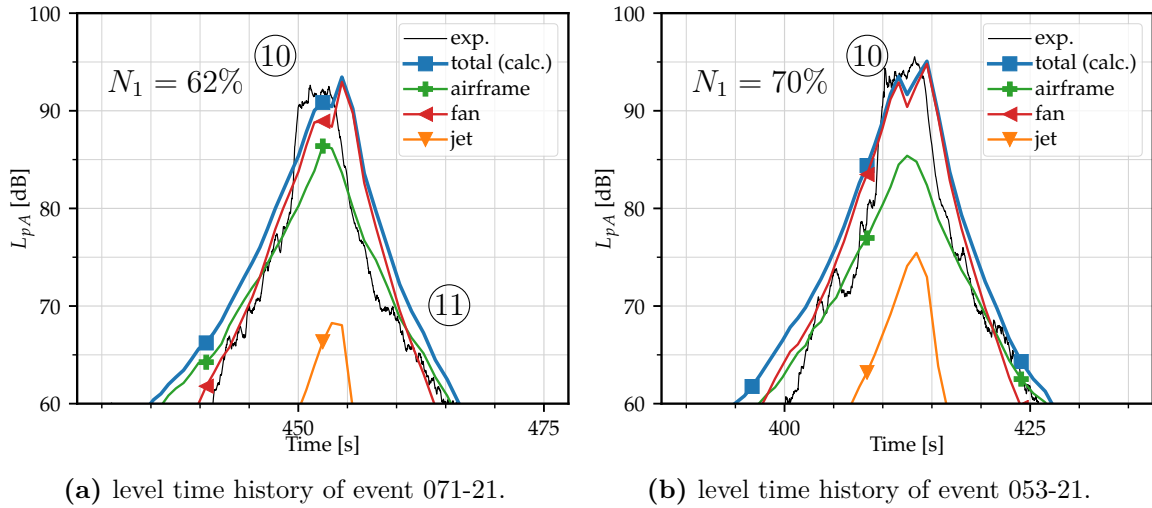


**Figure 4.12:** Measured Parchim and calculated PANAM level time histories for medium-thrust approach events: 071-21 and 053-21.

the airplane flies over the Microphone 21 at a height of 120 m, such that the atmosphere attenuates just a little.

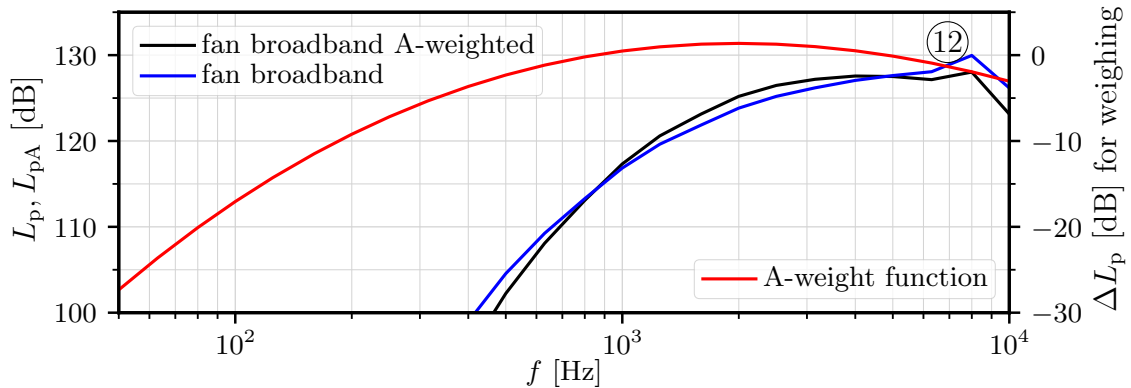


**Figure 4.13:** Fan broadband noise third-octave spectrum for event 086-21 in  $60^\circ$  direction and A-weighting function. The higher sound pressure level at 8 kHz (12) is caused by a discontinuity in the liner model and, hence, caused by the predicted fan sound emission.

At low altitudes, the 8 kHz third-octave band dominates the ground noise, but at higher altitudes this frequency is attenuated by the atmosphere, not determining the A-weighted SPL anymore. This means that as soon as the liner model is updated, PANAM will underestimate the noise level. The farther the airplane flies away from the microphone, the more the high frequency fan sound is attenuated by the atmosphere, making the lower-frequency airframe sound to prevail, see (11) in Figure 4.12. Within the 30 dB downtime the increase in the A-weighted SPL shows an offset of about +5 dB and its decrease matches visually well, if the time shift of  $-2$  sec would be applied to the prediction. Both, airframe and fan noise, contribute to the overall sound pressure levels within the 30 dB downtime. However, sound

pressure levels that are more than 10 dB below the maximum do usually not contribute significantly to the noise assessment by integral metrics.<sup>3</sup>

In Figure 4.12b, the predicted maximum A-weighted SPL matches with the measured one. During the increase and the decrease within the 20 dB downtime the predicted sound pressure levels are about 4 to 5 dB above the measured levels.

The aforementioned approach events have been investigated in detail in Figure 4.14, which presents the reverse-calculated spectra for five events at their overhead position.

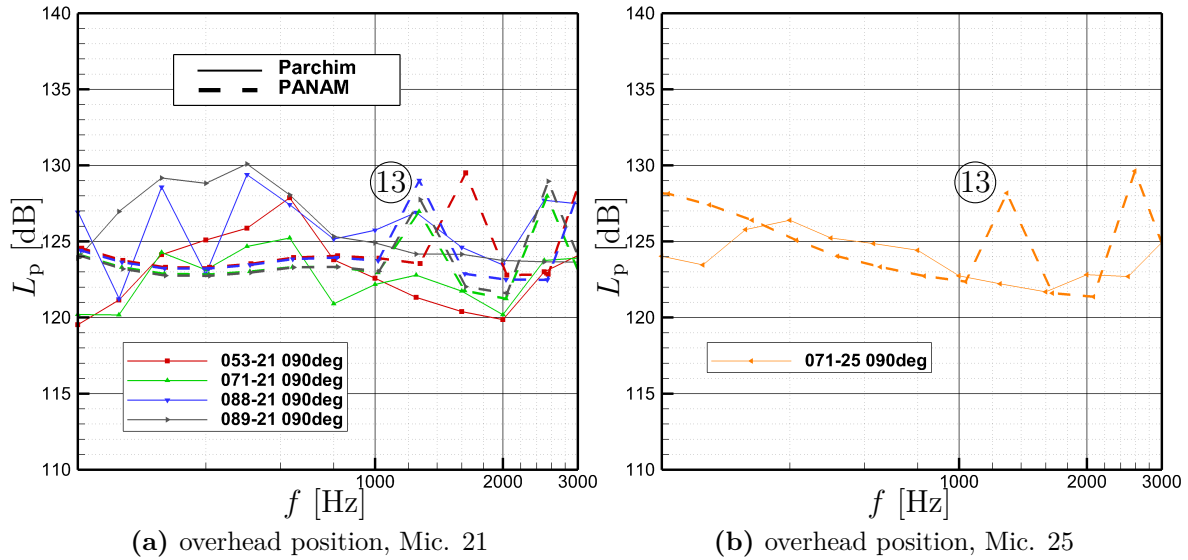


**Figure 4.14:** Measured spectra reverse-calculated to the fictitious point sound source at the airplane’s height and PANAM-calculated sound emission spectra for the medium thrust approaches for five representative events at the two microphone positions: 21 and 25. (13) shows the prediction of fan tones that have not been measured.

In the frequency range of 200 Hz to 630 Hz, PANAM under-predicts the third-octave bands by about 4 dB compared to the measurements. In addition, PANAM predicts some too loud third-octave bands, which cannot be found in the measured spectra (13) in Figure 4.14. These louder third-octave bands are caused by fan tones. These fan tones are the ones predicted by the Kontos model, however, without attenuating them by the liner. To understand the context, it is helpful to understand PANAM. PANAM predicts the attenuation through the liner for broadband and tonal sound, for fan inlet and aft sound, as well as for buzz-saw sound separately. Hence, there are five different attenuation spectra: one for each component of the fan noise model that has been described in Section 2.2.1 on page 13. In this case, PANAM has calculated the attenuation for the tonal sound components as zero. Conclusively, the fan tones are unattenuated. PANAM predicted that the broadband

<sup>3</sup>The depicted noise levels have been recorded by microphones located close to the ground track. Later, the airplane designs will be assessed by the Awakening Index and, hence, also the sound pressure level to the sideline is of interest. When the 15 dB deduction for tilted windows is considered, all sound pressure levels above  $\approx 47$  dB are relevant because they cause additional awakening reactions that contribute to the Awakening Index. Conclusively, sound pressure levels caused by a large distance from the microphone are also of interest. Nevertheless, the sound pressure levels at the side of the ground track should be measured for this purpose because the sound emission directionality of the components is different in the longitudinal direction than to the side.

sound is attenuated by 3 to 4 dB between 1000 Hz and 4500 Hz. Hence, when calculating attenuation with PANAM, it can be expected that the fan tones are lowered by at least 3 dB because liner are effective for reducing certain frequencies. Correct attenuation by the liner would also result in an under-prediction of the sound pressure levels at medium-thrust engine settings.

### 4.4.3 Departures at Full Thrust

Figure 4.15 shows two representative A-weighted SPL time histories at departure. The predicted A-weighted SPL time history (—) contains the component-wise individual A-weighted SPLs, where the separately depicted buzz-saw sound is a part of fan sound.

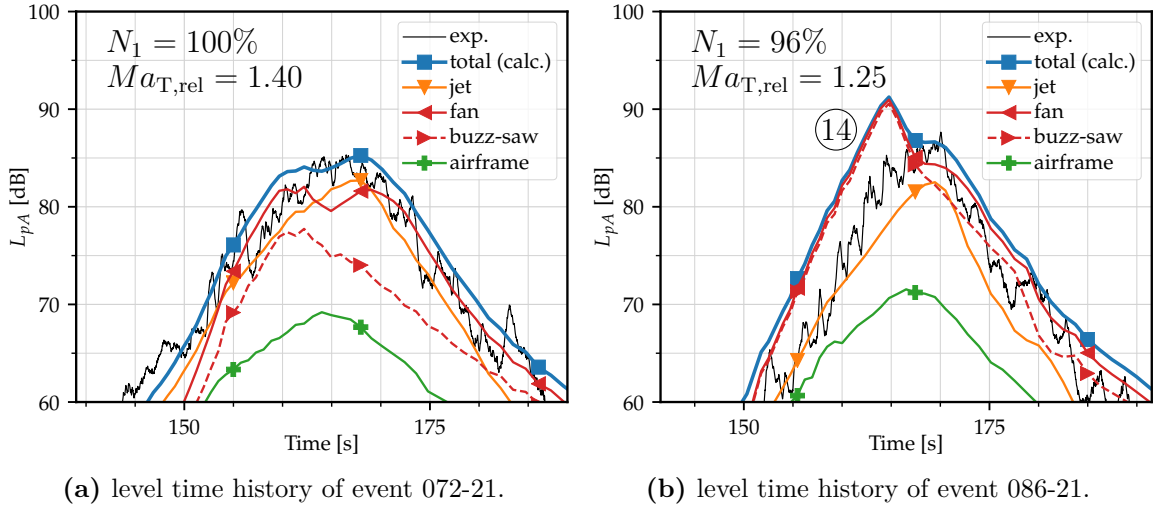


**Figure 4.15:** Measured Parchim and calculated PANAM A-weighted SPL time histories for the two full-thrust departure events: 072-21 and 086-21. The separately depicted buzz-saw A-weighted SPL is part of the fan A-weighted SPL. Buzz-saw sound is strongly over-predicted.

In Figure 4.15a, the A-weighted SPL time histories of measurement and prediction matches well. In the A-weighted maximum SPL, a deviation of  $\Delta L_{pA,max} = 0.5$  dB has been found. The engine speed is at  $N_1 = 100\%$  with a relative tip Mach number at  $Ma_{T,rel} = 1.40$ . PANAM predicts a fan lobe due to directionality, which is not measured distinctively. According to the predictions, fan and jet sound are dominant whereas the airframe sound is recessive.

In the second example, in Figure 4.15b, the engine speed is reduced to  $N_1 = 96\%$  with a relative tip Mach number of  $Ma_{T,rel} = 1.25$ . The value of the buzz-saw sound is predicted too high (14) when compared to the measurements. The reason is that the peak SPL is modeled at  $Ma_{T,rel} = 1.15$  and  $Ma_{T,rel} = 1.25$  for the one-half and one-quarter of the blade passing frequency, respectively, which is also visualized in Figures 4.17a and 4.17b. Before investigating the buzz-saw noise model in Table 4.7, the third-octave band spectrum is investigated.

Figure 4.16 shows the measured and predicted spectrum in the direction  $30^\circ$  prior to overhead for six events at two microphone positions. Strong buzz-saw sound is predicted in the frequency range of 400 to 2000 Hz (15), however, not measured. Hence, the buzz-saw noise model has been investigated in the following paragraph.

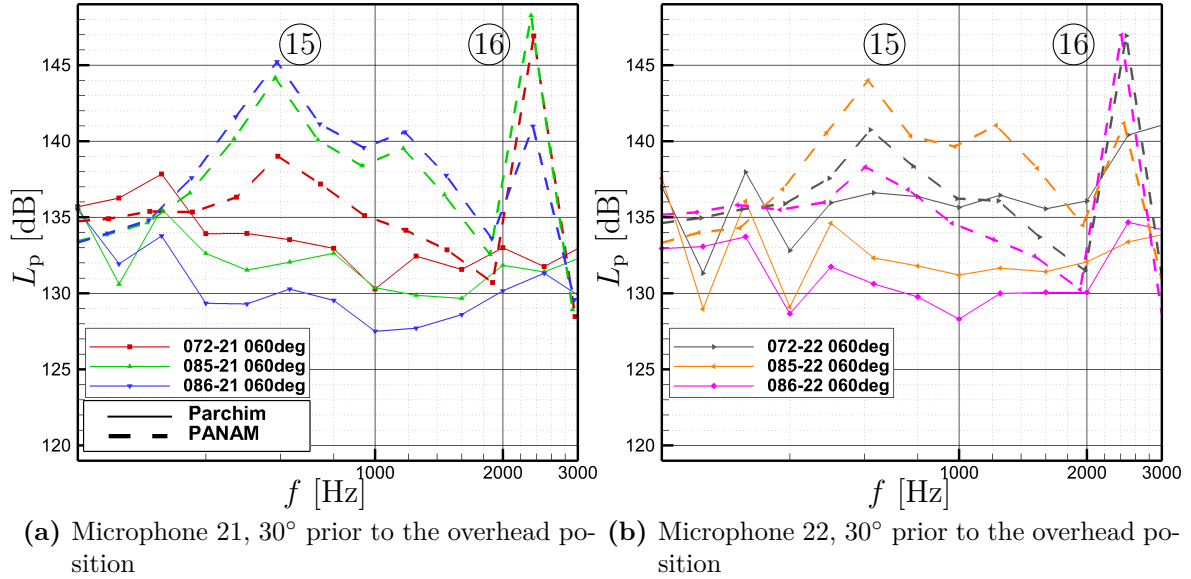


**Figure 4.16:** Measured spectra reverse-calculated to the fictitious point sound source at the airplane's height and PANAM-calculated sound emission spectra for full-thrust departures for  $30^\circ$  prior to the overhead position at the two microphones, 21 and 22, for three events each. Prediction prior to the buzz-saw noise model modification. (15) results from loud predicted buzz-saw sound and (16) results from loud predicted fan tones.

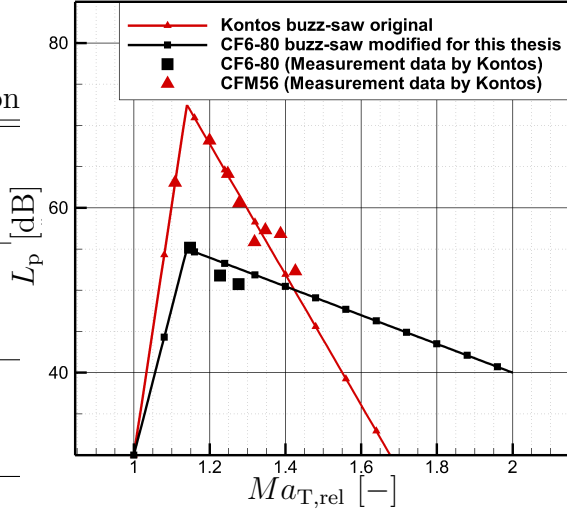
Due to this strong over-prediction of the buzz-saw sound, the buzz-saw noise model will be reassessed by investigating the spectral sound provided in Kontos' model description [136]. Hereby, this investigation has been limited to the engine speeds  $N_1 = 2850 \frac{1}{min}$  and  $N_1 = 3150 \frac{1}{min}$  (87% and 96%  $N_1$ , respectively) [136, Appendix M, considering Appendix B] towards the  $\alpha^* = 60^\circ$  and  $70^\circ$  directions. Both (a) measured engine sound and the respective (b) predicted fan inlet sound have been extracted from the references [136, Appendix M, pages 144 and 146] and [136, Appendix B, pages 52 and 54], respectively. It is assumed that (a1) fan inlet and (a2) buzz-saw sound are the dominant sound sources in these directions. Therefore, the modeled fan sound (b1) has been subtracted from the measured engine sound (a), to obtain the buzz-saw sound (a2). These extracted buzz-saw SPLs (a2) are about 13 dB and 5 dB below the predicted buzz-saw SPLs (b2) for  $N_1 = 2850 \frac{1}{min}$  and  $N_1 = 3150 \frac{1}{min}$ , respectively. It can be concluded that the buzz-saw SPL (b2) is over-predicted. Moreover, the buzz-saw sound (a2) of the CF6-80 had not been considered while developing the buzz-saw noise model [136, Page 40].

Instead, the buzz-saw noise model had been adjusted to the CFM56 engine. Due to the great over-prediction of the buzz-saw SPL at two engine speeds, the coefficients of this model have been adjusted for this present work. Also, Arntzen [11] modified the coefficients of the buzz-saw model for his noise studies, however, without describing the modification method or any coefficients. Within this study, the coefficients have been adjusted, as described in the following paragraph.

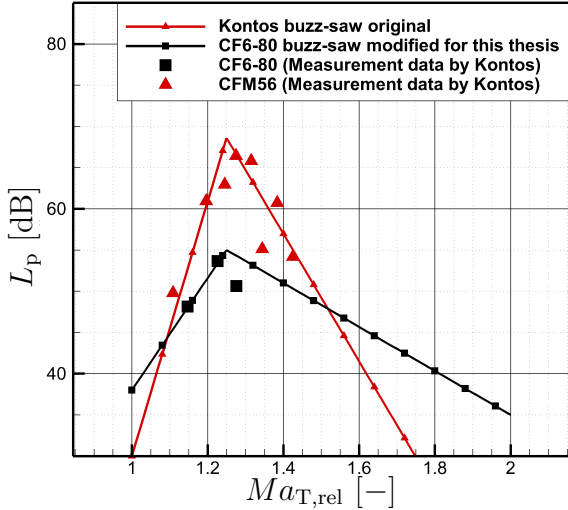
The normalized noise levels of the CF6-80 over fan tip Mach number from reference [136, Figure 4.6.5 to 4.6.6] have been utilized for this adaptation. The new coefficients have been determined through a curve fit. The new and old coefficients are listed in Table 4.7 and depicted in Figure 4.17. The SPL of the adjusted buzz-saw noise model is low compared to

the fan tones and broadband sound. The factors for the  $f = \frac{1}{8}$ BPF have been kept because there was no data available to justify an adaptation.

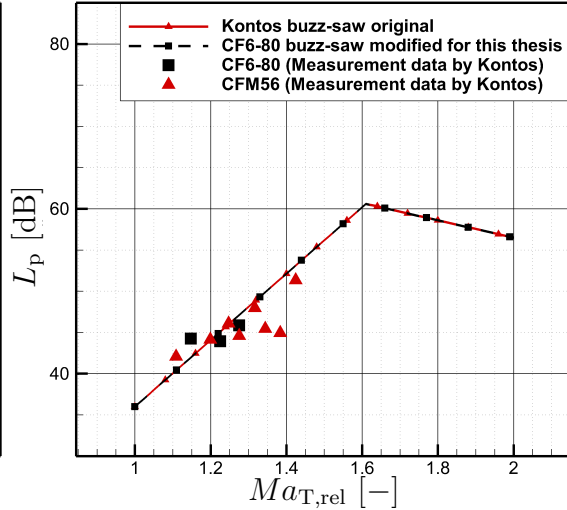
| $\frac{f}{\text{BPF}}$ | $Ma_{T,\text{rel}}$ | Kontos original | $L_p$<br>CF6-80 modification |
|------------------------|---------------------|-----------------|------------------------------|
| $\frac{1}{2}$          | 1                   | 30.0            | 30.0                         |
|                        | 1.14                | 72.5            | 55.0                         |
|                        | 2                   | 4.4             | 40.0                         |
| $\frac{1}{4}$          | 1                   | 30.0            | 38.0                         |
|                        | 1.25                | 68.0            | 55.0                         |
|                        | 2                   | 10.5            | 35.0                         |
| $\frac{1}{8}$          | 1                   | 36.0            | 36.0                         |
|                        | 1.61                | 60.6            | 60.6                         |
|                        | 2                   | 56.5            | 56.5                         |



(a) buzz-saw component noise for  $f = \frac{1}{2}$ BPF



(b) buzz-saw component noise for  $f = \frac{1}{4}$ BPF

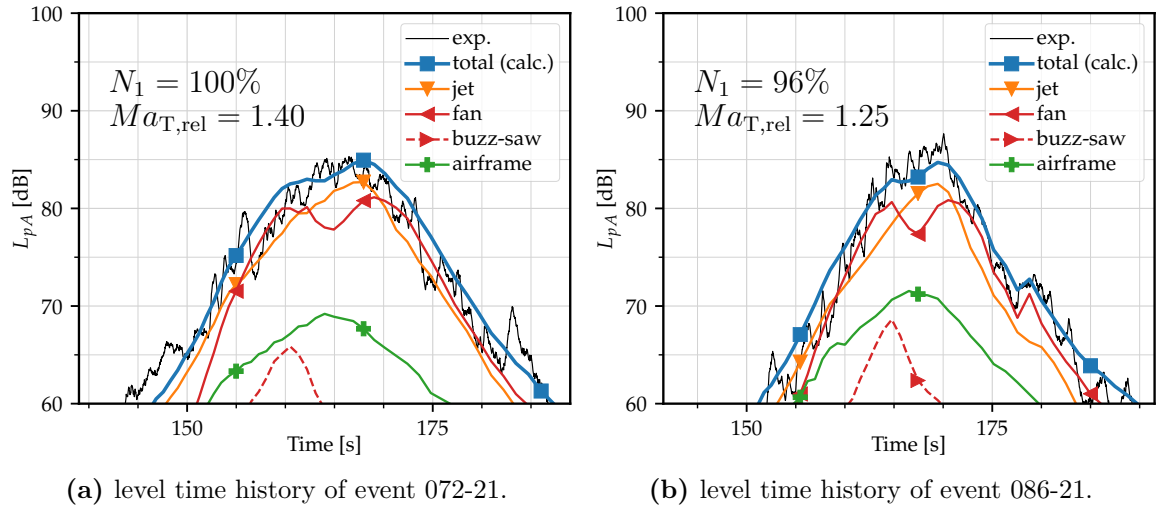


(c) buzz-saw component noise for  $f = \frac{1}{8}$ BPF

**Figure 4.17 & Table 4.7:** Old and new coefficients for the buzz-saw component of the fan noise model. Data extracted from reference [136, Figures 4.6.5 to 4.6.6].

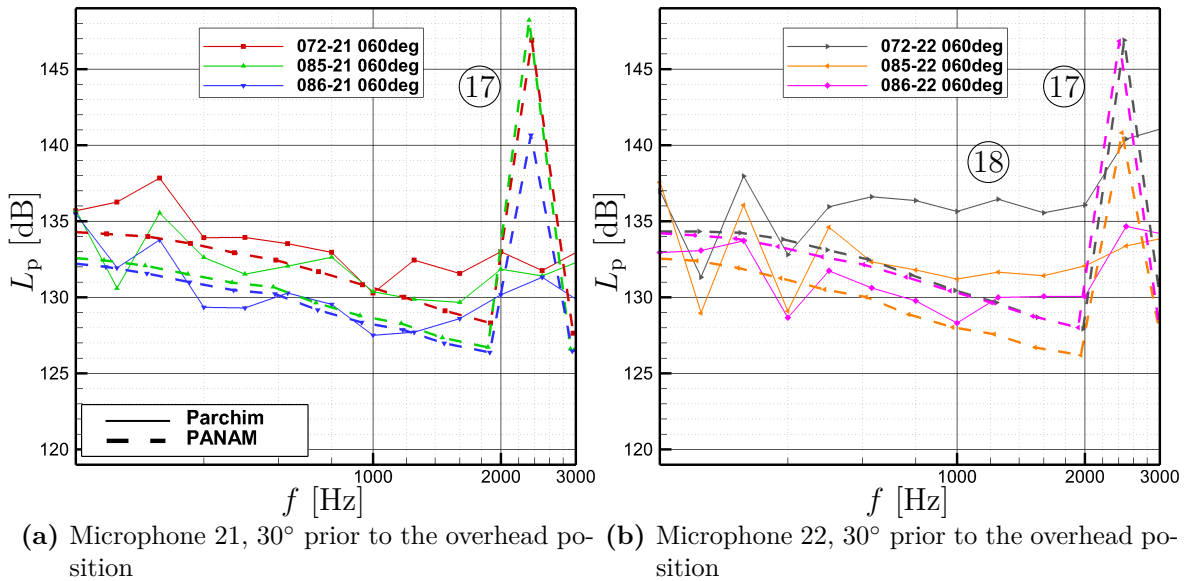
The A-weighted SPL time history at departure, which includes the buzz-saw noise model adjustment, has been shown in Figure 4.18. Particularly for the  $N_1 = 96\%$  case in Figure 4.18b, the predicted A-weighted SPL time history matches much better with the measured one.

Figure 4.19a shows the reverse-calculated emission third-octave band levels at departure in  $30^\circ$  prior to overhead position based on measurements recorded at Microphone 21, as well as the respective simulations. After the buzz-saw noise model adaptation, the measured and predicted third-octave band spectra match well with each other. PANAM over-predicts distinctly the fan tones, which are not found in the measurements (17). In contrast to the medium-thrust case, here the liner attenuates the fan tones by 4 dB. However, these third-octave bands are still caused by the fan tones, which are predicted too loud, although they



**Figure 4.18:** Measured Parchim and calculated PANAM level time histories for the two full-thrust departure events, 072-21 and 086-21. The update of the buzz-saw noise model coefficients has been applied.

have been predicted to be ‘cut-off’. In Figure 4.19b at Microphone 22, the event 072-22 is an outlier (18).



**Figure 4.19:** Measured spectra reverse-calculated to the fictitious point sound source at the airplane’s height and PANAM-calculated sound emission spectra for 30° prior to the overhead position at two microphones for three full-thrust events each. The buzz-saw noise model modification has been applied.

At overhead position the third-octave band spectra match well up to the 1600 Hz third-octave band at Microphone 21, see Figure 4.20a. Whereas, this is not the case for Microphone 22 where a considerable difference exists between the values, see 4.20b. At 2000 Hz PANAM

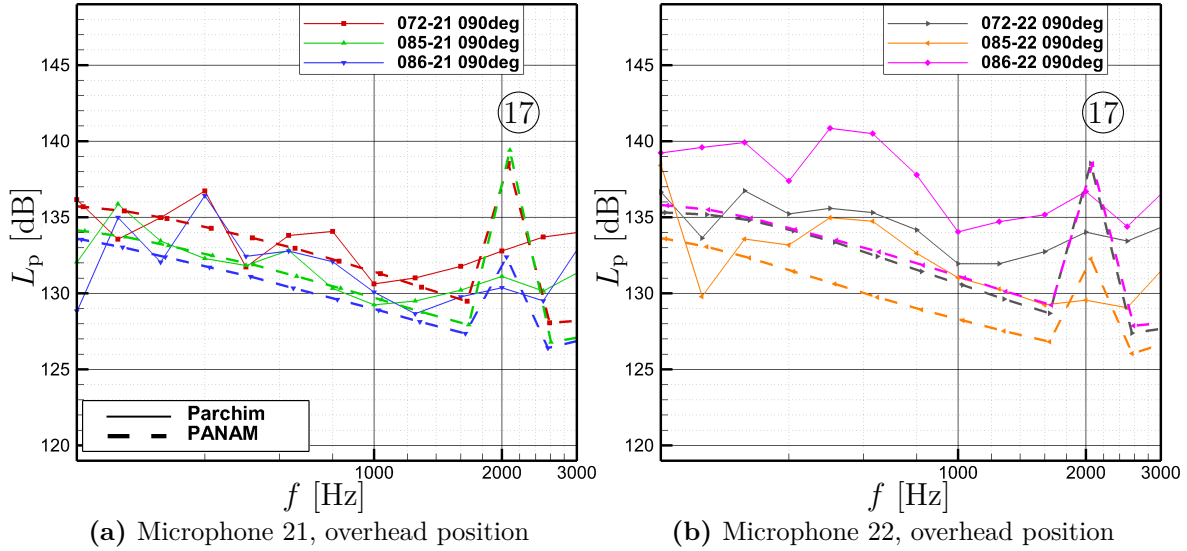


**Figure 4.20:** Measured spectra reverse-calculated to the fictitious point sound source at the airplane’s height and PANAM-calculated sound emission spectra for the overhead position for three full thrust events at two microphones each. The buzz-saw noise model modification has been applied.

predicts strong fan tones (17) at microphone positions 21 and 22. Neither the predicted fan inlet tones nor the fan aft tones can be found in the measured third-octave band spectrum.

## 4.5 Summary of the Chapter

PANAM has been found suitable to predict the airframe noise, and PrADO to model the large and heavy B747-400. The A-weighted airframe sound and the fan sound at medium thrust are under-predicted by PANAM by about 2 dB, although 1.9 dB over-predicted A-weighted SPLs were expected due to the simulation of hard ground. Furthermore, the engine broadband sound is under-predicted. This under-prediction, when investigating the third-octave band levels, is compensated by the over-prediction in the fan tones or the discontinuity in the liner model. Once the liner model behaves as expected, PANAM under-predicts airplane noise during approach by roughly 4 dB. Therefore, the engine and liner models need to be checked. The buzz-saw noise model has been modified to effectively model the CF6-80 buzz-saw sound emission.

The B747-400 masses calculated by PrADO coincide well to the official payload range chart. Only the center of gravity position differs, which does barely affect the noise prediction. Additionally, the predicted fuel consumption is in proximity to the official payload range chart data, which also indicate that the engine performance map comprises appropriate data. Furthermore, the correlation of engine speed and thrust of the predicted engine map showed good agreement with official Boeing data. Therefore, this PrADO model of the B747-400 is used as the reference airplane in this thesis.

# 5 | Target Function and Flight Procedures

This chapter deals with the important aspect of the assessment of the airplanes and associated procedures, post the validation of applied models and tools in the previous chapter. Section 5.1 focuses on the description of the area under investigation. Section 5.2 describes the index to assess the ground noise, which is called Awakening Index (AWI) and based on the Awakening Criterion by the DLR. Cost is very important to airlines, therefore, the Direct Operating Cost Index (DOCI) as a second assessment parameter is described in Section 5.3. The target function described in Section 5.4 is used to select the *optimal* airplanes for each technology level. The target function considers the Awakening Index and the Direct Operating Cost Index. Section 5.5 describes the approach and departure procedures. Section 5.6 states the design mission.

## 5.1 Area Under Investigation

The area under investigation is important because a small area leads to a different rank order than a large area. In this study, a large area has been chosen to consider not only high noise levels, but also the wide-spread lower sound pressure levels around airports. For example, an extremum of a very small area would be a single point. It is known from preliminary studies that the sound pressure level at a single location is not representative for an entire area. On the other hand, a very large area implies the challenge to weigh low, medium and high sound pressure levels against each other.

Figure 5.1 shows the area under investigation for assessing ground noise exposure. It covers a length of 50 km before and after the runway thresholds and 5 km to each side. The assumed runway length is 4.0 km, corresponding to three of the four runways of the Frankfurt Airport, Germany. Thus, the total area under investigation is 104 km long. The light green field, which stretches 2 km in front of and behind the runway, as well as 1 km on both sides, is uninhabited. It is assumed that this area is part of the airport, contains industrial area, traffic routes or forest land. For example, in Frankfurt this area consists of forest and airport area while at Germany's Düsseldorf Airport the closest population lives approximately 800 m away from the western approach threshold. The area under investigation is 1040 square kilometers, of which 1024 square kilometers being populated.

This study assumes a homogeneous population density of 1000 people per square kilometer within the populated area. This homogeneous population density could be easily multiplied with a certain population distribution. A generic population distribution representing an average population distribution for the world's major airports is still unavailable.

Noise [157], for example, used a homogeneous population density of 231 people per square kilometer in his investigations, which corresponds to the average population density in the

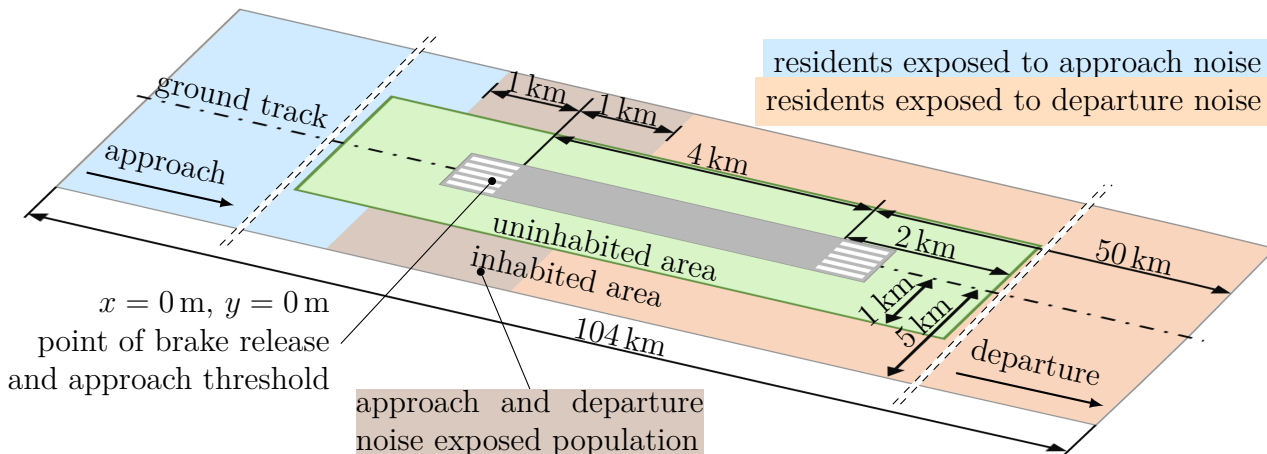


**Figure 5.1:** Sketch of the area under investigation, including the runway, the uninhabited, and the inhabited area around the airport with a population density of 1000 people per square kilometer.

Federal Republic of Germany. The population density is higher and inhomogeneous in areas around metropolises [84]. Realistic population density maps for Europe are available on the website of the European Environment Agency [67]. As already pointed out by Blinstrub [32], distinct approach and departure procedures generate varied ground noise at each location and can lead to different quietest trajectories for varied population distributions. Studies on generic airport layouts by Bernardo et al. [21, 22] stated the population distribution in combination with routing being an important assessment parameter. Hence, the population density around a generic airport is considered to be relevant in order to assess the ground noise of airplanes.

In this populated area of 1024 square kilometers live a total of 1,024,000 people. Residents sideways of the airport are exposed to the noise during both approach and departure. Thus, 16000 of the residents have been considered twice: once at approach, and once at departure. The areas that have been considered twice are colored ■ in Figure 5.1. Approaches and takeoffs have been independently investigated to find the characteristics, which determine the ground noise of these flight phases.

A few low-frequency sounds transmit beyond the investigated area. However, the investigated area is sufficiently large to rank the airplanes by their ground noise. Additionally, the noise protection zones for nighttime flights at Frankfurt Airport are fully covered by the area under investigation [229]. Hence, the area size as depicted in Figure 5.1 has been used to investigate the ground noise. The refinement study has led to a grid resolution of four cells per kilometer, sufficient to change the size of contour areas of selected sound exposure levels by less than one per mil.

## 5.2 Noise Assessment Index

A noise assessment index is required to compare the ground noise of a large number of airplane designs. Such an index should also account for redistributed ground noise to consider when more or less people are affected by any modification of the airplane or the flight procedure.

A given airplane can generate varying noise pollution along and beside the ground track by changing the approach and departure trajectory [32]. Furthermore, modifying the airplane and employing low-noise technologies alters the flight performance and trajectory, which redistributes the ground noise closer to or away from the airport. For example, an airplane may approach an airport and deploy its high-lift devices at high altitude, e.g., 40 km ahead of the approach threshold. The high-lift device noise will have an impact on the ground over a long distance, however, about 20 km before the approach threshold the airplane will be slower compared to one that deploys its high-lift devices at this position. The faster airplane will generate more noise at this later point. However, this affects a smaller area closer to the airport.

The available metrics have been found insufficient to assess airplane noise with consideration of the affected population. Ranking of the airplanes by their certification levels [118, 122], for example, does not necessarily lead to a fair ranking by their noise pollution at other locations. These certification levels only represent the ground noise locally at the three certification points without taking the whole area into account. An index considering the whole noise-affected population can be more expedient to assess the airplanes.

As yet, no assessment index is available to consider such a redistribution of ground noise when comparing two or more airplanes with the same mission specifications. The Frankfurter Fluglaermindex 2.0 (FFI 2.0) [230], for example, is a tremendous step forward with a focus on what the index from this Section 5.2 tracks: considering the noise exposure of the widespread population. However, the FFI 2.0 uses the AzB noise classes of the airplanes, and calculates the exposure from that. The aim of this research is airplane noise reduction in favor of the residents near airports. Established metrics have been combined to consider such a redistribution of ground noise and to achieve the greatest possible benefit for the residents and airlines, which is a compromise of low noise and low cost.

Noise can cause both additional awakenings and annoyance of the residents. Waking up during sleep is completely natural. However, noise events during deep sleep can disrupt the natural sleep cycle and provoke additional wake-up responses in a person, during the important sleep phases. These additional wake-up responses compromise the human body's recovery [18] and are called **awakening reaction** in the remainder of this thesis. Awakening is the strongest form disrupting the sleeping organism [19] and undisturbed sleep is necessary for health and psycho-motility performance [15, 219].

In contrast, noisy events can also cause annoyance. Annoyance refers to disturbances caused by noise events that occur when the person is awake. Annoyance will not be discussed further in this thesis.

The probability of awakening response ( $P_{\text{AWR}}$ ) in percent can be evaluated by Eq. (5.1).

$$P_{\text{AWR}}[\%] = 1.894 \cdot 10^{-3}(L_{pA,\text{max}})^2 + 4.008 \cdot 10^{-2}L_{pA,\text{max}} - 3.3243 \quad (5.1)$$

Eq. (5.1) only depends on the A-weighted maximum SPL ( $L_{pA,\text{max}}$ ) [18]. The sound pressure level predicted by PANAM is the outdoor sound pressure level. It has been reduced by 15 dB to represent tilted bedroom windows [34]. An upgrade of the awakening probability, thus an upgrade of Eq. (5.1), is in progress within the SIAM project and will consider more input parameters than the A-weighted maximum sound pressure level. Multiplying the awakening probability ( $P_{\text{AWR},i}$ ) with the area element ( $A_i$ ) and the population density ( $\rho_{\text{pop},i}$ ) gives the number of additional awakening reactions ( $N_{\text{AWR},i}$ ) in the respective area element. The additional awakening reactions of each area element can be summed up to the total amount

of additional awakening reactions ( $N_{\text{AWR}}$ ) as given in Eq. (5.2).

$$N_{\text{AWR}} = \sum_i \frac{P_{\text{AWR},i}}{100\%} \cdot \rho_{\text{pop},i} \cdot A_i \quad (5.2)$$

The additional awakening reactions will be determined for approach and departure individually, and will be summed up to an overall number of additional awakening reactions. The Awakening Index (AWI) follows from the additional awakening reactions of each airplane design relative to the additional awakening reactions caused by the reference B747-400 ( $N_{\text{AWR,ref}}$ ) as per Eq. (5.3).

$$\text{AWI} = \frac{N_{\text{AWR}} - N_{\text{AWR,ref}}}{N_{\text{AWR,ref}}} \cdot 100\% \quad (5.3)$$

This Awakening Index directly shows the reduction or increase in additional awakening reactions due to a noise reduction technology relative to the reference airplane. A value of  $-10\%$  means ten percent less additional awakening reactions as caused by the reference airplane, whereas a value of  $+5\%$  means five percent more additional awakening reactions. Note that an Awakening Index of  $-40\%$  means  $25\%$  less awakening reactions than an Awakening Index of  $-20\%$ . The Awakening Index is one important part of the target function, which is used to rank the airplanes by their ground noise. This index can easily be calculated individually for the approach- and departure-induced additional awakening reactions. If the Awakening Index is given either for approach or departure, then it is labeled Approach Awakening Index ( $\text{AWI}_{\text{app}}$ ) and Departure Awakening Index ( $\text{AWI}_{\text{dep}}$ ), respectively. This Awakening Index, compared to the Frankfurter Fluglaerminindex 2.0, also considers a redistribution, as well as a changed flight performance of each airplane. Thus, even minor differences in improved aerodynamics are considered and reflected. The second part of the target function is the direct operating cost, which is described in the next section.

### 5.3 Direct Operating Cost Index

The direct operating cost in the unit cost per passenger and per kilometer includes costs for manufacturing, cabin and flight crew, fuel and insurance, as well as additional airport fees. This direct operating cost analysis refers to the methods described by Heinze [99], which is based on the work by Pohl [165], Lichte [139] and Dehning [51]. This direct operating cost method was originally developed for medium-haul airplane that make several flights per day. Therefore, this method assumes that the airplanes operate approximately 4198 hours per year. In particular, when only outbound and return flights are assumed on long-haul routes, the 4198 operating hours are very optimistic because the airplane is often parked for several hours. It still has to be evaluated, if a direct operating cost method with one flight per day delivers more realistic results.

The direct operating cost throughout this study is predicted for the maximum payload flight of 415 passengers and 26.234 t cargo. Since direct operating cost is expressed in cost per seat per kilometer, cargo must be converted to revenue-equivalent seats: one tonne cargo has been set equivalent to five seats. Hence, the cargo has been considered as additional 131.17 passengers in the calculation of the cost per passenger kilometer. Flight and cabin crew costs have been procured from Eurocontrol [70] and airport fees from Fraport airport fees [81]. An interest rate of 2.7% on the investment cost has also been considered as per the Airbus bonds [securities identification number: A1HJMH].

Even though the direct operating cost (DOC) is a single number, it has been set in relative to the direct operating cost of the reference airplane ( $\text{DOC}_{\text{ref}}$ ) as in Eq. (5.4).

$$\text{DOCI} = \frac{\text{DOC} - \text{DOC}_{\text{ref}}}{\text{DOC}_{\text{ref}}} \cdot 100\% \quad (5.4)$$

The Direct Operating Cost Index (DOCI) makes the cost of each airplane directly comparable to the reference airplane's direct operating cost ( $\text{DOC}_{\text{ref}}$ ). The next section discusses the target function, meaning the weighing of the Direct Operating Cost Index against the Awakening Index.

## 5.4 Target Function

The parameter study yields a Pareto front from which an airplane will be selected. The selection of the airplane is based on Direct Operating Cost Index and Awakening Index and will be named optimal airplane. Hence, to make the airplanes comparable, this section presents the weighing of the ground noise against the cost. The aim is to identify how much Awakening Index translates into Direct Operating Cost Index.

For this weighing, the lack in productivity of the people due to noise induced awakenings has been assessed in monetary value as follows: It is assumed that disturbed sleep negatively affects the productivity by 20%, when the awakening occurred during the deep sleep. As per the Atlas Method, the Gross National Income in Germany has been US-\$136.29 per day [14]. For an assumed decrease of 20% work performance, when a person sleeps bad due to the additional awakening reaction, the economic damage accounts for approximately \$27.26 per capita per day.

Around 17,000 awakening reactions have been caused by the reference airplane in the area under investigation. Hence, 170 awakening reactions correspond to one percent Awakening Index. Nevertheless, one percent Awakening Index creates cost in the amount of  $170 \cdot \$27.26 = \$4634.2$ .

As per the above stated DOC method, a single flight costs \$365,316. Hence, one percent DOCI corresponds to \$3,653.

The question arises, how much must the Awakening Index be weighed against the DOCI? One percent Awakening Index costs  $1.27 (= \frac{\$4,634.2}{\$3,653})$  times more than one percent DOCI for a single flight per night.

In order to select the optimal airplane, a minimum of the sum of the DOCI in percent and 1.27 times the AWI in percent is selected. This target function, however, is just one of the many possibilities to select an optimal airplane with regard to AWI and DOCI. Note that this target function extremely emphasizes the additional awakening criterion. If more flights per night would be conducted, the flight cost would have a greater impact on the economic effects, i.e., the Direct Operating Cost Index would have to be weighed more than the cost of additional awakening reactions. The optimal airplane for low additional awakening reactions might vary, if the input parameters, such as area under investigation, population distribution, or even the flight procedures presented in the following Section 5.5, are changed.

## 5.5 Procedures for Noise Assessment

Departure and approach procedures are significant in the investigation of low-noise airplane designs. Hence, the following subsections present the procedures used in this thesis to assess the ground noise.

Such trajectories have been simulated at maximum takeoff weight and maximum landing weight, respectively, to cover the worst-case scenarios regarding ground noise. The flight simulations have been conducted in a standard atmosphere, hence at a temperature of  $15^{\circ}\text{C}$ , a pressure of  $101,325\text{ Pa}$ , and an air density of  $1.225\frac{\text{kg}}{\text{m}^3}$  on ground. Temperature, pressure, and density are calculated for a dry gas mixture. However, for the sound propagation and its attenuation through the atmosphere a relative humidity of 70 % on ground has been assumed, that corresponds to an absolute humidity of  $8.97 \cdot 10^{-3}\frac{\text{kg}}{\text{m}^3}$ . Additionally, trajectories and noise propagation are predicted for still air, i.e., without wind or gust.

### 5.5.1 Departure

Approximately three-quarter of the overall additional awakening reactions are caused by the departure and, hence, it dominates the selection of the optimal airplane design. However, the departure procedure is assumed to not influence the ranking of the airplanes by their Departure Awakening Index within one technology level. The ground noise of a variety of airplanes along a fixed departure procedure correlates strong with the averaged climb response that is the ground track length to reach a certain height. The rank order of airplanes by their averaged climb response is assumed to be the same for various engine power settings<sup>1</sup>, because the airplanes, which climb steeper or accelerate better at one engine setting, do also climb steeper or accelerate better at another power setting.

The ICAO-A procedure [72] has been selected as the reference departure, as it is well known and documented. It is depicted in Figure 5.2 to give an overview about the different segments and in Figure 5.3 by the black line. The Aircraft Noise and Performance Database (ANP) [45] provides the thrust setting of the engine for the investigated maximum takeoff rating. The thrust at an airspeed of  $91\frac{\text{m}}{\text{s}}$  has been used to determine the engine speed from the engine map used in PANAM for both takeoff and cutback. When the CF6-80 engine is mounted on the airplane, the departure is flown with  $N_{1,\text{to}} = 104\%$  during takeoff and reduced to  $N_{1,\text{cb}} = 98\%$  at power cutback. The cutback occurs at a height of 457 m (1500 ft) and this reduced cutback engine speed is maintained for the subsequent climb. Later, in Chapter 7 an ultra-high bypass ratio (UHBR) engine is mounted on further versions of the airplane. The UHBR engine features a higher thrust lapse when the airspeed is increasing. To make the trajectories that have been flown with the UHBR engine comparable to the trajectories flown with the CF6-80 engine, the takeoff and cutback engine speeds have been adapted for the UHBR engine. Using this ultra-high bypass ratio engine in Sections 7.2 to 7.4, the takeoffs are conducted at  $N_{1,\text{to}} = 108\%$ , which is reduced to  $N_{1,\text{cb}} = 101\%$  at the cutback height. At these engine speeds, the ultra-high bypass ratio engine provides at  $91\frac{\text{m}}{\text{s}}$  the same thrust as the CF6-80 engine.

To get a better understanding of the ICAO-A procedure relative to other ones, further procedures with a modified cutback height as well as takeoff and cutback engine speed have been investigated and plotted in Figure 5.3. This figure provides an overview how the Awakening Index alters with a changing departure procedure. The power cutback height has been altered within 305 m to 610 m (1000 to 2000 ft) in 152 m steps, and both takeoff

---

<sup>1</sup>The focus is on engine power settings for which all airplanes can depart.

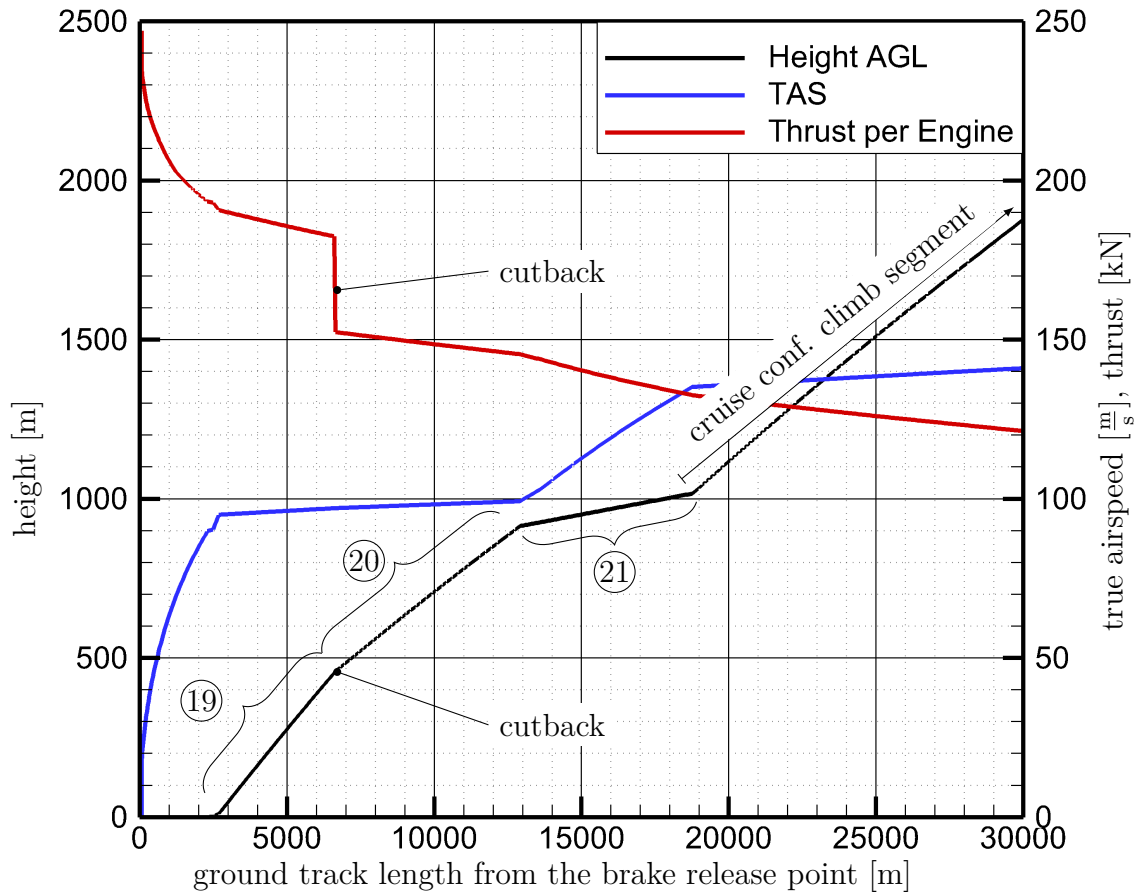


**Figure 5.2:** Segments of the ICAO-A departure procedure as named in this study.

- ①9: takeoff-thrust climb segment
- ②0: cutback-thrust climb segment
- ②1: cutback-thrust acceleration segment

The cruise configuration departure segment continues up to a height of 3048 m (10000 ft). Above this height, it is unknown how the airplane flies because an acceleration up to the cruise speed is allowed.

and cutback engine speeds have been independently varied from 94% to 110% in 2% steps. However, the main focus remains on the qualitative behavior instead of the exact path of each trajectory. The line color represents the Departure Awakening Index, where the blue lines denote fewer additional awakening reactions and the red ones more additional awakening reactions. The quietest departure conducts the takeoff using high engine speed of  $N_{1,to} = 108\%$  up to the highest investigated cutback height of 610 m, and reduces the power setting here to  $N_{1,cb} = 94\%$ . In such a trajectory, the airplane gains a certain height, here 1200 m, over short ground track length, which is called averaged climb response. The engine speed is reduced at the cutback height to lower the engine sound emission. The airplane flies loudest when the takeoff is performed with a reduced engine speed of  $N_{1,to} = 94\%$ , which is increased to  $N_{1,cb} = 110\%$  at the cutback height. In such a trajectory, the airplane is at lower height when the jet sound becomes dominant.

Note, that the engine speed setting, which causes the lowest Awakening Index, depends on the noise source ranking by their respective loudness. Identical to Figure 5.3, in Figure A.5.0.1 the Departure Awakening Index is also investigated studying the same trajectories using a different noise source ranking. For the study in Figure A.5.0.1, the coefficients

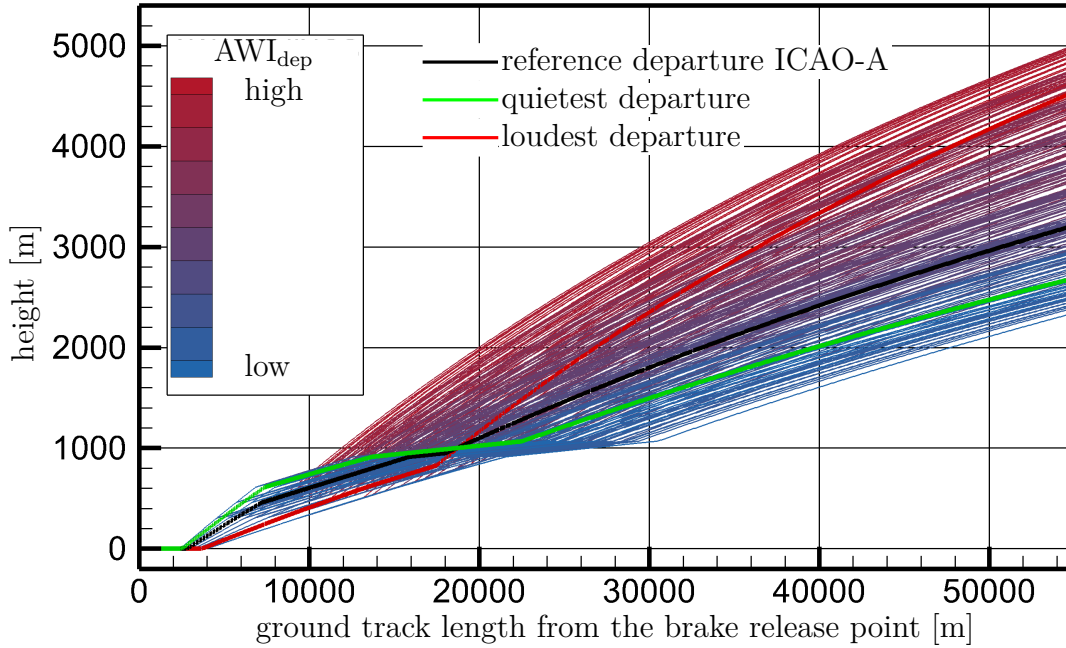


**Figure 5.3:** Study of different departure thrust settings and cutback heights flown by the reference airplane. The reference departure procedure is the ICAO-A procedure depicted by the black line. It has been compared with procedures flown at different engine speeds for takeoff, after cutback, and performing the cutback at three different heights. The color gives a qualitative value of the Departure Awakening Index ( $AWI_{dep}$ ), showing whether a procedure causes more or less additional awakening reactions. The red and green line show the loudest and the quietest departure procedure, respectively. All trajectories have been flown by the reference B747-400.

of the original Kontos buzz-saw noise model have been applied. Buzz-saw sound is more prevalent in the original Kontos model than in the modified one. As seen in Figure A.5.0.1, the airplanes at lower engine speeds cause more awakening reactions due to dominating buzz-saw sound. At higher engine speeds the buzz-saw sound lowers, experiencing a reduction in awakenings, yet with a louder jet sound. The quietest trajectory is a compromise of the ones with the jet sound causing most of the additional awakening reactions and the one with the buzz-saw sound causing most of the additional awakening reactions.

### 5.5.2 Approach

Since different airplanes distinguish in their flight performance, different trajectories are optimal for different airplanes. The optimal approach trajectory could be determined in a fifth dimension of the parameter study, in which different glide paths would be examined. However, to avoid an additional dimension in the parameter study and thus reduce the computational effort, a definite approach procedure is needed that always provides an individual, low-noise flight path. An approach procedure with the following criteria, which are ranked in order of priority, has been investigated [37, 134]:

1. entering  $-3^\circ$  final approach segment at 914 m (3000 ft) as standard
2. stabilization height at 304 m (1000 ft) as standard

3. landing gear deployment at 457 m (1500 ft) as standard
4. engine idling from any height relevant for ground noise to stabilization point
5. no acceleration
6. most delayed high-lift system deployment
7. approach at a speed of  $v \geq 1.3 \cdot v_{\text{stall}}$

The criteria from 1 to 6 have been fulfilled throughout the whole study, and the approach speed in criterion 7 in some cases has been found faster than  $1.3 \cdot v_{\text{stall}}$ . This approach speed becomes a key factor for ground noise later in Section 6.2, Section 6.3.1, and Figure 6.6.

The criterion 7 has been implemented into the trajectory software FLIPNA. The approach speed of  $v = 1.3 \cdot v_{\text{stall}}$  is selected, referred from *Demonstration of Static Longitudinal Stability* of the EASA Certification Specifications for Large Aeroplanes [66, CS-25.125 'Landing']. This speed is about 6 % faster than the slowest allowed approach speed of  $v = 1.23 \cdot v_{\text{stall}}$  to make this procedure feasible. Therefore, the  $v = 1.3 \cdot v_{\text{stall}}$  will be referred to as the *slowest feasible velocity* in the rest of this thesis.

These criteria 1 to 7 result in a trajectory as shown in Figure 5.4 that also shows the various segments of the approach procedure. This constant approach speed results in a slightly increasing descent angle, i.e., approaching flatter along the cruise configuration segment because the engine's idle thrust increases slightly with increasing air density. According to Eq. (3.1), the minimum thrust defines the optimal descent angle, as the glide ratio remains constant during the airplane flies in cruise configuration.

This procedure, further in this thesis, will be termed *low drag minimum power* procedure as it has been derived from the LDLP and CDA. It differs from the CDA by an individual and optimal trajectory slope along the first descent section as well as a constant and slowest feasible approach speed. After the cruise configuration approach segment, this procedure has a horizontal segment to decelerate as along the horizontal segment of the LDLP procedure. However, the horizontal segment of the LDLP is much longer than absolutely necessary. Flying the low drag minimum power approach, the airplane descends at an optimum glide angle, approaching as slow as feasible by adjusting the pitch. As soon as the horizontal segment is entered, the high-lift devices are deployed. This segment is used to decelerate and kept as short as possible, before intercepting the final approach segment. Note, that this low drag minimum power procedure is flown at the absolute limits in terms of low speed and latest possible high-lift device deployment. Ultimately, pilots flying the low drag minimum power approach will need electronic assistance, such as the Low Noise Augmentation System [1, 2, 193] because a precision flight is required. This low drag minimum power method helps to determine the noise reduction potential of airplanes. It also helps to understand the relationship between airplane design, flight performance, and airplane noise.

This *low drag minimum power* procedure has been compared against a parameter study over CDA and SCDA procedures, as depicted in Figure 5.5. All trajectories have been simulated with the reference airplane, the PrADO model of the B747-400. As LDLP procedures with a longer horizontal segment than necessary cannot be calculated by FLIPNA, SCDA procedures have been used as an alternative. However, unlike the LDLP approaches, SCDAes have no horizontal segment. The slope of the SCDAes varies from  $-4.0^\circ \leq \gamma_1 \leq -1.5^\circ$  and  $-4.0^\circ \leq \gamma_2 \leq -1.6^\circ$ . The CDAes are performed for descent angles ranging  $-4.0^\circ \leq \gamma \leq -1.6^\circ$ . All these approaches enter the  $-3^\circ$  final approach segment at 914 m (3000 ft) height. As the airplane in cruise configuration would accelerate on slopes  $\gamma \leq -2.7^\circ$ , the high-lift devices are deployed in approach configuration on such sections. The most delayed location to deploy the high-lift devices is shortly before entering this final approach segment. Just

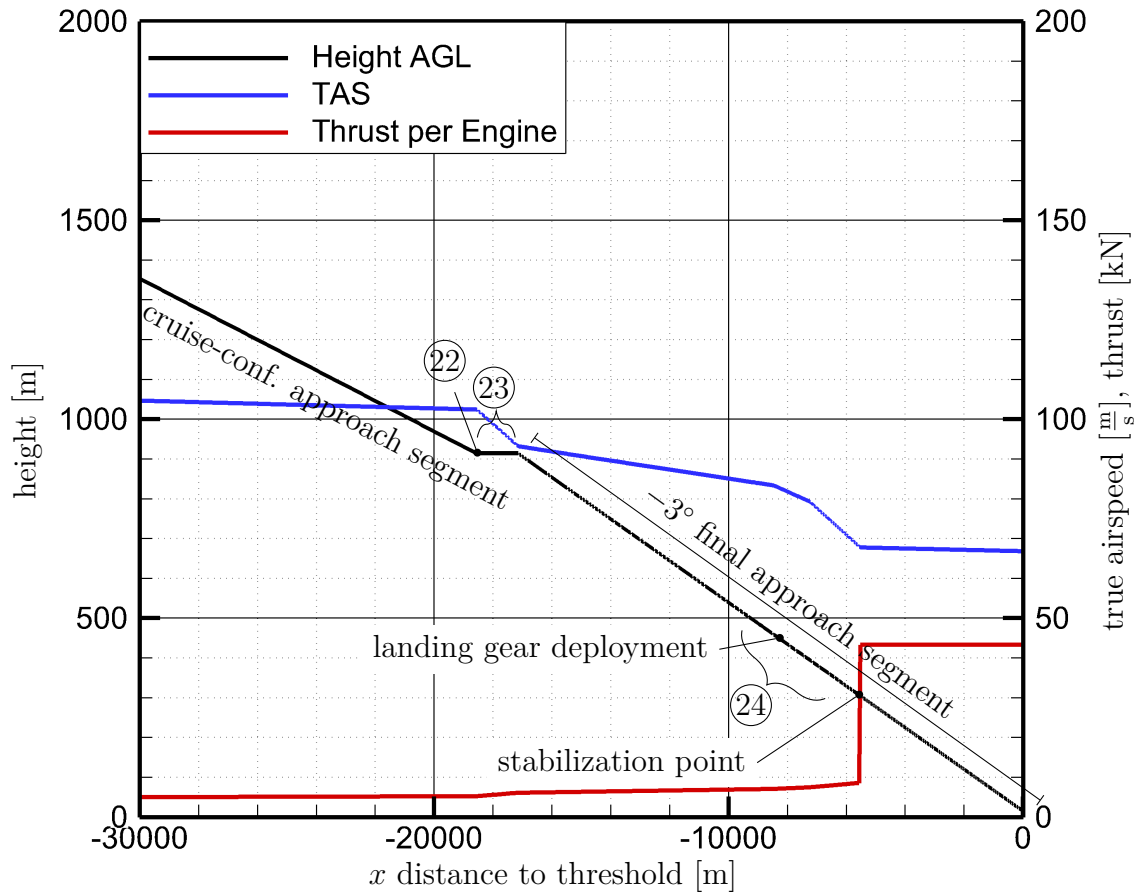


**Figure 5.4:** Low drag minimum power procedure. The cruise configuration approach segment is flown in cruise configuration at minimum speed. Along the horizontal segment, the airplane decelerates in approach configuration. At 17 km before the approach threshold, the airplane intercepts the  $-3^\circ$  final approach segment. The high-lift devices are deployed in landing configuration when required. At a height of 457 m (1500 ft), the landing gear is deployed. At a height of 305 m (1000 ft), the airplane stabilizes.

- ②②: high-lift devices deployment to approach configuration
- ②③: horizontal segment
- ②④: high-lift devices deployment to landing configuration when required

after the landing gear deployment at 457 m (1500 ft) height, the high-lift devices are further extended to landing configuration. The airplane decelerates to its landing speed until the stabilization height of 305 m (1000 ft). At the stabilization point, the engine is spooled up to compensate for the drag and maintain the landing speed.

All trajectories within the aforementioned range have been plotted in Figure 5.5. The two black and green lines represent the approach trajectories causing the lowest Approach Awakening Index. The dashed red line represents the approach trajectory causing the highest Approach Awakening Index.

Two distinct blocks of approach trajectories have been identified. The first block distinguishes from the second one by the location of the high-lift device deployment: far before entering final approach segment, or shortly before entering the final approach segment. The first block lies below the quietest approach and the second block below the loudest approach. The flatter the airplane approaches, the more thrust is required. The second block consists

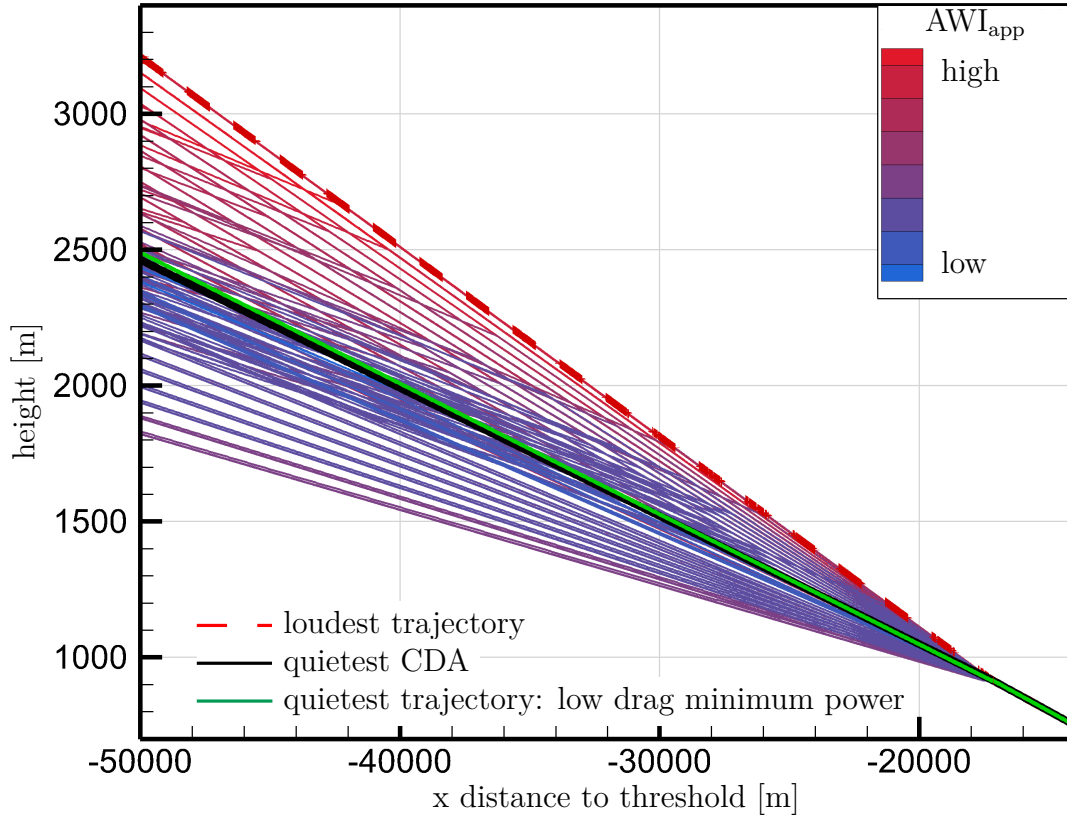


**Figure 5.5:** Approach procedure study over CDA, SCDA, and the low drag minimum power procedure. The red line depicts the loudest approach trajectory and the two green and black lines represent the quietest approach trajectories. All trajectories have been calculated using the reference airplane, the PrADO model of the B747-400.

of all the trajectories including steeper segments where high-lift devices have been deployed to prevent the acceleration of the airplane. High-lift devices cause drag that is compensated by increasing the engine thrust, which in turn increases the ground noise. However, this increased engine thrust does not determine the Approach Awakening Index. The loudest trajectories are at the continuous descent approach with  $\gamma = -4.0^\circ$  and the segmented continuous descent approach with  $\gamma_2 = -4.0^\circ$ . The trajectories of the second block generate a higher Approach Awakening Index when the second segment is steeper. This is due to the fact that these airplanes decelerate along the trajectories: the steeper the trajectory, the faster the reference airplane when the area under investigation begins. However, it would be a fallacy to conclude that steeper approaches are noisier. This is because the result is likely to be different when a larger area under investigation is chosen.

However, it can be concluded that approaches are very likely to cause fewer awakening reactions when the high-lift devices are deployed very late: just prior entering the final approach segment. Again, the flatter the trajectory, the more engine thrust is required to prevent the airplane from becoming too slow, leading to more ground noise.

The quietest approach trajectory is the low drag minimum power approach. The airplane already flies at the slowest feasible speed. It generates minimum additional awakening reactions, as it delays the high-lift device deployment to the maximum extent, which keeps the noise-affected area small. This procedure considers the airplane's individual stall speed and descent angle and, hence, the flight path is individual for each landing weight and flight performance. The airplane is quieter when it is flying faster in cruise configuration compared to flying slower using high-lift devices.

Instead, flying the quietest continuous descent approach causes around 2% more awakenings compared to the low drag minimum power approach as the airplane flies lower and the engine is at higher thrust setting to maintain the speed. As evident from the above analysis, the trajectories flown in cruise configuration tend to cause a lower Approach Awakening Index, when they are flown steeper, and a higher Departure Awakening Index, when they are flown flatter. The reasons are less distance to the residents and more required engine thrust to maintain the approach speed.

Finally, the low drag minimum power procedure is promising in providing a definite low-noise trajectory utilizing the airplane's individual flight capabilities. Each of the airplanes investigated in Chapters 6 and 7 exhibits a slightly different flight performance and, thus, needs a slightly disparate glide slope to approach at the slowest allowed speed. Hence, the low drag minimum power approach is the reference approach procedure in this study.

## 5.6 Design Mission

This section describes the design mission that forms the reference for all airplanes in this study. All flights have been simulated at maximum payload capability of the B747-400. The maximum payload for this airplane consists of 415 passengers and 26,234 kg cargo. One passenger is assumed to weight 99 kg inclusive of the average summer and winter luggage weight [71, page 218]. With this maximum payload of 67.319 t, the airplane can fly 10,602 km [13, Figure 3.2.1], being set as the reference range.

The design speed of the B747-400 is  $Ma_{cr} = 0.85$ . It was kept constant for the airplanes with engines mounted under the wing. For the airplane with the engines mounted above the wing, the cruise speed was adjusted to account for the nacelle's impact on the wave drag as further described in Section 7.1. Area under investigation, approach and departure procedures, Awakening Index, and Direct Operating Cost Index are used to further assess the basic airplane designs when they fly this design mission.

# 6 | How Planform Parameters Affect Ground Noise

This chapter focuses on the parameter study of three planform parameters. The aim is to investigate the noise reduction potential of the B747-400 by only modifying the planform. As a modification of wing design changes the airplane’s flight performance, the capability to lower the ground noise can be influenced as early as the conceptual design phase by selecting the appropriate planform.

The three planform parameters leading-edge sweep, wing area, and aspect ratio have been considered, and their values have been varied to study a total of 700 airplane designs apart from the reference one. Their effects on the flight performance, on the trajectories, and ultimately on the ground noise have been investigated. The ground noise is quantified by the Awakening Index. The values of these planform parameters have been varied within the ranges as listed in Table 6.1.

**Table 6.1:** Parameters that have been varied and their respective range for the parameter study of the basic airplane, i.e., without applying noise-reducing technologies. 700 of the 720 possible combinations have been successfully calculated.

| Parameter                   | Minimum | Maximum | Resolution | No. of sample points |
|-----------------------------|---------|---------|------------|----------------------|
| leading-edge sweep [°]      | 26      | 44      | 2          | 10                   |
| wing area [m <sup>2</sup> ] | 500     | 660     | 20         | 9                    |
| aspect ratio [-]            | 6.5     | 10.0    | 0.5        | 8                    |

When the leading-edge sweep is lowered, the wing weight decreases as less material is required because the bending moments around the  $y$ -axis are lowered. The reduced wing weight lowers the overall airplane weight, leading to less fuel consumption. Lower airplane weight might, in turn, affect the optimal wing area, which can then also be reduced. This might decrease the drag, fuel consumption, and structural mass. Hence, a parameter study has been conducted using the PrADO-PANAM tool chain to investigate these effects and their impact on the ground noise. For all airplane designs under consideration, the Departure and Approach Awakening Indices are investigated, considering the maximum takeoff weight and maximum landing weight, respectively.

To assess the airplane designs using the overall Awakening Index, the approach- and departure-induced awakening reactions have been equally weighted, appreciating there are as many landings as takeoffs. Airplane designs causing minimum additional awakening reactions during departure are not necessarily the same designs causing minimum additional awakenings during approach. Weighing departure and approach awakening reactions differ-

ently would change the target function and would therefore ultimately influence the selection of the most promising low-noise design. The airplane, which is selected in this chapter, is named basic airplane.

Hence, the following two Sections 6.1 and 6.2 discuss the necessary characteristics to obtain a low-noise airplane during departure and approach, respectively. They show correlation coefficients of selected variables with either the Departure or Approach Awakening Index. The correlation coefficients with the Overall Awakening Index are shown in Figure A.6.0.2. Section 6.3 discusses the respective influence of each planform parameter on the Awakening Index, followed by Section 6.4, which determines the optimal airplane design based on the target function. Section 6.5 will determine the basic airplane's prevailing sound sources. Section 6.6 compares the trajectories and the ground noise of the basic airplane with the ones of the reference airplane. The last Section 6.7 provides a conclusion of this chapter.

## 6.1 Departure Situation

The Pearson's correlation coefficient ( $r$ ) [162] is one of the most used classification numbers to describe the linear correlation between variables [199]. This correlation coefficient is used to identify linear relations between variables that are worth being investigated for causality. The correlation coefficient is calculated using the Eq. (6.1).

$$r = \frac{N \sum(xy) - (\sum x)(\sum y)}{\sqrt{[N \sum(x^2) - (\sum x)^2][N \sum(y^2) - (\sum y)^2]}} \quad (6.1)$$

Eq. (6.1) consists of number of pair of scores ( $N$ ) and the variables to investigate the correlation for  $(x,y)$ . In Figure 6.1, e.g,  $x$  is the Departure Awakening Index,  $y$  is the variable investigated, and  $N$  is the number of airplanes. The Pearson's correlation coefficient lies in  $r \in [-1,1]$ , with  $r = 1$  and  $r = -1$  representing a perfect linear relation with a positive and negative slope, respectively, and  $r = 0$  represents uncorrelated values [199].

The p-value is used to determine statistical significance. Values of  $p$  below 0.05 are considered to be statistically significant.

Figure 6.1 shows how the selected, investigated variables correlate with the Departure Awakening Index when departing as per the ICAO-A procedure. These variables have been selected for various reasons such as (a) their values correlate highly with the Departure Awakening Index, (b) the assumption that their values correlate highly with the Departure Awakening Index, (c) being design parameters, or (d) being useful to characterize an airplane design.

The highest Pearson's correlation coefficient has been found for the pair of the ground track length until a height of 1200 m is reached and the Departure Awakening Index. This variable combination has a Pearson's correlation coefficient of 0.99 (25). The runway reference point is the location of brake release. Factors such as takeoff roll distance, climb capability in takeoff configuration, acceleration capability after cutback, and climb capability after acceleration collectively result in this ground track length up to a flight height of 1200 m. The reciprocal of this ground track length is termed an averaged climb response. This length and its corresponding Departure Awakening Index of each airplane is shown in Figure A.6.1.4.

There is a logical reason for this high correlation coefficient, which is illustrated in Figure A.6.1.5. The engine sound prevails the departure-induced awakening reactions. Since the engine speed depends only on the flight height, the engine power and the noise emission also depend, in a first approximation, only on the flight height. If an airplane climbs flatter,

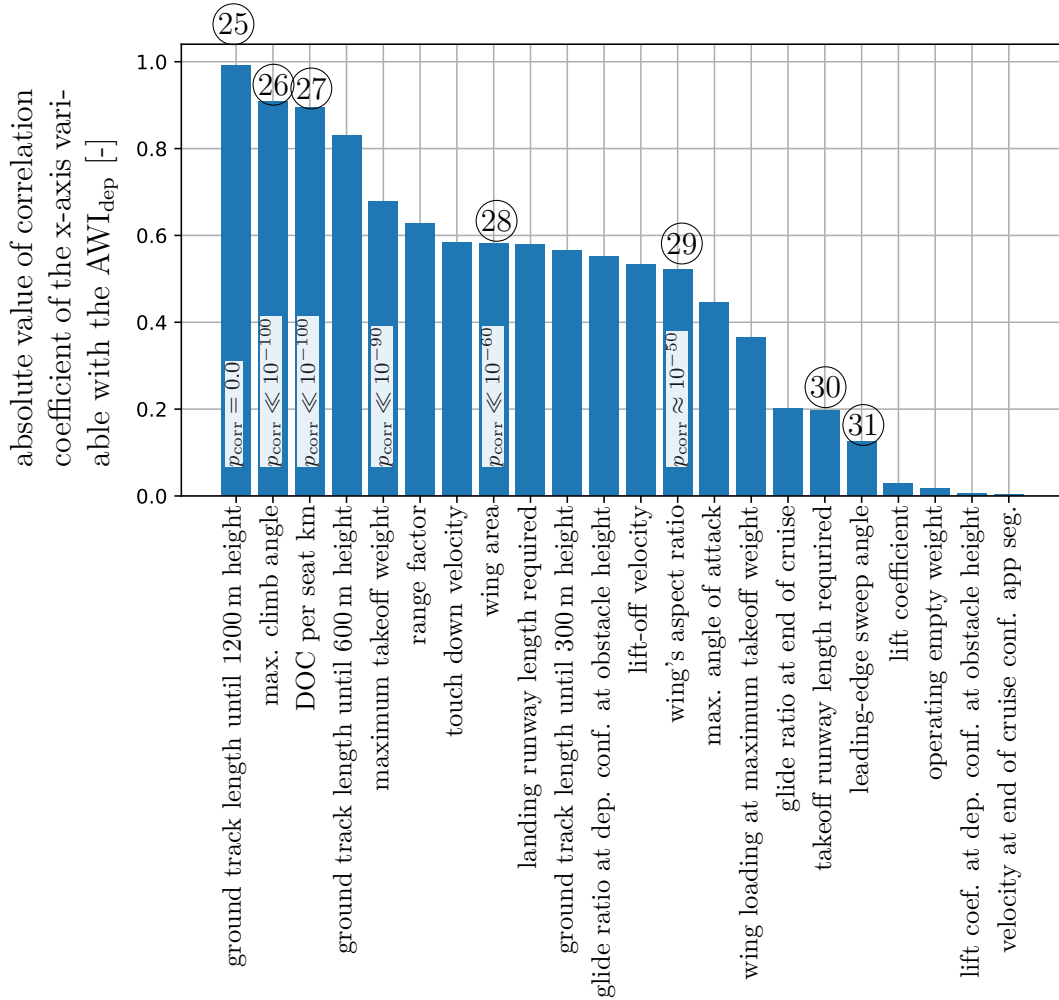


**Figure 6.1:** Absolute value of the Pearson’s correlation coefficient of various variables with the Departure Awakening Index ( $AWI_{dep}$ ). The averaged climb response (25) has the highest correlation coefficient. As anticipated, the maximum climb angle (26) also has a high correlation coefficient of 0.9. Focusing on the three planform parameters, the wing area (28) has the highest correlation coefficient of 0.58. However, none of the selected design parameters has a direct impact, and all parameters collectively contribute to a low-noise basic airplane during departure. The correlation coefficients with the Overall Awakening Index, i.e., for departure and approach, are shown in Figure A.6.0.2.

then the same or higher sound pressure levels impact on the ground over a larger area. In addition, ground noise near the airport does not count where the airplane is low because this area is uninhabited.

Figure 6.2 shows the trajectories flown by the airplanes from the parameter study. Each airplane flies the ICAO-A procedure with  $N_{1,to} = 104\%$  and  $N_{1,cb} = 98\%$ . When the airplane is at a height of 1200 m, the acceleration segment is completed and the airplane continues to climb in cruise configuration and at the maximum allowed speed of  $130 \frac{m}{s}$ . A low maximum takeoff weight and high glide ratio are found to be the active contributors to a high averaged climb response.

This averaged climb response is synonymous with the distance required to achieve the same mass-specific total energy, since all airplanes are at the same height and speed. Hence,

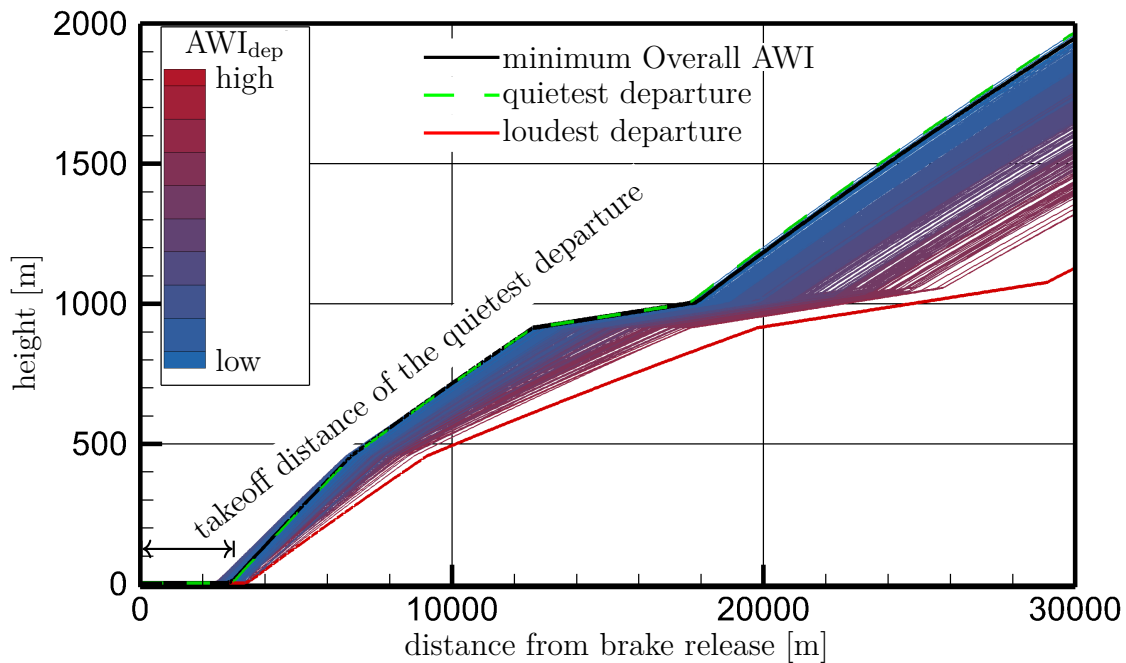


**Figure 6.2:** Trajectories of all airplanes from the basic airplane study flying the ICAO-A procedure. The quietest airplane (green dashed line) can reach a height of 1200 m in a shorter distance than the other airplane designs, although the takeoff runway distance required is not the shortest. However, the quietest airplane accelerates to a higher speed on the runway, and then climbs steeper due to lower weight. As the airplane is already at faster speed, the high-lift devices are retracted earlier compared to slower airplanes. The trajectory of the airplane that causes the lowest Overall AWI (black line) is very similar to the trajectory of the quietest airplane design because the departure causes most awakenings and, hence, dominates the selection of the overall quietest airplane design.

the airplane causing the least awakening reactions is a light one that dissipates the least energy provided by the engine. Light means that the airplane does not have to be the lightest. Instead, it means that the airplane that reaches this mass-specific total energy needs the shortest distance.

The wing design parameters interact with each other, as summarized in Table 6.2. Many of these interactions are counteracting as, e.g., a decrease in the aspect ratio causes a lower glide ratio and an increase of it leads to a heavier wing. Both effects have the potential to increase the ground noise during departure due to more required cruise fuel and more structural weight. A certain combination of parameter values results in an optimum. Thus, the collective interaction of the design parameters wing area, aspect ratio, and leading-edge sweep determines the minimum Departure Awakening Index.

**Table 6.2:** Effects of decreasing and increasing values of the planform parameters on the averaged climb response. Each decrease and increase in the parameter values has positive and negative effects on the averaged climb response. All advantageous effects have been listed in the upper part of the table, and disadvantageous effects have been listed in its lower part.

Legend:  
 increasing with an advantageous  or disadvantageous  effect  
 decreasing with an advantageous  or disadvantageous  effect  
 '⇒' – leading to

|  advantageous effects on avg. climb response      |  |  |
|--|--|--|
| parameter  | effects, if parameter value is increased   | effects, if parameter value is decreased   |
| area   | <ul style="list-style-type: none"> <li>• wing loading </li> </ul>   | <ul style="list-style-type: none"> <li>• wing mass </li> <li>• wetted surface  ⇒<br/>drag  ⇒ fuel mass </li> </ul> |
| aspect ratio   | <ul style="list-style-type: none"> <li>• lift efficiency </li> </ul>  | <ul style="list-style-type: none"> <li>• wing mass </li> <li>• fuel mass </li> </ul>   |
| sweep  | <ul style="list-style-type: none"> <li>• cruise drag  ⇒<br/>fuel mass </li> </ul>  | <ul style="list-style-type: none"> <li>• wing mass </li> <li>• fuel mass </li> <li>• circulation efficiency </li> </ul>   |
|  disadvantageous effects on avg. climb response |  |  |
| parameter  | effects, if parameter value is increased   | effects, if parameter value is decreased   |
| area   | <ul style="list-style-type: none"> <li>• wing mass </li> <li>• cruise drag  ⇒<br/>fuel mass </li> </ul> | <ul style="list-style-type: none"> <li>• wing loading </li> </ul>   |
| aspect ratio   | <ul style="list-style-type: none"> <li>• wing mass </li> <li>• fuel mass </li> </ul>   | <ul style="list-style-type: none"> <li>• glide ratio </li> <li>• lift efficiency </li> <li>• fuel mass </li> </ul>  |
| sweep  | <ul style="list-style-type: none"> <li>• wing mass </li> <li>• lift efficiency </li> </ul>   | if wave drag occurs: <ul style="list-style-type: none"> <li>• fuel mass </li> <li>• structural mass </li> </ul>  |

Figure 6.2 shows that the takeoff roll distance of the quietest airplane is a median one as compared to the other designs. Furthermore, the takeoff roll distance does not correlate with the Departure Awakening Index (30). The wing area (28) of this airplane is smaller compared to the reference. This smaller wing area has two advantages, a higher wing loading and a lighter manufacturer empty weight. The advantage of the higher wing loading is that the airplane's liftoff speed is increased. More of the acceleration is conducted at the high takeoff thrust setting on the runway before the engine thrust is reduced at the cutback position. This leads to a steeper climb along the first climb segment and shortens the acceleration

segment, which is flown at the cutback thrust. Note that the acceleration segment always ends at  $130 \frac{\text{m}}{\text{s}}$ . Additionally, the high-lift devices, which increase the drag compared to cruise configuration, are retracted earlier.

A lighter airplane has a higher thrust-to-weight ratio. An airplane with a high thrust-to-weight ratio and a high glide ratio, is the ideal property for a low-noise departure. Such an airplane conducts the departure at comparatively greater heights, which increases the distance to the residents and allows the airplane to reach the cutback altitude earlier. The exact values of the design parameters have to be determined in a holistic optimization process.

Initially, it was assumed that the climb angle (26) correlates the most with the awakenings [32]. However, the climb angle, which is plotted against the Departure Awakening Index in Figure A.6.1.3, is not the sole factor. Instead, the ground track length up to a flight height of 1200 m conditions the Departure Awakening Index.

Note that this outcome has been drawn using only the ICAO-A takeoff procedure and only one type of engine, the CF6-80. Only when any sound source at maximum allowed speed would surpass the engine sound pressure level at climb speed, the outcome is expected to change. Since clean wing airframe sound sources are usually below the sound pressure levels of engines, this finding is expected to be very reliable, even for similar departure procedures. However, this still needs to be finally verified.

The following section discusses the influence of the planform parameters on the Approach Awakening Index.

## 6.2 Approach Situation

All airplane designs have been investigated using the low drag minimum power procedure described in Section 5.5.2. Most of the airplanes fly at 1.3 times the stall speed. This corresponds to the lower velocity limit of 1.23 times the stall speed including an additional margin of 6 % [66, CS-25.125 'Landing']. The engine is set to flight idle, therefore it contributes very little to the ground noise. The Pearson's correlations have been utilized to identify the key factors responsible to achieve a low-noise airplane design at approach.

Figure 6.3 shows the Pearson's correlation coefficients of the respective investigated variables with the Approach Awakening Index. The Approach Awakening Index correlates highest with the velocity at the end of the cruise configuration segment (32). Hence, Crichton's statement that the ground noise correlates with the stall speed can be confirmed [47, p. 2].

The airplane that has a slow approach velocity has three advantages. It requires less deceleration prior to entering the  $-3^\circ$  final approach segment and, hence, the high-lift devices are deployed later. This later deployment of the high-lift devices at lower velocities reduces its ground noise due to delayed starting noise contour areas and lower sound pressure levels. Furthermore, slower velocities associate also with a reduction of clean-wing trailing-edge sound along the cruise configuration segment. Note, the clean-wing trailing-edge sound, which is usually considered to be a non-dominant sound source, contributes to the awakening reactions, which will be shown later in Section 6.5 on page 80.

The same absolute value of correlation coefficient, which was found for the approach speed, was also found for the engine thrust at the same location, the end of the cruise configuration segment. The airplane's thrust setting is at idle and the engine thrust is inversely proportional to the flight velocity. Hence, the velocity at which the airplane flies in cruise configuration leads to both correlations. However, only the velocity at the end of the cruise configuration segment is the reason for the high correlation with the Approach Awakening Index.

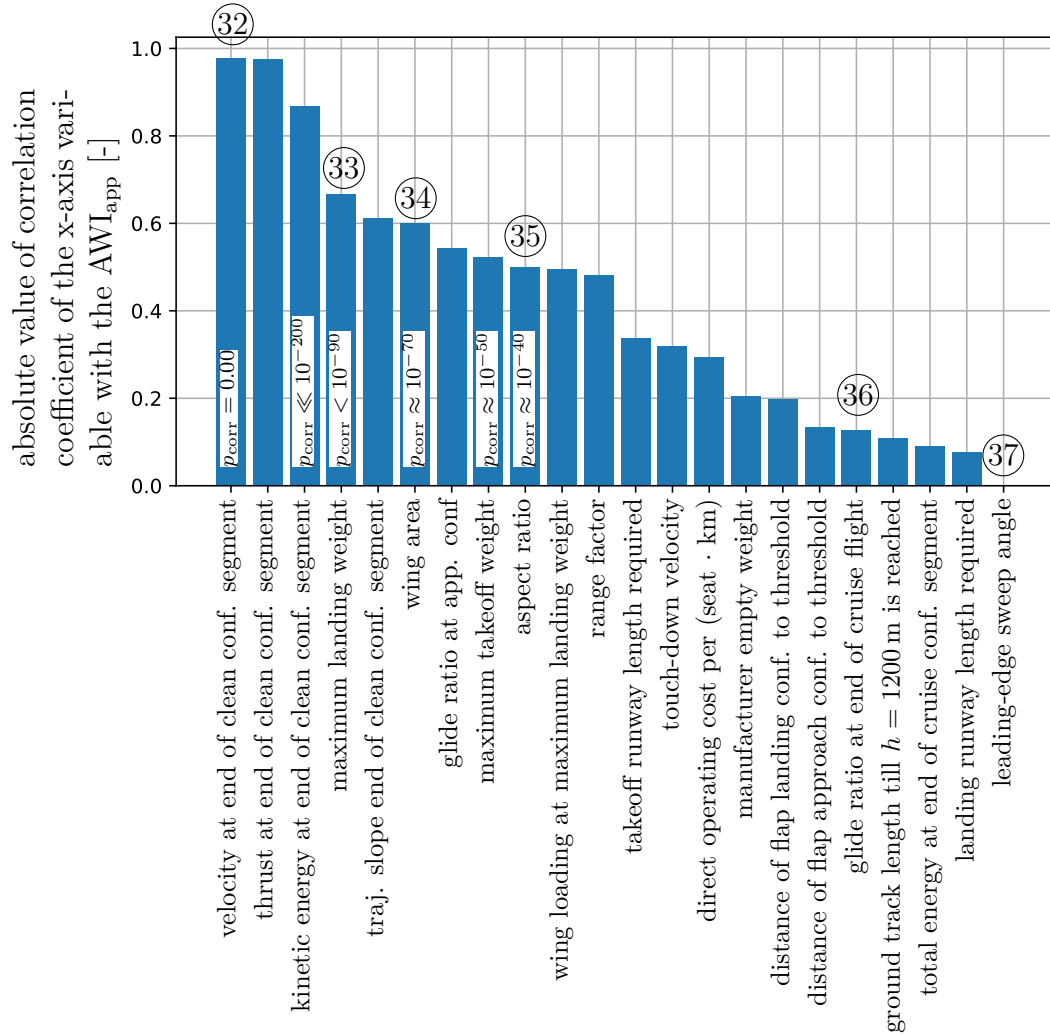


**Figure 6.3:** Absolute value of the Pearson's Correlation Coefficient of various variables with the Approach Awakening Index ( $AWI_{app}$ ). The approach velocity (32) and thrust along the idle approach segment have the highest correlation coefficient. However, the idle thrust is a consequence of the approach velocity, and the approach velocity is the cause for the ground noise. The wing area (34), compared to the other two design parameters, has the highest correlation coefficient. The correlation coefficients with the Overall Awakening Index are shown in Figure A.6.0.2.

Beside Crichton's hint of the stall speed correlating strongly with the ground noise levels, it was initially assumed that a low glide ratio (36) would result in low ground noise. Nevertheless, the glide ratio's correlation coefficient with the Approach Awakening Index is low. A lower glide ratio is equivalent to a steeper approach angle, see Eq. (3.1), therefore, the airplane flies higher. However, airplanes, which have a lower glide ratio, tend to approach faster. The faster approach speed in cruise configuration increases the awakening reactions far before entering the final approach segment, although the noise levels in cruise configuration are low compared to the ones in approach configuration. Additionally, the sound pressure levels are higher when the high-lift devices are deployed at faster velocities.

The influences of the planform parameters are complex. Changing the value of one planform parameter has effects such that, in turn, changes in the other parameter values would be beneficial. Even though the correlation coefficient of the Approach Awakening

Index is highest with the wing area (34) among the three planform parameters, none of them alone determines this index. Aspect ratio (35) and leading-edge sweep (37) have a comparatively low correlation coefficient with the Approach Awakening Index. Furthermore, values such as kinetic, potential, and total energy at the end of the cruise configuration approach segment have been investigated. The kinetic energy covered, additionally to the approach velocity, the maximum landing weight. The potential energy scales linearly with the maximum landing weight (33). Albeit, the investigated energies do not correlate the most with the Approach Awakening Index.

The ground track length up to a flight height of 1200 m, which features the highest correlation with the Departure Awakening Index, presents a lower correlation coefficient of around 0.10 with the Approach Awakening Index. Thus, the values of the planform parameters that lead to a low-noise approach differ from those that lead to a low-noise departure. Table 6.3 lists the effects of changing the values of the wing design parameters on the approach speed in cruise configuration.

One fun fact is that the Approach Awakening Index correlates higher with the required takeoff-runway length than it does with the required landing runway length. The correlation of the Awakening Index with both takeoff and landing runway length is statistical significant, with p-values of smaller than 0.001 and 0.046, respectively.

The slow approach speed in cruise configuration has been found to be the crucial criterion resulting from a high glide ratio and a low wing loading. The high glide ratio can be achieved by a large aspect ratio. The low wing loading can be achieved by a large wing area and low landing weight. A low wing sweep reduces the wing mass but can increase the fuel requirements. Since the effect of the lower wing sweep on wing mass counteracts the effects of the larger wing area and increased aspect ratio on wing mass, it is concluded: the optimal combination of planform parameter values should be determined by a holistic optimization.

**Table 6.3:** Effects of decreasing and increasing values of the planform parameters on the velocity at the end of the cruise configuration segment. Each decrease and increase of the parameter values has positive and negative effects on the approach speed. All advantageous effects have been listed in the upper part of the table, and disadvantageous effects have been listed in its lower part.

Legend:  
 increasing with an advantageous  or disadvantageous  effect  
 decreasing with an advantageous  or disadvantageous  effect  
 '⇒' – leading to

|  advantageous effects on slow approach speed      |  |   |
|--|--|---|
| parameter  | effects, if parameter value is increased   | effects, if parameter value is decreased  |
| area   | <ul style="list-style-type: none"> <li>wing loading </li> </ul>   | <ul style="list-style-type: none"> <li>wing mass </li> <li>wetted surface  ⇒ drag  ⇒ fuel mass  ⇒ structural weight </li> </ul> |
| aspect ratio   | <ul style="list-style-type: none"> <li>wing efficiency  ⇒ lift out of same wing area </li> </ul>   | <ul style="list-style-type: none"> <li>wing mass </li> </ul>   |
| sweep  | <ul style="list-style-type: none"> <li>fuel mass  ⇐ wave drag </li> </ul>  | <ul style="list-style-type: none"> <li>wing mass </li> <li>more lift </li> </ul>  |
|  disadvantageous effects on slow approach speed |  |   |
| parameter  | effects, if parameter value is increased   | effects, if parameter value is decreased  |
| area   | <ul style="list-style-type: none"> <li>wing mass </li> <li>wetted surface  ⇒ drag  ⇒ fuel mass  ⇒ structural mass </li> </ul> | <ul style="list-style-type: none"> <li>wing loading </li> </ul>  |
| aspect ratio   | <ul style="list-style-type: none"> <li>wing mass </li> </ul>  | <ul style="list-style-type: none"> <li>wing efficiency </li> </ul>   |
| sweep  | <ul style="list-style-type: none"> <li>wing mass </li> <li>lift </li> </ul>  | if wave drag occurs: <ul style="list-style-type: none"> <li>fuel mass  ⇒ structural mass </li> </ul>  |

## 6.3 Effects of Planform Parameters on the Awakening Index

This section shows the influence of each of the investigated planform parameters on the Awakening Index.

The following subsections show the effects of each design parameter on the Awakening Index and their underlying reasons. Section 6.3.1 addresses the aspect ratio, Section 6.3.2 approaches the wing area, and Section 6.3.3 is about the leading-edge sweep.

### 6.3.1 Aspect Ratio

Among the three planform parameters, the aspect ratio exhibits the greatest correlation with the Overall Awakening Index at a coefficient of  $r = 0.71$ . The aspect ratio's impact on the Awakening Index is shown in Figures 6.4 and A.6.3.8. Only airplanes with a leading-edge sweep angle of  $36^\circ$  are depicted in this subsection. In addition, reference is also made to results of leading-edge sweep angles of  $28^\circ$  and  $44^\circ$ . At this leading-edge sweep angle of  $36^\circ$ , the lowest Awakening Indices for all wing areas lie around an aspect ratio of 8.5 and 9.0. The minimum Awakening Index is found for a value of the aspect ratio of 8.5 and a wing area of  $540\text{m}^2$ . Starting from this minimum, the Awakening Index rises with both higher and lower values of the aspect ratio. At higher values of the aspect ratio, this is caused by a faster approach speed. At lower values of the aspect ratio, the rising is caused by a worse averaged climb response and a faster approach speed.

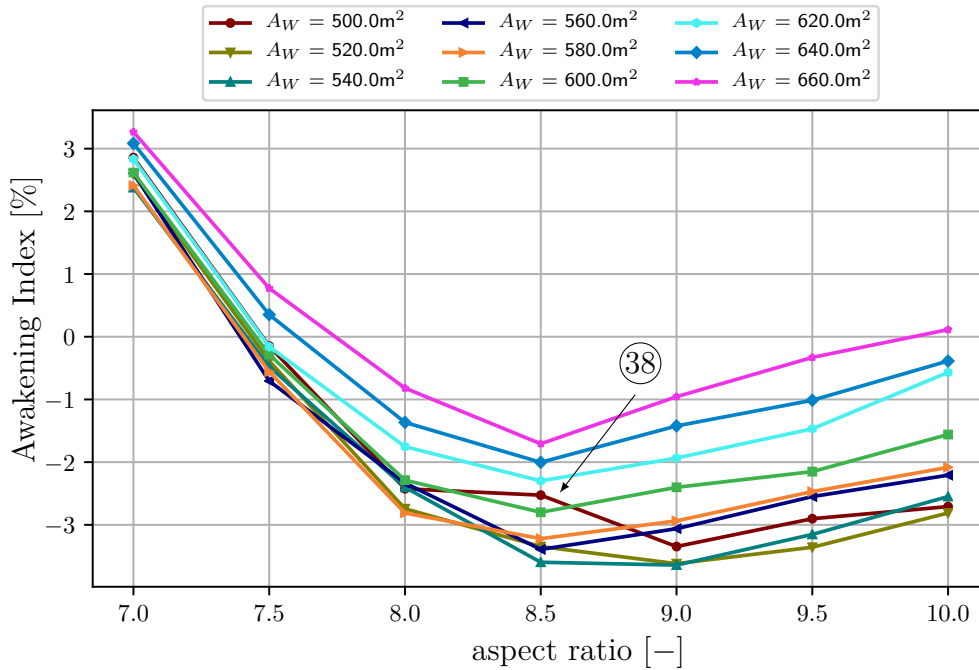


**Figure 6.4:** Overall Awakening Index over the aspect ratio for  $\varphi_{LE} = 36^\circ$  and all the wing areas ( $A_W$ ). The same data is depicted in Figure A.6.3.8 as a contour plot.

The Departure Awakening Index correlates the most with the ground track length up to a flight height of 1200 m. Thus, both values are plotted against each other in Figure 6.5. This distance becomes longer for lower values of the aspect ratio and also for larger wing areas. Although this occurrence holds true for all investigated sweep angles, the effect of the aspect ratio becomes less distinct at higher sweep angles and clearer at lower sweep angles. This is shown in Figures A.6.3.11 and A.6.3.12.

The Departure Awakening Index rises with lower values of the aspect ratio because the averaged climb response decreases. This decrease in the averaged climb response is caused by worse aerodynamics. Lower values of the aspect ratios lead to the glide ratio in cruise configuration being lower as well as the flaps being deployed over a longer distance. This takeoff flap setting causes a lower glide ratio compared to cruise configuration, resulting in higher dissipation of the energy provided by the engine. This dissipation obviously lowers

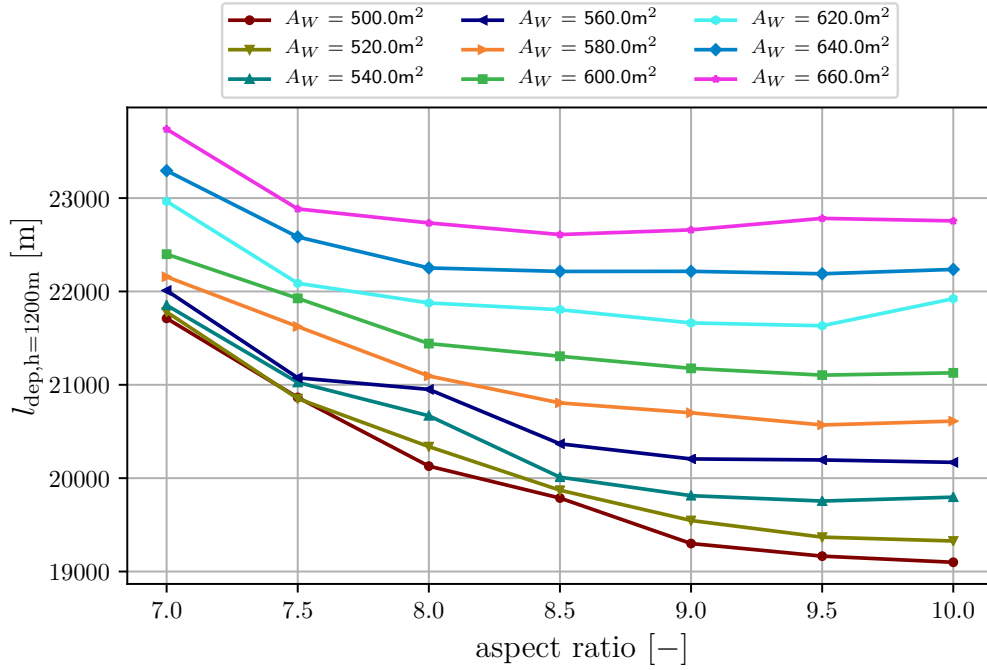


**Figure 6.5:** Ground track length up to a flight height of 1200 m ( $l_{\text{dep},h=1200\text{m}}$ ) over the aspect ratio for the leading-edge sweep angle of  $\varphi_{\text{LE}} = 36^\circ$  and all the wing areas ( $A_W$ ).

the total energy of the airplane even more when applied over a longer distance, which in turn leads to a worse averaged climb response.

Regarding the Approach Awakening Index, the greatest correlation coefficient has been found for the glide speed at the end of the cruise configuration segment. The effect of the aspect ratio on this criterion is shown in Figure 6.6. For values of the aspect ratio above 8.0, the maximum angle of attack decreases along with the maximum lift coefficient, which leads to a slightly increased velocity at the end of the cruise configuration segment.

For values of the aspect ratio lower than 8.5, the faster approach speed has nothing to do with a higher stall speed. Instead, it is a consequence of the approach procedure and the lower glide ratio of the affected airplanes. Along these approaches, the engine is kept at idle until the stabilization point is reached, even beyond the lowering of the landing gear and the deployment of the high-lift devices in the landing configuration. This means that the airplanes decelerate along the final approach segment because their glide ratio in approach and landing configuration is low. The reason for the higher Approach Awakening Indices towards lower aspect ratios is that the glide ratio of the airplanes, which have a low aspect ratio, reduced to a point that forces these airplanes to enter the final approach segment faster than  $1.3 \cdot v_{\text{stall,gse}}$  to glide at idle up to the stabilization point. Remember that two of the restrictions are that acceleration is prohibited and the airplanes glide at constant indicated airspeeds along their cruise configuration segment. The prohibited acceleration results in the need to deploy high-lift devices prior to entering the final approach segment. The strong deceleration along the final approach segment necessitates that the airplanes intercept in this segment at a faster speed than  $1.3 \cdot v_{\text{stall,gse}}$ . Thus, the slowest possible velocity is now the same as the one required, when the airplane intercepts the final approach segment. This velocity is kept constant along the whole cruise configuration segment.

The faster approach by airplanes that have a lower aspect ratio could be avoided by:

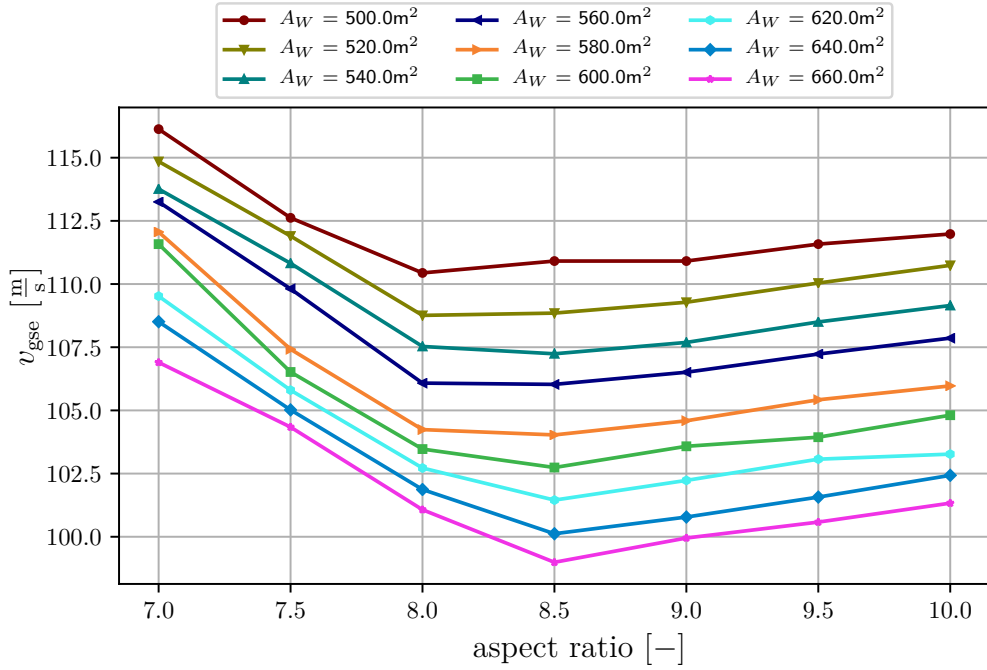


**Figure 6.6:** Velocity at the end of the cruise configuration segment ( $v_{gse}$ ) over the aspect ratio at the leading-edge sweep angle of  $\varphi_{LE} = 36^\circ$  and all the wing areas ( $A_W$ ).

1. allowing acceleration along the final approach segment, which makes later deployment of the high-lift devices possible
2. drag compensation through thrust increase (e.g., thrust = 1.1 · idle thrust)
3. lowering the interception height.

Allowing acceleration (1) could be one measure to further reduce the noise. The even later deployment of the high-lift devices would be an additional advantage, which would lead to smaller areas affected by high-lift device sound. Furthermore, the increase in the engine thrust (2) could be advantageous. This requires further investigation. The consensus has been that the engine becomes a prevailing sound source in landing configuration when the landing velocity has to be held constant beyond the stabilization point. However, this segment is flown in approach configuration. Moreover, the engine needs to provide only a little more thrust to reduce the deceleration, since a reduction of the deceleration, not its elimination, is all that is needed. This slight thrust increase is one of the easiest measures to avoid a faster approach speed. Adjusting the interception height (3) might cause safety issues and, hence, is not further discussed.

In Figure 6.4, a supposed outlier can be seen at location (38). In this case it is a superposition of more approach- and departure-induced awakening reactions, as can be seen in Figures A.6.3.9 and A.6.3.10 on page 159 at positions (98) and (99). Here, the averaged climb response is worse and the approach speed is higher than expected. The decreased averaged climb response is due to a combination of slightly increased takeoff mass and lower glide ratio. The approach speed is  $0.3 \frac{\text{m}}{\text{s}}$  faster than expected due to slightly lower maximum lift. This maximum lift is a combination of the maximum lift of the wing, which provides lift as expected, and the downforce of the tailplane. The latter has to be slightly larger because the center of gravity lies further to the front compared to the other airplanes and the lever

arm of the horizontal stabilizer is slightly shorter. The horizontal stabilizer is mounted further to the front. These lead overall to the slightly lower glide ratio, which also results in a poorer averaged climb response during takeoff. Thus, the airplane causes a roughly 1% higher Awakening Index than expected.

### 6.3.2 Wing Area

Figure 6.7 shows the Awakening Indices plotted against the wing area. Starting from the respective minimal Awakening Index, it increases with larger and smaller wing areas.

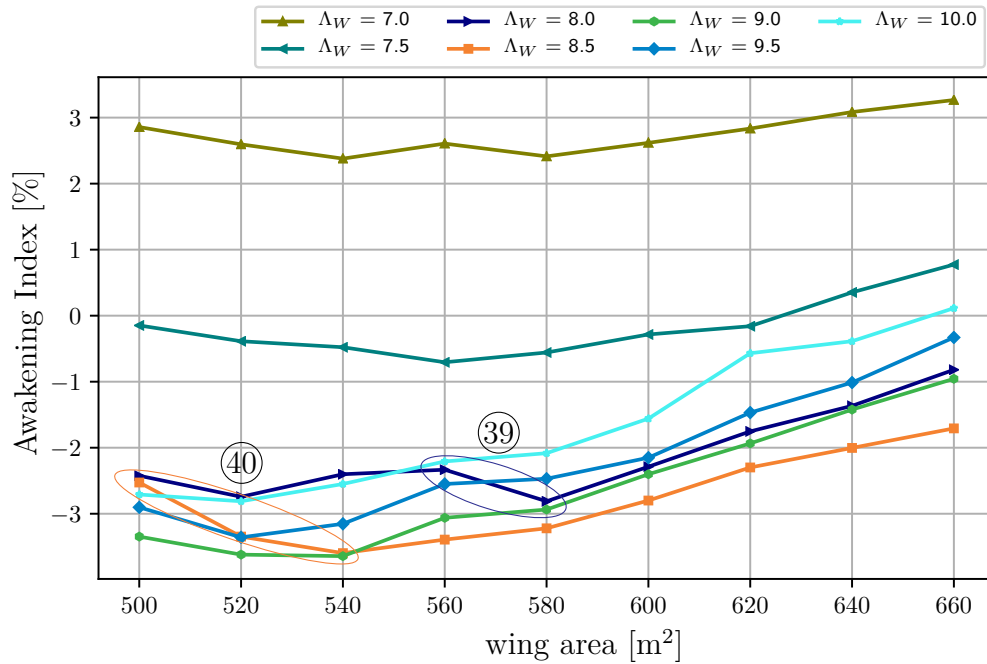
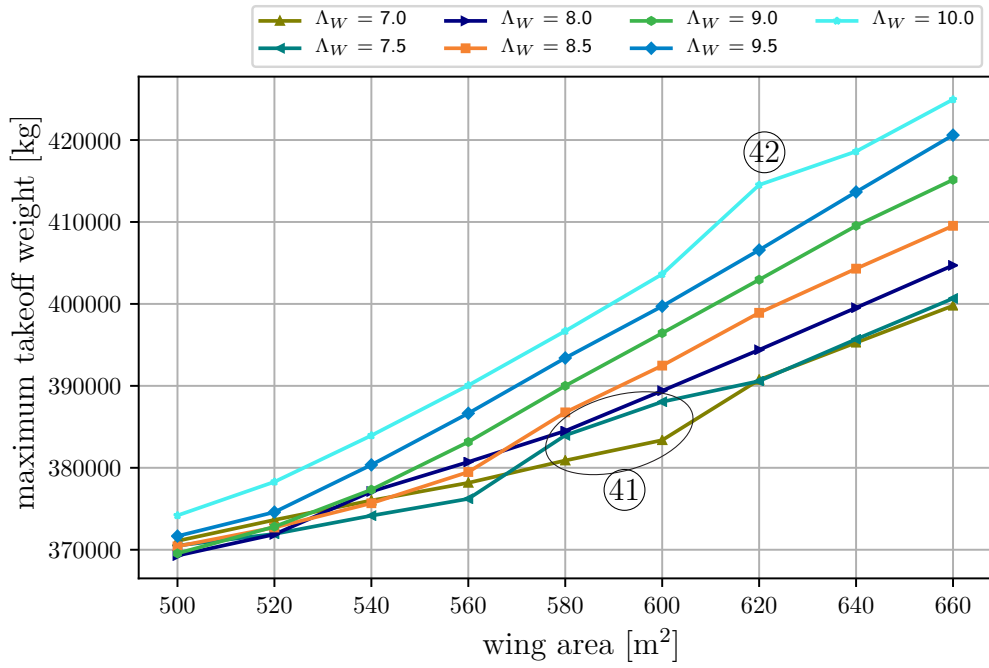


**Figure 6.7:** Overall Awakening Index (AWI) over the wing area for the leading-edge sweep angle of  $\varphi_{LE} = 36^\circ$  and all aspect ratios ( $\Lambda_W$ ). The same data is depicted in Figure A.6.3.15 as a contour plot.

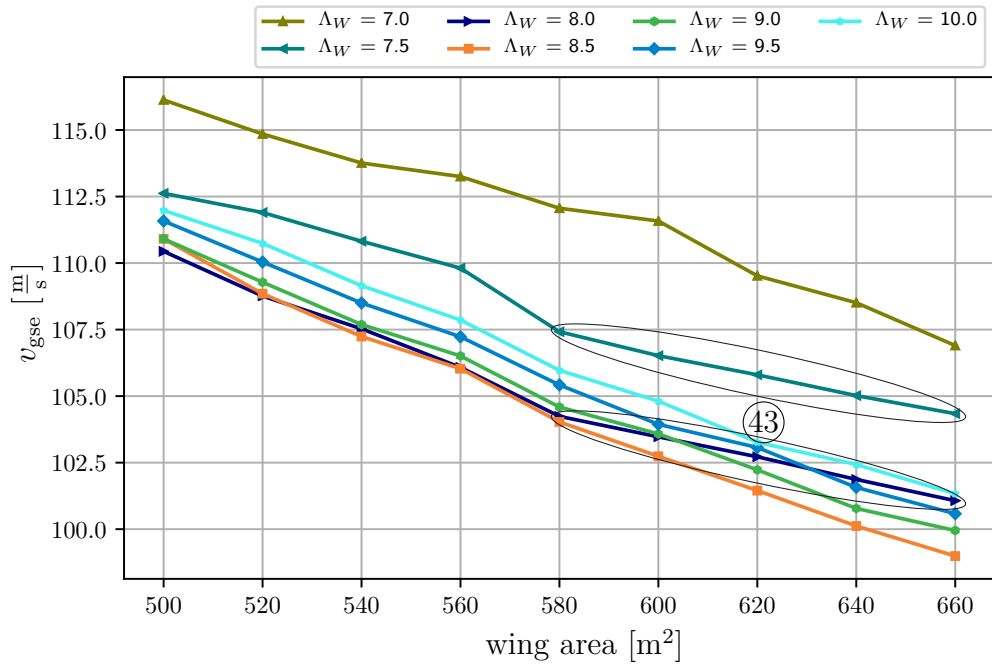
Figure 6.8 shows that the manufacturing empty weight and the trip fuel mass increase with larger wing areas. This means that both increased mass and increased drag due to the larger surface, could be the reasons for the worse averaged climb response. Therefore, the total energy after a ground track length of 12 km has been investigated for both the whole airplane mass and specific per kilogram. The mass-specific total energy, in contrast to the airplane’s total energy, decreases significantly as the wing area enlarges. This shows that the effect of additional mass on the averaged climb response outweighs the impact of the additional drag due to the enlarged surface. Additionally, with smaller wing areas, the environment benefits from a lower fuel consumption<sup>1</sup>, see Figure A.6.3.16.

Figure 6.9 shows the velocity at the end of the cruise configuration segment plotted against the wing area for seven values of the aspect ratio. The larger the wing area, the lower the wing loading, which results in a reduced cruise-configuration approach velocity, leading to a decrease in Approach Awakening Index.

<sup>1</sup>Fuel consumption is assumed to correlate with environmental impact, but a probably higher  $NO_x$  emission due to higher combustion temperatures has not been considered.



**Figure 6.8:** Maximum takeoff weight over the wing area for leading-edge sweep angle  $\varphi_{LE} = 36^\circ$  and all aspect ratios ( $\Lambda_W$ ).



**Figure 6.9:** Velocity at the end of the cruise configuration segment ( $v_{gse}$ ) over the wing area for the leading-edge sweep angle  $\varphi_{LE} = 36^\circ$  and all aspect ratios ( $\Lambda_W$ ).

The wing area yields contrary effects on the Departure and Approach Awakening Indices and, hence, a compromise is necessary to achieve the optimal wing area. The more awakenings are caused by the departure, the greater its dominance on the selection of an optimal airplane.

The behavior of the Awakening Index at location (39) is a superposition of the approach- and departure-induced awakening reactions. Here, the aerodynamic center of the entire airplane moves aft as the wing area increases. It should be noted that the aerodynamic center of the wing is always at the same lengthwise location because the wing position has been shifted accordingly. At these two values of the wing area, 560 and 580 m<sup>2</sup>, the aerodynamic center of the airplane remains in the same place, while the center of gravity of the airplane moves backward a little more than 100 mm for the larger wing area. This gives the airplane a lower static margin and the horizontal stabilizer generates less downforce. Thus, the glide ratios during takeoff and approach are slightly increased. This is where superposition effects come into play: with a better glide ratio, the airplane climbs better. As a result, the high-lift devices are retracted earlier during departure, which in turn increases the climb performance. Additionally, less fuel is required during cruise, which lowers the structural mass lowering both takeoff and landing weight.

At approach, the horizontal stabilizer generates more lift (less downforce) as the wing area increases. This lowers the approach speed of the airplane with a wing area of 580 m<sup>2</sup>.

Also at location (40), i.e., the airplanes with wing areas of and smaller than 540 m<sup>2</sup> at an aspect ratio value of 8.5, the Awakening Index increases due to the superposition of more approach- and departure-induced awakening reactions. For this value of aspect ratio, the center of gravity location moves further forward than the aerodynamic center position with progressively smaller wing areas. Thus, the airplane becomes longitudinally more stable. Toward smaller wing areas, the airplanes generally become lighter. For this aspect ratio, the weight decrease toward smaller wing areas is less than for the comparison airplanes. This also affects fuel requirements, which fall less toward smaller wing areas than the fuel requirements of the airplanes with other aspect ratios. During takeoff, the higher weight and more downforce of the horizontal stabilizer cause the high-lift devices to retract later. Both, in turn, lead to a lower averaged climb response. On approach, the larger static margin leads to slightly lower glide ratios and earlier extension of the high-lift devices.

The unexpected higher value of the takeoff weight at location (42) also affects the Departure Awakening Index. The reason for this outlier lies in the flight simulations, which required a particularly large horizontal stabilizer here. In this case, the particularly large horizontal stabilizer area leads to more drag, a lower glide ratio in cruise flight, and an increased takeoff weight. The takeoff weight, in turn, is made up of a much heavier tailplane weight, a heavier fuselage weight, and more fuel weight. These reduce the averaged climb response, and thus raise the Departure Awakening Index. The Approach Awakening Index is not affected.

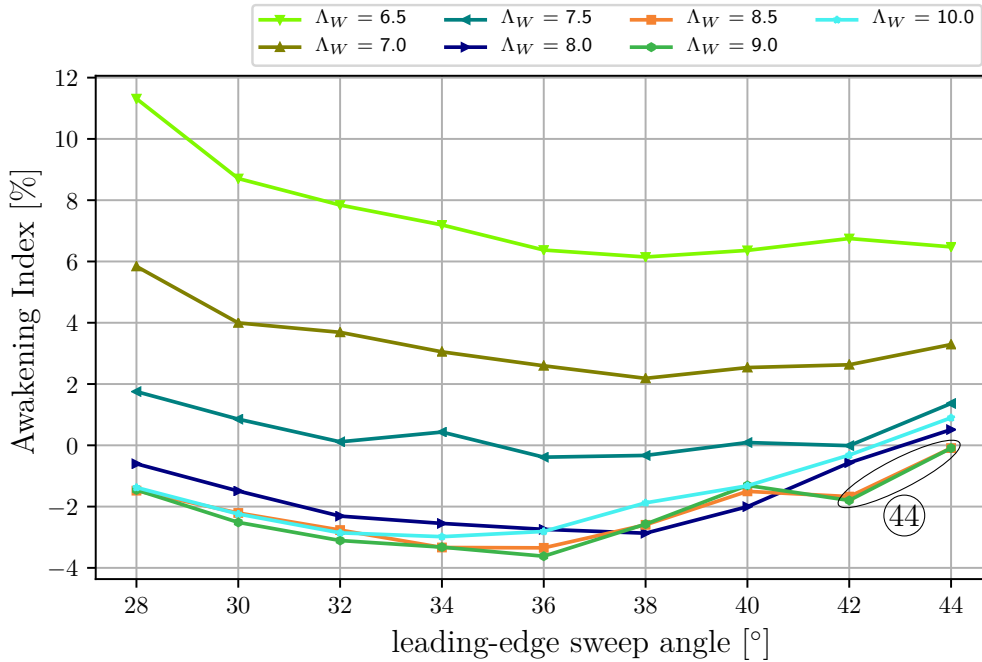
Also, at location (41), the variation in takeoff weight of the airplane with an aspect ratio of 7.5 compared to the airplane with an aspect ratio of 7.0 is due to a significantly larger horizontal stabilizer. The effects are the same as already at the point (42).

Figure 6.9 shows that a flatter decrease in approach speed for wing areas larger than 580 m<sup>2</sup> for both aspect ratios 7.5 and 8.0 (43). The flatter decrease is due to the lower glide ratios that force the airplanes to enter the final approach segment at faster speeds. This would actually also be the case for the aspect ratio of 7.0, however, there the horizontal stabilizer counteracts this. For the airplanes with an aspect ratio of 7.0 and wing areas of 620 m<sup>2</sup> and larger, the downforce of the horizontal stabilizer is significantly lower, so that the glide ratios are higher and the approach speeds are lower.

### 6.3.3 Sweep

The correlation of the wing's leading-edge sweep angle and the Awakening Index exhibits a correlation coefficient of 0.1, which means almost no correlation. This holds true for its correlation with the Approach Awakening Index. However, for such parabolic distributed data, as the Departure Awakening Index for the investigated leading-edge sweep angles, Figure A.6.3.7, the Pearson's correlation coefficient can only be applied piecewise at the most.

Figure 6.10 shows the Awakening Index over the leading-edge sweep angle for various aspect ratios at a constant wing area of  $520 \text{ m}^2$ . The minimum Awakening Indices for each aspect ratio are found at leading-edge sweep angles between  $34^\circ$  and  $38^\circ$ .



**Figure 6.10:** Overall Awakening Index (AWI) over the leading-edge sweep angle for the wing area  $A_W = 520 \text{ m}^2$  and all the aspect ratios ( $\Lambda_W$ ). The same data is depicted in Figure A.6.3.17 as a contour plot.

The rising values of the Awakening Index with higher and lower sweep angles are generated by the departure. The sweep angle has a very low effect on the approach speed and, thus, on the Approach Awakening Index, see Figure A.6.3.18. Both lower and higher sweep angles have a direct impact on the maximum takeoff weight, as depicted in Figure 6.11. This growing maximum takeoff weight directly affects the averaged climb response and causes a higher Departure Awakening Index.

Towards lower sweep angles, the wave drag and the required trip fuel mass increase, because the cruise speed is held constant. Towards higher sweep angles, especially at higher aspect ratios, the manufacturing empty weight increases since the torsion stiffness of the wing has to be retained. This additional weight also leads to more required trip fuel, see Figures A.6.3.19 and A.6.3.20. The longer and slimmer the wings, the lower the area moment of inertia. The area moment of inertia, in a first step, has to be held constant resulting in more required material. In a second step, the lever arm is increased because the span is increased. This requires a higher area moment of inertia, achieved by an additional amount of material.

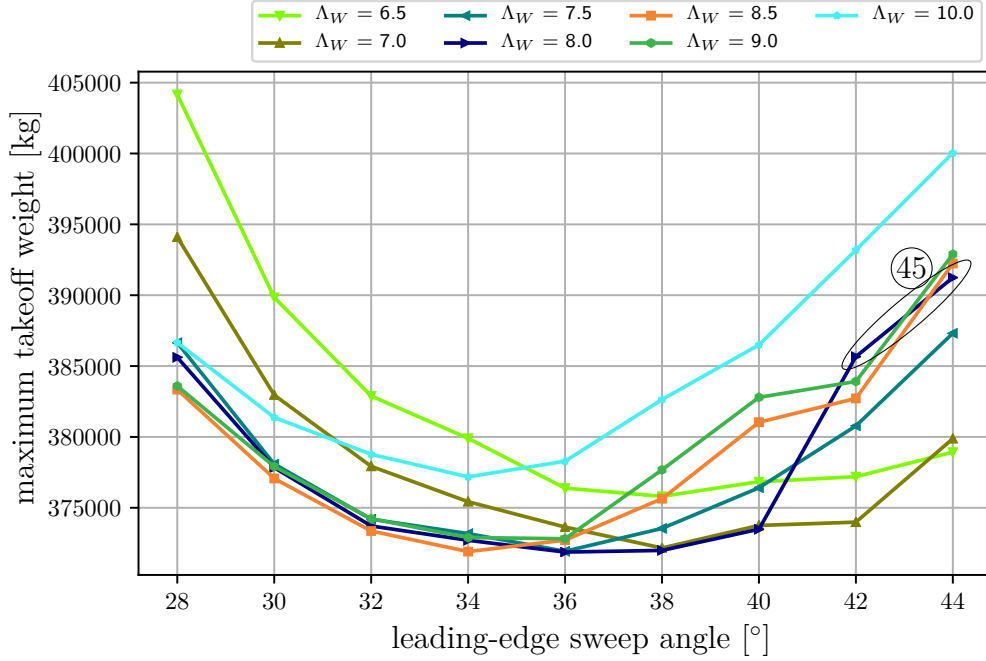


**Figure 6.11:** Maximum takeoff weight (MTOW) over the leading-edge sweep angle for the wing area of  $A_W = 520 \text{ m}^2$  and all the aspect ratios ( $\Lambda_W$ ).

The effect of the leading-edge sweep angle on the Approach Awakening Index is very low, although its influence on the cruise configuration approach velocity is noticeable. When selecting the airplanes from Figure A.6.2.6, which approach at the same speed, a tendency of high sweep angles causing lower Approach Awakening Indices is noticeable. E.g., when selecting the airplanes at  $v_{gse} = 105 \frac{\text{m}}{\text{s}}$ , along the horizontal line in the Figure A.6.2.6, then the airplanes that have higher sweep angles cause a lower Approach Awakening Index. This happens because the Kruger flap, the trailing-edge flap, and the clean wing noise source models depend on the respective leading-edge and trailing-edge sweep angle. The higher these angles, the lower their noise generation, compare Eq. (2.1).

The discontinuous curves in the Figures 6.10 to 6.12, which are marked with (44), (45), and (46), have all a connection to the horizontal stabilizer size. This affects the moment equilibrium, the drag, and, hence, the mass.

First, the two values of aspect ratio of 8.5 and 9.0 are discussed (44). The four marked airplanes of the leading-edge sweep angles  $42^\circ$  and  $44^\circ$  record a lower downforce of the horizontal stabilizer during the approach. This is also the case during cruise flight, so these four airplanes use 5 tonnes less cruise fuel than would be expected from an extrapolated curve of leading-edge sweep angles less than  $42^\circ$ . Therefore, these airplanes are lighter at departure, but also lighter at approach. As a result, the averaged climb response and the approach speed are lower.

However, for the airplanes with aspect ratio of 8.0 and leading-edge sweep angles greater than  $40^\circ$  (45), the horizontal stabilizer is twice as large and twice as heavy as would be expected from extrapolating the curve of leading-edge sweep angles less than  $42^\circ$ . The root of the problem lies in the simulation of critical flight situations. Therefore, fuel consumption is also higher in cruise flight because drag is larger. The takeoff weight increases about 10 tonnes more and the landing weight about 6 tonnes more than expected from an extrapolation of the curves. During takeoff, this has a comparatively strong effect on the averaged climb

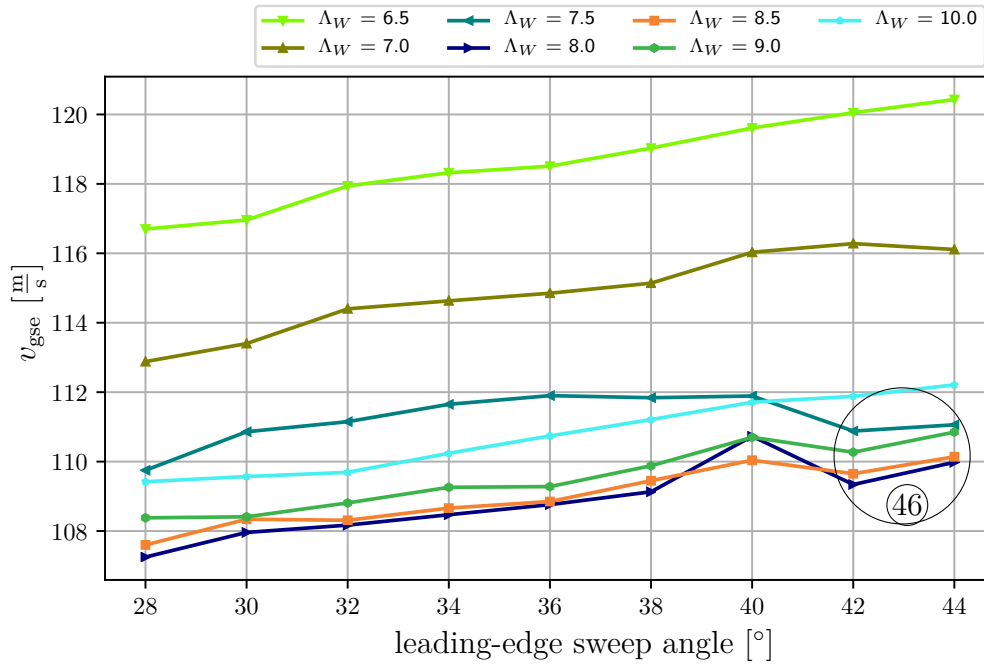


**Figure 6.12:** Velocity at the end of the cruise configuration segment ( $v_{gse}$ ) over the leading-edge sweep angle for the wing area  $A_W = 520 \text{ m}^2$  and all the aspect ratios ( $\Lambda_W$ ).

response. During landing, however, the center of gravity is about 80 cm farther behind the aerodynamic center of the wing than is the case for the airplanes with smaller horizontal stabilizers. Therefore, the tailplane makes so much less downforce that the total tailplane weight is compensated for on approach compared to the airplanes with a leading-edge sweep angle smaller than  $42^\circ$ . The entire approach can be performed at a lower approach speed. It should be noted here that the slightly higher approach speed of the airplane with a leading-edge sweep angle of  $40^\circ$  and an aspect ratio of 8.0 is a common pattern, and only the two leading-edge sweep angles of  $42^\circ$  and  $44^\circ$  are the outliers (46).

## 6.4 Airplane Selection

Figure 6.13 shows the Awakening Index and the Direct Operating Cost Index of each airplane of the parameter study with varying combinations of the wing design parameters, i.e., leading-edge sweep, wing area, and aspect ratio. Each mark represents one airplane design and is colored according to the respective value of the aspect ratio. The same airplanes, but colored according to their corresponding leading-edge sweep angle and wing area, are plotted in Figures A.6.4.21 and A.6.4.22, respectively.

The reference airplane, the PrADO model of the B747-400, represents the 0% Awakening Index and 0% Direct Operating Cost Index. The selected low-noise and cost-effective airplane has been marked with a red circle in Figure 6.13 and features the following planform parameter values:  $36^\circ$  for the leading-edge sweep angle,  $520 \text{ m}^2$  for the wing area, and 9.0 for the aspect ratio. The airplane that causes the lowest Awakening Index is obtained with a  $20 \text{ m}^2$  larger wing area and the same leading-edge sweep angle and aspect ratio. The two most cost-effective airplanes have been found to have a  $20 \text{ m}^2$  smaller wing area, the same leading-edge sweep angle, and two different values of the aspect ratios of 9.0 and 9.5.

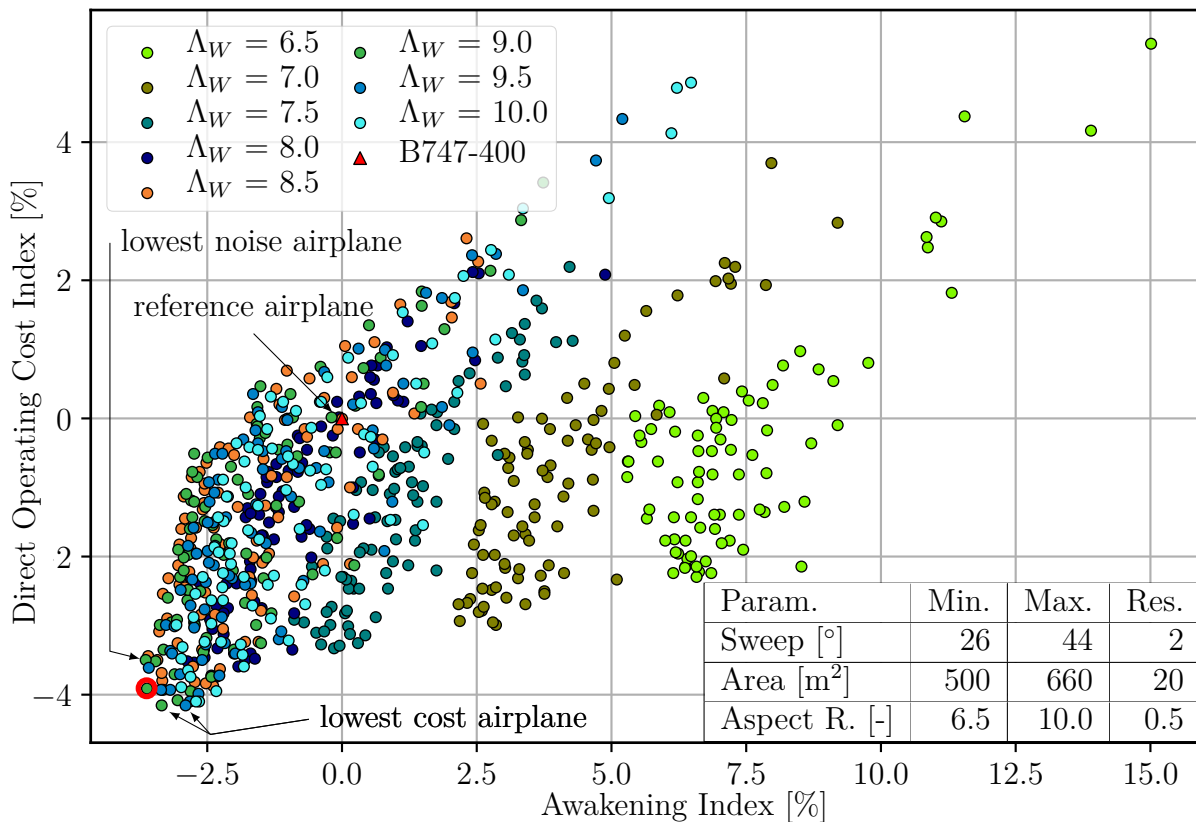


**Figure 6.13:** Direct Operating Cost Index (DOCI) and Overall Awakening Index (AWI) for the basic airplane designs with the origin representing the direct operating cost and awakening reactions of the reference airplane. Each mark represents one airplane design. All airplanes flew the ICAO-A departure and the low drag minimum power approach procedure. The red circled marker is the selected optimum, defined by  $\varphi_{LE} = 36^\circ$ ,  $A_W = 520 \text{ m}^2$ , and  $\Lambda_W = 9.0$ . To determine the planform parameters of the other airplane designs, combine this figure with Figures A.6.4.21 and A.6.4.22, which show the same data colored by leading-edge sweep angle and wing area, respectively.

This emphasizes that the design parameters are codependent and collectively contribute to an optimal design. Note that here the optimal design is based on the simulation setup in Chapter 5. If any of these input parameters change, it is expected that an entirely different combination of planform parameters leads to the optimal airplane.

Remarkable, too, is that the Pareto front in Figure 6.13 consists of only 3 airplanes: the airplane with the lowest Awakening Index, the selected airplane, and the airplane with the lowest Direct Operating Cost Index and the lower Awakening Index. The determination of the optimal airplane appears simple even without an objective function. It should be noted here that all airplanes have been calculated at a cruise Mach number of  $Ma_{cr} = 0.85$ . This means that airplanes with a lower leading-edge sweep angle already fly in the speed range of the wave drag. Airplanes with a higher leading-edge sweep angle could fly faster, but are built heavier. They cannot make up for this disadvantage by conducting more flights in their lifetime. Therefore, it is likely that this Pareto front is so small because of the

boundary conditions: the cruise Mach number. However, more studies are required to prove this dependency of the Pareto front size of the boundary conditions.

Figure 6.13 shows that not only the Awakening Index but also the Direct Operating Cost Index can be lowered compared to the reference. The assumption that the manufacturer developed an economical airplane addresses the following queries as below:

- Are the PrADO models, which have been used to calculate the airplanes' critical Mach number, reasonable?

According to data provided by Raymer, the results of the critical Mach number for super-critical profiles calculated by PrADO are plausible [180, Fig. 4.20]. The same has been supported by Heinze, the main PrADO developer. From this, it can be concluded that the basic input for the drag prediction at various sweep angles and high Mach numbers is correct.

- Is it plausible that the direct operating cost can be lowered?

Reduction in leading-edge sweep angle from the reference  $42^\circ$  to  $36^\circ$  can significantly lower the cost, since the region of high wave drag is not entered at the design Mach number of 0.85. At this lower sweep angle and with a smaller wing area, a lighter airplane can be built, although the value of the aspect ratio is higher compared to the reference. The smaller wing area reduces the wetted surface and, hence, the airplane's drag and fuel consumption.

- Why has the manufacturer not yet tried to reduce the direct operating cost?

The reason is probably that the B747 project has been based on the C-5A military freighter [35], whose focus was put on achieving a high cruise speed. The B747-400's maximum speed is at Mach 0.92 [13]. Hence, it was developed with a high sweep angle.

The sweep angle of  $36^\circ$  of the selected basic airplane means that an airspeed faster than  $Ma = 0.85$  leads to high wave drag and thus to high fuel consumption. This increases both the environmental impact and the cost. Therefore, the maximum speed at which flying is still possible is significantly lowered.

## 6.5 Awakening Distribution Caused by the Basic Airplane

This section identifies the respective dominating noise sources during departure and approach of the optimal airplane design selected in the previous section. Different sound sources originating from various airplane components may, individually or collectively, affect the ground noise at varying degrees during different phases of the departure and approach. The aim of this section is to examine which noise reduction technologies are suitable to be applied. An overview of the sound sources, and their associated airplane components is listed in Table 6.4.

**Table 6.4:** List of sound sources regarding the legend of the plots showing the awakening probability, the respective sound sources, and which components they contain. The respective noise source models used are listed in Table 4.6.

| sound source |   |
|--------------|---|
| legend       | components  |
| fan          | fan   |
| jet          | jet   |
| engine       | fan + jet   |
| landing gear | landing gear  |
| led          | leading-edge high-lift devices  |
| ted          | trailing-edge high-lift devices or clean wing trailing edge             |
| wing         | leading and trailing-edge high-lift devices or clean wing trailing edge |
| airframe     | wing + landing gear   |

The probability of awakening caused by the departure is depicted in Figure 6.15.<sup>2</sup> As its legend is uncommon, it is explained in Figure 6.14. Each apex of the legend corresponds to the dominance of the respective sound source. In the hexagon at each apex, this sound source causes more than 86% of the A-weighted sound intensity. In the center, each sound source contributes one-third to the A-weighted sound intensity. The gray hexagon covers a contribution of each sound source in the range of 28.5% to 42.8% of the A-weighted sound intensity.

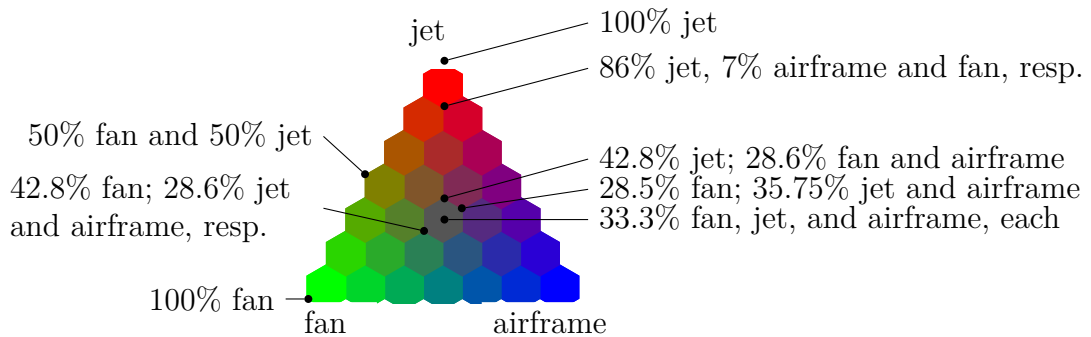


**Figure 6.14:** This manual explains the legend that shows the dominating noise sources on the ground. The colors represent the intensity of A-weighted sound of three sound sources. Each apex represents 100% dominance, while the center means an equal contribution of each sound source to the A-weighted sound intensity on the ground. Some noise sources are a bundle of single noise source components, which are listed in Table 6.4.

The symbol size in Figure 6.15 represents the probability of waking up due to the noise event, which is termed awakening probability. However, it is actually an additional awakening probability, since awakening reactions are not only caused by aircraft noise. A symbol size as large as an area element, i.e., 250 m times 250 m, corresponds to the maximum occurring

<sup>2</sup>SUMATRA Open-Source PDF Reader is suggested as the best software to view these plots.

awakening probability. This maximum awakening probability serves as the reference for all plots in the entire thesis. Two squares of the same size therefore represent the same probability of awakening. A white area without a symbol, such as in Figure 6.16, stands for zero awakening probability. Since these plots combine information about the dominating noise sources and their awakening probability, summarized in color and symbol size, these plots serve more for qualitative than quantitative assessment.

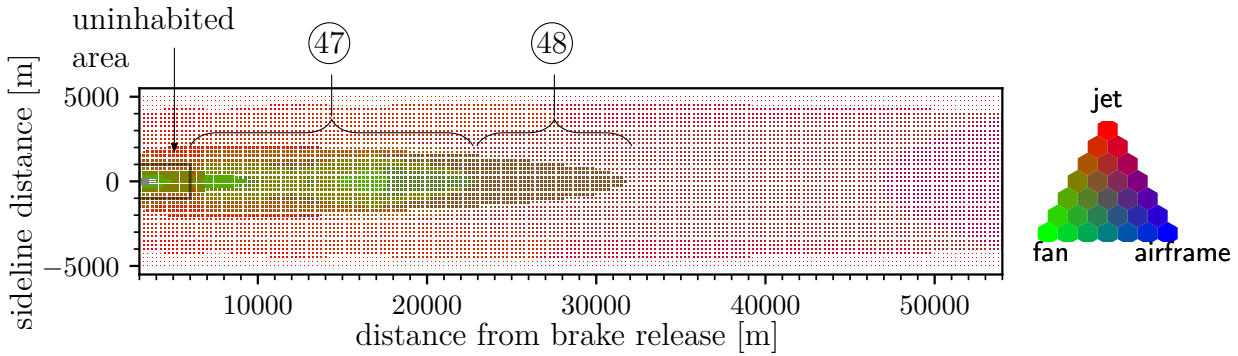


**Figure 6.15:** Dominating noise sources during departure of the **basic airplane**, i.e., prior to mounting low noise technologies. The departure is dominated by jet sound, and in the marked area (47) also by fan sound. As fan sound is highly attenuated by the atmosphere, jet sound becomes more prevailing in (48). The SUMATRA open-source PDF viewer is recommended as the best software to view these plots.

Jet noise causes the high awakening probability, which is distributed across the investigated area, as visible in Figure 6.15. Since the fan sound occurs at higher frequencies than jet sound, fan sound is stronger attenuated by the atmosphere during propagation. Hence, the fan sound is prevalent only from the uninhabited airport premises up to about 23 km behind the brake release point and about 1.2 km to both sidelines (47). As early as after the 23 km ground track length, the jet sound becomes prevalent ((48) brown color) and, ultimately, dominates the whole remaining area under investigation. Reducing the jet sound will be highly beneficial for inhabitants in most of the investigated area. The noise contributed by the airframe is negligible during this departure.

Figures 6.16 and A.6.5.23 show that the airframe noise causes most of the awakening reactions during approach. Across a 4 km wide strip from  $-50$  km to about  $-18$  km along the ground track (49), trailing-edge sound dominates. Furthermore, the fan sound contributes about one-third of the sound intensity here, despite the engine being in idle along this cruise configuration segment. Around 18 km before the touchdown, the airplane enters the  $-3^\circ$  final approach segment and the high-lift devices are deployed to decelerate and maintain the required lift. As long as the airplane is fast, Kruger flap noise (50) swells up. At 9 km before touchdown, the landing gears are deployed (51) making them the dominant noise source. This holds true, until the flaps are deployed to landing configuration (violet area) and the engine is spooled up (52) to stabilize, i.e., maintain flight speed. This area is dominated only by the fan sound, as the jet sound is recessive at such medium-thrust settings.

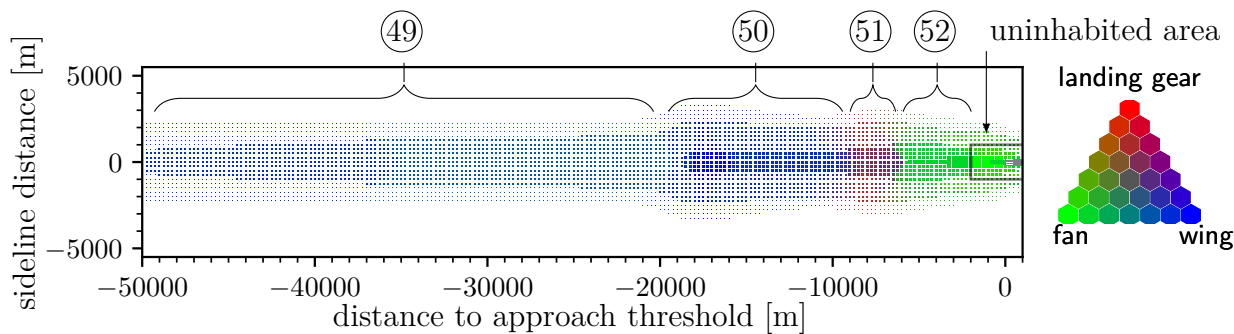


**Figure 6.16:** Dominant noise sources during approach of the **basic airplane** prior to mounting low noise technologies. The approach is dominated by wing noise in (49) and (50), and in the marked area (52) also by fan noise. The same data, but only showing airframe sound sources, is depicted in Figure A.6.5.23.

## 6.6 Awakening Distribution Caused by the Reference Airplane

In this section, the dominating noise sources of the reference airplane are investigated. Additionally, the difference between the A-weighted maximum SPLs of the basic airplane and the reference airplane is shown.

In order to make a well-founded comparison of the ground noise of the two airplanes, the departure and approach trajectories are initially shown in Figure 6.17.

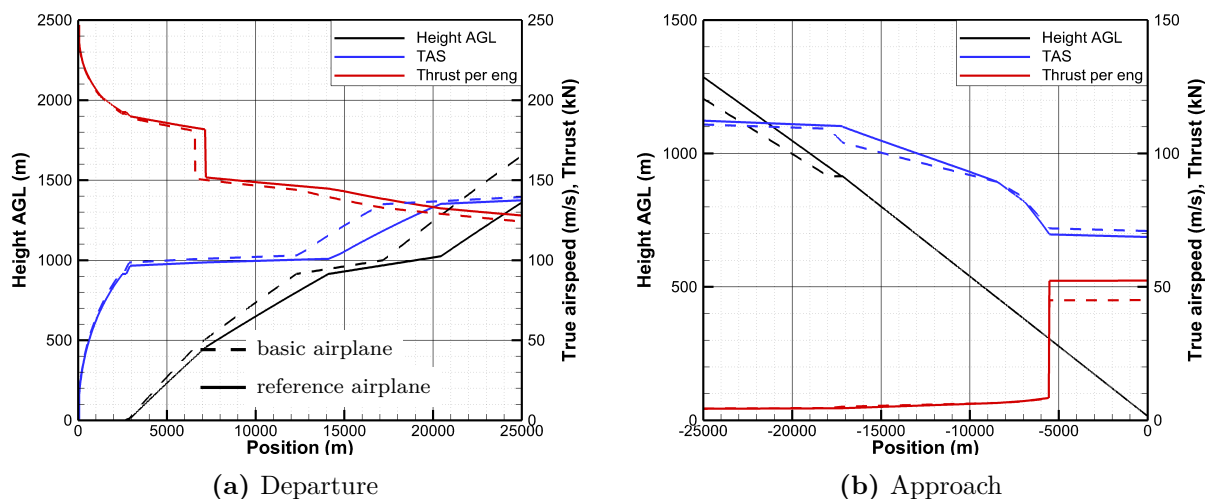


**Figure 6.17:** Departure and approach trajectories of the basic airplane compared to the reference airplane. The graphs show two trajectories, thrust, and true airspeed for the two airplanes, respectively.

Along the departure, Figure 6.17a, the basic airplane climbs steeper and accelerates within a shorter distance than the reference airplane, so its averaged climb response is higher. Therefore, the total flight path is higher, thus the sound pressure level on the ground, and consequently the awakening probability, is lower. Due to the higher climb angle, the basic

airplane performs the cutback about 500 m earlier. The differences in engine thrust result from the difference in speed and altitude.

The approach in Figure 6.17b is described against the direction of flight. Due to the higher glide ratio of the basic airplane compared to the reference airplane, the drag in the landing configuration is lower, thus the speed after the stabilization point is kept constant with less thrust. Before the stabilization point, the landing gear is deployed at a height of 457 m and the high-lift systems at a slightly lower height. The higher glide ratio in the approach configuration also results in lower deceleration of the basic airplane along the final approach segment. However, this means that it enters the final approach segment slower, so that it already reduces speed beforehand on a horizontal segment. The reference airplane, on the other hand, decelerates so much on the final approach segment that the horizontal segment is almost non-existent. Before the horizontal segment, both airplanes descend at 1.3 times their respective stall speeds.

Figure 6.18 shows the departure-induced awakening probability of the reference airplane colored according to the causative sound source.

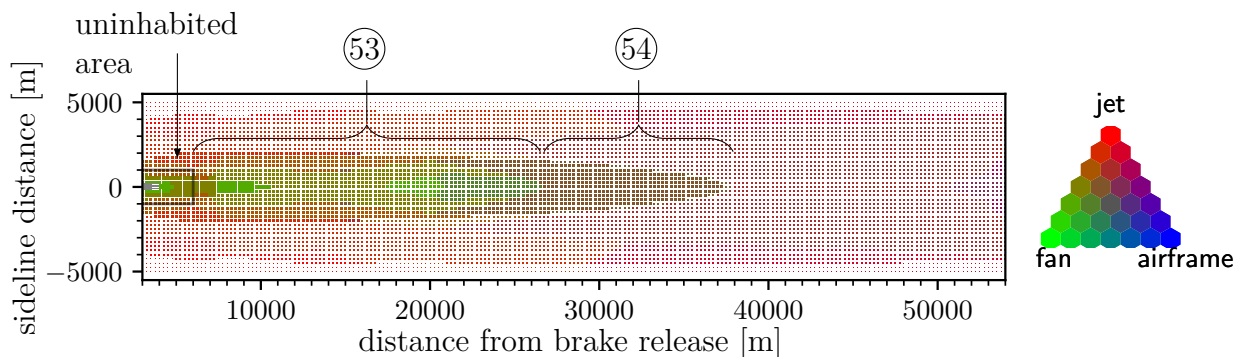


**Figure 6.18:** Dominating noise sources during departure of the **reference airplane**. The departure is dominated by jet sound, and in the marked area (53) also by fan sound. This fan sound dominated area is larger than the one of the basic airplane. Since fan sound is highly attenuated by the atmosphere when the airplane reaches more height, in area (54) jet sound becomes more prevailing.

Most of the area is marked in red and is dominated by jet noise. Along the flight track until about 26 km behind the brake release point, fan noise contributes to more than 50% of the sound intensity on the ground (53). Through the cutback, the jet sound decreases over-proportionately, thus here the fan sound on the ground becomes more dominant. The proportion of fan noise to the ground noise decreases somewhat between about 11 and 18 km, and then increases again. The decrease in the fan-noise component is due to the increasing atmospheric attenuation with increasing altitude. The increase in the fan-noise component between 18 and 21 km is since the fan-sound emission increases with increasing speed along the acceleration segment. As the distance to the population increases, i.e., with increasing altitude and with increasing lateral distance, the proportion of fan sound continues to decrease (54), thus jet noise causes most of the additional awakening reactions.

Figure 6.19 shows the difference in A-weighted maximum SPL at departure between the basic airplane and the reference airplane.

At marker (55), the basic airplane reaches cutback altitude 500 m earlier than the reference airplane because it climbs more steeply. After the cutback point, the climb angle is

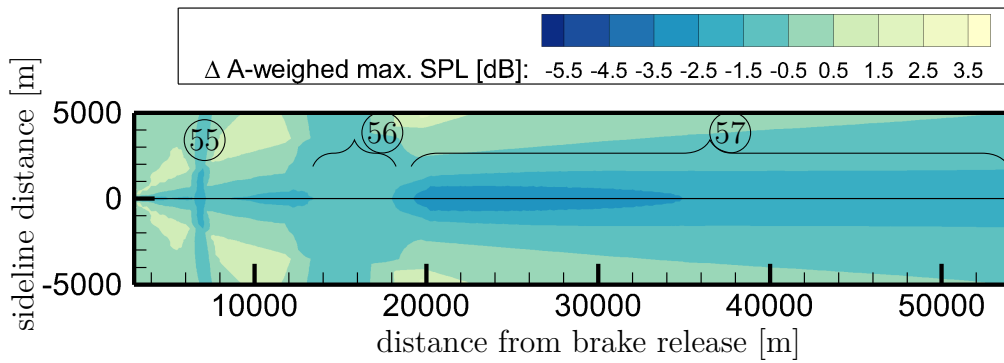


**Figure 6.19:** Difference in the A-weighted maximum SPL during departure of the basic airplane compared to the reference airplane.

also larger, so the acceleration segment is started earlier. This causes the end of the basic airplane’s acceleration segment to overlap with the first half of the reference airplane’s acceleration segment. The basic airplane is faster here, and therefore the fan sound emission is also higher. This leads to a short segment where the ground noise reduction is lower (56) than on the previous and the following segment (57).

Figure 6.20 shows the approach-induced awakening probability of the reference airplane colored according to the causative sound source. The same approach-induced awakening probability by the reference airplane, however, colored only according to the airframe noise sources, is depicted in Figure A.6.6.24.

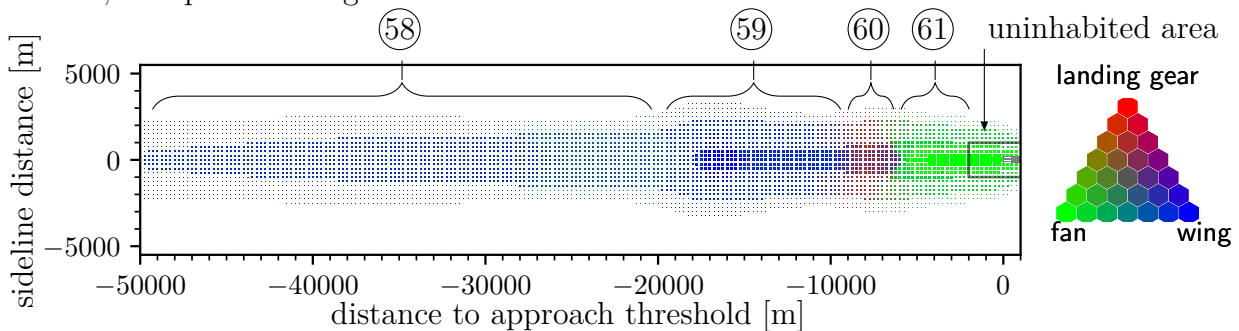


**Figure 6.20:** Dominating noise sources during approach of the **reference airplane** and, hence, prior to mounting low noise technologies. The same data, but showing relevant approach noise sources, has been depicted in Figure A.6.6.24 on page 168.

Section (58) is dominated by trailing-edge noise of the wing. In section (59), the high-lift systems are in the approach configuration. The Kruger flaps cause the most awakening probability here. Later, in section (60) the landing gear is deployed, and shortly thereafter the high-lift systems are extended to the landing position (purple section). In the last section (61) after the stabilization point, fan noise predominates because here the engine is accelerated to compensate for the drag of the high-lift systems and the landing gear. This is because after the stabilization point, the approach speed must be kept constant.

Figure 6.21 shows how much quieter or louder the basic airplane is compared to the reference airplane along the approach. The difference in the A-weighted maximum sound pressure level is shown. In addition, the area where the basic airplane does not cause any awakening probability is blanked out.

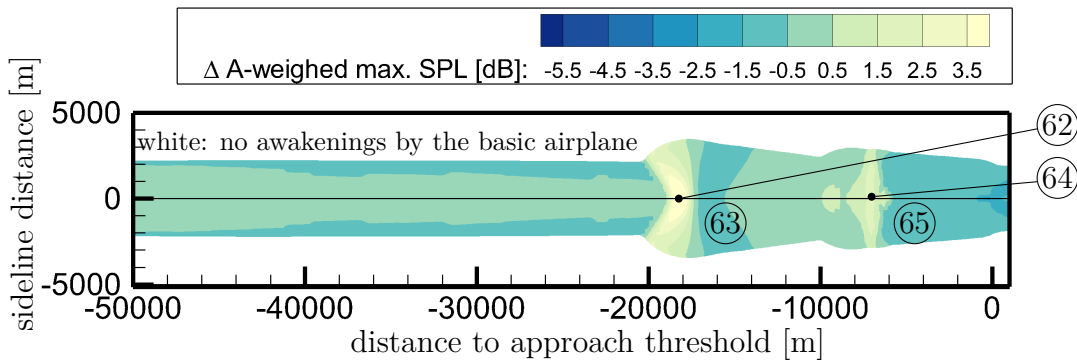


**Figure 6.21:** Difference in the A-weighted maximum SPL during approach of the basic airplane compared to the reference airplane. The increase at (62) results from the 500 m earlier Kruger flap deflection at 18 km before the approach threshold. In the area (63) the ground noise is lowered due to the slower approach speed, and hence less noise generation by the high-lift devices. The increase in sound pressure level at location (64) is due to the high-lift systems being deployed to the landing configuration 230 m earlier. In the area (65), less thrust is required, which results in less ground noise.

Initially, the basic airplane causes an about 0.5 dB lower sound pressure level than the reference airplane along the ground track of the segment flown in cruise configuration. At location (62), the high-lift systems are deployed 500 m earlier in the approach configuration. This results in sound pressure levels, which are up to 4 dB higher compared to the reference airplane, but also a slower entry into the final approach segment, so that the basic airplane is quieter here (63) than the reference airplane. The increase in the sound pressure level at location (64) is due to the fact that the high-lift systems are deployed 230 m earlier into the landing configuration. The lower drag of the basic airplane in landing configuration ultimately results in less thrust needed, so it becomes between 0.5 and 1.5 dB quieter after the stabilization point on the ground (65).

The small areas marked by (62) and (64) have so much more awakening reactions that in total more people are awoken by the basic airplane compared to the reference airplane. Therefore, the Approach Awakening Index is higher than that of the reference airplane. However, the departure causes so many fewer awakening reactions that the Overall Awakening Index is less than zero, so overall fewer people woke up than would have by the reference airplane.

## 6.7 Chapter Conclusion

A low-noise airplane along departure can be achieved by a high glide ratio and low takeoff weight. Both components result in a high thrust-to-weight ratio and, hence, a steeper climb. Additionally, a small wing area causes prolonged acceleration on the runway, which mainly shortens the acceleration segment and heightens the remaining flight path. As the engine is the dominant reason for the ground noise along departure and its ground noise depends – in a first approximation – only on the height, the airplanes with a higher averaged climb response cause a lower Departure Awakening Index.

A low-noise approach is realized when the airplane flies as slow as feasible along the cruise configuration segment because

- (a) the wing trailing edge generates less sound,
- (b) the high-lift devices are deployed later, and
- (c) the high-lift devices are deployed at a slower flight speed.

Factor (a) is achieved by a combination of low wing loading and a high maximum lift coefficient. The factors (a) & (b) contribute to a smaller noise affected area and the factors (a) & (c) to lower sound pressure levels.

Optimal values of the three planform parameters leading-edge sweep, wing area, and aspect ratio function co-dependently to achieve an overall low-noise airplane design. The planform of the airplane that has the lowest Departure Awakening Index differs from the one of the airplane that has the lowest Approach Awakening Index. Thus, the values of the planform parameters of the selected airplane are a compromise between the ones for low-noise departure and approach. As the departure causes more additional awakening reactions than the approach, it has a greater influence on the Awakening Index and, hence, the selection of the optimal airplane and the quietest airplane.

Although the jet sound contribution to the approach-induced awakenings is negligible, it leads the total additional awakening reactions. Therefore, reducing the jet sound by increasing the engine's bypass ratio is recommended to achieve the greatest effect in lowering the Awakening Index.



## 7 | Ground Noise Reduction by Low-Noise Technologies

This chapter discusses the impact of the low-noise technologies on the wing planform and the ground noise. Each of the noise-reducing technologies also changes the flight characteristics of the airplane. This means that ground noise is not only reduced by the lower noise generation, but is also changed by altered flight characteristics. This change can result in a reduction, an increase, or a redistribution of ground noise. The impact of these noise-reducing technologies on the departure and approach trajectories of the respectively selected airplane and their ultimate noise reduction potential is studied. A parameter study of the planform, such as in the previous chapter, is performed to obtain the optimal wing design for each applied technology.

The following noise-reducing technologies are investigated in the Sections 7.1 to 7.4: fan sound shielding, UHBR engines to reduce jet sound, droop nose and brush to reduce wing sound, and fairings to decrease landing gear sound. Each of these technologies introduces a new technology level, which also contains all technologies of the respective previous technology level. These technology levels are listed in Table 7.1. They have been applied in the order of their respective relevance, which has been determined from examining the sound source dominance on the ground, as shown in Figures 6.15 and 6.16, for example.

These new airplane designs still utilize the same materials as used in the reference airplane, making the effects directly attributable to the usage of the noise-reducing technologies. The exception being the droop nose, which replaces the Kruger flaps. It requires flexible materials, which are also lighter.

Table 7.2 gives an overview of the investigated technology levels and lists the planform parameters, their respective ranges, and resolution considered in the simulations.

**Table 7.1:** List and description of the investigated noise-reducing technologies. As these technologies have been applied sequentially, each technology step contains the noise mitigation technology of the previous level.

| Label | Description   | Info in     |
|-------|---|-------------|
| ref   | <b>reference</b> airplane: B747-400 with CF6-80 engine<br>$\varphi_{LE} = 42^\circ$ , $A_W = 561.93 \text{ m}^2$ , and $\Lambda_W = 7.1789$   | Chapter 4   |
| basic | selected airplane from planform parameter study<br>$\varphi_{LE} = 36^\circ$ , $A_W = 520 \text{ m}^2$ , and $\Lambda_W = 9.0$  | Chapter 6   |
| eow   | <b>Engine Over Wing</b> : CF6-80 engine has been mounted above the wings to shield the fan sound.   | Section 7.1 |
| neo   | <b>New Engine Option</b> : DKO20 engine mounted above the wings. The DKO20 engine is a UHBR engine replacing the CF6-80.  | Section 7.2 |
| lnw   | <b>Low Noise Wing</b> : Technologies for wing noise reduction. Kruger flaps at the leading edge (l.e.) have been replaced by a droop nose, and the blunt trailing edge has been furnished with a brush. | Section 7.3 |
| lgf   | <b>Landing Gear Fairings</b> are mounted to reduce the landing gear noise.  | Section 7.4 |

**Table 7.2:** List of the design parameters and their ranges for all technology levels. Each section represents one technology level. 720 of the 1144 possible value combinations were examined. Preliminary studies containing some simplifications indicated to search for the optimum at lower sweep angles. Finally, all the optima have been found at high sweep angles since the cruise speed has a significant impact on the Direct Operating Cost Index, which is a component of the target function. The abbreviations can be extracted from Table 7.1.

| Airplane             | Design Parameter  | Value                  |                   |                    | Simulations |
|----------------------|---|------------------------|-------------------|--------------------|-------------|
| ref from Chapter 4   | l.e. sweep [°]<br>wing area [m <sup>2</sup> ]<br>aspect ratio [–] | 42<br>561.93<br>7.1789 |                   |                    | 1           |
| Technology Level     | Design Parameter  | Min.                   | Max.              | Resolution         | Simulations |
| basic from Chapter 6 | l.e. sweep [°]<br>wing area [m <sup>2</sup> ]<br>aspect ratio [–] | 26<br>500<br>6.5       | 44<br>660<br>10   | 2.0<br>20.0<br>0.5 | 720         |
| eow                  | l.e. sweep [°]<br>wing area [m <sup>2</sup> ]<br>aspect ratio [–] | 16<br>500<br>7.5       | 40<br>700<br>11.0 | 2.0<br>20.0<br>0.5 | 720         |
| neo                  | l.e. sweep [°]<br>wing area [m <sup>2</sup> ]<br>aspect ratio [–] | 16<br>500<br>7.5       | 40<br>700<br>11.0 | 2.0<br>20.0<br>0.5 | 720         |
| lnw                  | l.e. sweep [°]<br>wing area [m <sup>2</sup> ]<br>aspect ratio     | 16<br>500<br>7.5       | 40<br>700<br>11.0 | 2.0<br>20.0<br>0.5 | 720         |
| lgf                  | l.e. sweep [°]<br>wing area [m <sup>2</sup> ]<br>aspect ratio [–] | 16<br>500<br>7.5       | 40<br>700<br>11.0 | 2.0<br>20.0<br>0.5 | 720         |
| $\Sigma$             |   |                        |                   |                    | 3601        |

## 7.1 Fan Noise Shielding

It has been determined in the previous chapter that jet sound of the basic airplane is the prevailing sound source. Replacing the engine mounted under the wing with an ultra-high bypass ratio one would reduce jet noise but this is not readily feasible due to insufficient space below the wing. However, mounting it over the wing solves this problem, but it is crucial to first investigate the effects of the over-the-wing mounted engine before replacing the engine with an ultra-high bypass ratio one. This allows to observe the effects of the displaced engine position and to identify the most beneficial combination of values of the planform parameters taking the changed aerodynamics and flight mechanics into consideration. The airplane that utilizes fan sound shielding by the wing of the CF6-80 engine, is named engine-over-wing airplane (eow) and shown in Figure 7.1. In this section, the selected engine-over-wing airplane is compared to the selected basic airplane from the previous chapter.

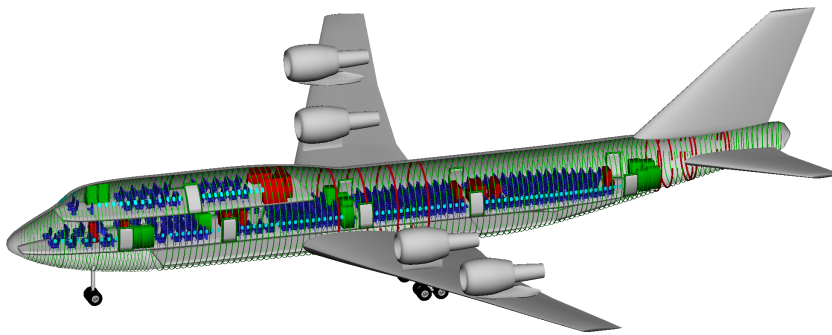


**Figure 7.1:** Engine-over-wing airplane

The benefit of positioning the engine above the wing is the shielding of the fan sound [3, 24, 116, 147]. The wing acts as a noise barrier and reflects the fan sound up into the sky, thus less of it reaches the ground, which, in turn, reduces the ground noise in favor of the residents.

The displacement effect due to the pylons, which accelerate the streamlines on the wing's suction side, lowers the pressure on the suction side. Due to this lower pressure, lift is increased [17, Figure 12]. However, the lack of surface area occupied by the pylons can also cause a lower lift [17, Figure 15].

This effect of the streamline displacement on the lift has been excluded from the scope of this thesis because of the following estimation: Potential Flow Theory, with reference to the source code provided by Barba and Mesnard [16], has been used for this assessment. The code has been modified to integrate the pressure field around the investigated NACA0010 profile. This profile models the pylon as an airfoil with an infinite span mounted perpendicular to the wing's chord surface<sup>1</sup> to study the impact of the displacement effect on the wing's lift. The pressure difference of the flow caused by the pylon and the ambient flow is added to the pressure distribution on the wing's suction side, as can be surmised from Figure 7.2. Neglecting the changes on the wing's pressure side, a total increase of the lift coefficient of less than  $10^{-2}$  has been observed, resulting in a velocity reduction of less than  $0.4 \frac{\text{m}}{\text{s}}$  at a flight speed of  $80 \frac{\text{m}}{\text{s}}$ . When this velocity reduction is applied to the landing gear noise model, which exhibits the greatest velocity dependency, a total reduction of less than 0.15 dB in sound

---

<sup>1</sup>The chord surface would be the chord plane, if the wing would not be twisted.

pressure level is predicted. This reduction in sound pressure level is negligible in relation to the efforts invested in its estimation, thus the displacement effect remains unaccounted for.

Mounting the engines above the wings opens up the opportunity to shorten the landing gears. However, the same cannot be done to the large B747-400 fuselage, as the present landing gear length is necessary to enable the required rotation during liftoff. Shorter struts would lower the maximum available rotation angle. This, in turn, could be compensated by positioning the landing gear further to the back. However, this would result in a shorter lever arm of the horizontal stabilizer to pitch the airplane. Hence, a larger empennage would be required and the resulting forces cause a higher load on the fuselage. Ultimately, the landing gear position and its length have been kept constant in this thesis. However, the size of the landing gear has been adjusted according to the loads and is represented by the landing gear weight, which is calculated for each airplane design.

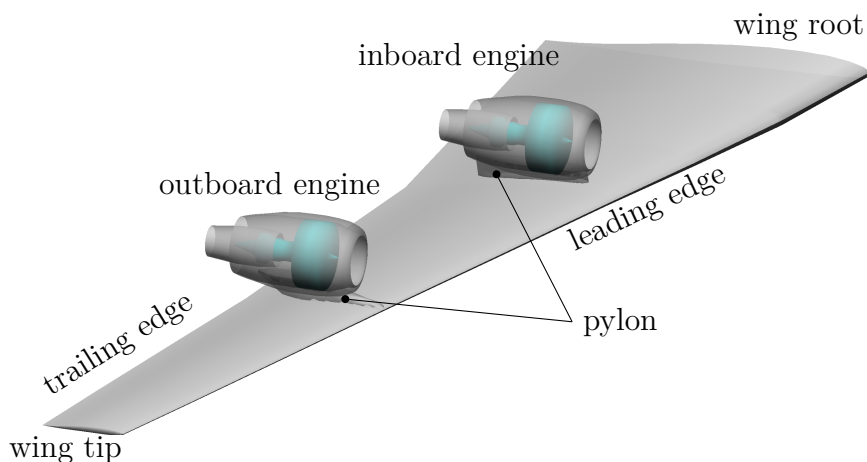


**Figure 7.2:** Pylons perpendicular to the wing’s chord plane. To estimate the effect of the pylon on the wing’s lift, it is modeled as a NACA0010 airfoil with infinite span mounted perpendicular to the wing’s chord plane. Infinite span means that the flow around the airfoil has been modeled two-dimensional. Its pressure field is integrated over the intersection surface of the pressure field and the suction side of the wing.

Over-the-wing mounted engines might increase the drag at high speeds during cruise flight. Mach dependent drag data for possible over-the-wing engine positions has been determined by Fujino and Kawamura [83] and Hooker et al. [108]. Using the conventional forward-under-wing position as a reference, the two authors investigated over-the-wing engines located upstream, halfway of the chord length, and downstream.

The drag data provided by Fujino and Kawamura has been applied to all airplanes with over-the-wing mounted engines as the best available estimate. Engines and pylons compress the streamlines and accelerate the flow. At a constant speed above the critical Mach number, the presence of the pylon on the wing’s suction side would drastically increase the wave drag, depending on the pylon’s position. This also means that the critical Mach number would be reduced, which would result in a transition to the supersonic flow at lower speeds. The compression shocks would occur at lower Mach numbers. Hence, the cruise Mach number ( $Ma_{cr}$ ) of each airplane is set to the value of  $Ma_{cr} = 0.66 \cdot \frac{1}{\cos \varphi}$  [83, estimated from Figure 22]. This cruise Mach setting avoids the enormous increase in the fuel consumption and, thus, avoids aborting of PrADO simulations. Higher sweep angles offer the advantage of

faster cruise speeds. Faster cruise speeds enable the airplanes to fly more kilometers during the airplanes' lifetime, which increase their revenue.

The drag data [83] was originally provided for a small business jet using a wing with a  $17^\circ$  sweep angle at 25% chord. In this work, however, the drag data is applied to one of the largest passenger airplanes in operation, making it operate just above its critical Mach number. In addition, two engines are mounted above one half-wing, while only one engine was mounted on the business jet's half wing. Therefore, future investigations have to conclude whether the dimensionless data by Fujino and Kawamura can be applied to the aerodynamics of such a large airplane.

Mounting engines over the wing can also be beneficial to the fuel consumption. When the engine's inlet is placed close to the wing's trailing edge, it can reduce the drag [192, 224]. It is advisable to not only shield the most dominant sound emission direction, but also to ascertain the optimal engine position with respect to the minimum ground noise for both approach and departure conditions. A study that determines the optimal position is required since the resulting ground noise is collectively influenced by (a) the pitch of the airplane, (b) the operation-dependent directionality, (c) the operation-dependent sound emission of the various engine components, and (d) the height-dependent atmospheric attenuation. The optimal position has been determined from the Figure 7.3 individually for inboard and outboard engines by placing all engines virtually either inboard or outboard, shifting them lengthwise in steps of 0.5 m, while keeping the vertical distance to the chord line. The minimum Awakening Index determines the optimal fan disk center position. Optimal engine positions measured from the airplane nose are located at 32.56 m for the inboard and 38.52 m for the outboard engines. These absolute values of the engine position are exemplary, since the engine positions are relative and will vary as soon as the leading-edge sweep angle, the wing area, or the aspect ratio is changed. However, this relative engine position has been determined only once for the CF6-80 engine, and once for the ultra-high bypass ratio engine, in order to limit the computational time within reasonable limits for the preliminary design.

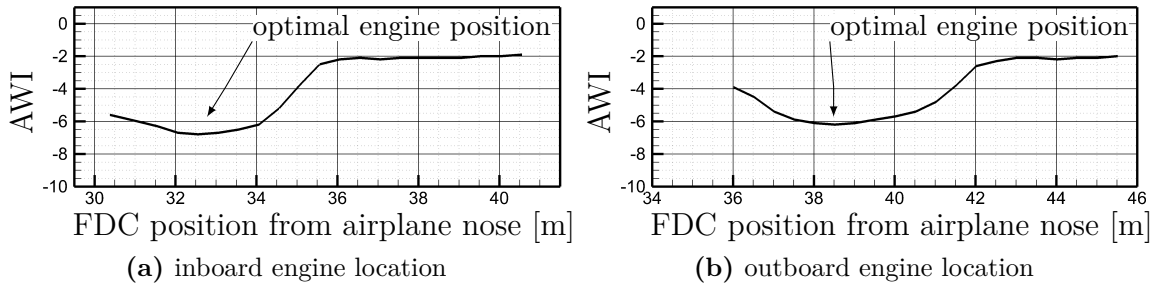


**Figure 7.3:** Awakening Index (AWI) over x-position of the fan disc center ( $x_{ac,FDC}$ ) of the engine-over-wing airplane using the split fan sound source method. The optimal inboard and outboard engine positions have been derived from these investigations.

For another sound source ranking of the engine components another engine position could be beneficial. A different sound source ranking can already emerge when using another power setting resulting from a varied departure procedure. It turns out that low-noise airplanes can only be identified using a holistic approach.

The consequence of the planform on the empennage size has already been considered, however just mentioned briefly, in the previous Chapter 6. The areas of the horizontal and vertical stabilizer, which have been suggested by PrADO, have been adjusted in the entire

thesis using the factors from Section 4.1. This affects mass, drag, and flight performance of the airplanes.

As the placement of engines over the wing affects the optimal planform, a wing design study like the one in Chapter 6 has been conducted to achieve the best airplane according to the target function from Section 5.4. As discussed earlier, this engine placement, chord-wise centered above the wings, leads to a reduced cruise speed and a suboptimal aerodynamic efficiency causing the fuel consumption to increase, which results in additional structural weight and adversely affects the flight performance. The parameter study of the wing design enables to reduce negative effects by achieving an optimal planform to keep both the Awakening Index and Direct Operating Cost Index low. The results of this parameter study are shown in Figure 7.4, displaying the Direct Operating Cost Index of each airplane plotted against its respective Awakening Index. The color of the marker shows the respective aspect ratio.

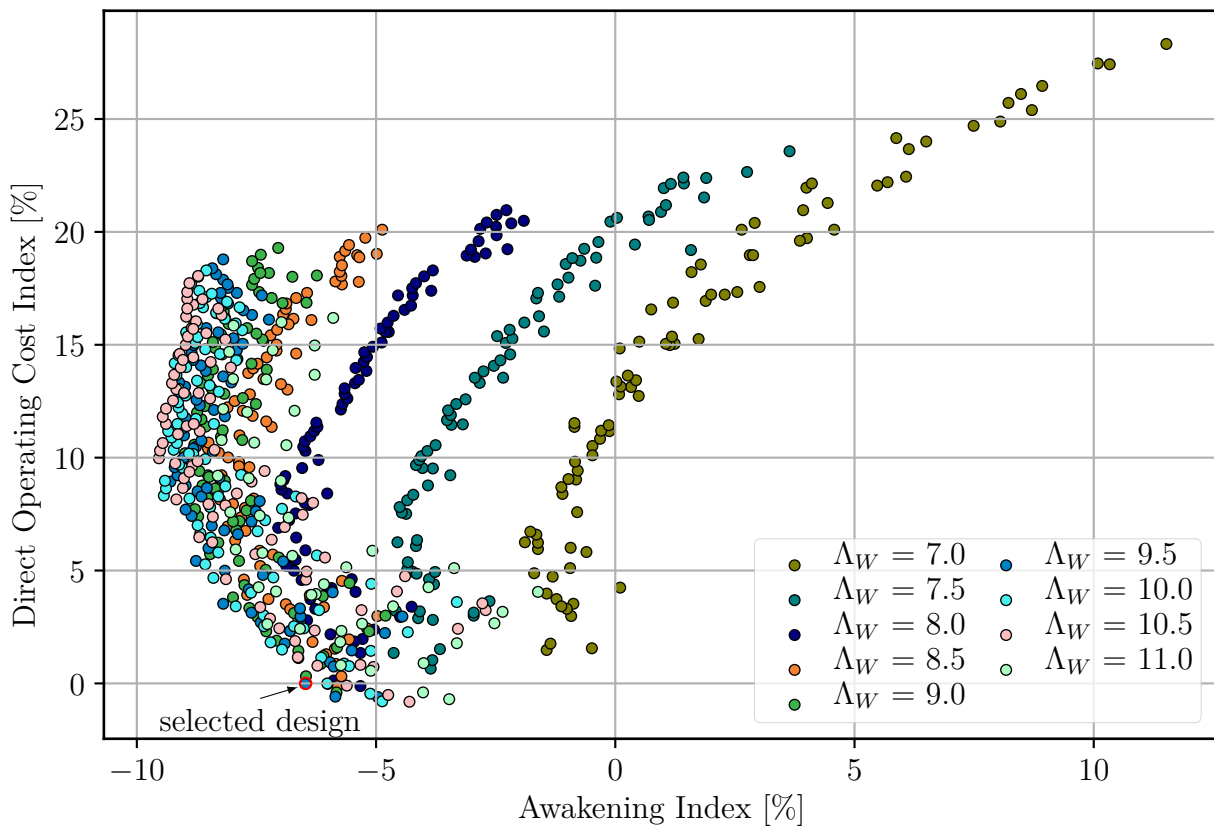


**Figure 7.4:** Direct Operating Cost Index over Awakening Index of the engine-over-wing airplane. Each point corresponds to one airplane design, and shows its Direct Operating Cost Index and caused Awakening Index. The color stands for the aspect ratio ( $\Lambda_W$ ), as it has been the design parameter with the highest correlation coefficient. The same airplanes, though distinguished by color according to their wing area and leading-edge sweep angle, are shown in Figures A.7.1.25 and A.7.1.26, respectively.

The optimal airplane according to the target function has a leading-edge sweep angle of  $40^\circ$ , a wing area of  $540 \text{ m}^2$ , and an aspect ratio of 9.5. The airplane with the lowest Direct Operating Cost Index and the one with the lowest Awakening Index have both been recorded at an aspect ratio of 10.5. As in the parameter study of the basic airplane, the aspect ratio

is not the only driving parameter, the factors wing area and sweep angle also influence the Awakening Index and Direct Operating Cost Index.

Compared to the basic airplane, the Pareto front of the engine-over-wing airplane consists of more airplanes. With much finer resolution of the step size of all three planform parameters, one would most likely have a continuous front rather than a few individual airplanes sticking out, as is the case here. This larger Pareto front is most likely due to the cruise speed that depends on the leading-edge sweep angle. Additional studies are needed for conclusive proof, as the scope of this study is insufficient for this conclusion.

**Table 7.3:** Airplane data of the engine-over-wing airplane design (eow) compared to the basic airplane and reference airplane (ref).

| Airplane<br>Variable            | eow     | $\Delta$ to basic [%] | $\Delta$ to ref [%] |
|---------------------------------|---------|-----------------------|---------------------|
| leading-edge sweep [°]          | 40      |                       | -14.30              |
| Wing area [m <sup>2</sup> ]     | 540.0   | 3.85                  | -3.90               |
| Aspect ratio [-]                | 9.500   | 5.56                  | 32.33               |
| Span [m]                        | 72.92   | 4.56                  | 12.37               |
| Max. aircraft length [m]        | 70.86   | 0.17                  | 0.10                |
| Max. aircraft height [m]        | 20.06   | 1.31                  | 0.60                |
| Design range [km]               | 10602   | 0.00                  |                     |
| Cruise Mach [-]                 | 0.841   | -1.06                 | -1.06               |
| Cruise altitude [ft]            | 12.43   | 1.06                  | -0.88               |
| Lift/Drag [-]                   | 18.27   | -5.97                 | 5.73                |
| Max. lift coefficient [-]       | 1.395   | 3.79                  | 3.33                |
| Static thrust [N]               | 1090120 | 0.00                  |                     |
| Engine diameter [m]             | 2.692   | 0.00                  |                     |
| Bypass ratio [-]                | 5.100   | 0.00                  |                     |
| SFC in cruise [g/N/h]           | 0.060   | -1.33                 | -0.50               |
| Max. takeoff weight [kg]        | 398848  | 6.98                  | 2.25                |
| Max. landing weight [kg]        | 288057  | 4.96                  | 3.78                |
| Operating empty weight [kg]     | 189484  | 5.64                  | 6.15                |
| Manufacturer empty mass [kg]    | 173846  | 6.13                  | 6.83                |
| Fuselage weight [kg]            | 38956   | 0.50                  | -0.98               |
| Wing weight [kg]                | 55330   | 11.62                 | 25.91               |
| Fuel mass (design mission) [kg] | 125103  | 12.72                 | -2.86               |
| Takeoff distance [m]            | 3176    | +13.60                | +6.70               |
| Takeoff speed $v_2$ [m/s]       | 85.20   | 0.80                  | 3.12                |
| Landing field length [m]        | 2295    | 1.96                  | 11.08               |
| Landing speed [m/s]             | 71.22   | 0.47                  | 3.74                |
| DOC [EURO per seat km]          | 0.053   | 4.05                  | -0.02               |

The data of the selected engine-over-wing airplane is summarized in Table 7.3. The 26 t (+7%) increased maximum takeoff weight compared to the basic airplane is expected to significantly impact the Departure Awakening Index, as the increased mass leads to a worse averaged climb response. Furthermore, the wing area rose by 3.9%, whereas the maximum landing weight increased by 5%. Thus, the wing loading is increased, which could potentially lead to a faster stall speed and possibly increases the Approach Awakening Index. Both the

higher stall speed and higher Approach Awakening Index, however, are not the case, as is explained in the paragraph after next.

The departure and approach trajectories, airspeeds, and thrusts of the engine-over-wing airplane in comparison to the basic airplane are depicted in Figure 7.5. As the maximum takeoff weight of the engine-over-wing airplane is 7% higher, this airplane requires a longer takeoff roll distance. Its higher wing loading leads to a faster takeoff safety speed. Both factors put together increase the takeoff roll length by 13.6%.

During the approach along the cruise configuration segment, the engine-over-wing airplane flies  $3 \frac{\text{m}}{\text{s}}$  slower than the basic airplane due to a  $0.6^\circ$  higher maximum angle of attack and, hence, a higher maximum lift coefficient. In addition, its glide ratio is slightly higher. Thus, the engine-over-wing airplane deploys the high-lift devices 700 m earlier than the basic airplane, as it decelerates less along the final approach segment. Beyond the stabilization point, the higher glide ratio of the engine-over-wing airplane leads to lower engine thrust compared to the basic airplane.

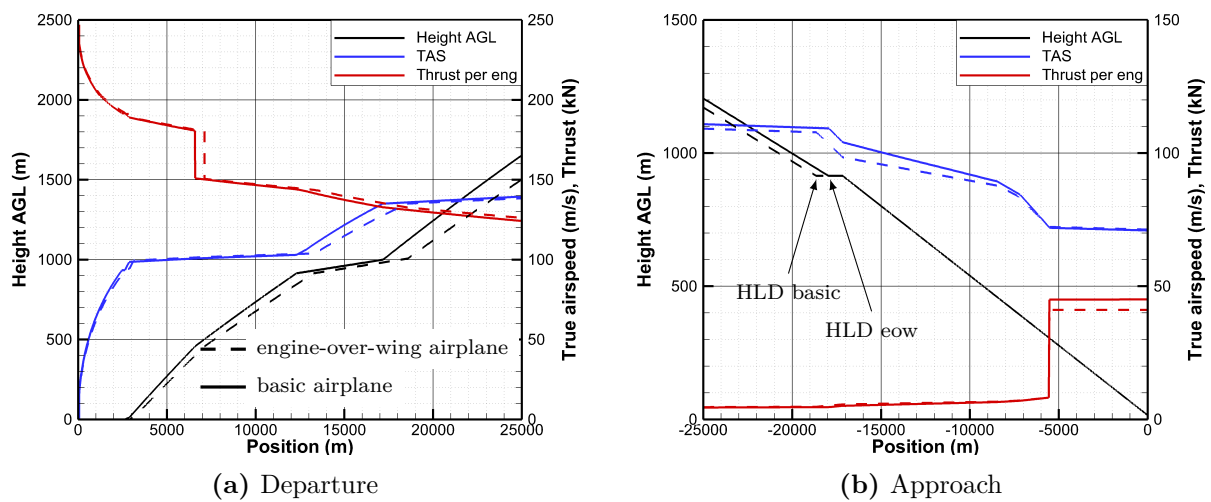
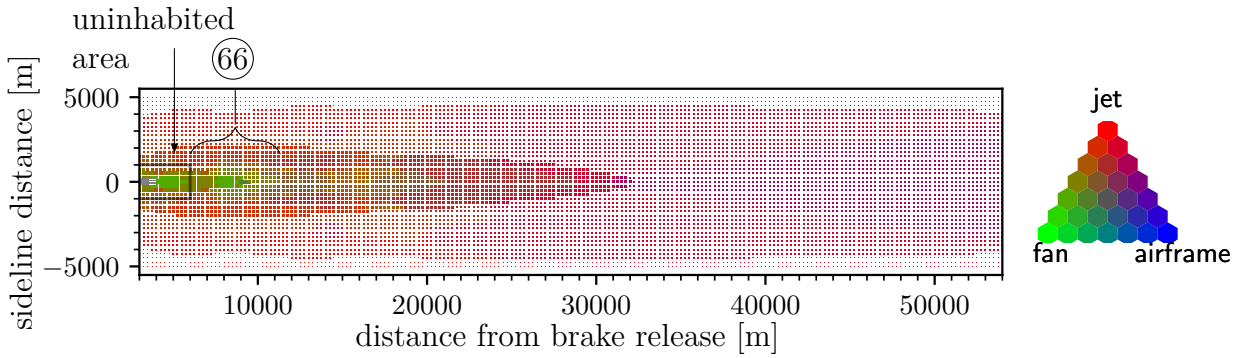


**Figure 7.5:** Departure and approach trajectories of the engine-over-wing airplane and the basic airplane. The graphs show two trajectories, thrust, and true airspeed for the two selected airplanes, respectively.

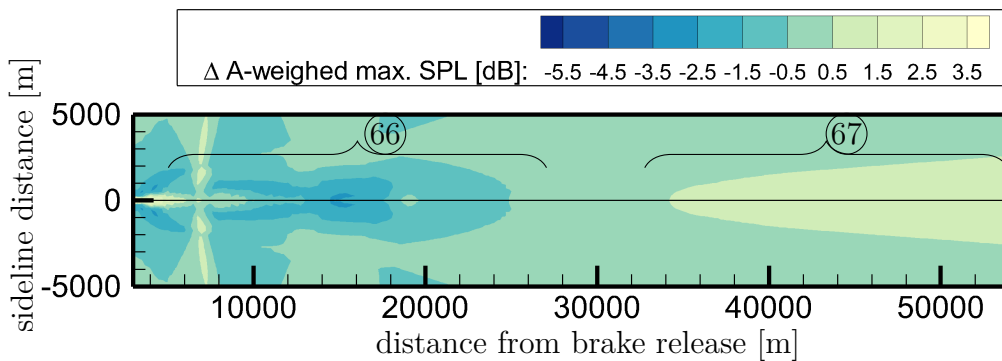
Figure 7.6 shows<sup>2</sup> a jet sound dominated awakening probability during departure and Figure 7.7 identifies, how much the A-weighted maximum SPL changed for this engine-over-wing airplane, compared to the basic airplane. Although this airplane holds a worse climb performance due to the increased takeoff weight, the ground noise is lowered because the fan sound (66) is shielded by the wings. In this jet noise dominated area, awakening probability and A-weighted maximum SPL are barely reduced and even slightly increased after 34 km of the ground track and onward (67), along the ground track.

As shown in Figures 7.8 and A.7.1.27, the awakening probability during approach is mainly caused by the wing noise, which consists of clean-wing trailing-edge noise (68), flap noise, and Kruger flap noise (69). Later, along the final approach segment, ground noise is dominated by landing gear noise (70), landing gear noise mixed with flap noise (violet), and fan noise (71). The Approach Awakening Index has been reduced to  $-7.8\%$  for the engine-over-wing airplane.

<sup>2</sup>SUMATRA Open Source PDF Reader is suggested as the best software to view these plots.



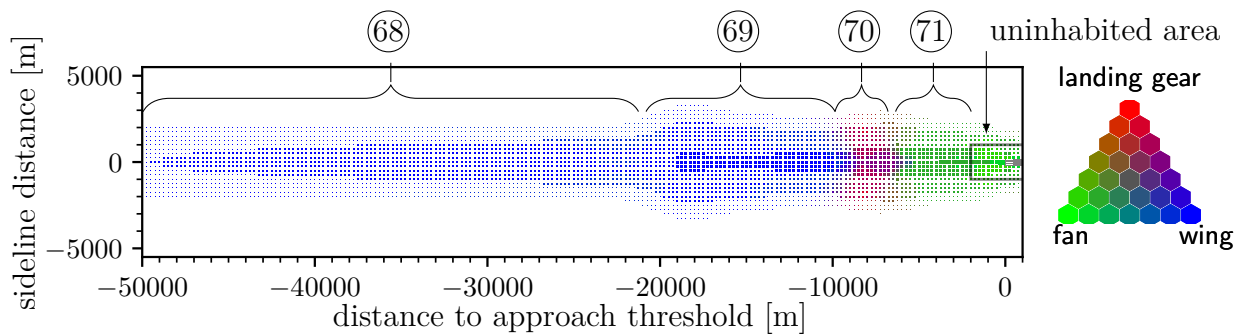
**Figure 7.6:** Dominating noise sources of the engine-over-wing airplane during departure. Most of the awakening probability is caused by jet sound (red). The fan contributes only for about 12 km along the ground track and 800 m to both sides to around half or more of the sound intensity. As the airplane reaches more height, the frequencies of the fan are more attenuated than the ones of the jet. Thus, the jet dominates the ground noise along the final climb segment.



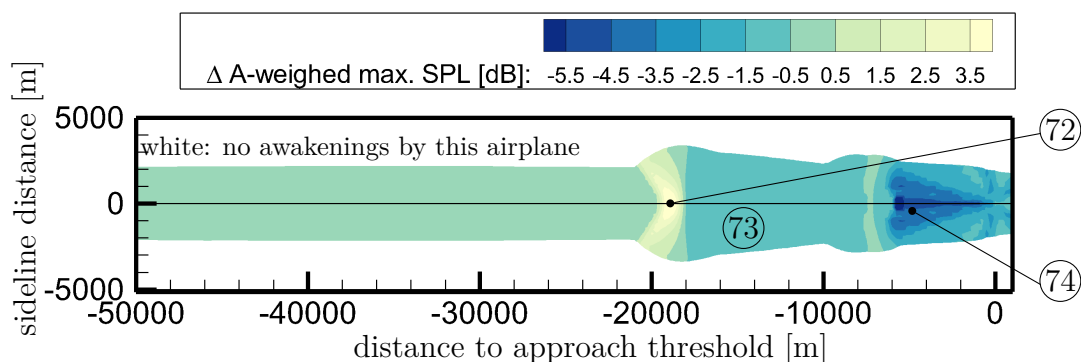
**Figure 7.7:** Difference in the A-weighted maximum SPL during the departure of the engine-over-wing airplane compared to the basic airplane. In the area (66), the fan sound shielding reduced the overall A-weighted SPL. In most of the area, the differences in the A-weighted maximum SPL are less than  $\pm 0.5$  dB. About 34 km after the brake release point (67), the increase of the A-weighted maximum SPL exceeds 0.5 dB due to a worse climb performance and, hence, a shorter distance to the population.

Figure 7.9 presents the difference in A-weighted maximum SPL of the engine-over-wing airplane compared to the basic airplane during approach.

Along the ground track, where the corresponding flight path has been flown in cruise configuration, the A-weighted SPL deviates less than 0.5 dB. However, the engine-over-wing airplane has a higher glide ratio and, hence, it intercepts the horizontal segment for deceleration 700 m earlier than the basic airplane. This causes the increase in A-weighted maximum SPL at location (72). The engine-over-wing airplane is slower when intercepting the final approach segment, though. The population closer to the airport, which is affected by the noise along the final approach segment before the landing gear is deployed, benefits from this lower speed in area marked by (73). After the stabilization point (74), the marginally increased glide ratio leads to less required thrust to stabilize. This lower thrust and the fan sound shielding reduce the fan induced ground noise.



**Figure 7.8:** Dominating noise sources and the awakening probability of the engine-over-wing airplane during approach. In section (68), the airplane descends in cruise configuration. Then the flaps and Kruger flaps are deployed, and the airplane enters the  $-3^\circ$  final approach segment (69) with the Kruger flaps dominating the ground noise. Prior to reaching the stabilization point, the landing gear, and later full flaps, are deployed (70) to prepare for landing and to fly as slowly as feasible. At the stabilization point, the engine is spooled up to maintain a constant airspeed. The ground noise area (71) is dominated by the fan noise. The same ground noise showing only airframe sound sources is depicted in Figure A.7.1.27.



**Figure 7.9:** Difference in the A-weighted maximum SPL during approach of the engine-over-wing airplane compared to the basic airplane. Over most of the area under investigation, the A-weighted maximum SPL is lower due to a slower approach speed, fan sound shielding, and lower engine speed setting. The increase at (72) results from deflection of the Kruger flaps, which is happening 500 m earlier at about 18 km away from the approach threshold. In the area of (73), the ground noise is lower due to the slower approach speed and, hence, less noise generated by the dominating high-lift devices. In the area (74), fan sound shielding and the lower thrust reduce the fan ground noise collectively.

In the section to follow, the jet sound will be significantly reduced by employing an ultra-high bypass ratio engine, as jet noise causes most of the additional awakening reactions.

## 7.2 Jet Noise Reduction

With reference to the previous section, jet sound is observed as a prevailing sound source and is lowered to reduce the Awakening Index. As mentioned in the previous section, mounting ultra-high bypass ratio engines is feasible when placed over the wings. The higher propulsion efficiency of ultra-high bypass ratio engines lowers the specific fuel consumption. This, however, is counteracted by the increased drag due to the larger wetted surface area of the nacelle, but in total still leading to less fuel consumption. The airplane equipped with an ultra-high bypass ratio engine has been named new-engine-option airplane (neo). In this section, the selected new-engine-option airplane is compared to the selected engine-over-wing airplane from the previous section.

The ultra-high bypass ratio engine was modeled using the software GTLab, which was also applied to calculate the existing CF6-80 engine. The CF6-80 engine map has been compared with and successfully validated by manufacturer data, as per Section 4.1 on page 32. Hence, it is assumed that the engine map of the ultra-high bypass ratio engine, which exists only virtually, is also reliable, making the results obtained using this engine viable. However, one question arose as discussed in Chapter 8.

A comparable operation mode of the ultra-high bypass ratio engine with the CF6-80 one is required. There are two possible comparable operating modes: same engine speeds or comparable engine speeds. The same engine speeds have been found to be insufficient for the following reason: When the ultra-high bypass ratio engine is operated at the same engine speeds as the CF6-80, then it would lead to lower thrusts due to a higher thrust lapse rate of the ultra-high bypass ratio engines. Such lower thrusts would negatively affect the averaged climb response of the airplane, bringing the sound sources closer to the residents. This is compensated by the second option, which increases the engine speed of the ultra-high bypass ratio engine to  $N_{1,to} = 108\%$  and  $N_{1,cb} = 101\%$ , as described in Section 5.5.1 on page 54. This method has the advantage that the engine provides the same engine thrust at least in one flight condition of  $91 \frac{m}{s}$  close to the ground.

The airplane data, after mounting the ultra-high bypass ratio engine, is listed in Table 7.4. The selected optimal airplane design exhibits an aspect ratio of 7.5, a 10.7% reduced wing area and a  $4^\circ$  higher leading-edge sweep angle than the engine-over-wing airplane. Employing this new ultra-high bypass ratio engine significantly reduces fuel requirements. In addition, smaller wing area and reduced cruise fuel mass allow for a lower structural weight due to the reduced operational strain. This leads to a 12.5% reduced maximum takeoff weight and an almost 11.2% lower maximum landing weight, both potentially lowering the ground noise.

The departure is depicted in Figure 7.10a. As the takeoff weight of the new-engine-option airplane is reduced by 12.5% compared to the engine-over-wing airplane, the thrust-to-weight ratio is also significantly higher. This makes it possible for the airplane to liftoff within a shorter distance, to climb steeper, and to accelerate to the maximum allowed  $130 \frac{m}{s}$  within a shorter distance.

The approach, which can be seen in Figure 7.10b, is described in the opposite direction of the flight direction. After the stabilization point, the new-engine-option airplane flies at a slightly slower speed compared to the engine-over-wing airplane because the maximum lift coefficient is higher due to the increased maximum angle of attack. The maximum angle of attack is higher because the aspect ratio is lower. Along this section beyond the stabilization point, higher engine thrust is required due to the lower glide ratio of this airplane in landing configuration. Before the stabilization point, this lower glide ratio causes the airplane to decelerate more. Thus, it has to enter the final approach segment faster,

**Table 7.4:** Airplane data of the new-engine-option airplane (neo) compared to the engine-over-wing airplane (eow) and reference airplane (ref).

| Airplane<br>Variable            | neo    | $\Delta$ to eow [%] | $\Delta$ to ref [%] |
|---------------------------------|--------|---------------------|---------------------|
| leading-edge sweep [°]          | 40     |                     |                     |
| Wing area [m <sup>2</sup> ]     | 500.0  | -7.41               | -11.02              |
| Aspect ratio [-]                | 7.500  | -21.05              | 4.47                |
| Span [m]                        | 62.63  | -14.11              | -3.48               |
| Max. aircraft length [m]        | 70.71  | -0.21               | -0.11               |
| Max. aircraft height [m]        | 19.82  | -1.20               | -0.60               |
| Design range [km]               | 10602  |                     |                     |
| Cruise Mach [-]                 | 0.833  | -0.99               | -2.04               |
| Cruise altitude [ft]            | 12.36  | -0.56               | -1.44               |
| Lift/Drag [-]                   | 16.02  | -12.32              | -7.29               |
| Max. lift coefficient [-]       | 1.365  | -2.15               | 1.11                |
| Static thrust [N]               | 933224 | -14.39              | -14.39              |
| Engine diameter [m]             | 3.000  | 11.44               | 11.44               |
| Bypass ratio [-]                | 12.000 | 235.00              | 235.00              |
| SFC in cruise [g/N/h]           | 0.050  | -16.64              | -17.05              |
| Max. takeoff weight [kg]        | 349170 | -12.46              | -10.48              |
| Max. landing weight [kg]        | 255678 | -11.24              | -7.88               |
| Operating empty weight [kg]     | 161989 | -14.51              | -9.25               |
| Manufacturer empty mass [kg]    | 146396 | -15.79              | -10.04              |
| Fuselage weight [kg]            | 37823  | -2.91               | -3.86               |
| Wing weight [kg]                | 38245  | -30.88              | -12.97              |
| Fuel mass (design mission) [kg] | 105803 | -15.43              | -17.85              |
| Takeoff distance [m]            | 2593   | -18.36              | -12.87              |
| Takeoff speed $v_2$ [m/s]       | 82.83  | 0.18                | 0.25                |
| Landing field length [m]        | 2099   | -8.54               | 1.59                |
| Landing speed [m/s]             | 69.71  | -2.12               | 1.54                |
| DOC [EUR per seat km]           | 0.051  | -4.42               | -4.43               |

which, in turn, requires almost no deceleration along the horizontal segment making it much shorter. Hence, its cruise-configuration descent section is higher than the one of the engine-over-wing airplane. Additionally, this segment is flown at slower airspeeds due to lower wing loading.

Figures 7.11 and 7.12 illustrate the awakening probability caused by the departure of the new-engine-option airplane and the differences in A-weighted maximum SPLs compared with the engine-over-wing airplane. The population affected by the noise during departure benefits the most from the jet sound reduction due to the ultra-high bypass ratio engine. The jet noise is so far reduced that it contributes negligibly to the awakening probability across most of the area. Hence, airframe and fan noise prevail, although their sound emission is also lowered (75) (76). The fan sound source is lower due to the new engine, and the airframe sound is reduced because the trailing edge of the wing is shorter. A short segment along the ground track, 14 to 17 km after point of brake release, realizes a comparatively lower reduction (77) in the A-weighted maximum SPL. This is due to the earlier starting acceleration segment of the new-engine-option airplane: the new-engine-option airplane is faster in the

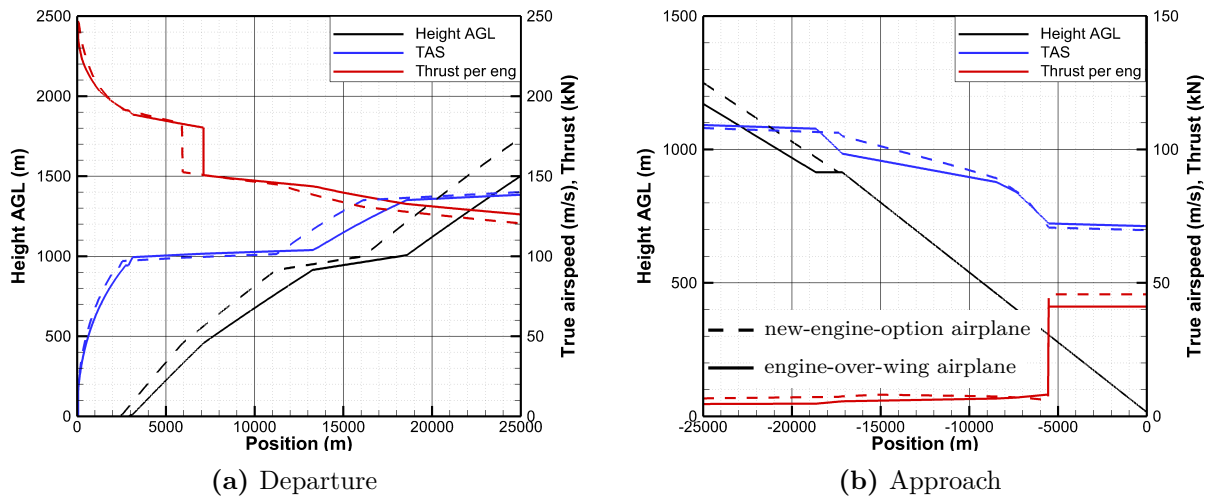


**Figure 7.10:** Departure and approach trajectories of the new-engine-option airplane and the engine-over-wing airplane. The graph shows two trajectories, thrusts, and true airspeeds for the two selected airplanes. At departure, the new-engine-option airplane lifts off within a shorter distance, climbs steeper, and keeps the acceleration segment shorter. During approach, the new-engine-option airplane flies higher than the engine-over-wing airplane along the cruise configuration segment. After the stabilization point, more thrust is required to stabilize.

second half of its acceleration segment than the engine-over-wing airplane in the first half of its acceleration segment, which leads to comparatively louder fan sound due to higher speeds of the new-engine-option airplane. The slightly greater distance to the ground does not compensate for the louder fan sound emission. However, the remaining investigated area benefits even more from this better climb and acceleration performance. Due to the strong dependency of wing trailing-edge sound on the flight speed, this noise source emerges when the airplane accelerates, and ultimately dominates the remaining area, which is affected by the sound generated along the climb segment in cruise configuration.

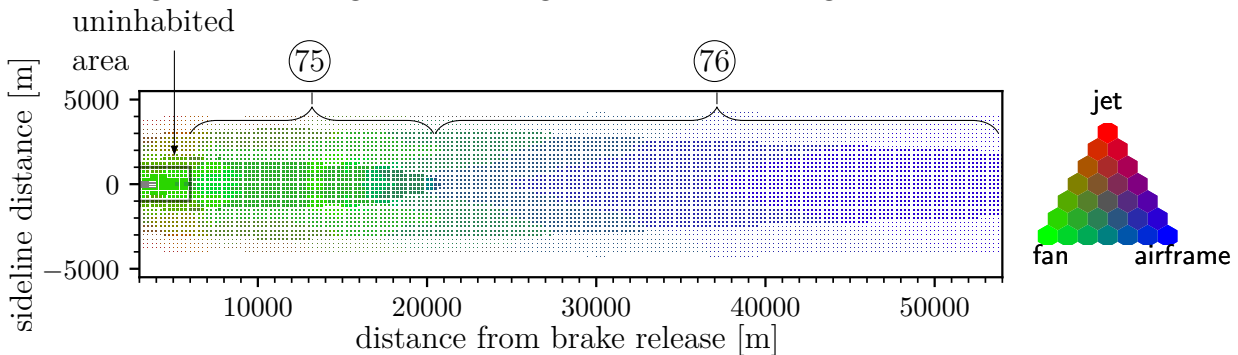


**Figure 7.11:** Dominating noise sources of the new-engine-option airplane during departure. Jet noise has been reduced to negligible values, and dominates the awakening probability only in the area up to 7 km behind the brake release point to the sideline. Most of the awakening probability has been caused by fan noise (75) and airframe noise (76). An additional achievement is a more narrow area of the awakening reactions of only 4 km to the sideline.

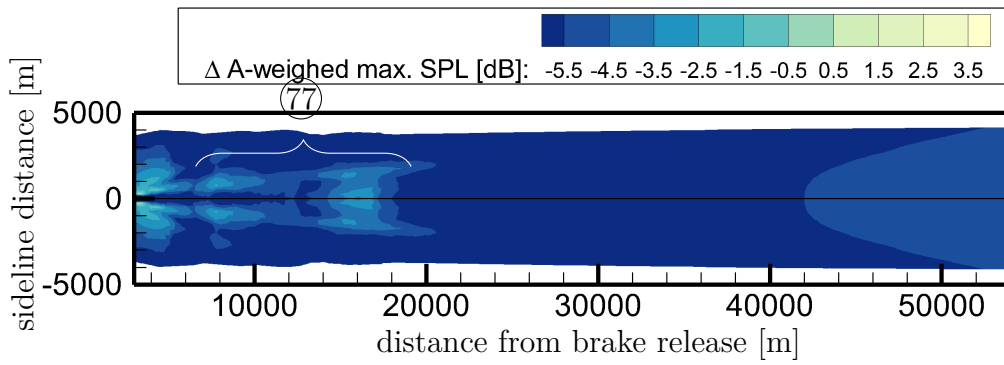


**Figure 7.12:** Difference in the A-weighted maximum SPL of the new-engine-option airplane compared to the engine-over-wing airplane during departure. Across a wide area, the A-weighted maximum SPL has been reduced by more than 5.5 dB. In the area (77), where fan sound dominates, the A-weighted maximum SPL has been reduced by at least 2.5 dB, but generally even more.

The approach awakening probability of the new-engine-option airplane and the distinction in A-weighted maximum SPL to the engine-over-wing airplane are depicted in Figures 7.13 and 7.14, respectively. Implementing the new ultra-high bypass ratio engine reduces the landing weight by 11.2 t, as smaller wing area and less fuel requirements reduce the overall structural weight. For example, at 30 km before the approach threshold, this leads to a lower emission of sound by about 0.7 dB A-weighted SPL. However, along the ground track that is affected by the sound along clean configuration segment (78), the A-weighted maximum SPL is even about 1.5 dB lower.

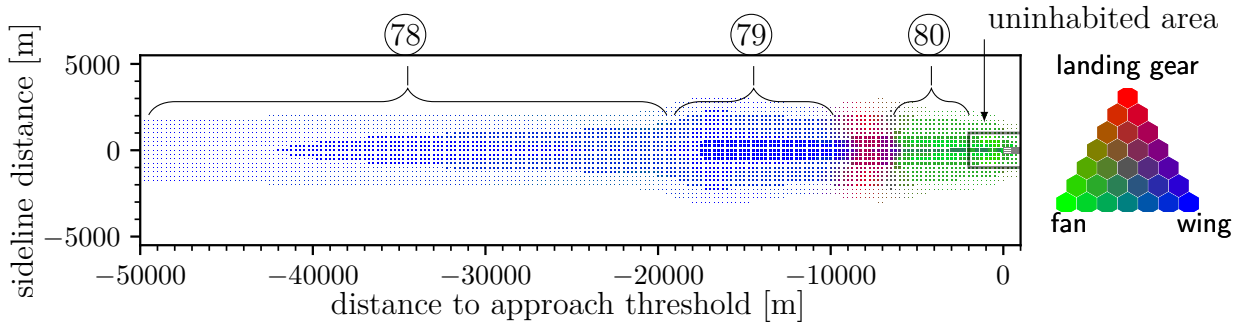


**Figure 7.13:** Dominating noise sources of the new-engine-option airplane during the approach. Figure A.7.2.31 shows the same approach and its corresponding awakening probability with colors referencing the airframe noise sources. The value of the awakening probability in section (78) is dominated by clean-wing trailing-edge noise, and later in section (79), by the Kruger flap noise. The landing gear noise dominated area is ended by the fan noise generated after the stabilization point (80).

Thus, the flight situation, pertaining to the A-weighted maximum SPL at 30 km before the approach threshold, has been investigated. The A-weighted maximum SPL over time and the distance between point of sound emission and microphone over A-weighted maximum SPL have been depicted in Figure 7.15.

A sound emission direction of  $\alpha^* = 67^\circ$  causes the A-weighted maximum SPL on the ground of both the airplanes. However, due to the 70 m greater height and the slightly

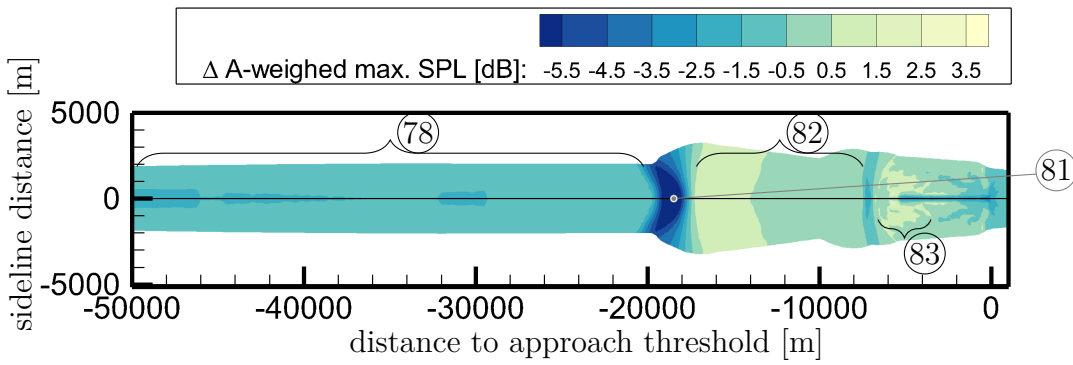
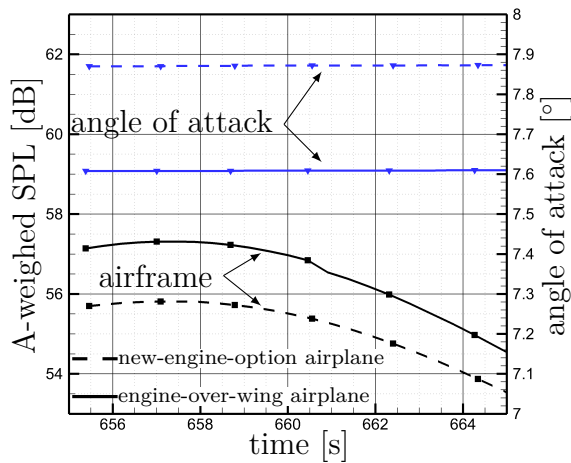
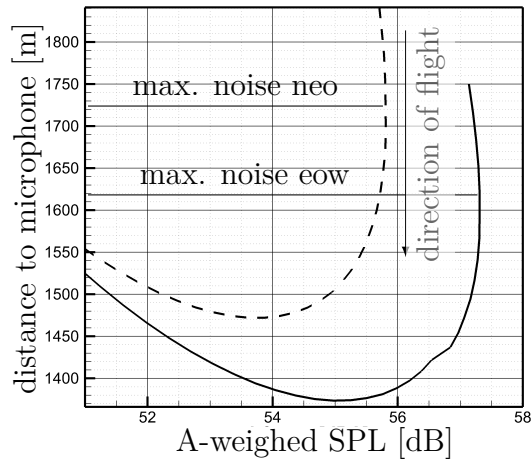


**Figure 7.14:** Difference in the A-weighted maximum SPL of the new-engine-option airplane compared to the engine-over-wing airplane during approach. The reduction in ground noise along the cruise configuration descent section (78) is caused by a shorter trailing edge of the wing and a longer transmission distance through the atmosphere, as the emission sound pressure levels deviate by only 0.7 dB.



(a) Angle of attack and A-weighted wing trailing-edge SPL on ground over time.



(b) Distance between point of emission and the microphone on ground on y-axis plotted over the A-weighted wing trailing-edge SPL on the x-axis.

**Figure 7.15:** A-weighted SPL at 30 km before approach threshold on the ground track. The graphs compare the new-engine-option airplane to the engine-over-wing airplane. The A-weighted SPLs on the ground are caused by airframe sound in both cases and differ by 1.5 dB, while the emitted A-weighted SPLs differ by 0.7 dB. The distance between point of sound emission and microphone location on the ground differs by 125 m. This longer distance is mainly caused by the 70 m higher segment in combination with the direction angle. The  $0.3^\circ$  difference in angle of attack also contributes, as the trailing-edge noise source model has a high directionality. Both A-weighted maximum SPLs, evaluated from the data file, are marked by the horizontal black lines. The graph itself indicates shorter distances, however, the marked data corresponds to the data from the level time history data file.

higher angle of attack, the distance between the point of sound emission and the microphone on ground is 125 m longer for the new-engine-option airplane than for the engine-over-wing airplane, as plotted in Figure 7.15b. The sound is more attenuated by both the longer propagation through the atmosphere and the more geometric attenuation.

As the horizontal segment of the new-engine-option airplane is shorter, the high-lift devices are set to approach configuration 1300 m further. This reduces the ground noise in the area (81) drastically. However, the faster approach speed increases the Kruger flap induced ground noise along the segment marked by (82). The deployment of landing gear and high-lift devices to landing configuration at a slightly faster airspeed has no significant impact. Beyond the stabilization point, the fan sound model predicts quieter fan aft sound emission of the ultra-high bypass ratio engine compared to the CF6-80 one, although the thrust is higher. This is visible on and along the ground track. However, the CF6-80 fan aft noise is at higher frequencies, and thus is more attenuated by the atmosphere, making the ultra-high bypass ratio fan aft sound louder on the ground to the sideline (83).

In the section to follow, the awakening reactions will be reduced by employing low-noise wing technologies to lower the remaining airframe noise dominance along departure and approach.

### 7.3 Wing Noise Reduction

After assessing the technologies in previous sections to curb the fan and jet sound, this part deals with the technology to curtail the wing sound. The Kruger flaps and trailing-edge flaps are now the leading contributors to the additional awakening probability during approach, as evident in Figures 7.13 and A.7.2.31. Moreover, Figure 7.11 shows that the wing in cruise configuration is responsible for a large part of the additional awakening probability during departure. The droop nose at the leading edge and the brush at the trailing edge are most promising noise reduction technologies to reduce the additional awakening probability. Brushes made of steel, for example, are used in turbines for sealing [107]. Therefore, they have already been proven to be suitable for a highly stressful application. However, research on porous trailing edges has been going on for more than 50 years, but they have not yet been used. Therefore, in this work, brushes will ultimately be utilized to reduce trailing-edge noise. The airplane selected from this parameter study is named low-noise-wing airplane (lnw).

The high-lift devices at the leading edge, i.e., the Kruger flaps, are replaced by the droop nose to eliminate the wing's leading-edge sound source. The use of a droop nose is assumed to decrease the maximum angle of attack by  $6.5^\circ$  [169, Fig. 10]. Thus, the maximum lift coefficient is lowered, which increases the approach velocity. Additionally, it is assumed that the usage of a droop nose reduces the wing mass [175, Fig. 16] by 1.2% ( $\approx 460$  kg), which offers an additional potential to lower approach and departure noise. Conclusively, the usage of a droop nose affects the flight performance, therefore its overall effect on the ground noise is investigated.

The wing's trailing edge is equipped with a brush. The flight conditions during approach feature a high angle of attack and Strouhal numbers of 0.9 at the wing's trailing edge. Accordingly, the noise reduction potential of approximately 3 dB from the reference [214, Fig. 14c right] has been determined. Herr [103, Chap. 4.2.3] provided more details about material and orientation of the brush fibers. Fiber spacing is a crucial parameter. The greatest noise reduction can be achieved by tightly packed and lengthwise oriented fibers. Their noise reduction capability is independent from material flexibility. It is assumed that

such a brush extension increases the wing weight by 0.2% ( $\approx 75$  kg), with the increase being relative to the weight prior to mounting the droop nose. The brush's weight has been estimated for a volume of 60 m span, 8 mm thickness, 98 mm length,  $1690 \frac{\text{kg}}{\text{m}^3}$  ( $92\% \cdot 1150 \frac{\text{kg}}{\text{m}^3}$  density of nylon +  $8\% \cdot 7900 \frac{\text{kg}}{\text{m}^3}$  density of stainless steel), and a packing density of  $\frac{\pi}{4}$  for packed cylinders. The weight of the bracket has been estimated to be an additional 20% of the weight of the brush. The length of the brush fibers corresponds to the estimated boundary layer thickness of 98 mm for a Reynolds number of  $57.4 \cdot 10^6$  with a reference length of 9.5 m.

**Table 7.5:** Airplane data of the low-noise-wing airplane (lnw) compared to the new-engine-option airplane (neo) and reference airplane (ref).

| Airplane                        |        |                     |                     |
|---------------------------------|--------|---------------------|---------------------|
| Variable                        | lnw    | $\Delta$ to neo [%] | $\Delta$ to ref [%] |
| leading-edge sweep [°]          | 40     |                     |                     |
| Wing area [m <sup>2</sup> ]     | 500.0  | 0.00                | -11.02              |
| Aspect ratio [-]                | 7.500  | 0.00                | 4.47                |
| Span [m]                        | 62.63  | 0.00                | -3.48               |
| Max. aircraft length [m]        | 70.71  | 0.00                | -0.11               |
| Max. aircraft height [m]        | 19.82  | 0.00                | -0.60               |
| Design range [km]               | 10602  | 0.00                |                     |
| Cruise Mach [-]                 | 0.833  | 0.00                | -2.04               |
| Cruise altitude [ft]            | 12.36  | 0.00                | -1.44               |
| Lift/Drag [-]                   | 16.01  | -0.06               | -7.35               |
| Max. lift coefficient [-]       | 1.365  | 0.00                | 1.11                |
| Static thrust [N]               | 933224 | 0.00                | -14.39              |
| Engine diameter [m]             | 3.000  | 0.00                | 11.44               |
| Bypass ratio [-]                | 12.000 | 0.00                | 235.00              |
| SFC in cruise [g/N/h]           | 0.050  | 0.02                | -17.04              |
| Max. takeoff weight [kg]        | 348560 | -0.17               | -10.64              |
| Max. landing weight [kg]        | 255181 | -0.19               | -8.06               |
| Operating empty weight [kg]     | 161524 | -0.29               | -9.51               |
| Manufacturer empty mass [kg]    | 145930 | -0.32               | -10.32              |
| Fuselage weight [kg]            | 37812  | -0.03               | -3.89               |
| Wing weight [kg]                | 37826  | -1.09               | -13.92              |
| Fuel mass (design mission) [kg] | 105669 | -0.13               | -17.95              |
| Takeoff distance [m]            | 3091   | 19.21               | 3.86                |
| Takeoff speed $v_2$ [m/s]       | 82.76  | -0.08               | 0.17                |
| Landing field length [m]        | 2095   | -0.17               | 1.42                |
| Landing speed [m/s]             | 69.64  | -0.10               | 1.44                |
| DOC [EURO per seat km]          | 0.051  | -0.06               | -4.49               |

The data of the selected low-noise-wing airplane has been listed in Table 7.5. Its planform parameters correspond to the ones from the selected new-engine-option airplane. The various weights, such as cruise fuel weight, as well as landing and takeoff weight are almost identical with the ones from the selected new-engine-option airplane. The wing mass exhibits the most considerable difference, with a reduction of 1.1%. The maximum takeoff weight and the maximum landing weight are reduced by 0.17% and 0.19%, respectively.

A longer takeoff roll distance is required to lift off with a reduced maximum angle of attack, as shown in Figure 7.16a and listed in Table 7.5. After the cutback point, the low-noise-wing airplane climbs steeper, leading to both airplanes entering the acceleration segment after the same ground track distance to the brake release point. As the low-noise-wing airplane flies faster already at the beginning of the acceleration segment due to the lower maximum lift coefficient, it completes the acceleration segment in both shorter ground track distance and duration.

The approach shown in Figure 7.16b is described in the opposite direction of the flight direction. The final approach segment beyond the stabilization point is flown at faster airspeed by the low-noise-wing airplane, as the maximum lift coefficient is lower compared to the new-engine-option airplane. Moreover, the droop nose causes less drag compared to the Kruger flaps during this final approach segment because the maximum angle of attack is reduced requiring less engine thrust to stabilize. Before the stabilization point, the high-lift devices are set to landing configuration and the landing gear is deployed at a height of 457 m. Due to the reduced drag, the airplane decelerates less. Thus, it has to enter the final approach segment at a slower speed. Consequently, this low-noise-wing airplane starts the horizontal segment earlier to decelerate, bringing the whole cruise configuration segment down by about 30 m. The ground noise generated along these trajectories is investigated in the following paragraphs.

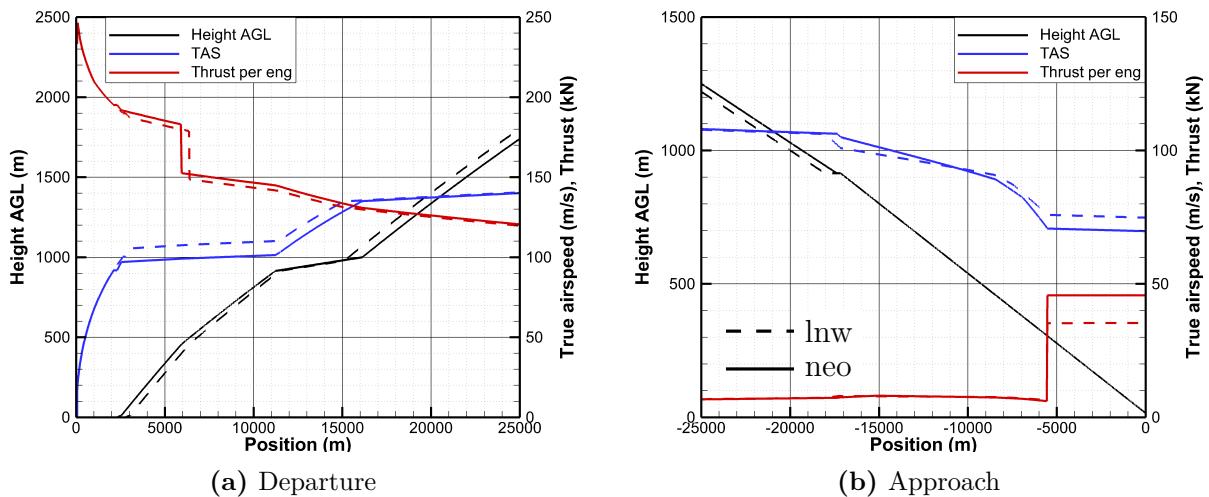


**Figure 7.16:** Departure and approach trajectories of the low-noise-wing airplane and the new-engine-option airplane. The graphs show trajectories, thrusts, and true airspeeds for the two selected designs. Figure 7.16a: Due to the reduced maximum angle of attack, the airplane has to accelerate to faster speeds to lift off. It climbs steeper after cutback. Due to the already faster airspeed, the acceleration segment is kept shorter and, hence, the low-noise-wing airplane joins the last climb segment about one kilometer earlier than the new-engine-option airplane. Figure 7.16b: The deployed droop nose reduces the drag compared to the Kruger flap and, hence, the deceleration along the  $-3^\circ$  final approach segment is lowered. The lower maximum angle of attack leads to an increased speed after the stabilization point but also to less drag and engine thrust.

Figures 7.17 and 7.18 show the approach-induced awakening probability of the low-noise-wing airplane and the distinction in its A-weighted maximum SPLs compared to the new-

engine-option airplane. Especially along the first 12 km, the faster climb of this low-noise-wing airplane leads to louder fan sound due to a higher relative blade tip Mach number and, hence, more ground noise (86) along the ground track. Additionally, the sideline residents within the range of  $1.5\text{ km} \leq y \leq 4.0\text{ km}$  benefit slightly from less jet sound due to the increased takeoff speed. As the low-noise-wing airplane is already faster, the acceleration segment is completed earlier, resulting in the final climb segment being higher. Along this final climb segment, the trailing-edge-induced ground noise becomes more dominant, as the atmosphere increasingly attenuates the fan sound. Since the former new-engine-option airplane caused a high departure-induced awakening probability due to the wing's trailing-edge noise (76), this low-noise-wing airplane greatly benefits (85) from using a brush. Additionally, the residents benefit from the greater height of the airplane.

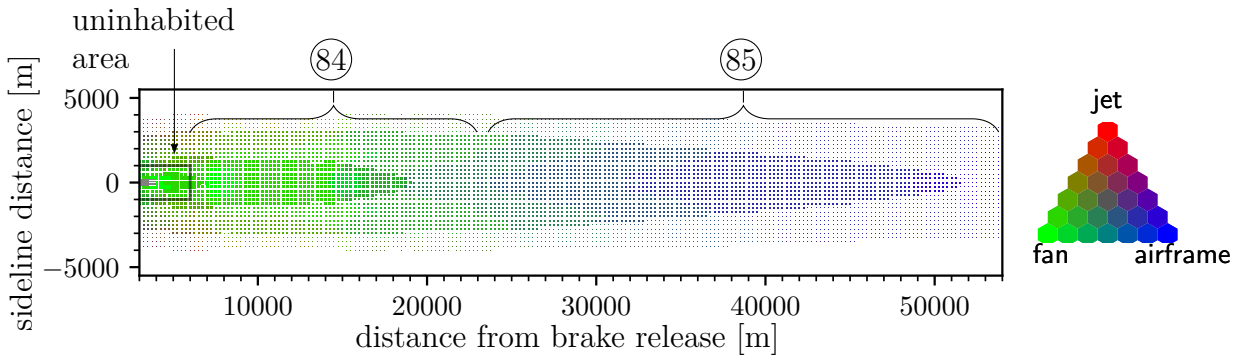


**Figure 7.17:** Dominating noise sources of the low-noise-wing airplane during departure. After the uninhabited area, fan noise becomes more dominant (84) along the ground track, compared to the engine-over-wing airplane. When the airplane reaches greater heights, airframe noise dominates the awakening probability (85). However, this airframe noise is already lower than the one of the new-engine-option airplane.

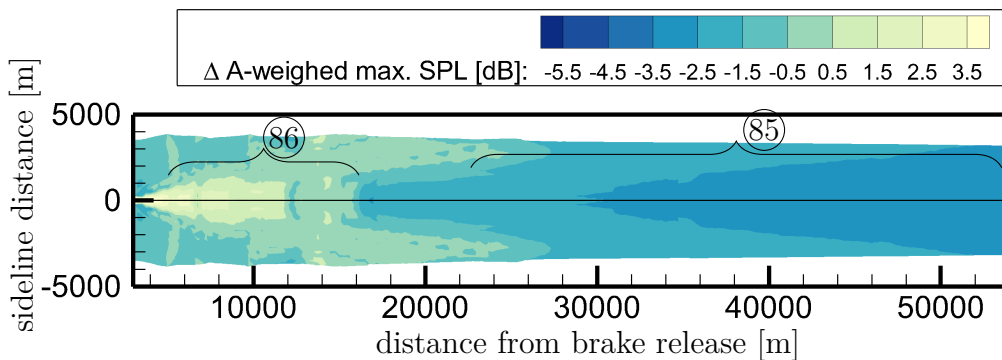


**Figure 7.18:** Difference in the A-weighted maximum SPL during the departure of the low-noise-wing airplane compared to the new-engine-option airplane.

The approach-induced awakening probability and the difference in A-weighted maximum SPL are shown in Figures 7.19 and 7.20. All reductions in ground noise along the section (90) are achieved due to the trailing-edge sound reduction. The Kruger flap sound is eliminated (91) by employing the droop nose, reducing the A-weighted maximum SPL by more than 5.5 dB. Surprisingly, it is not the landing gear noise that becomes more dominant at location

(93), but the flap noise (88). The low-noise-wing airplane sets the flaps to landing configuration 280 m before the new-engine-option airplane because the drag and maximum lift are lowered. Note that the noise increasing towards the sideline of location (93) causes awakenings only within a 2 km stretch, thus, its significance is limited. The ground noise caused by the landing gear is visible in (92). After the stabilization point, the overall sound pressure level is lower. The engine emits less fan sound at a lower engine speed (89). Due to the  $4 \frac{m}{s}$  faster approach speed, the sound emission of the landing gear and the flaps increases. Ultimately, all three sound sources, airframe, engine, and landing gear, contribute approximately equally to the overall A-weighted sound intensity on the ground. Yet, the engine dominates the additional awakening probability of the sideline residents because the shielding functions less effective to the side.

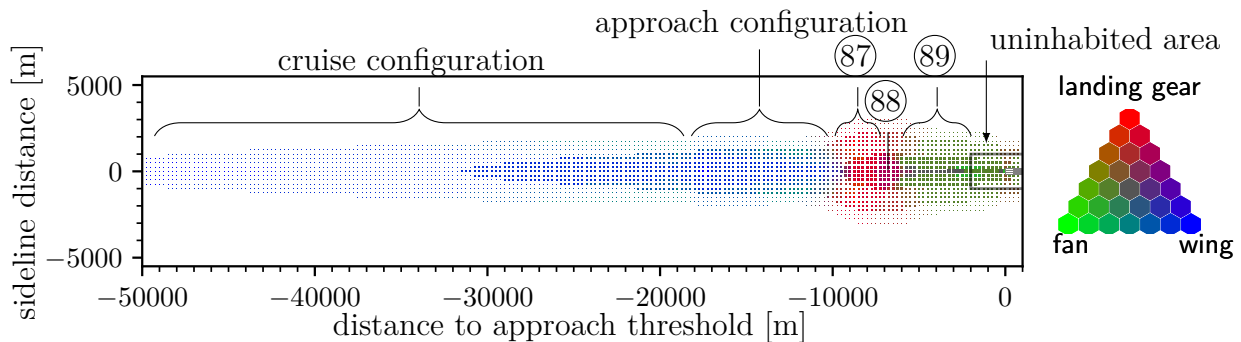


**Figure 7.19:** Dominating noise sources of the low-noise-wing airplane during the approach. Figure A.7.3.35 shows the same approach and its corresponding awakening reactions with colors reflecting the airframe noise sources. The wing trailing edge sound emission has been reduced, and the sound source 'Kruger flap' eliminated. Therefore, in the flight sections in cruise and approach configuration, the fan sound rises sideways and contributes up to 50% of the sound intensity. The fan sound comes to the foreground because the airframe sound has been reduced and the fan sound is shielded less forward to the side. As soon as the landing gear is deployed, it dominates the ground noise (87) until the high-lift devices are set to landing configuration (88). Beyond the stabilization point, the engine dominates the ground noise (89), as it compensates for the drag. In this final approach segment, along the ground track, all three components, landing gear, fan, and wing noise, contribute to the ground noise roughly equally, represented by the gray squares. To the sideline, the area in olive green indicates a mainly fan and landing gear induced awakening probability.

The noise reduction technologies, droop nose and brush, greatly reduced the high-lift device sound sources. The landing gear, as the only remaining unmodified sound source, is to be lowered by means of a landing gear fairing, whose effects will be analyzed in the following section.

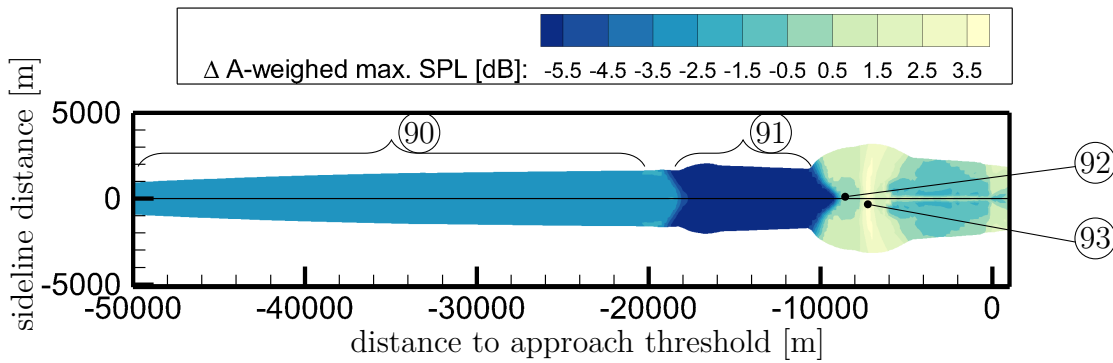


**Figure 7.20:** Difference in the A-weighted maximum SPL during the approach of the low-noise-wing airplane compared to the new-engine-option airplane.

## 7.4 Landing Gear Noise Reduction

As per Figures 7.13 and 7.19, the landing gears make a minor contribution to the awakening probability. The contribution is comparatively small because the landing gear is deployed as late as possible at a height of 457 m. However, landing gears are the remaining unmodified sound sources and become more significant after the other sources have been reduced. For safety reasons, pilots usually deploy landing gears before they absolutely have to, thereby exposing a larger area on ground to landing gear sound than strictly necessary. Therefore, this section focuses on the investigation of the landing gear fairing as a noise reduction technology. Such an airplane has been named landing-gear-fairing airplane (lgf).

A study by Dobrzynski [57] shows that implementing landing gear fairings can reduce the A-weighted SPL by up to 8 dB. This can be achieved at the optimal toe-down bogie angle, which has a considerable impact on the sound generation. A conservative value of 5 dB is subtracted from the sound pressure level, which is calculated by the landing gear noise model, to consider the effect of the fairings. This broadband reduction can be applied because the one-third-octave bands that determine the A-weighted SPL were measured with such a lower value.

Since the fairings redirect the air stream around the struts, tubes, and cables, a landing gear drag reduction of 30 % was determined by Quayle and has been considered in this investigation [173, Fig. 21]. This drag reduction lowers the deceleration capability during approach. However, during the OPENAIR project, a slight increase in landing gear drag was measured for a blocker plate mounted on a landing gear as large as the A320 one [167, fig. 46]. A fairing, such as it could be mounted on this landing gears is depicted in Figure 7.21.

The fairings increase the manufacturer empty mass. This increase in mass is assumed to be +1% of the landing gear mass and is approximately 150 kg. Their effect on the takeoff weight and landing weight is calculated by PrADO.

The addition of fairings to the landing gear has almost no effect on the airplane design and data, as listed in Table 7.6. The most considerable change of  $-1.3\%$  is in the takeoff roll distance. Masses and cost are almost the same, as the planform parameters are the same as for the low-noise-wing airplanes.

As per Figure 7.22a, the departure trajectories, with and without landing gear fairings, are visually identical. The lower drag during acceleration on the runway and the slightly increased landing gear weight have a negligible effect on the trajectory. Hence, the following

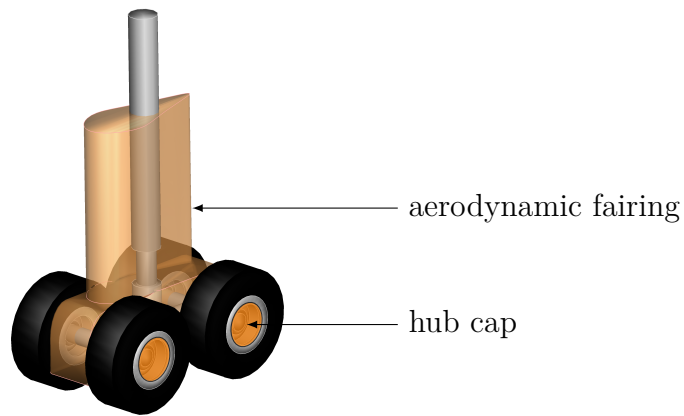


**Figure 7.21:** Landing gear fairing of the landing-gear-fairing airplane. The aerodynamic shape allows minimum drag and, therefore, is expected to minimize the interaction sound source. The hub cap is to lower noise generation in the hub. However, engineers still have to assure brake cooling. Supporting struts and side-says would have to be integrated smartly.

paragraphs focus only on the approach-induced ground noise, and the departure-induced ground noise is not described.

Along the approach trajectory, as shown in Figure 7.22b, the flight speeds are almost identical and the thrust differs only beyond the stabilization point. The approach trajectory is described in opposite direction of flight. From the stabilization point onwards, the engine speed is lower, as the landing gear fairings reduce the airplane's drag. Prior to reaching the stabilization point, the landing gear is deployed and the high-lift devices are set to landing configuration. Since the landing gear creates less drag, the approach speed prior to the landing gear deployment at a height of 457 m can be  $1.25 \frac{\text{m}}{\text{s}}$  slower. Hence, the landing-gear-fairing airplane enters the horizontal deceleration segment slightly earlier, which leads to an insignificant 6.5 m lower cruise configuration segment.

The landing-gear-fairing airplane reduces the approach-induced awakening reactions by 11.4 %, which corresponds to 3.3 % fewer additional overall awakening reactions. This reduction is achieved due to less landing gear noise emission (94) (96) and lower engine noise emission (95) along the final approach segment, as shown in Figures 7.23 and 7.24. The reduction of the landing gear noise after mounting the fairings is obvious. Whereas, the engine noise reduction is achieved due to less landing gear drag, making it possible for the engine to run at a lower engine speed (97). The small increase in ground noise around 18 km before the approach threshold is caused by the slightly earlier start of the horizontal segment, where the high-lift devices have been deflected. This segment cannot be shortened because the airplane would have to fly the cruise configuration segment slower than the 1.3 times the stall speed.

Note that no interaction noise was calculated in these simulations. However, this sound source becomes more dominant as the other sound sources fade. In this case, the landing gears were still mounted under the wing, making the interaction sound source between landing gear and flap likely an issue. However, due to the aerodynamic fairing it is assumed that the interaction noise would also be lower compared to the landing gear without fairings, when the wake is weak.

The following section lists the quietest airplane designs of each technology level for the departure, approach, and a combination thereof.

**Table 7.6:** Airplane data of the landing-gear-fairing airplane (lgf) compared to the low-noise-wing airplane (lnw) and reference airplane (ref).

| Airplane<br>Variable            | lgf    | $\Delta$ to lnw [%] | $\Delta$ to ref [%] |
|---------------------------------|--------|---------------------|---------------------|
| Leading-edge sweep [°]          | 40     |                     |                     |
| Wing area [m <sup>2</sup> ]     | 500.0  | 0.00                | -11.02              |
| Aspect ratio [-]                | 7.500  | 0.00                | 4.47                |
| Span [m]                        | 62.63  | 0.00                | -3.48               |
| Max. aircraft length [m]        | 70.71  | 0.00                | -0.11               |
| Max. aircraft height [m]        | 19.82  | 0.00                | -0.60               |
| Design range [km]               | 10602  | 0.00                |                     |
| Cruise Mach [-]                 | 0.833  | 0.00                | -2.04               |
| Cruise altitude [ft]            | 12.36  | 0.00                | -1.44               |
| Lift/Drag [-]                   | 16.02  | 0.06                | -7.29               |
| Max. lift coefficient [-]       | 1.365  | 0.00                | 1.11                |
| Static thrust [N]               | 933224 | 0.00                | -14.39              |
| Engine diameter [m]             | 3.000  | 0.00                | 11.44               |
| Bypass ratio [-]                | 12.000 | 0.00                | 235.00              |
| SFC in cruise [g/N/h]           | 0.050  | -0.02               | -17.05              |
| Max. takeoff weight [kg]        | 348802 | 0.07                | -10.58              |
| Max. landing weight [kg]        | 255379 | 0.08                | -7.99               |
| Operating empty weight [kg]     | 161709 | 0.11                | -9.41               |
| Manufacturer empty mass [kg]    | 146116 | 0.13                | -10.21              |
| Fuselage weight [kg]            | 37818  | 0.02                | -3.87               |
| Wing weight [kg]                | 37842  | 0.04                | -13.88              |
| Fuel mass (design mission) [kg] | 105722 | 0.05                | -17.91              |
| Takeoff distance [m]            | 3051   | -1.29               | 2.52                |
| Takeoff speed $v_2$ [m/s]       | 82.78  | 0.02                | 0.19                |
| Landing field length [m]        | 2097   | 0.07                | 1.49                |
| Landing speed [m/s]             | 69.67  | 0.04                | 1.49                |
| DOC [EURO per seat km]          | 0.051  | 0.02                | -4.47               |

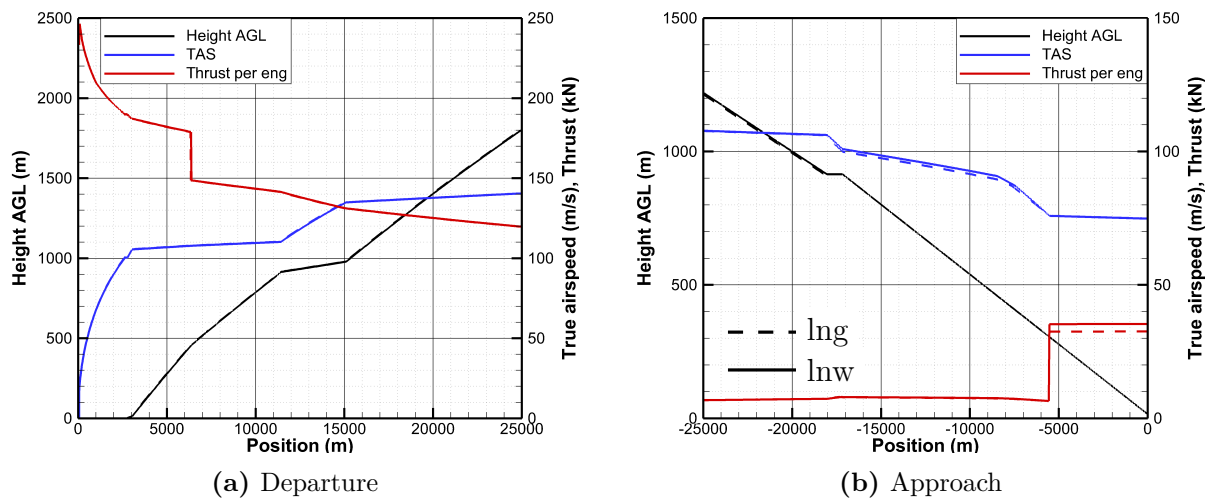


**Figure 7.22:** Departure and approach trajectories of the landing-gear-fairing airplane and the low-noise-wing airplane. The graphs show trajectories, thrusts, and true airspeeds for two selected designs.

Figure 7.22a: The differences in the departure trajectories are negligible.  
 Figure 7.22b: The approach trajectories differ due to the reduced landing gear drag. Hence, the deceleration is lower and the airplane enters the  $-3^\circ$  final approach segment at a lower airspeed.

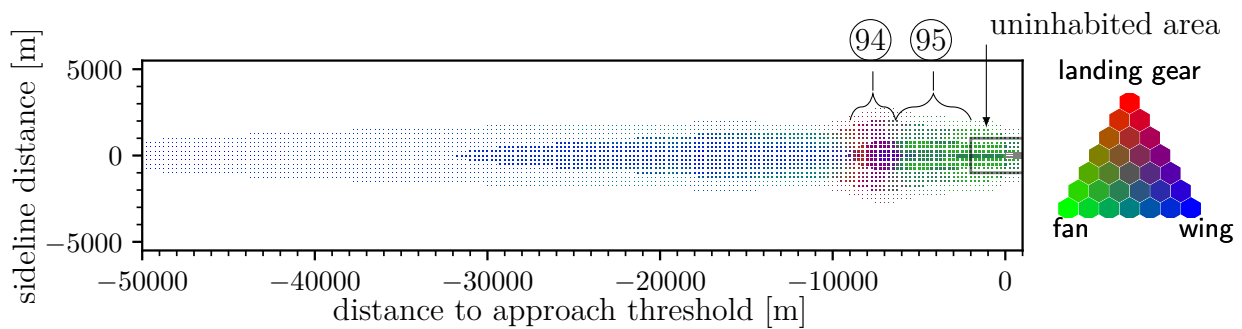


**Figure 7.23:** Dominating noise sources of the landing-gear-fairing airplane during approach. Figure A.7.4.36 shows the same approach and its corresponding awakening probability with colors referencing the airframe noise sources. The main difference is that the bulgy landing gear dominated area from the low-noise-wing airplane (87) turned into a mixture of landing gear and flap noise (94). As the landing gear sound has been reduced by the fairing, the area (95) is dominated more by fan and high-lift device noise.

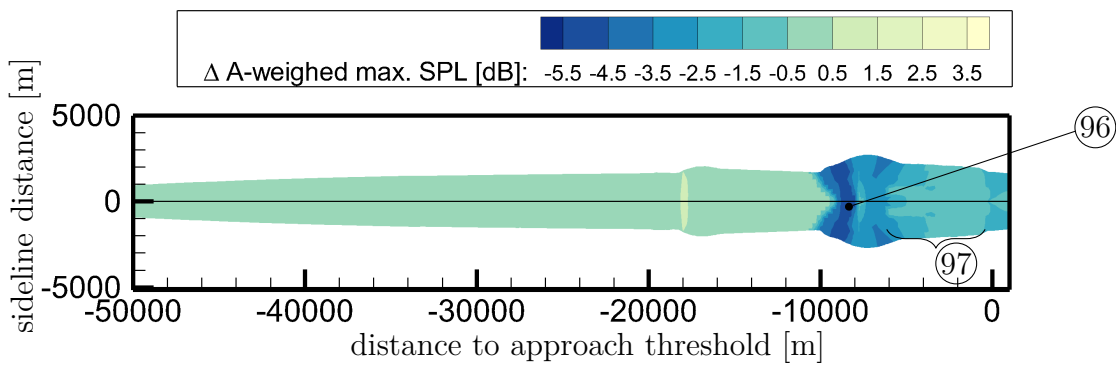


**Figure 7.24:** Difference in the A-weighted maximum SPL during approach of the landing-gear-fairing airplane compared to the low-noise-wing airplane. The landing gear has been deployed at a lower airspeed causing less ground noise at (96). The residents in the area marked by (97) benefit from the reduced required thrust due to the lower landing gear drag.

## 7.5 Quietest Airplane Designs

The previous sections selected the optimal airplane designs by the minimum value of the target function, which is a combination of Awakening Index and Direct Operating Cost Index, and is described in Section 5.4. This section lists the quietest airplanes in Table 7.7, i.e., the airplanes with the respective lowest Awakening Index, without considering their Direct Operating Cost Index. In all cases, the quietest airplanes have been more expensive than the selected ones.

**Table 7.7:** List with the values of the planform parameter for the quietest airplane designs. Each section represents one technology level and each row characterizes one airplane design, which is the quietest one in one of the categories Departure Awakening Index, Approach Awakening Index, or Overall Awakening Index.

| Airplane                      | Low-Noise Category | $\varphi_{LE}$ [°] | $A_W$ [m <sup>2</sup> ] | $\Lambda_W$ [–] | Awak. Index [%] | Awak. Index app. [%] | Awak. Index dep. [%] |
|-------------------------------|--------------------|--------------------|-------------------------|-----------------|-----------------|----------------------|----------------------|
| ref from Chapter 4            | total              | 42                 | 561.93                  | 7.1789          |                 | 0.0                  |                      |
| basic airplane from Chapter 6 | total              | 36                 | 540                     | 9.0             | -3.64           | -2.55                | -3.94                |
|                               | app                | 36                 | 660                     | 8.5             | -1.71           | -18.25               | +2.81                |
|                               | dep                | 36                 | 500                     | 10.0            | -2.71           | +8.81                | -5.85                |
| engine-over-wing airplane     | total              | 28                 | 600                     | 10.5            | -9.54           | -6.84                | -19.42               |
|                               | app                | 18                 | 680                     | 9.5             | -8.19           | -35.70               | -0.68                |
|                               | dep                | 32                 | 500                     | 11.0            | -6.75           | +2.92                | -9.39                |
| new-engine-option airplane    | total              | 30                 | 580                     | 8.5             | -44.88          | -28.97               | -49.22               |
|                               | app                | 20                 | 700                     | 9.5             | -43.28          | -42.23               | -43.57               |
|                               | dep                | 30                 | 500                     | 11.0            | -43.07          | -6.42                | -53.08               |
| low-noise wing                | total              | 30                 | 540                     | 9.0             | -58.06          | -48.12               | -60.77               |
|                               | app                | 20                 | 700                     | 9.5             | -55.99          | -62.02               | -54.34               |
|                               | dep                | 30                 | 500                     | 11.0            | -57.17          | -36.98               | -62.69               |
| landing gear fairing          | total              | 30                 | 540                     | 9.5             | -59.37          | -53.05               | -61.09               |
|                               | app                | 20                 | 700                     | 9.5             | -57.03          | -66.90               | -54.34               |
|                               | dep                | 22                 | 700                     | 9.0             | -57.03          | -66.90               | -54.34               |
|                               |                    | 30                 | 500                     | 11.0            | -58.64          | -43.61               | -62.74               |

For each technology level, one quietest airplane design of each of the following three categories is listed: *total* – overall minimum Awakening Index, *app* – minimum Approach Awakening Index, and *dep* – minimum Departure Awakening Index. These Awakening Indices are listed in the columns, which additionally contain the three design parameters of leading-edge sweep, wing area, and aspect ratio.

In general, the quietest airplanes during approach have a large wing area and a low sweep angle, both of which enable a slower stall speed. Their aspect ratio lies within the range of

8.5 to 9.5. In contrast, during departure, the quietest airplane designs have a smaller wing area and, hence, a higher wing loading. Such airplanes accelerate to faster speed on the runway, which shortens the acceleration segments flown with the cutback thrust and leads to an earlier start of the final climb segments. Additionally, the smaller wing surface saves material, which reduces the takeoff weight. Both, the better averaged climb response and the slower approach speed, lower the Departure and Approach Awakening Indices, respectively.

The values of the planform parameters, which cause the lowest Overall Awakening Indices, are closer to the values that cause the lowest Departure Awakening Indices than to the ones causing the lowest Approach Awakening Indices. That is because the departure causes more awakening reactions than the approach and, hence, dominates the Overall Awakening Index. However, departures are more flexible than approaches in terms of routing and avoiding flying over populated areas. Therefore, it needs to be verified, if the assumed homogeneous population distribution is suitable for the departure noise assessment. Moreover, it is assumed that the population density close to the ground track is lower than further away because the airplanes route around populated area while departing. This would lead to a lower dominance of the Departure Awakening Index in the selection of the airplane design.

## 7.6 Chapter Conclusion

This chapter demonstrated the consecutive application and impact of low-noise technologies mounted on airplanes based on the PrADO model of the B747-400. Table 7.8 summarizes the three Awakening Indices during approach, departure, and overall for all selected airplane designs, i.e., the airplanes selected by the combination of Overall AWI and DOCI.

**Table 7.8:** List with the values of the planform parameters of the selected airplane designs. Each row represents one technology level and shows the respective Awakening Index for approach, departure, and both combined.

| airplane                                | $\varphi_{LE}$<br>[°] | $A_W$<br>[m <sup>2</sup> ] | $\Lambda_W$<br>[-] | Awak. Index<br>[%] | Awak. Index<br>app. [%] | Awak. Index<br>dep. [%] |
|---|-----------------------|----------------------------|--------------------|--------------------|-------------------------|-------------------------|
| reference<br>airplane from<br>Chapter 4 | 42                    | 561.93                     | 7.1789             |                    | 0.0                     |                         |
| basic airplane<br>from Chapter 6        | 36                    | 520                        | 9.0                | -3.26              | +0.48                   | -4.74                   |
| engine-over-wing<br>airplane            | 40                    | 540                        | 9.5                | -6.48              | -7.80                   | -6.12                   |
| new-engine-option<br>airplane           | 40                    | 500                        | 7.5                | -43.82             | -17.14                  | -51.11                  |
| low-noise-wing<br>airplane              | 40                    | 500                        | 7.5                | -55.90             | -44.35                  | -59.05                  |
| landing-gear-f.<br>airplane             | 40                    | 500                        | 7.5                | -57.36             | -50.66                  | -59.19                  |

All technology levels of this chapter reduced both Departure Awakening Index and Approach Awakening Index, and thus the Overall Awakening Index. The only exception was the basic airplane from the previous Chapter 6, which elevated the Approach Awakening Index. Within the approach noise affected area, the faster flight speed partially leads to increased noise generation by other components. This redistributes the awakening probability. Therefore, it should be assessed individually whether it is beneficial to condense most of the ground noise at a small area or to distribute it over a larger area at lower sound pressure levels.

To redistribute the ground noise fairly, a representative population distribution is required. Representative, in this case, means an average population distribution, which has been determined by taking into account the routes, runways, and the population around the airports being served by this airplane type. Moreover, the flight route utilization should be considered in the weighing of the population because some flight routes might be dominated by either smaller or larger airplanes. This is necessary to achieve a population distribution, which can be utilized to equitably assess and rank the airplanes. Obviously, such a population distribution and its corresponding investigation area differs for each airplane size and type because large airplanes do not serve small airports.

The greatest noise reduction achieved by one technology step was by replacing the engine. The greatest reduction in Awakening Indices was observed when all noise-reducing technologies were applied.



## 8 | Discussion

This thesis demonstrates the influence of the three design parameters, wing area, aspect ratio, and leading-edge sweep, when considered collectively along with sequentially applied low-noise technologies to investigate the ground noise at approach and departure. Resulting effects such as changed aerodynamics<sup>1</sup>, structure and fuel masses, flight mechanics<sup>2</sup>, as well as stall speeds<sup>3</sup> have been considered. The main findings obtained through this parameter study are discussed in the following section. It is followed by the Outlook presenting ideas for future research and improvements.

### 8.1 Main Findings

Ground noise has been found to be dependent on both, airplane designs and trajectories [24, 33]. This work focused on achieving a low-noise airplane by utilizing the flight performance along with tailored approach trajectories. Using this investigation method, a slow approach speed and a high averaged climb response have been identified as the characteristics responsible for rendering an airplane design into a low-noise one.

The terms *low noise* and *quiet* mean, according to the target function, less additional awakening reactions in total. This is an important note because for some residents the respective noise level became louder. However, when measuring in awakening reactions, the ground noise became less.

A low-noise approach and a low-noise departure is determined by different criteria. Thus, an airplane design favorable for a low-noise approach might be disadvantageous for the departure-induced ground noise. The values of the planform parameters, which result in a low-noise airplane at approach, differ from the ones responsible for a low-noise airplane at the departure.

#### Approach Speed

The approach speed in cruise configuration is highly associated with the ground noise during approach. Since the minimum speed is usually a multiple of the stall speed, the finding of Crichton et al. [47, p. 2], who stated that noise is strongly correlated with stall speed, can be confirmed. However, the dependency of the stall speed on the approach-induced ground noise can be more accurately defined as a dependency on approach speed, as evident from Figure A.6.2.6 in combination with Figure 6.6. The findings from Figure 6.6, in which the approach velocity and the Approach Awakening Index rose without an increasing stall

---

<sup>1</sup>Influenced by sweep, wetted area, shock induced drag by over-the-wing mounted engines

<sup>2</sup>Size and mass of the horizontal and the vertical stabilizer, respectively

<sup>3</sup>Individual stall speed at cruise, approach, landing, and departure configuration, respectively, for each airplane design

speed, necessitate this rather more precise formulation of the approach speed. An airplane with a high drag (low glide ratio) in approach configuration decelerates so much along the final approach segment that it might require an approach velocity faster than  $1.3 \cdot v_{\text{stall,gse}}$ . Remember that acceleration is prohibited during the low drag minimum power approach, and therefore the airplane has to be in approach configuration along the final approach segment. A faster approach velocity increases the sound generation when high-lift devices are deployed. Additionally, a high drag necessitates more engine thrust beyond the stabilization point, which results in louder engine ground noise. A slower approach speed results in three advantageous properties: a quieter approach in cruise configuration; a later high-lift device deployment; and a lower sound generation when high-lift devices are deployed. A slower approach speed is achieved by reducing the airplane weight and increasing the wing area, which lower the wing loading as well as increase its maximum lift.

### **Averaged Climb Response**

Along the departure, the airplane design with the highest averaged climb response is also the quietest one. This averaged climb response encompasses required takeoff runway length, climb performance, and acceleration performance. The performance along the respective sections is promoted by high glide ratio and low mass. A small wing area causes high liftoff speeds. Hence, the airplane accelerates to higher velocities on the runway. This is done at the comparatively higher takeoff thrust, thus at a shorter distance compared to an acceleration along the acceleration segment. Hence, the acceleration segment, which is flown at the lower cutback thrust setting, is kept shorter, as it always ends at  $130 \frac{\text{m}}{\text{s}}$ . Crichton et al. [47, p. 2] found that the stall speed serves as the driving criterion for ground noise at the takeoff certification point. Thus, the sound pressure level at this certification point seems to be not representative for a large area affected by noise during takeoff. Conclusively, airplane designers should consider the ground noise pollution distributed over a larger area instead of the certification points, when they design airplanes with low ground noise in the benefit of the residents.

### **Why Design Criteria Differ Compared to Previously Published Results**

Hileman et al. [104] found in their study that airplanes with a small leading-edge sweep angle and a large wing area were quieter and that airplanes with a large sweep angle and a small wing area, which were also more fuel efficient, were noisier. This result can be understood to the extent that the researchers only studied the noise at the certification points. Due the constant takeoff weight in their study, the airplanes having a large wing area are higher above the departure certification point, and thus quieter. However, this study came to a different conclusion. This is mainly because an entire populated area was considered in the noise assessment, and the impacts of airplane design on the takeoff weight. This discrepancy in results also emphasizes how important the target function and the methods are, by which low-noise airplanes are determined. It will also become clear from the remainder of this discussion that even this study is still far from the optimal metric for fairly selecting airplanes.

### **Design Criteria**

To ensure the airplanes of any study are comparable, it is good to only keep the payload and the design range constant because these two criteria are among the most important

criteria for airlines. In addition, costs play a very important role. The time, i.e., also the travel duration and thus the cruising speed, are included in the cost. Therefore, it has been proven to be very useful to examine the airplanes in terms of cost. However, if other factors, such as the planform, were held constant, then this constraint would hinder innovation because the airplanes may be built more efficiently with a different planform. This can be derived from Tables 7.7 and 7.8, which show that the planform changed along with the technology level. Higher efficiency reduces fuel consumption, thus lowering weight and ground noise during takeoff. Particularly with respect to ground noise studies, it has been shown that a modified wing planform can serve better altered flight characteristics due to new technologies. Therefore, when retrofitting low-noise technologies into existing airplanes, the wing's location and shape should be optimized to serve the new requirements. Furthermore, takeoff weight has a strong impact on the ground noise during departure, and should not be held constant when investigating ground noise.

In this study, the position of the wing's aerodynamic center has been kept constant. In retrospect, this turned out to be disadvantageous, since the stability margin is different for each airplane. It is favorable to keep the stability margin constant in the future investigations when comparing airplanes. The stability margin affects airplane noise in two ways: first, through fuel consumption, and thus takeoff weight. The more aerodynamic stable airplanes are, the more fuel they require, and thus are heavier and noisier. Second, the downforce of the horizontal stabilizer reduces the lift of the airplane. Therefore, an airplane whose horizontal stabilizer generates more downforce must approach faster. However, as described earlier, approach speed correlates with ground noise. Hence, a more appropriate parameter than the position of the wing's aerodynamic center must be selected here. This parameter could be the static margin or the static margin divided by the aerodynamic mean chord.

### **Wing Planform Optimization Needed**

For the low-noise-wing and landing-gear-fairing technology levels, the planform of the respective optimal airplane remained constant. However, this could have been caused by the limited range of parameter values. These airplanes with the aforementioned technology levels have the highest investigated sweep angle, the lowest aspect ratio, and the smallest wing area. Hence, further investigation is needed to verify whether the design parameter values found are the optimal ones.

### **Why an Open Descent Approach Procedure is Needed**

This paragraph compares the low drag minimum power procedure with a continuous descent approach one. The focus is put on the ranking of the airplanes that fly along both procedures, when the available airplanes have distinct flight performance. The low drag minimum power procedure utilizes the individual flight performance of each airplane to minimize its ground noise. This is achieved by approaching at the slowest allowed speed of  $1.3 \cdot v_{\text{stall}}$ . Along the first descent section the speed is maintained by adjusting the pitch angle accordingly, which is called open descent. If the slope of the cruise configuration descent segment would be set to a fixed slope, then each airplane design would either accelerate or decelerate along this segment. Accelerating airplanes would deploy their high-lift devices earlier than decelerating airplanes to avoid acceleration. Decelerating airplanes would have to enter this segment at faster speeds than  $1.3 \cdot v_{\text{stall}}$ . Alternatively, more engine speed would be required to avoid deceleration or earlier deployment of high-lift devices. These three options contribute to more ground noise, making an airplane that approaches in cruise

configuration and has the engine speed set close to idle to one of the quietest ones. The segment slope defines the optimal effective glide ratio, which is required to fly the segment in cruise configuration and with the engine at idle. A trajectory with a fixed angle would limit the choice of airplanes from the beginning. This would be a kind of pre-selection. Therefore, an open descent is required to utilize individual flight characteristics. The low drag minimum power procedure features an open descent at the minimum allowed speed. Thus, other airplanes than the quietest one flying the continuous descent approach procedure might approach even with less awakening reactions.

## Requirements for an Open Descent Approach Procedure

Note that the low drag minimum power procedure can only be flown by pilots as precisely as required with the assistance of a flight computer. Hence, it is more suitable for future flight operations when airplanes are even more automated. Oppermann [160] provided a basis called Low Noise Augmentation System (LNAS) [1, 2, 193], currently under development at DLR and in a test phase on Lufthansa's A320 airplanes. This LNAS enables pilots to fly as required to approach with the minimum noise emission, while considering the present (weather) conditions.

## PANAM Validated for a Large and Long-Haul Airplane

In Chapter 4, PANAM has been successfully validated using B747-400 flyover measurements. Furthermore, the noise models are parametric and PANAM has also been validated for the mid-sized A319 airplane [24]. Therefore, PANAM can predict the ground noise of intermediate sized airplanes as well. Nevertheless, the fan noise model and the liner model should be checked again. If the update turns out as expected, PANAM would underestimate the noise by about 4 dB.

However, attention has to be paid to the range of validity of the noise models. In particular, the trailing-edge noise model for the wing in cruise configuration should be mentioned here. This model is valid up to a lift coefficient of  $C_L = 0.5$  according to the reference Lockard and Lilly [143, Section 5.2]. Yet, along the approach segment in cruise configuration, the airplanes have a lift coefficient of  $C_L \approx 0.7$ . Therefore, this model is no longer valid here. Unfortunately, trailing-edge noise is expected to become louder than predicted when the lift coefficient increases above the upper validity limit. This means that the trailing-edge noise in cruise configuration has been under-predicted in this investigation. Consequently, there is a need to upgrade PANAM with a clean-wing trailing-edge noise model that is valid for lift coefficients larger than  $C_L = 0.5$ . The main findings in this work are in all likelihood not affected by this issue, since a slow approach speed causes a quiet approach because the high-lift devices are deployed later and at lower speeds. These high-lift devices cause a majority of the awakening reactions during approach. However, louder trailing-edge noise in cruise configuration would raise the importance of the cruise configuration approach segment. The takeoff noise prediction is only affected along a short section of the acceleration segment.

## Round-The-Clock Flight Operation

The noise reduction, which has been achieved through the application of all noise-reducing technologies, supports to an around-the-clock flight operation. The achieved noise reduction, however, does not permit an unconstrained one. Applying the noise-reducing technologies lowers the additional awakening reactions caused by the approach to a narrow strip, which

bulges close to the airport, see Figure 7.23. When the population around an airport lives outside of the noise affected area, then an all-night landing could be permitted. As smaller the noise-affected area, as more likely this is. Obviously, this would have to be individually permitted for each airport by considering the local population distribution. The departure-induced awakenings are so widespread that allowing departures throughout the night presents a bigger challenge.

### **Improving the Low Drag Minimum Power Approach Procedure**

Blinstrub mentioned that a late high-lift device deployment decreases the ground noise [33, p. 105], which has been supported by preliminary studies within this thesis. He concluded that a consideration of a  $-3^\circ$  continuous descent approach and a  $-4.5^\circ$  modified continuous descent approach are sufficient when assessing low-noise airplane designs, if approach trajectories cannot be investigated in parameter studies [33, p. 107]. Additionally, he suggested performing parameter studies, if the simulation capacities are available. The study in Figure 5.5 found that the ground noise can be reduced by flying the low drag minimum power approach procedure. An additional advantage is that parameter studies of approach trajectories can be avoided. This procedure delivers a tailored approach trajectory for each flight performance. However, accumulated experience with this procedure suggests that there is further need for improvement on the following points:

- can acceleration be allowed on the final approach segment to extend the high-lift devices even later?
- can the height of entry into the final approach segment be adjusted according to the aerodynamics of the airplane?
- is it possible to fly with a slightly higher idle thrust along the final approach segment when necessary?

A positive answer to any of these questions contributes to later high-lift device deployment, and therefore to less noise pollution at approach.

### **Implications for the Engine Map**

These findings from the low drag minimum power approach lead directly to yet another awareness. The engine map must not only provide particularly reliable data in the range around the design operating condition, but also close to idle thrust setting. For the purposes of this study, it is assumed that the engine map provides reliable data. Yet, manageable doubts arose with regard to the quality of the UHBR engine data. The mass flow through the UHBR engine has almost doubled, while the inlet area increased by 25% compared to the CF6-80 engine. The respective quality assurance is required.

## **8.2 Outlook**

### **Environmental Impact**

In recent years, the environmental impact, such as the carbon dioxide emission, is one of the most prominent global issues attracting researchers' attention. Instead of assessing the airplanes by their carbon dioxide emission, this study uses direct operating cost, which include fuel consumption as well as other factors. The fuel consumption is approximately

proportional to the carbon dioxide emissions. Fuel combustion also generates nitric oxides and water. The emission of nitric oxides and water [75] at different flight heights impacts the climate differently [49, 82]. Hence, more variables are suggested when optimizing the airplanes with a focus on environmental impact. Due to limited simulation capacity, these variables have been omitted from this parameter study and should be considered in future optimizations.

## Lightweight Materials

All investigated airplanes feature the same technology level in terms of materials employed<sup>4</sup>. More noise reduction might be feasible by applying lightweight materials to reduce the airplane weight. This could further lower the ground noise as it further improves the airplane's averaged climb response at departure and its wing loading or the sound source length, i.e, the trailing-edge length, at approach.

## Additional Parameters

Future scopes of investigations of low-noise airplanes can include additional parameters such as (1) the variety of the population density distribution, (2) the average airplane payload factor, and (3) the study of different departure procedures. These three parameters have been omitted from the current analyses but are discussed in the following paragraphs.

### 1. Population Distribution

The present research has considered a homogeneous population density, which is not a true representation in reality. However, for a meaningful evaluation of low-noise airplanes, a generic population density distribution representing the world's airports is needed. Consideration should be given to the population density distributions residing in the vicinity of airports served by the particular airplane type and affected by the particular routes used by that airplane type. This requires one population distribution per aircraft type. Since the population density distribution, multiplied by the area element and the respective awakening probability, results in the additional awakening reactions, the population density distribution serves as a critical factor in airplane and trajectory evaluations. This leads to the following interesting question: How does the population distribution around an airport influence the selection of the airplane? Departure induces most of the awakenings and, hence, dominates the ranking of the airplanes. However, throughout the departure, airplanes fly around cities and towns to reduce the noise pollution of the residents. This has been omitted from this thesis, due to the assumption of a homogeneous population distribution. However, flying around cities leads to fewer additional awakening reactions triggered by departure and, thus, to a greater weighing of the approach-induced ground noise in the Awakening Index. Consequently, the question arises, what would a representative population density distribution look like when the served airports and flight routes were considered?

---

<sup>4</sup>One exception is the droop nose.

## 2. Payload Factor

Almost all takeoffs by actual airplanes are conducted lighter than the maximum takeoff weight. 50 % of all B747-400 flights are performed at a takeoff weight that is roughly 60 t or more below the maximum takeoff weight [126, Fig. A-1]. This means that 50 % of all flights are conducted more than 12% lighter than maximum takeoff weight. In this thesis, all flights have been simulated at maximum takeoff weight to represent the worst-case scenario. Maximum takeoff weight results from a 100 % payload factor and a flight over the entire design range. However, it is assumed that the payload factor influences the ranking of the airplanes. The higher the quotient of maximum payload to operating weight, the more the departure-induced ground noise benefits from a lower payload factor. This is because for each airplane design, this quotient differs, as the payload is kept constant and the operating weight differs. With respect to the reference airplane, a 20 % reduction in payload implies a decrease in takeoff weight (TOW) of 3.45 %. With the same change in payload mass, the takeoff weight of the low-noise-wing airplane lowers by 3.86 %. Both estimates have to additionally consider the influence on the fuel mass, which amplifies these effects. When lightweight materials are applied, the quotient of maximum payload to operating weight becomes even higher and, thus this effect becomes more significant. This leads to the question: Does the design of the quietest airplane change when the payload factor changes? If the simulated payload factor affects the optimal design of the airplane, it leads directly to the question: When analyzing low-noise airplanes, which payload factor should be considered?

## 3. Departure Procedure

- (a) It has been demonstrated that departure procedures with both less and more awakening reactions than caused by the ICAO-A one exist. Yet, it is still unknown which departure procedure should be simulated when determining the quietest or optimal airplane design out of many. It is assumed that the departure procedure has no effect on the ranking of the airplanes by their Departure Awakening Index. The reason for that is the assumption that the ranking of the airplanes by their acceleration and climb performance is assumed to be independent of the thrust setting. The engine speed setting is equal for each airplane at departure. It is assumed that those airplanes, which climb steeper and accelerate faster at one engine speed setting, will also climb steeper and accelerate faster at other engine speed settings. However, the investigated departure procedure has caused about three-quarter of the additional overall awakening reactions. Therefore, it has a great impact on the Overall Awakening Index and the corresponding ranking of the airplanes. Quieter departures due to another procedure lead to a stronger weighing of the approach, and vice versa for louder departures. Thus, a different departure procedure leads to a different ranking of the airplanes. This leads to the question: Which departure procedure should be employed when investigating a low-noise airplane?
- (b) Another aspect is that the airplanes, which accelerate to a higher speed on the runway, also have a steeper climb. The quietest airplane may be light, but it is not the lightest. It is concluded that even the lift-off speed should be included when optimizing the takeoff flight procedure. This is because even the lift-off speed is expected to change the optimal airplane design. When the airplanes climb steeper at a higher speed,

thereby lowering the takeoff-induced ground noise, then this also leads to a greater weighing of the approach-induced awakening reactions in the ranking of the airplanes.

### **New Noise Assessment Metrics are Needed**

An ongoing research project called SIAM, commenced in July 2020, is at work to upgrade the currently recognized Awakening Criterion. The Awakening Index has been derived from the current Awakening Criterion [18]. The utilized Awakening Criterion is based on the A-weighted maximum sound pressure level. It misses criteria, such as the event's sound volume rise rate and duration. More convenient metrics are yet to be developed. The already tested area sizes of the 70 dB, 80 dB, 85 dB, and 90 dB sound exposure level contours, have been proven to be non-productive. They lack the consideration of lower and higher noise levels that also affect the residents of the area under investigation. During preliminary studies, the same set of airplanes has been differently ranked by the 79 dB and the 80 dB sound exposure level contour area criterion. This happened because along a fixed-slope descent trajectory the airplane decelerated and, hence, its sound generation became quieter while reducing the distance to the ground. The 79 dB sound exposure level contour was triggered, but not the 80 dB contour. One airplane, which was best in the ranking by the 80 dB contour area, was poorly ranked by the 79 dB contour area. The A-weighted maximum sound pressure level of about 64 dB and 65 dB causes these sound exposure level contours. Such a difference of 1 dB is the threshold of noticing a difference in the loudness and, hence, should result in the same rank order.

To cope with this inability to adequately rank the airplanes, the area under investigation has been integrated: at first, the area elements were weighed by the sound exposure level; subsequently, these weighed area elements have been integrated. A factor of 2 per 10 dB corresponding to human hearing sensation and a factor of 10 per 10 dB associated with sound intensity have been applied. For example, a lower threshold of 70 dB sound exposure level has been set. The size of an area element has been weighed with a factor of 2, if the sound exposure level has been 10 dB above the lower threshold and with 4 for 20 dB above the lower threshold. These weighed areas have been integrated and the result is an imaginary area, which grows exponentially with the increasing sound pressure level. Such imaginary areas have been used to rank the airplanes. Ranking the airplanes by the Awakening Index leads to a ranking comparable to one using the aforementioned weighing of the area elements with a factor of 2 per 10 dB. Lacking other options, the Awakening Criterion has been selected and employed in the end. Conclusively, these examples of the ranking by the sound exposure level contour area and the weighing by the imaginary area indicate the need to develop an airplane noise assessment method that ranks the airplanes beneficial to the residents around airports.

### **UHBR Engines in the Under-Wing Position**

Mounting the engines over the wing leads to less noise reduction than expected because the takeoff weight increases due to the greater fuel consumption. Instead, replacing the engine with an ultra-high bypass ratio engine drastically reduces the Awakening Index. Hence, the noise reduction capability achieved by mounting the ultra-high bypass ratio engine in the forward-under-wing position should be investigated in further studies. Such a location could offer advantages in terms of fuel consumption and maintenance. In case of the B747-400, this engine location under the wing would result in necessary modifications of the landing gear length and even its location.

## **Beneficial Locations for Over-The-Wing Mounted Engines**

It has to be noted that the engine location in this thesis has been determined from an optimal fan sound shielding. However, studies also found favorable engine-over-wing locations, which reduce the fuel consumption. These locations are assumed to shield less fan sound. Yet, this study has not investigated such an engine-over-wing position due to the focus on the engine position, which causes the least additional awakening reactions: a location mid over the wing. The engine integration is such a complex task that no conclusion can be drawn here. There are still too few studies which have focused on the combination of noise-reducing and fuel-saving engine positions. Therefore, more research is needed to investigate this interesting topic.

## **Propeller and Open-Rotor**

Propeller engines can have advantages in terms of environmental impact. These advantages apply in particular to cruise Mach numbers below 0.85 [195, Fig. 2]. Once lower cruise Mach numbers are acceptable, propellers may become interesting. The lower fuel mass can have a positive effect on ground noise, especially during takeoff. However, the propellers must be built as quietly as possible to reduce noise pollution for the population. In addition, today's propellers are known to emit a very dominant tonal sound, which can be very annoying. Low-frequency sound is also transmitted better into the interior of the building, which is negative for undisturbed sleep. Therefore, future research on propeller airplanes must always consider the protection of the public.

## **Requirements for the Maximum Benefit of the Low Drag Minimum Power Procedure**

The applied low drag minimum power procedure utilizes slowest feasible flight speeds of the airplanes to reduce their ground noise. Slowest possible approach speeds might disturb the distance of stagger, which has been planned by flight control [10]. To successfully combine the staggering and the slowest feasible approach speed, a foresighted planning is necessary. Such planning would have to be computer-aided. Presuming that detailed (weather) data is available, a computer-aided flight control could stagger airplanes hours before landing by adjusting their cruise speeds accordingly. Such foresighted planning would help airplanes to maintain the required distance from each other. This would continue to ensure a high utilization of the runways, although the airplanes approach at their individual low-noise approach speeds.

## **Increasing Height of the Approach**

If drag can be generated quietly without reducing lift, then the approach can be conducted steeper. This would make the approach higher, but still be performed slowly. Such device could be similar to spoilers on a glider<sup>5</sup>, or they could be short-chorded slats, such as of a louver<sup>6</sup>, that extend vertically out of the wing, forming a sort of biplane or multi-plane.

---

<sup>5</sup>Idea originally by Jan Delfs, Sep. 19<sup>th</sup>, 2019

<sup>6</sup>Idea originally by Georg Koppenwallner, Feb. 06<sup>th</sup>, 2021

## **Validation of the Drag Data**

Drag data by Fujino, originally determined for business sized airplanes, were utilized to estimate the effect of over-the-wing mounted engines. The applicability of these models to large airplanes has not been proven yet, and therefore some validation is required. The aerodynamics could be validated using CFD simulations. However, note that only using fast simulations enable large parameter studies. Hence, CFD can be only used for validation, but not implemented in parameter studies.

## **General View on the Results**

This discussion has listed many open questions in the research community. Some of them have implications for other aspects and open further queries. Worth mentioning here are how lightweight materials affect aircraft noise, and how it upgrades the importance of correct payload utilization. Staggering of the airplanes for landing can be the origin of another chain effect. If staggering can happen hours before landing, both the population affected by the noise of a holding pattern and the environment would benefit. Cost can also be reduced.

To summarize, low-noise aircraft design is very complex. Therefore, holistic approaches are needed that take as many effects as possible into account. At the same time, the number of parameters that are simultaneously varied and studied must be kept low to keep computation times at an acceptable level. Therefore, further studies are necessary to better understand the dependencies between aircraft noise and aircraft design. The varied parameters can be reduced by making a smart pre-selection of parameter values with appropriate prior knowledge.

## 9 | Conclusion

A four-dimensional parameter study has been performed to lower the ground noise of large four-engine airplanes. The three planform parameters create the first three dimensions: leading-edge sweep, wing area, and aspect ratio. The low-noise technologies that are sequentially implemented span the fourth dimension. These low-noise technologies include fan sound shielding, ultra-high bypass ratio engine, droop nose, trailing-edge brush, and landing gear fairings. The airplanes are based on the PrADO model of the B747-400, which is the reference airplane. The awakening reactions caused by this reference airplane form the reference for the whole investigation and constitute the basis of the Awakening Index.

The main research question inquired about the potential of noise reduction both with and without low-noise technologies of large tube-and-wing airplanes. Omitting noise reducing technologies, but rearranging the planform, already saved 3.6% additional awakening reactions. Applying all investigated noise-reducing technologies reduces the awakening reactions more significantly. The additional awakening reactions have been reduced by 57.4% for the selected optimal airplane compared to the reference. If higher cost and a higher fuel consumption are acceptable, a reduction by up to 59.4% is possible.

As each noise reduction technology yields a different flight performance, one research sub-question addressed: What are the effects of selected and sequentially applied low-noise technologies on the ground noise?

Table 9.1 lists the reduction of additional awakening reactions relative to the respective previous technology level.

**Table 9.1:** List of the reduction of additional awakening reactions for the selected airplane designs relative to the previous technology level, i.e., the respective row above. Each row represents one technology level.

| technology level / respective optimal airplane | reduction in total awakenings compared to the respective previous technology level [%] |
|--|--|
| reference airplane (ref)                       |  |
| basic airplane (basic)                         | -3.26  |
| engine-over-wing airplane (eow)                | -3.32  |
| new-engine-option airplane (neo)               | -39.92   |
| low-noise-wing airplane (lnw)                  | -21.50   |
| landing-gear-fairing airplane (lgf)            | -3.31  |

The greatest effect has been achieved by replacing the CF6-80 engine with the ultra-high bypass ratio one, which radically lowered the additional awakening reactions by almost 40%

compared to the engine-over-wing airplane. Also, the use of a droop nose eliminated leading-edge sound and of a brush lowered the wing's trailing-edge sound, which significantly lowered the additional awakening reactions by 21.5% compared to the new-engine-option airplane. Additionally, a changed flight performance reduced the ground noise at departure. Each technology level lowered the overall awakening reactions. This also applies to the Approach and Departure Awakening Indices, with the exception that the basic airplane caused more awakening reactions during approach than the reference airplane to facilitate even less additional awakening reactions during departure. It should also be noted that the A-weighted maximum sound pressure level is increased compared to the respective previous technology level at some locations. Thus, the ground noise has been redistributed. Conclusively, each low-noise technology has more advantages than disadvantages in terms of ground noise pollution for a homogeneously distributed population.

The reductions of the awakening reactions, as listed in Table 9.1, are only valid for the given order of the low-noise technologies, as the reduction in ground noise depends on the dominance of the respective sound source. Additionally, these reductions are only valid for the selected airplanes, as they also depend on the flight performance, which, in turn, is influenced by each low-noise technology. The optimal airplanes may already differ at another target function, resulting in a difference in the noise reduction potential.

This leads to the very interesting question: What are the consequences of the sequentially applied low-noise technologies to the airplane design? The planform of the five respective quietest airplanes of each technology level varies. Each mounted technology changes the flight performance, which could be optimized by a modified planform. Additionally, when investigating the basic airplanes, which are the variants without mounted low-noise technologies, the quietest five percent of these airplanes form a region, which extends across the remaining three-dimensional space. If one parameter value is lowered, the others should be adjusted. The decrease and increase of each design parameter value has respective advantages and disadvantages to the additional awakening reactions. Hence, a comprehensive consideration of all design parameters is required while finding low-noise airplanes. Instead of a parameter study, an optimization is suggested to find low-noise and cost-efficient airplanes.

However, which features identify an airplane as low noise, and how does altering the planform parameters contribute to that? Both the approach speed and the ground track length up to a flight height of 1200 m have been established to correlate the most with the Approach and Departure Awakening Index, respectively. Therefore, to design low-noise airplanes, these two features are the most significant ones. All design parameters contribute collectively to achieve these characteristics, rather than having an independent impact. However, the planform parameters for low-noise airplanes at the departure differ from those at the approach. Thus, a compromise is required to obtain an airplane that is optimal for both departure and approach. Note that the noise reduction capability during the approach also depends on the flight procedure, which is supposed to utilize the airplanes' low-noise flight features.

Further, answering the research questions in this thesis lead to many new research questions. First of all, the influences of various parameters are still unknown, such as the population distribution, the loading factor, or the departure procedure. Moreover, the evaluation metric opens further research potential.

In addition to these research questions, PANAM proved to be suitable for predicting noise for large, long-range airplanes such as the B747-400, in addition to mid-size airplanes.

# Index

- DOC, 52
- airplane
  - reference, 28–32
  - selection, *see* target function
- approach, 66
  - low drag minimum power, 56–57
  - procedure, 56–60
- aspect ratio, 70
- averaged climb response, 54, 62
- awakening probability, 51, 81
- awakening reaction, 51
- cda, 57
- climb response, 62
- cut-off, 14, 47
- density
  - air, 54
- departure, 62
  - procedure, 54
- deployment
  - high-lift devices, 56
  - landing gear, 56
- design
  - mission, 60
  - range, 60
  - speed, 60
- drag
  - over-the-wing engine, 93
- engine
  - over-the-wing drag, 93
- event, 35
- fan
  - sound source, 13
- final approach segment, 56
- flap
  - side edge, 10
- ground track length, 62
- high-lift device
  - deployment, 56
- humidity
  - in simulations, 54
- installation effects
  - sound source, 16
- jet
  - sound source, 15
- landing gear
  - deployment, 56
  - sound source, 11
- low drag minimum power, 56–57
- measurements
  - Parchim, 33–36
- pressure
  - in simulations, 54
- procedure
  - approach, 56–60
  - departure, 54
- range
  - design, 60
  - ferry flight, 30
- reference
  - approach, 56–60
- runway reference point
  - measurement campaign, 34
  - parameter study, 62
- shielding, 24
- sound source
  - fan, 13
  - flap side edge, 10
  - high-lift devices, 9
  - installation effects, 16
  - jet, 15
  - landing gear, 11

- splitting, 24
- speed
  - approach, 57
  - design, 60
  - stall, 57
- stabilization height, 56
- stabilization point, 56
- sweep, 76
  
- target function, 53
- temperature
  - in simulations, 54
  
- wake-up response, 51
- weather conditions
  - simulation, 54
- wind
  - in simulations, 54
- wing area, 73

# Bibliography

- [1] Abdelmoula, F. and Scholz, M. “LNAS - A Pilot Assistance System for Low-Noise Approaches with Minimal Fuel Consumption”. In: *31st Congress of the International Council of the Aeronautical Sciences (ICAS 2018)*. Belo Horizonte, Brazil, Sept. 2018, pp. 1–14. URL: <https://elib.dlr.de/122229/>.
- [2] Abdelmoula, F., Scholz, M., and Kühne, C. G. *Erprobung und Bewertung des Low Noise Augmentation System (LNAS)*. Tech. rep. DLR-IB-FT-BS-2017-15. Braunschweig: German Aerospace Center (DLR), Jan. 2017, pp. 1–90. URL: <https://elib.dlr.de/111517/>.
- [3] Agarwal, A. and Dowling, A. P. “Low-Frequency Acoustic Shielding by the Silent Aircraft Airframe”. In: *AIAA Journal* 45.2 (Feb. 2007), pp. 358–365. ISSN: 0001-1452. DOI: 10.2514/1.19351.
- [4] Airbus. *Family Figures*. Booklet. Farnborough 2018 Edition. 2018.
- [5] Almoneit, D. and Pott-Pollenske, M. *MODAL Statustreffen 16.07.2014, Lufthansa Frankfurt AP1.1/AP1.3/AP1.4 - Zellenlärm Boeing B747-400*. Presentation. July 2014.
- [6] Almoneit, D. and Pott-Pollenske, M. “Zellenlärm Boeing B747-400: Arbeiten im Projekt MODAL”. Presentation. German Aerospace Center (DLR). Apr. 2013.
- [7] Andreou, C., Graham, W., and Shin, H.-C. “Aeroacoustic Study of Airfoil Leading Edge High-Lift Devices”. In: *12th AIAA/CEAS Aeroacoustics Conference (27th AIAA Aeroacoustics Conference)*. Aeroacoustics Conferences. American Institute of Aeronautics and Astronautics, May 2006. DOI: 10.2514/6.2006-2515.
- [8] Antoine, N. E. and Kroo, I. M. “Aircraft Optimization for Minimal Environmental Impact”. In: *Journal of Aircraft*. Vol. 41. 4. American Institute of Aeronautics and Astronautics, 2004, pp. 790–797. DOI: 10.2514/1.71.
- [9] Antoine, N. E. and Kroo, I. M. “Framework for Aircraft Conceptual Design and Environmental Performance Studies”. In: *AIAA Journal*. Vol. 43. 10. Albany, NY: American Institute of Aeronautics and Astronautics, Oct. 2005, pp. 2100–2109. DOI: 10.2514/1.13017.
- [10] Archambault, N. “Speed uncertainty and speed regulation in conflict detection and resolution in Air Traffic Control”. In: *ICRAT 2004, 1st International Conference on Research in Air Transportation*. Zilina, Slovakia, Nov. 2004. URL: <https://hal-enac.archives-ouvertes.fr/hal-01021734>.
- [11] Arntzen, M. and Simons, D.G. “Modeling and synthesis of aircraft flyover noise”. In: *International Journal of Aeroacoustics* 13.5-6 (June 2015). NLR-TP-2015-287, pp. 449–462.

- [12] Aulich, A.-L. et al. “Fan casing contouring under consideration of aeroacoustics, mechanics, aeroelasticity, and whole engine performance”. In: *CEAS Aeronautical Journal*. Ed. by DLR. Vol. Volume: 8. 1. Springer Verlag, 2017, pp. 157–166. DOI: 10.1007/s13272-016-0226-z.
- [13] *B747-400 Airplane Characteristics for Airport Planning*. Boeing Commercial Airplanes. Seattle, Washington, Dec. 2002.
- [14] Bank, T. W. *Germany: GNI per capita, Atlas Method (current US-Dollar)*. Website. Sept. 2020. URL: <https://data.worldbank.org/country/germany?view=chart>.
- [15] Banks, S. and Dinges, D. F. “Behavioral and Physiological Consequences of Sleep Restriction”. In: *Journal of Clinical Sleep Medicine JCSM*. Vol. 3. 5. American Academy of Sleep Medicine, Aug. 2007, pp. 519–528. URL: <https://www.ncbi.nlm.nih.gov/pmc/articles/PMC1978335/>.
- [16] Barba, L. A. and Mesnard, O. “Aero Python: Classical Aerodynamics of Potential Flow Using Python”. In: *Journal of Open Source Education*. Vol. 2(15). 45. JOSE, May 2019, pp. 1–3. DOI: 10.21105/jose.00045.
- [17] Barche, J. “Tragflügelentwurf am Beispiel des Verkehrsflugzeugs VFW 614”. In: *Zeitschrift für Flugwissenschaften*. Vol. 22. 4. DGLR, Apr. 1974, pp. 101–115.
- [18] Basner, M., Griefahn, B., and Berg, M. van den. “Aircraft Noise Effects on Sleep: Mechanisms, Mitigation and Research Needs”. In: *Noise & Health*. Vol. 12. 47. Wolters Kluwer, May 2010, pp. 95–109. DOI: 10.4103/1463-1741.63210.
- [19] Basner, M., Samel, A., and Isermann, U. “Aircraft Noise Effects on Sleep: Application of the Results of a Large Polysomnographic Field Study”. In: *The Journal of the Acoustical Society of America*. Vol. 119. Acoustical Society of America ASA, Feb. 2006, pp. 2772–2784. DOI: 10.1121/1.2184247.
- [20] Becker, R. et al. “Development of a Gas Turbine Performance Code and its Application to Preliminary Engine Design”. In: *Deutscher Luft- und Raumfahrtkongress (DLRK)*. Bremen, Sept. 2011. URL: <https://elib.dlr.de/73232/>.
- [21] Bernardo, J. E., Kirby, M., and Mavris, D. “Development of Generic Airport Categories for Rapid Fleet-Level Noise Modeling”. In: *Journal of Aerospace Operations*. Vol. 3. 2. IOS Press, 2015, pp. 91–119. DOI: 10.3233/AOP-150045.
- [22] Bernardo, J. E. et al. “Analysis of Aircraft Vehicle Class Contributions to Airport Noise Exposure”. In: *Journal of Aerospace Operations*. Vol. 4. 4. IOS Press, 2017, pp. 185–206. DOI: 10.3233/AOP-160062.
- [23] Berton, J. J. *Noise reduction Potential of Large Over-The-Wing Mounted, Advanced Turbofan Engines*. Tech. rep. TM-2000-210025. Cleveland, Ohio, USA: NASA - Glenn Research Center, Apr. 2000.
- [24] Bertsch, L. “Noise Prediction within Conceptual Aircraft Design”. PhD thesis. TU Braunschweig, 2013. DOI: 10.34912/n0is3-d3sign.
- [25] Bertsch, L., Dobrzynski, W., and Guérin, S. “Tool Development for Low-noise Aircraft Design”. In: *14th AIAA/CEAS Aeroacoustics Conference*. Ed. by Aircraft, J. of. Vol. 47. Engineering Notes 2. AIAA. Vancouver, Canada, 2008, pp. 694–699. ISBN: 3928628143. DOI: 10.2514/1.43188.

- [26] Bertsch, L., Heinze, W., and Lummer, M. “Application of an Aircraft Design-To-Noise Simulation Process”. In: *14th AIAA Aviation Technology, Integration, and Operations Conference*. American Institute of Aeronautics and Astronautics, June 2014. DOI: 10.2514/6.2014-2169.
- [27] Bertsch, L. and Isermann, U. “Noise Prediction Toolbox Used by the DLR Aircraft Noise Working Group”. In: *Inter-Noise*. Innsbruck, Austria, 2013.
- [28] Bertsch, L., Schäffer, B., and Guérin, S. “Towards an Uncertainty Analysis for Parametric Aircraft System Noise Prediction”. In: *12th ICBEN Congress on Noise as a Public Health Problem*. Zürich, June 2017, pp. 1–12.
- [29] Bertsch, L. et al. “Flyover Noise Measurements of a Spiraling Noise Abatement Approach Procedure”. In: *Journal of Aircraft*. Vol. 48. 2. American Institute of Aeronautics and Astronautics, 2011, pp. 436–448. DOI: 10.2514/1.C001005.
- [30] Bertsch, L. et al. “The Aircraft Noise Simulation Working Group (ANSWr) - Tool Benchmark and Reference Aircraft Results”. In: *Aeroacoustics Conferences*. American Institute of Aeronautics and Astronautics, May 2019. DOI: 10.2514/6.2019-2539.
- [31] Bertsch, L. et al. “The Parametric Aircraft Noise Analysis Module - status overview and recent applications”. In: *17th AIAA/CEAS Aeroacoustics Conference (32nd AIAA Aeroacoustics Conference)*. Portland, Oregon: American Institute of Aeronautics and Astronautics, 2011, pp. 1–24.
- [32] Blinstrub, J. “Immission-Based Noise Reduction within Conceptual Aircraft Design”. Forschungsbericht DLR-FB-2019-12, ISSN: 1434-8454. Phd Thesis. TU Braunschweig, 2019. DOI: [https://doi.org/10.34912/f18ght\\_n01s3](https://doi.org/10.34912/f18ght_n01s3).
- [33] Blinstrub, J., Bertsch, L., and Heinze, W. “Assessment of the Noise Immission along Approach and Departure Flightpaths for Different SFB 880 Vehicle Concepts”. In: *AIAA Aviation Forum*. AIAA 2018-2818. American Institute of Aeronautics and Astronautics, June 2019, pp. 1–21. DOI: 10.2514/6.2018-2818.
- [34] BMU. *Act for Protection against Aircraft Noise*. Federal Ministry for the Environment, Nature Conservation and Nuclear Safety. Gesetz zum Schutz gegen Fluglärm. Dec. 2007.
- [35] Boeing. *747 Commercial Transport/YAL-1*. Z. URL: <http://www.boeing.com/history/products/747.page>.
- [36] Boeing. *Statistical Summary of Commercial Jet Airplane Accidents: Worldwide Operations 1959 – 2016*. July 2017. URL: [www.boeing.com/news/techissues/pdf/statsum.pdf](http://www.boeing.com/news/techissues/pdf/statsum.pdf).
- [37] Boguhn, O. et al. *Leiser Flugverkehr II*. Abschlussbericht zum Projekt „Leiser Flugverkehr II“. German Aerospace Center (DLR), Dec. 2007.
- [38] Bokor, A. “Attenuation of sound in lined ducts”. In: *Journal of Sound and Vibration* 10.3 (Nov. 1969), pp. 390–403. ISSN: 0022-460X. URL: <http://www.sciencedirect.com/science/article/pii/0022460X6990217X>.
- [39] Bridges, J. E., Khavaran, A., and Hunter, C. A. “Assessment of Current Jet Noise Prediction Capabilities”. In: *14th AIAA/CEAS Aeroacoustics Conference*. September. Vancouver: American Institute of Aeronautics and Astronautics, 2008, pp. 5–7.

- [40] Brooks, T. F. and Hodgson, T. H. “Trailing Edge Noise Prediction from Measured Surface Pressures”. In: *Journal of Sound and Vibration*. Vol. 78. 1. Elsevier, Sept. 1981, pp. 69–117. DOI: 10.1016/S0022-460X(81)80158-7.
- [41] Brooks, T. F. and Humphreys, W. M. J. “Flap-edge Aeroacoustic Measurements and Predictions”. In: *Journal of Sound and Vibration*. Vol. 261. 1. Elsevier, Mar. 2003, pp. 31–74. DOI: 10.1016/S0022-460X(02)00939-2.
- [42] Bundesministerium für Umwelt, Naturschutz und Reaktorsicherheit. *Bekanntmachung der Anleitung zur Datenerfassung über den Flugbetrieb (AzD) und Anleitung zur Berechnung von Lärmschutzbereichen (AzB)*. technische Regelwerke IG I 7- 50123-1/1. Bundesministerium für Umwelt, Naturschutz und Reaktorsicherheit, Nov. 2008.
- [43] Burley, C. L. and Lopes, L. V. *ANOPP2 : Progress Update*. presentation. Cleveland, OH, 2011.
- [44] Burnazzi, M. and Radespiel, R. “Design and Analysis of a Droop Nose for Coanda Flap Applications”. In: *Journal of Aircraft*. Vol. 51. 5. American Institute of Aeronautics and Astronautics (AIAA), 2014, pp. 1567–1579. DOI: 10.2514/1.c032434.
- [45] Centre, E. E. *The Aircraft Noise and Performance (ANP) Database: An international data resource for aircraft noise modellers*. Software. Feb. 2018. URL: <http://www.aircraftnoisemodel.org/>.
- [46] Choudhari, M. M. and Khorrami, M. R. “Slat Cove Unsteadiness: Effect of 3D Flow Structures”. In: *44th AIAA Aerospace Sciences Meeting and Exhibit*. AIAA 2006-211. American Institute of Aeronautics and Astronautics. Reno, Nevada: AIAA, Jan. 2006, pp. 1–20. DOI: 10.2514/6.2006-211.
- [47] Crichton, D. et al. “Design and Operation for Ultra Low Noise Take-Off”. In: *45th AIAA Aerospace Sciences Meeting and Exhibit*. Reno, Nevada: American Institute of Aeronautics and Astronautics, 2007.
- [48] Curle, N. “The influence of solid boundaries upon aerodynamic sound”. In: *Royal Society of London*. Vol. 231. Series A. Mathematical and Physical Sciences 1187. Communicated by M.J. Lighthill. The Royal Society, Sept. 1955, pp. 505–514. DOI: 10.1098/rspa.1955.0191.
- [49] Dahlmann, K. et al. “Can we reliably assess climate mitigation options for air traffic scenarios despite large uncertainties in atmospheric processes?” In: *Transportation Research Part D: Transport and Environment* 46 (2016), pp. 40–55. ISSN: 1361-9209. DOI: 10.1016/j.trd.2016.03.006.
- [50] Daigle, G. A., Piercy, J. E., and Embleton, T. F. W. “Line-of-sight propagation through atmospheric turbulence near the ground”. In: *The Journal of the Acoustical Society of America* 74.5 (Nov. 1983), pp. 1505–1513. ISSN: 0001-4966. DOI: 10.1121/1.390152.
- [51] Dehning, U. “Berechnung der direkten Betriebskosten von Transportflugzeugen”. MA thesis. Braunschweig: Institut für Flugzeugbau und Leichtbau, TU Braunschweig, 1982.
- [52] Delany, M. E. and Bazley, E. N. “Acoustical Properties of Fibrous Absorbent Materials”. In: *Journal of Applied Acoustics*. Vol. 3. 2. Elsevier, Apr. 1970, pp. 105–116. DOI: 10.1016/0003-682X(70)90031-9.

- [53] Deutsches Zentrum für Luft- und Raumfahrt. *Leiser Flugverkehr*. Final project report. 2004.
- [54] Diedrich, A. et al. “Multidisciplinary Design and Optimization of the Silent Aircraft”. In: Aerospace Sciences Meetings. American Institute of Aeronautics and Astronautics, Jan. 2006. DOI: 10.2514/6.2006-1323.
- [55] Dittmar, J. H., Woddward, R. P., and MacKinnon, M. J. “Fan noise reduction achieved by removing tip flow irregularities behind the rotor - forward arc test configurations”. In: *NASA Technical Memorandum 83616*. Ed. by ASA. Vol. 75. S79. The Journal of the Acoustical Society of America, 1984. DOI: 10.1121/1.2021618.
- [56] Dobrzynski, W., Rossignol, K. S., and Almoneit, D. *Handbuch zum modularen Quellmodell für das Umströmungsgeräusch von Verkehrsflugzeugen test PROFAN (PRediction MOdel For Airframe Noise) - Version 4.0* -. Tech. rep. German Aerospace Center (DLR), 2011.
- [57] Dobrzynski, W. et al. “Experimental Assessment of Low Noise Landing Gear Component Design”. In: *International Journal of Aeroacoustics* 9.6 (July 2010). DOI: 10.1260/1475-472X.9.6.763.
- [58] Dobrzynski, W. “Almost 40 Years of Airframe Noise Research: What Did We Achieve?” In: *Journal of Aircraft*. Vol. 47. 2. American Institute of Aeronautics and Astronautics (AIAA), Mar. 2010, pp. 353–367. DOI: 10.2514/1.44457.
- [59] Dobrzynski, W. *Konfigurationen 2020*. Abschlussbericht 2003-2006 K2020-DLR-000-017-P4. Institute of Aerodynamics and Flow Technology, German Aerospace Center (DLR), July 2007.
- [60] Dobrzynski, W. and Buchholz, H. “Full-scale Noise Testing on Airbus Landing Gears in the German Dutch Wind Tunnel”. In: *3rd AIAA/CEAS Aeroacoustics Conference*. American Institute of Aeronautics and Astronautics, May 1997. DOI: 10.2514/6.1997-1597.
- [61] Dobrzynski, W. and Pott-Pollenske, M. “Slat Noise Source Studies for Farfield Noise Prediction”. In: *7th AIAA/CEAS Aeroacoustics Conference*. May. Maastricht: American Institute of Aeronautics and Astronautics, 2001.
- [62] Dobrzynski, W., Pott-Pollenske, M., and Almoneit, D. *Auswertung der Messdaten aus simulierten Landeanflügen an einer B747-400 der Deutschen Lufthansa zur Validierung des DLR Quellmodells PROFAN für das Zellengeräusch*. Research rep. IB 124-2011. Braunschweig: German Aerospace Center (DLR), Feb. 2011.
- [63] Dobrzynski, W. et al. “Airframe Noise Studies on Wings with Deployed High-lift Devices”. In: *4th AIAA/CEAS Aeroacoustics Conference*. 98-2337. American Institute of Aeronautics and Astronautics. Toulouse, France: AIAA, June 1998. DOI: 10.2514/6.1998-2337.
- [64] Dowling, A. P. and Hynes, T. “Towards a Silent Aircraft”. In: *The Aeronautical Journal*. This paper is an updated version of the 93rd Wilbur and Orville Wright Lecture, December 2004. Cambridge University Press, Aug. 2006, pp. 487–494. DOI: 10.1017/S000192400000138X.
- [65] Dunn, D. G. and Peart, N. A. *Aircraft Noise Source and Contour Estimation*. Tech. rep. NASA CR-114649. National Aeronautics and Space Administration, July 1973.

- [66] EASA. *Certification Specifications for Large Aeroplanes CS-25*. Amendment 26. European Aviation Safety Agency, Dec. 2020. URL: [https://www.easa.europa.eu/sites/default/files/dfu/cs-25\\_amendment\\_26\\_0.pdf](https://www.easa.europa.eu/sites/default/files/dfu/cs-25_amendment_26_0.pdf).
- [67] EEA, E. E. A. *Population density disaggregated with Corine land cover 2000*. 2009. URL: <https://www.eea.europa.eu/data-and-maps/data/population-density-disaggregated-with-corine-land-cover-2000-2/#tab-gis-data>.
- [68] Elmenhorst, E. M. et al. *Untersuchung der Fliegbarkeit von Lärmoptimierten Anflugverfahren durch den Piloten*. DLR Forschungsbericht. 2005.
- [69] Elmenhorst, E.-M. et al. *Pilot Workload During Approaches: Comparison of Simulated Standard and Noise-Abatement Profiles*. 2009. DOI: 10.3357/asem.2382.2009.
- [70] EUROCONTROL. *ASTERIX Part 17 Category 004 Appendix A Coding rules for "Reserved Expansion Field"*. 2008.
- [71] FAA. *AC120-27E, Aircraft Weight And Balance Control*. Federal Aviation Administration. AC120-27E. 2005.
- [72] FAA. *AC91-53, Noise Abatement Departure Profiles*. Federal Aviation Administration. AC No: 91-53A. 1993.
- [73] FAA. *Type Certificate Data Sheet E13NE*. Federal Aviation Administration. Feb. 2007.
- [74] Fethney, P. "An experimental study of airframe self-noise". In: *Aeroacoustics Conferences*. American Institute of Aeronautics and Astronautics, Mar. 1975. DOI: 10.2514/6.1975-511.
- [75] Fichter, C. et al. "The impact of cruise altitude on contrails and related radiative forcing". In: *Meteorologische Zeitschrift* 14.4 (Sept. 2005), pp. 563–572. DOI: 10.1127/0941-2948/2005/0048.
- [76] Filler, L. "Swept Edge to Reduce the Noise Generated by Turbulent Flow over the Edge". In: *The Journal of the Acoustical Society of America*. Vol. 59. 3. Acoustical Society of America ASA, 1976. DOI: 10.1121/1.380921.
- [77] Fink, M. R. *Airframe Noise Prediction Method*. Tech. rep. FAA-RD-77-29. U.S. Department of Transportation, Federal Aviation Administration, Mar. 1977.
- [78] Fink, M. R. "Approximate Prediction of Airframe Noise". In: *Journal of Aircraft* 13.11 (Nov. 1976), pp. 833–834. DOI: 10.2514/3.58718.
- [79] Fink, M. R. and Bailey, D. A. *Airframe Noise Reduction Studies and Clean-Airframe Noise Investigation*. NASA Contractor Report 159311. National Aeronautics and Space Administration, Apr. 1980. URL: <https://ntrs.nasa.gov/archive/nasa/casi.ntrs.nasa.gov/19800024667.pdf>.
- [80] Fink, M. R. and Bailey, D. A. "Model Tests of Airframe Noise Reduction Concepts". In: *6th Aeroacoustics Conference*. AIAA. Hartford, CT, U.S.A.: American Institute of Aeronautics and Astronautics, June 1980. DOI: 10.2514/6.1980-979.
- [81] Fraport. *Airport Charges according to Art. 19b Air Traffic Act (LuftVG) Charges for Central Ground Handling Infrastructure*. Entgeltordnung. Hessisches Ministerium für Wirtschaft, Energie, Verkehr und Wohnen, Jan. 2020. URL: <https://www.fraport.de/content/fraport/de/business-partner/airlines-cargo/flughafenentgelte.html>.

- [82] Frömring, C. et al. “Aviation-induced radiative forcing and surface temperature change in dependency of the emission altitude”. In: *J. Geophys. Res.* 117.D19 (Oct. 2012). ISSN: 0148-0227. DOI: 10.1029/2012JD018204.
- [83] Fujino, M. and Kawamura, Y. “Wave-Drag Characteristics of an Over-the-Wing Nacelle Business-Jet Configuration”. In: *Journal of Aircraft*. Vol. 40. 6. American Institute of Aeronautics and Astronautics, Nov. 2003, pp. 1177–1184. DOI: 10.2514/2.7207.
- [84] Gallego, F. J. “A Population Density Grid of the European Union”. In: *Population and Environment*. Ed. by Springer. Vol. 31. 6. Springer, May 2010, pp. 460–473. DOI: 10.1007/s11111-010-0108-y.
- [85] Goldstein, M. E. “Aeroacoustics of Turbulent Shear Flows”. In: *Annual Review of Fluid Mechanics*. Vol. 16. Annual Reviews, 1984, pp. 263–285. URL: <https://www.annualreviews.org/doi/pdf/10.1146/annurev.fl.16.010184.001403>.
- [86] Greatrex, F. B. and Brown, D. M. “Progress in Jet Engine Noise Reduction”. In: *Advances in Aeronautical Sciences: Proceedings of the First International Congress in the Aeronautical Sciences, Madrid, 8-13 September 1958, Band 1*. Vol. 1. 1. International Congress in the Aeronautical Sciences. Madrid, Sept. 1958, pp. 364–392.
- [87] Guo, Y. “Prediction of flap side edge noise”. In: Aeroacoustics Conferences. American Institute of Aeronautics and Astronautics, May 1999. DOI: 10.2514/6.1999-1804.
- [88] Guo, Y. “A Study on Local Flow Variations for Landing Gear Noise Research”. In: *14th AIAA/CEAS Aeroacoustics Conference (29th AIAA Aeroacoustics Conference)*. AIAA 2008-2915. Vancouver, Canada, 2008. DOI: 10.2514/6.2008-2915.
- [89] Guo, Y. “Aircraft Flap Side Edge Noise Modeling and Prediction”. In: *17th AIAA/CEAS Aeroacoustics Conference (32nd AIAA Aeroacoustics Conference)*. American Institute of Aeronautics and Astronautics, June 2011. DOI: 10.2514/6.2011-2731.
- [90] Guo, Y., Burley, C. L., and Thomas, R. H. “Modeling and Prediction of Krueger Device Noise”. In: *22nd AIAA/CEAS Aeroacoustics Conference*. American Institute of Aeronautics and Astronautics (AIAA), May 2016. DOI: 10.2514/6.2016-2957.
- [91] Hansell, A. L. et al. “Aircraft Noise and Cardiovascular Disease near Heathrow Airport in London: Small Area Study”. In: *British Medical Journal BMJ*. Vol. 5432. 347:f5432. British Medical Association, Oct. 2013, pp. 1–10. DOI: 10.1136/bmj.f5432.
- [92] Hansen, L. U., Heinze, W., and Horst, P. “Blended Wing Body Structures in Multi-disciplinary Pre-design”. In: *Springer-Verlag* 36.1 (2007), pp. 93–106. DOI: 10.1007/s00158-007-0161-z.
- [93] Hardin, J. C. et al. *Prediction of airframe noise*. Tech. rep. NASA TN D-7821. Hampton, Va.23665: NASA, Feb. 1975.
- [94] Hardoy, M. C. et al. “Exposure to aircraft noise and risk of psychiatric disorders: the Elmas survey”. In: *Social Psychiatry and Psychiatric Epidemiology* 40.1 (Jan. 2005), pp. 24–26. ISSN: 1433-9285. URL: <https://doi.org/10.1007/s00127-005-0837-x>.
- [95] Hartjes, S., Visser, H. G., and Heibly, S. J. “Optimization of RNAV Noise and Emission Abatement Departure Procedures”. In: *9th AIAA Aviation Technology, Integration, and Operations Conference (ATIO)*. Hilton Head, South Carolina: American Institute of Aeronautics and Astronautics, 2009. ISBN: 9781563479809.

- [96] Hebly, S. J. and Visser, H. G. “Advanced Noise Abatement Departure Procedures: Custom-optimised Departure Profiles”. In: *The Aeronautical Journal*. Vol. 119. 1215. Royal Aeronautical Society, May 2015, pp. 647–661. DOI: 10 . 1017 / S0001924000010733.
- [97] Hebly, S. J. and Visser, H. G. “Impact of Environmentally Optimized Departures on Runway Capacity”. In: *9th AIAA Aviation Technology, Integration, and Operations Conference (ATIO)*. September. Hilton Head, South Carolina: American Institute of Aeronautics and Astronautics, 2009, pp. 1–18.
- [98] Heidmann, M. F. *Interim Prediction Method for Fan and Compressor Source Noise*. Technical Report. Tech. rep. NASA-TM-X-71763. July 1979.
- [99] Heinze, W. “Ein Beitrag zur Quantitativen Analyse der Technischen und Wirtschaftlichen Auslegungsgrenzen Verschiedener Flugzeugkonzepte für den Transport Großer Nutzlasten”. PhD thesis. TU Braunschweig, 1994.
- [100] Heller, H. and DOBRZYNSKI, W. “Sound radiation from aircraft wheel-well/landing gear configurations”. In: *Aeroacoustics Conferences*. American Institute of Aeronautics and Astronautics, July 1976. DOI: 10.2514/6.1976-552.
- [101] Herr, M. “A Noise Reduction Study on Flow-Permeable Trailing-Edges”. In: *8th ONERA-DLR Aerospace Symposium (ODAS)*. ONERA/DLR. Göttingen: ONERA/DLR, Oct. 2007, pp. 1–10. URL: <https://elib.dlr.de/52821/>.
- [102] Herr, M. “Design Criteria for Low-Noise Trailing-Edges”. In: *13th AIAA/CEAS Aeroacoustics Conference (28th AIAA Aeroacoustics Conference)*. 2007. DOI: 10 . 2514/6.2007-3470.
- [103] Herr, M. “Trailing-Edge Noise - Reduction Concepts and Scaling Laws”. Forschungsbericht 2013-32. Dissertation, Forschungsbericht. TU Braunschweig, Sept. 2013. URL: <https://elib.dlr.de/87261/>.
- [104] Hileman, J. I. et al. “Airframe Design for Silent Fuel-Efficient Aircraft”. In: *Journal of Aircraft*. Vol. 47. 3. American Institute of Aeronautics and Astronautics, May 2010, pp. 956–969. DOI: 10.2514/1.46545.
- [105] Hileman, J. et al. “Airframe Design for "Silent Aircraft"”. In: *45th AIAA Aerospace Sciences Meeting and Exhibit*. AIAA 2007-453. 45th AIAA Aerospace Sciences Meeting and Exhibit. Reno, Nevada: AIAA, Jan. 2007, pp. 1–15. DOI: 10.2514/6.2007-453.
- [106] Hileman, J. I. et al. “Development of Approach Procedures for Silent Aircraft”. In: *45th AIAA Aerospace Sciences Meeting and Exhibit*. Reno, Nevada: American Institute of Aeronautics and Astronautics, 2007, pp. 1–14.
- [107] Holle, G. and Krishnan, M. “Gas turbine engine brush seal applications”. In: *Joint Propulsion Conferences*. American Institute of Aeronautics and Astronautics, July 1990. DOI: 10.2514/6.1990-2142.
- [108] Hooker, J. R. et al. “Over Wing Nacelle Installations for Improved Energy Efficiency”. In: *31st AIAA Applied Aerodynamics Conference*. Fluid Dynamics and Co-located Conferences AIAA 2013-2920. San Diego, CA: American Institute of Aeronautics and Astronautics, June 2013, pp. 1–39. DOI: 10.2514/6.2013-2920.

- [109] Horne, J. A. et al. “A Field Study of Sleep Disturbance: Effects of Aircraft Noise and Other Factors on 5,742 Nights of Actimetrically Monitored Sleep in a Large Subject Sample”. In: *Sleep* 17.2 (1994), pp. 146–159. ISSN: 0161-8105. URL: <https://doi.org/10.1093/sleep/17.2.146>.
- [110] Horstmann, K.-H. *Ein Mehrfach-Traglinienverfahren und seine Verwendung für Entwurf und Nachrechnung nichtplanarer Flügelanordnungen*. Research report. DFVLR-FB 87-51. 1988.
- [111] Howe, M. S. “A Review of the Theory of Trailing Edge Noise”. In: *Journal of Sound and Vibration*. Vol. 61. 3. Academic Press, Elsevier, Dec. 1978, pp. 437–465. DOI: 10.1016/0022-460X(78)90391-7.
- [112] Howe, M. S. “Aerodynamic Noise of a Serrated Trailing Edge”. In: *Journal of Fluids and Structures*. Vol. 5. 1. Elsevier, Jan. 1991, pp. 33–45. DOI: 10.1016/0889-9746(91)80010-B.
- [113] Howe, M. S. “Noise Produced by a Sawtooth Trailing Edge”. In: *The Journal of the Acoustical Society of America*. Vol. 90. 1. Acoustical Society of America ASA, Mar. 1991. DOI: 10.1121/1.401273.
- [114] Hussain, A. K. M. F. and Zaman, K. B. M. Q. “The ‘Preferred Mode’ of the Axisymmetric Jet”. In: *Journal of Fluid Mechanics*. Vol. 110. Cambridge University Press, Sept. 1981, pp. 39–71. DOI: 10.1017/S0022112081000608.
- [115] Hutcheson, F. V., Stead, D. J., and Plassman, G. E. “Experimental Study of Wake / Flap Interaction Noise and the Reduction of Flap Side Edge Noise”. In: *22nd AIAA/CEAS Aeroacoustics Conference*. AIAA 2016-2955. AIAA. Lyon, France: American Institute of Aeronautics and Astronautics, June 2016, pp. 1–15. DOI: 10.2514/6.2016-2955.
- [116] Hutcheson, F. V. et al. “Shielding of Turbomachinery Broadband Noise from a Hybrid wing Body Aircraft Configuration”. In: *AIAA AVIATION Forum*. American Institute of Aeronautics and Astronautics, June 2014. DOI: 10.2514/6.2014-2624.
- [117] ICAO. *Aircraft Operations. Volume I - Flight Procedures*. International Civil Aviation Organization. Doc 8168. 2006.
- [118] ICAO. *Environmental Technical Manual on the Use of Procedures in the Noise Certification of Aircraft*. Third Edition. International Civil Aviation Organization. 2004.
- [119] ICAO. *Guidance on the Balanced Approach to Aircraft Noise Management*. International Civil Aviation Organization. Doc 9829 AN/451. 2008.
- [120] Iemma, U. “Multi-disciplinary, community-oriented design of low-noise aircraft: the COSMA project”. In: *DE GRUYTER* (2016). DOI: 10.1515/noise-2016-0005.
- [121] Iemma, U., Vitagliano, F. P., and Centracchio, F. “Multi-objective Design Optimization of Sustainable Commercial Aircraft: Performance and Costs”. In: *International Journal of Sustainable Engineering* 10.3 (Dec. 2016), pp. 147–157. DOI: 10.1080/19397038.2016.1222461.
- [122] International Civil Aviation Organization. *Environmental Protection, Annex 16, Volume 1 Aircraft Noise OCR*. International Standards And Recommended Practices, 2008. ISBN: 9789292311087.
- [123] Isermann, U., Schmid, R., and Tontsch, I. *Umsetzung des ECAC Doc.29 in Hinblick auf deutsche Anforderungen*. L-6/2005 - 50.0317/2005. 2008.

- [124] ISO. *Acoustics - Attenuation of Sound During Propagation Outdoors*. Tech. rep. ISO 9613-1:1993. ISO, June 1993. URL: <https://www.iso.org/standard/17426.html>.
- [125] Jente, C. et al. “Experimental Investigation of Jet-Flap-Interaction Noise Sensitivity Due to Varying Flap Parameters at a UHBR Engine/High-Lift-Wing Installation”. In: *2018 AIAA/CEAS Aeroacoustics Conference*. Ed. by AIAA. AIAA AVIATION Forum AIAA 2018-3788. American Institute of Aeronautics and Astronautics, June 2018, pp. 1–22. DOI: 10.2514/6.2018-3788.
- [126] Jones, T. et al. *Statistical Data for the Boeing-747-400 Aircraft in Commercial Operations*. Final Report DOT/FAA/AR-04/44. U.S. Department of Transportation, Federal Aviation Administration, Jan. 2005.
- [127] Kachelmann GmbH, D. *Messwerte und Klimadaten mit Archiv ab dem Jahr 1781*. web. Dec. 2018. URL: <https://kachelmannwetter.com/de/messwerte/ludwigslust-parchim/temperatur/20080909-1500z.html>.
- [128] Kemp, N. H. and Sears, W. R. “Aerodynamic Interference Between Moving Blade Rows”. In: *Journal of the Aeronautical Sciences* 20.9 (Sept. 1953), pp. 585–597. DOI: 10.2514/8.2758.
- [129] Kemp, N. H. and Sears, W. R. “The Unsteady Forces Due to Viscous Wakes in Turbomachines”. In: *Journal of the Aeronautical Sciences* 22.7 (July 1955), pp. 478–483. DOI: 10.2514/8.3376.
- [130] Khorrami, M. R. *Understanding Slat Noise Sources*. Chamonix, France, 2003.
- [131] Khorrami, M. R., Singer, B. A., and Radeztsky, R. H. “Reynolds-Averaged Navier-Stokes Computations of a Flap-Side-Edge Flowfield”. In: *AIAA Journal* 37.1 (Jan. 1999), pp. 14–22. ISSN: 0001-1452. DOI: 10.2514/2.687.
- [132] Kim, S. J. et al. “Exposure-Response Relationship Between Aircraft Noise and Sleep Quality: A Community-based Cross-sectional Study”. eng. In: *Osong public health and research perspectives* 5.24955321 (Apr. 2014), pp. 108–114. ISSN: 2233-6052. URL: <https://www.ncbi.nlm.nih.gov/pmc/articles/PMC4064632/>.
- [133] Kipersztok, O. and SenGupta, G. “Flight Test of the 747-JT9D for Airframe Noise”. In: *Journal of Aircraft* 19.12 (Dec. 1982), pp. 1061–1069. DOI: 10.2514/3.44812.
- [134] König, R. et al. *Lärmarme An- und Abflugverfahren*. Abschlusspräsentation Projekt "Leiser Flugverkehr". Köln-Porz, Mar. 2004.
- [135] Koch, M. and Bertsch, L. “Engine Noise Source Placement for Shielding Calculation”. In: *Inter-Noise 2019*. Spanish Acoustical Society –SEA, June 2019, pp. 1–12. URL: <https://elib.dlr.de/127283/>.
- [136] Kontos, K. B., Janardan, B. A., and Glibe, P. R. *Improved NASA-ANOPP Noise Prediction Computer Code for Advanced Subsonic Propulsion Systems. Volume 1 ANOPP Evaluation and Fan Noise Model Improvement*. Tech. rep. 24. NASA, 1996.
- [137] Krejsa, E. A. and Valerino, M. F. *Interim Prediction Method for Turbine Noise*. Tech. rep. Cleveland, Ohio, 44135: Lewis Research Center, National Aeronautics and Space Administration, 1977. URL: <https://ntrs.nasa.gov/api/citations/19770006122/downloads/19770006122.pdf>.
- [138] Li, Y. et al. “Noise Sources Control of an Aircraft Landing Gear”. In: *13th AIAA/CEAS Aeroacoustics Conference*. Aeroacoustics Conferences. American Institute of Aeronautics and Astronautics, May 2007. DOI: 10.2514/6.2007-3465.

- [139] Lichte, M. *DOCAbsch"atzung mit Hilfe entwurfsspezifischer Werte*. Tech. rep. 421. VFW-Fokker, 1972.
- [140] Liersch, C. and Engelbrecht, T. *LIFTING\_LINE Handbook - Version 2.5*. Braunschweig: DLR, Jan. 2016.
- [141] Lockard, D. and Choudhari, M. "The Variation of Slat Noise with Mach and Reynolds Numbers". In: *17th AIAA/CEAS Aeroacoustics Conference (32nd AIAA Aeroacoustics Conference)*. American Institute of Aeronautics and Astronautics (AIAA), 2011. DOI: 10.2514/6.2011-2910.
- [142] Lockard, D. P. and Choudhari, M. M. "Noise Radiation from a Leading-Edge Slat". In: *15th AIAA/CEAS Aeroacoustics Conference*. Miami, FL, USA, 2009, pp. 1-16.
- [143] Lockard, D. P. and Lilley, G. M. *The Airframe Noise Reduction Challenge*. Technical Report. NASA/TM-2004-213013. Hampton, Virginia, Apr. 2004. DOI: 10.1.1.80.8946.
- [144] Low, J. K. C. *Ultra-High Bypass Ratio Jet Noise*. Tech. rep. NASA-CR-195394. Pratt and Whitney Aircraft; East Hartford, CT, United States, Oct. 1994.
- [145] Lummer, M. "Maggi-Rubinowicz Diffraction Correction for Ray-Tracing Calculations of Engine Noise Shielding". In: *14th AIAA/CEAS Aeroacoustics Conference (29th AIAA Aeroacoustics Conference)*. Vancouver, British Columbia, Canada: American Institute of Aeronautics and Astronautics, 2008. DOI: 10.2514/6.2008-3050.
- [146] Lummer, M. *The Ray-Tracing Program SHADOW 0.9.7*. DLR. Brunswick, Aug. 2009.
- [147] Manoha, E., Juvigny, X., and Roux, F. "Numerical Simulation of Aircraft Engine Installation Acoustic Effects". In: *Aeroacoustics Conferences*. American Institute of Aeronautics and Astronautics, May 2005. DOI: 10.2514/6.2005-2920.
- [148] Mazareanu, E. *Number of scheduled passengers boarded by the global airline industry from 2004 to 2020*. Mar. 2020. URL: <https://www.statista.com/statistics/564717/airline-industry-passenger-traffic-globally/>.
- [149] Michel, U. "Prediction of jet mixing noise in flight from static tests". In: *22nd AIAA/CEAS Aeroacoustics Conference*. American Institute of Aeronautics and Astronautics, May 2016. DOI: 10.2514/6.2016-2807.
- [150] Michel, U. and Ahuja, K. K. "On the Scaling of Jet Noise with Helmholtz Number Close to the Jet Axis". In: *20th AIAA/CEAS Aeroacoustics Conference*. 20th AIAA/CEAS Aeroacoustics Conference. AIAA. Atlanta, GA: American Institute of Aeronautics and Astronautics, June 2014. DOI: 10.2514/6.2014-2338.
- [151] Mistry, S., Smith, H., and Fielding, J. "Development of Novel Aircraft Concepts to Reduce Noise and Global Warming Effects". In: *Aviation Technology, Integration, and Operations (ATIO) Conferences*. American Institute of Aeronautics and Astronautics, Sept. 2007. DOI: 10.2514/6.2007-7753.
- [152] Molin, N. et al. "Prediction of low noise aircraft landing gears and comparison with test results". In: *12th AIAA/CEAS Aeroacoustics Conference (27th AIAA Aeroacoustics Conference)*. Vol. 7. May. Cambridge, Massachusetts: American Institute of Aeronautics and Astronautics, 2006.

- [153] Moreau, A., Guérin, S., and Stefan Busse. “A Method Based on the Ray Structure of Acoustic Modes for Predicting the Liner Performance in Annular Ducts with Flow”. In: *Proceedings of the NAG/DAGA 2009*. Rotterdam, Netherlands: NAG/DAGA International Conference on Acoustics, 2009, pp. 1248–1251.
- [154] Morfey, C. L. “Rotating Blades and Aerodynamic Sound”. In: *Journal of Sound and Vibration* 28. February (1973), pp. 587–617.
- [155] Morscheck, F. “Noise mitigation optimization of A-RNP /RNP AR approaches”. In: AIAA AVIATION Forum 0. American Institute of Aeronautics and Astronautics, June 2018. DOI: 10.2514/6.2018-3996.
- [156] Muzet, A. “Environmental noise, sleep and health”. In: *Sleep Medicine Reviews* 11.2 (Apr. 2007), pp. 135–142. ISSN: 1087-0792. URL: <http://www.sciencedirect.com/science/article/pii/S1087079206001055>.
- [157] Neise, W. *Zusammenfassender Schlussbericht Lärmoptimierte An- und Abflugverfahren (LAnAb)*. Final project report. Forschungsverbund Leiser Verkehr, Bereich Leises Verkehrsflugzeug. Berlin, Nov. 2007.
- [158] Nesbitt, E. et al. “Correlating Model-Scale & Full-Scale Test Results of Dual Flow Nozzle Jets”. In: Aeroacoustics Conferences. American Institute of Aeronautics and Astronautics, May 2002. DOI: 10.2514/6.2002-2487.
- [159] Oerlemans, S. and Pott-Pollenske, M. “An Experimental Study of Gear Wake/Flap Interaction Noise”. In: *10th AIAA/CEAS Aeroacoustics Conference*. Manchester, Great Britain: American Institute of Aeronautics and Astronautics, May 2004. DOI: 10.2514/6.2004-2886.
- [160] Oppermann, S. *Energiebasiertes Pilotenunterstützungskonzept für das präzise Einhalten von vertikalen Anflugprofilen*. Forschungsbericht, Dissertation DLR FB 2014-42, TU BS FB 2014-13. DLR Braunschweig / TU Braunschweig, 2014.
- [161] Patel, H. R. and Wilson, D. “Parametric Cycle Analysis of Adaptive Cycle Engine”. In: AIAA Propulsion and Energy Forum. American Institute of Aeronautics and Astronautics, July 2018. DOI: 10.2514/6.2018-4521.
- [162] Pearson, K. “Correlation coefficient”. In: *Royal Society Proceedings*. Vol. 58. 1895, p. 214.
- [163] Perennes, S. and Roger, M. “Aerodynamic Noise of a Two-dimensional Wing with High-lift Devices”. In: *4th AIAA/CEAS Aeroacoustics Conference*. Aeroacoustics Conferences AIAA-98-2338. AIAA. Toulouse, France: American Institute of Aeronautics and Astronautics, June 1998, pp. 772–782. DOI: 10.2514/6.1998-2338.
- [164] Pingstone, A. *British Airways Boeing 747-400 (G-CIVX) main undercarriages during landing at London Heathrow Airport, England*. Apr. 2006. URL: [https://en.wikipedia.org/wiki/Undercarriage\\_arrangements#/media/File:Ba\\_b747-400\\_g-civx\\_maingeardetail\\_arp.jpg](https://en.wikipedia.org/wiki/Undercarriage_arrangements#/media/File:Ba_b747-400_g-civx_maingeardetail_arp.jpg).
- [165] Pohl, H. “Ein Beitrag zur quantitativen Analyse des Einflusses von Auslegungsparameter auf den optimalen Entwurf von Verkehrsflugzeugen”. PhD thesis. Braunschweig: Institut für Flugzeugbau und Leichtbau, TU Braunschweig, 1986.
- [166] Pott-Pollenske, M., Alvarez-Gonzalez, J., and Dobrzynski, W. “Effect of Slat Gap on Farfield Radiated Noise and Correlation with Local Flow Characteristics”. In: *9th AIAA/CEAS Aeroacoustics Conference and Exhibit*. AIAA 2003-3228. Hilton Head, South Carolina, May 2003. DOI: 10.2514/6.2003-3228.

- [167] Pott-Pollenske, M. and Angland, D. *D4.1.16 Aerodynamic and Acoustic Test Report*. Test Report OPENAIR – FP7-234313. OPENAIR, Nov. 2013.
- [168] Pott-Pollenske, M. and Wild, J. “On the Noise Generation of Krueger Leading Edge Devices”. In: *21st AIAA/CEAS Aeroacoustics Conference*. Dallas, Texas: American Institute of Aeronautics and Astronautics, June 2015. DOI: 10.2514/6.2015-3142.
- [169] Pott-Pollenske, M., Wild, J., and Bertsch, L. “Aerodynamic and Acoustic Design of Silent Leading Edge Devices”. In: *20th AIAA/CEAS Aeroacoustics Conference*. Atlanta, Georgia: American Institute of Aeronautics and Astronautics, June 2014. DOI: 10.2514/6.2014-2076.
- [170] Pott-Pollenske, M. et al. “Airframe Noise Characteristics from Flyover Measurements and Prediction”. In: *12th AIAA/CEAS Aeroacoustics Conference (27th AIAA Aeroacoustics Conference)*. Cambridge, Massachusetts: American Institute of Aeronautics and Astronautics, May 2006. ISBN: 978-1-62410-021-5. DOI: 10.2514/6.2006-2567.
- [171] Prats, X., Puig, V., and Quevedo, J. “Equitable Aircraft Noise-Abatement Departure Procedures”. In: *Journal of Guidance, Control, and Dynamics* 34.1 (May 2011), pp. 192–203. DOI: 10.2514/1.49530.
- [172] Prats, X. et al. “Equitable Noise Abatement Departure Procedures”. In: *9th AIAA Aviation Technology, Integration, and Operations Conference*. Hilton Head, South Carolina: American Institute of Aeronautics and Astronautics, Sept. 2009. URL: <http://upcommons.upc.edu/e-prints/handle/2117/11199>.
- [173] Quayle, A. R. et al. “Landing Gear for a Silent Aircraft”. In: *45th AIAA Aerospace Sciences Meeting and Exhibit*. AIAA 2007-231. American Institute of Aeronautics and Astronautics. Reno, Nevada, Jan. 2007, pp. 1–15. DOI: 10.2514/6.2007-231.
- [174] Rackl, R. G. et al. *Airframe Noise Studies - Review and Future Direction*. Technical Report NASA/CR-2005-213767, Doc.ID 20050186546. NASA, June 2005. URL: <https://ntrs.nasa.gov/archive/nasa/casi.ntrs.nasa.gov/20050186546.pdf>.
- [175] Radespiel, R., Heinze, W., and L., B. “HIGH-LIFT RESEARCH FOR FUTURE TRANSPORT AIRCRAFT”. In: *Deutscher Luft- und Raumfahrt Kongress*. Sept. 2017.
- [176] Radeztsky Jr., R., Singer, B., and Khorrami, M. “Detailed measurements of a flap side-edge flow field”. In: *Aerospace Sciences Meetings*. American Institute of Aeronautics and Astronautics, Jan. 1998. DOI: 10.2514/6.1998-700.
- [177] Raney, J. “Development of a new computer system for aircraft noise prediction”. In: *Aeroacoustics Conferences*. American Institute of Aeronautics and Astronautics, Mar. 1975. DOI: 10.2514/6.1975-536.
- [178] Ravetta, P., Burdisso, R., and Ng, W. “Noise Control of Landing Gears Using Elastic Membrane-Based Fairings”. In: *13th AIAA/CEAS Aeroacoustics Conference (28th AIAA Aeroacoustics Conference)*. Rome, Italy: American Institute of Aeronautics and Astronautics, May 2007. DOI: 10.2514/6.2007-3466.
- [179] Ravetta, P., Burdisso, R., and Ng, W. “Wind Tunnel Aeroacoustic Measurements of a 26%-scale 777 Main Landing Gear”. In: *10th AIAA/CEAS Aeroacoustics Conference*. Manchester, Great Britain: American Institute of Aeronautics and Astronautics, May 2004. DOI: 10.2514/6.2004-2885.

- [180] Raymer, D. P. *Aircraft Design: A Conceptual Approach, Sixth Edition*. Ed. by Schetz, J. A. Sixth Edition. Playa del Rey, California: American Institute of Aeronautics and Astronautics, 2018. ISBN: 978-1-62410-490-9. DOI: 10.2514/4.104909.
- [181] Rego, L. et al. “Noise Amplification Effects due to Jet-Surface Interaction”. In: *AIAA Scitech 2019 Forum*. AIAA 2019-0001. San Diego, California: American Institute of Aeronautics and Astronautics, Jan. 2019, pp. 1–16. DOI: 10.2514/6.2019-0001.
- [182] Reichmuth, J. and Berster, P. “Past and Future Developments of the Global Air Traffic”. In: *Biokerosene, Status and Prospects*. Ed. by Kaltschmitt Martin, N. U. Berlin, Heidelberg: Springer, Aug. 2018. Chap. 2, pp. 13–31. ISBN: 978-3-662-53063-4. DOI: 10.1007/978-3-662-53065-8\_2.
- [183] Reitenbach, S. et al. “Collaborative Aircraft Engine Preliminary Design using a Virtual Engine Platform, Part A: Architecture and Methodology”. In: *AIAA SciTech Forum*. American Institute of Aeronautics and Astronautics, May 2020. DOI: 10.2514/6.2020-0867.
- [184] Rice, E. J. *Attenuation of Sound in Soft Walled Ducts*. Tech. rep. TMX-52442. NASA, 1968.
- [185] Rossian, L. et al. “Numerical and Experimental Insights into the Noise Generation of a Circulation Control Airfoil”. In: *2018 AIAA/CEAS Aeroacoustics Conference*. AIAA 2018-3139. AIAA. Atlanta, Georgia: American Institute of Aeronautics and Astronautics, June 2018, pp. 1–23. DOI: 10.2514/6.2018-3139.
- [186] Rossignol, K.-S. “Development of an empirical prediction model for flap side-edge noise”. In: *16th AIAA/CEAS Aeroacoustics Conference*. American Institute of Aeronautics and Astronautics, Inc., 2010.
- [187] Rossignol, K.-S. R. “Empirical prediction of flap tip noise”. In: *17th AIAA/CEAS Aeroacoustics Conference (32nd AIAA Aeroacoustics Conference)*. June. Portland, Oregon: American Institute of Aeronautics and Astronautics, 2011.
- [188] Rudnick, I. “The Propagation of an Acoustic Wave along a Boundary”. In: *The Journal of the Acoustical Society of America* 19.2 (June 2005). DOI: 10.1121/1.1916490.
- [189] Rudolph, K. C. *High-Lift Systems on Commercial Subsonic Airliners*. NASA Contractor Report 4746. 1996.
- [190] Saiyed, N. H., Mikkelsen, K. L., and Bridges, J. “Acoustics and Thrust of Quiet Separate-Flow High-Bypass-Ratio Nozzles”. In: *AIAA Journal*. Vol. 41. 3. AIAA, Mar. 2003, pp. 372–378. DOI: 10.2514/2.1986.
- [191] Sams, E. W. and Bresnahan, D. L. *Refan program. Phase 1: Summary report*. Tech. rep. NASA-TM-X-71456. Cleveland, OH, United States: NASA Lewis Research Center, Oct. 1973.
- [192] Savoni, L. and Rudnik, R. “Aerodynamic Assessment of Pylon-Mounted Over-the-Wing Engine Installations on a STOL Commercial Aircraft Concept”. In: *New Results in Numerical and Experimental Fluid Mechanics XI*. Ed. by Dillmann, A. et al. Cham: Springer International Publishing, 2018, pp. 51–60. ISBN: 978-3-319-64519-3.
- [193] Scholz, M. and Abdelmoula, F. “Active Noise Abatement Using the Newly Developed Pilot Assistance System LNAS”. In: *InterNoise*. Hong Kong, Aug. 2017.

- [194] Scott, R. A. “The propagation of sound between walls of porous material”. In: *Proceedings of the Physical Society* 58.4 (July 1946), pp. 358–368. ISSN: 0959-5309. URL: <http://dx.doi.org/10.1088/0959-5309/58/4/304>.
- [195] Seitz, A., Schmitt, D., and Donnerhack, S. “Emission comparison of turbofan and open rotor engines under special consideration of aircraft and mission design aspects”. In: *The Aeronautical Journal* (1968) 115.1168 (2011), pp. 351–360. ISSN: 0001-9240. DOI: 10.1017/s000192400000587x.
- [196] SENGUPTA, G. “Analysis of jet-airframe interaction noise”. In: *8th Aeroacoustics Conference*. American Institute of Aeronautics and Astronautics, Apr. 1983. DOI: 10.2514/6.1983-783.
- [197] Sharland, I. J. “Sources of noise in axial flow fans”. In: *Journal of Sound and Vibration* 1.3 (July 1964), pp. 302–322. ISSN: 0022-460X. URL: <http://www.sciencedirect.com/science/article/pii/0022460X64900689>.
- [198] Shearin, J. et al. “Model and full-scale large transport airframe noise”. In: *Aeroacoustics Conferences*. American Institute of Aeronautics and Astronautics, July 1976. DOI: 10.2514/6.1976-550.
- [199] Siebertz, K., Bebbler, D. van, and Hochkirchen, T. *Statistische Versuchsplanung*. Ed. by Springer. VDI-Buch book series. Springer Vieweg, Berlin, Heidelberg, 2017. ISBN: 978-3-662-55742-6. DOI: 10.1007/978-3-662-55743-3.
- [200] Siller, H et al. “Fly-Over Source Localisation On A Boeing 747-400”. In: *3rd Berlin Beamforming Conference*. Berlin, 2010, pp. 1–11.
- [201] Smith, G. T. and Lopes, L. V. *Modernization of ANOPP*. 2010.
- [202] Smith, M. “International aircraft noise measurement procedures - Expensive acquisition of poor quality data”. In: *Aeroacoustics Conferences*. American Institute of Aeronautics and Astronautics, Oct. 1977. DOI: 10.2514/6.1977-1371.
- [203] Smith, M. G. and Chow, L. C. “Prediction Method for Aerodynamic Noise from Aircraft Landing Gear”. In: *4th AIAA/CEAS Aeroacoustics Conference*. AIAA-98-2228. American Institute of Aeronautics and Astronautics. Toulouse, France, June 1998, pp. 153–161. DOI: 10.2514/6.1998-2228.
- [204] Smith, M. J. T. *Quieting a Quiet Engine-The RB211 Demonstrator Programme*. 1976. URL: <https://doi.org/10.4271/760897>.
- [205] Smith, M. and Chow, L. “Validation of a Prediction Model for Aerodynamic Noise from Aircraft Landing Gears”. In: *Aeroacoustics Conferences*. American Institute of Aeronautics and Astronautics, May 2002. DOI: 10.2514/6.2002-2581.
- [206] Smith, M. et al. “Modelling of Landing Gear Noise with Installation Effects”. In: *13th AIAA/CEAS Aeroacoustics Conference (28th AIAA Aeroacoustics Conference)*. AIAA 2007-3472. Rome, May 2007. DOI: 10.2514/6.2007-3472.
- [207] Smith, M. J. T. *Aircraft Noise*. Cambridge Aerospace Series. Cambridge: Cambridge University Press, 1989. ISBN: 0-521-33186-2.
- [208] Stone, J. R. *Interim Prediction Method for Jet Noise*. Tech. rep. TM-X-71618. NASA Lewis Research Center Cleveland, OH, United States: Nasa, Jan. 1974.
- [209] Stone, J. R., Groesbeck, D. E., and Zola, C. L. “Conventional Profile Coaxial Jet Noise Prediction”. In: *AIAA Journal* 21.3 (Mar. 1983), pp. 336–342. DOI: 10.2514/3.8077.

- [210] Stone, J. R., Krejsa, E. A., and Clark, B. J. *Jet Noise Modeling for Coannular Nozzles Including the Effects of Chevrons*. Tech. rep. September. 2003.
- [211] Stone, J. R., Krejsa, E. A., and Clark, B. J. *Jet Noise Modeling for Supersonic Business Jet Application*. Tech. rep. March. 2004.
- [212] Stone, J. R. et al. *Jet Noise Modeling for Suppressed and Unsuppressed Aircraft in Simulated Flight*. Tech. rep. March. 2009.
- [213] Streett, C. L. “Numerical Simulation of Fluctuations Leading to Noise in a Flap-edge Flowfield”. In: *36th AIAA Aerospace Sciences Meeting and Exhibit*. AIAA-98-0628. American Institute of Aeronautics and Astronautics. Reno: AIAA, Jan. 1998, pp. 1–12. DOI: 10.2514/6.1998-628.
- [214] Suryadi, A., Martens, S., and Herr, M. “Trailing Edge Noise Reduction Technologies for Applications in Wind Energy”. In: *23rd AIAA/CEAS Aeroacoustics Conference*. AIAA 2017-3534. AIAA. Denver, Colorado: American Institute of Aeronautics and Astronautics, June 2017, pp. 1–22. DOI: 10.2514/6.2017-3534.
- [215] Sutliff, D. L. et al. “Low-speed fan noise reduction with trailing edge blowing”. In: *8th AIAA/CEAS Aeroacoustics Conference & Exhibit*. June. American Institute of Aeronautics and Astronautics, 2002. URL: <http://multi-science.metapress.com/index/ap67kw1r064201jm.pdf>.
- [216] Tarnopolsky, A., Watkins, G., and Hand, D. J. “Aircraft noise and mental health: I. Prevalence of individual symptoms”. In: *Psychological Medicine* 10.4 (1980), pp. 683–698. ISSN: 0033-2917. DOI: 10.1017/s0033291700054982.
- [217] Thomas, R. H. et al. “Potential for Landing Gear Noise Reduction on Advanced Aircraft Configurations”. In: *22nd AIAA/CEAS Aeroacoustics Conference*. American Institute of Aeronautics and Astronautics (AIAA), May 2016. DOI: 10.2514/6.2016-3039.
- [218] Tyler, J. M. and Sofrin, T. G. *Axial Flow Compressor Noise Studies*. 1962. DOI: 10.4271/620532.
- [219] Walker, M. *Why We Sleep: The New Science of Sleep and Dreams*. Allen Lane, Sept. 2017. ISBN: 0241269067.
- [220] Walker, M. P. and Stickgold, R. “Sleep, Memory, and Plasticity”. In: *Annu. Rev. Psychol.* 57.1 (Apr. 2020), pp. 139–166. ISSN: 0066-4308. DOI: 10.1146/annurev.psych.56.091103.070307.
- [221] Walker, M. P. et al. “Dissociable stages of human memory consolidation and re-consolidation”. In: *Nature* 425.6958 (Oct. 2003), pp. 616–620. ISSN: 1476-4687. URL: <https://doi.org/10.1038/nature01930>.
- [222] Werner-Westphal, C., Heinze, W., and Horst, P. “Multidisciplinary Integrated Preliminary Design Applied to Future Green Aircraft Configurations”. In: *45th AIAA Aerospace Sciences Meeting and Exhibit*. January. Reno, Nevada: American Institute of Aeronautics and Astronautics, 2007, pp. 1–13.
- [223] Werner-Westphal, C., Heinze, W., and Horst, P. “Multidisciplinary Integrated Preliminary Design Applied to Unconventional Aircraft Configurations”. In: *Journal of Aircraft*. Vol. 45. 2. American Institute of Aeronautics and Astronautics, Mar. 2008, pp. 581–590. DOI: 10.2514/1.32138.

- [224] Wick, A. T. et al. “Hybrid Wing Body Performance Validation at the National Transonic Facility”. In: AIAA SciTech Forum. American Institute of Aeronautics and Astronautics, Mar. 2019. DOI: 10.2514/6.2017-0099.
- [225] Wild, J., Pott-Pollenske, M., and Nagel, B. “An integrated design approach for low noise exposing high- lift devices”. In: *3rd AIAA Flow Control Conference*. June. San Francisco, California, 2006, pp. 1–16.
- [226] Williams, J. E. F. and Hall, L. H. “Aerodynamic Sound Generation by Turbulent Flow in the Vicinity of a Scattering Half Plane”. In: *Journal of Fluid Mechanics*. Vol. 40. 4. Cambridge University Press, Mar. 1970, pp. 657–670. DOI: 10.1017/s0022112070000368.
- [227] Wilson, D. K. and Thomson, D. W. “Acoustic propagation through anisotropic, surface-layer turbulence”. In: *The Journal of the Acoustical Society of America* 96.2 (Aug. 1994), pp. 1080–1095. ISSN: 0001-4966. DOI: 10.1121/1.410384.
- [228] Wilson, N. J. “Developing the Rolls-Royce Tay”. In: *ASME International Gas Turbine and Aeroengine Congress and Exposition V002T02A017* (1988). ISSN: 978-0-7918-7919-1. URL: <https://doi.org/10.1115/88-GT-302>.
- [229] Wirtschaft Energie, V. u. W. Hessisches Ministerium für. *Lärmschutzbereich Flughafen Frankfurt*. Website. Access: 2020 May 20. Oct. 2007. URL: <https://wirtschaft.hessen.de/verkehr/luftverkehr/laermschutz/organisation/laermschutzbereich-flughafen-frankfurt>.
- [230] Wörner, J. et al. *Frankfurter Fluglärmindex 2.0*. Tech. rep. Kelsterbach: Forum Flughafen und Region Frankfurt, May 2019.
- [231] Zorumski, W. E. *Aircraft Noise Prediction Program Theoretical Manual Part 2*. Technical Report NASA-TM-83199-PT-2, L-14805-PT-2. Part 2: Noise Sources. NASA, Feb. 1982. URL: <https://ntrs.nasa.gov/search.jsp?R=19820012073>.



# A | Additional Figures

## Chapter 5

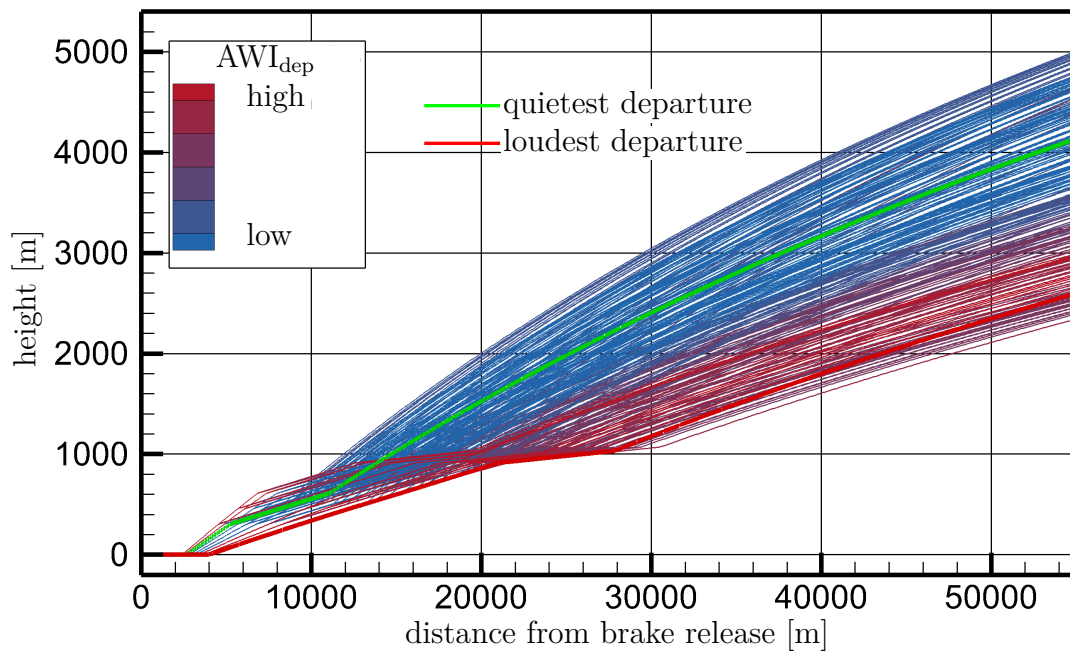


**Figure A.5.0.1:** Departure Awakening Index ( $AWI_{dep}$ ) as in Figure 5.3 with unmodified Kontos fan sound model. The color gives a tendency which procedure causes which value of the Departure Awakening Index. This figure is based on the same airplane, the same trajectories, and differs from Figure 5.3 only by the buzz-saw sound model.

# Chapter 6

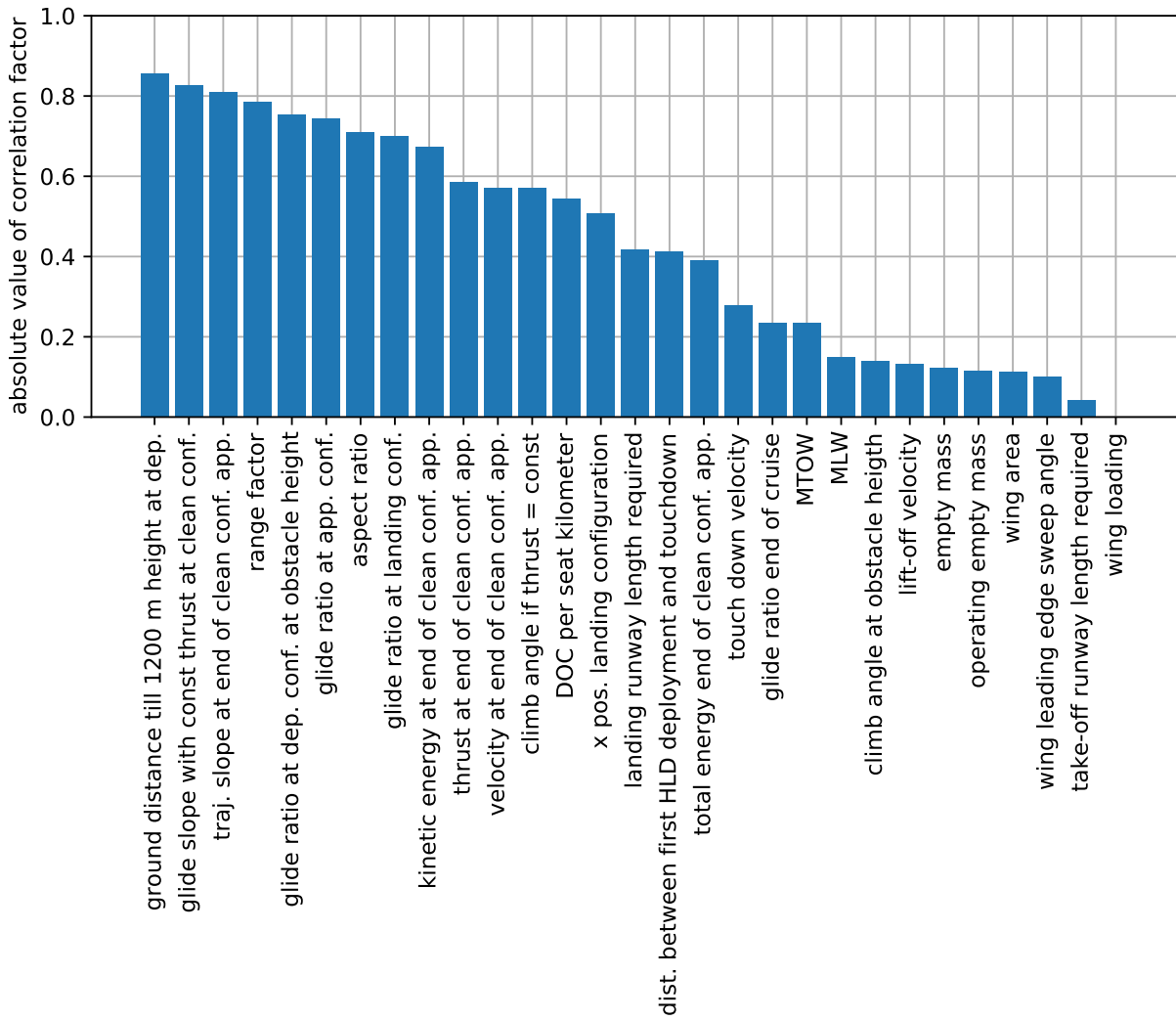


**Figure A.6.0.2:** Correlation coefficients of various variables with the Overall Awakening Index (AWI). The correlation coefficients with the Departure Awakening Index and Approach Awakening Index are shown in Figures 6.1 and 6.3, respectively.

## Departure Situation

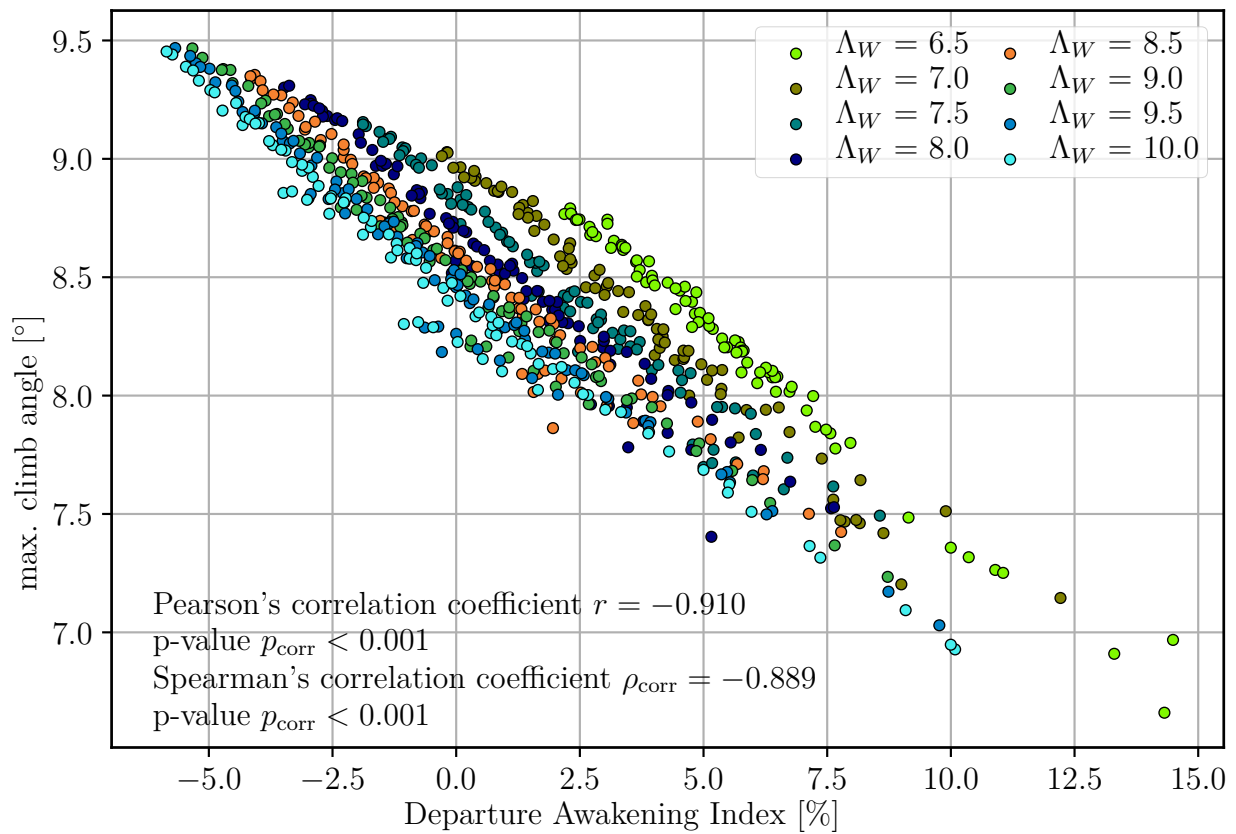


**Figure A.6.1.3:** Max. climb angle ( $\gamma_{\max}$ ) over the Departure Awakening Index of the basic airplane. The maximum climb angle has been calculated with a constant engine thrust for all airplanes considering the airplanes' masses and aerodynamics in departure configuration.

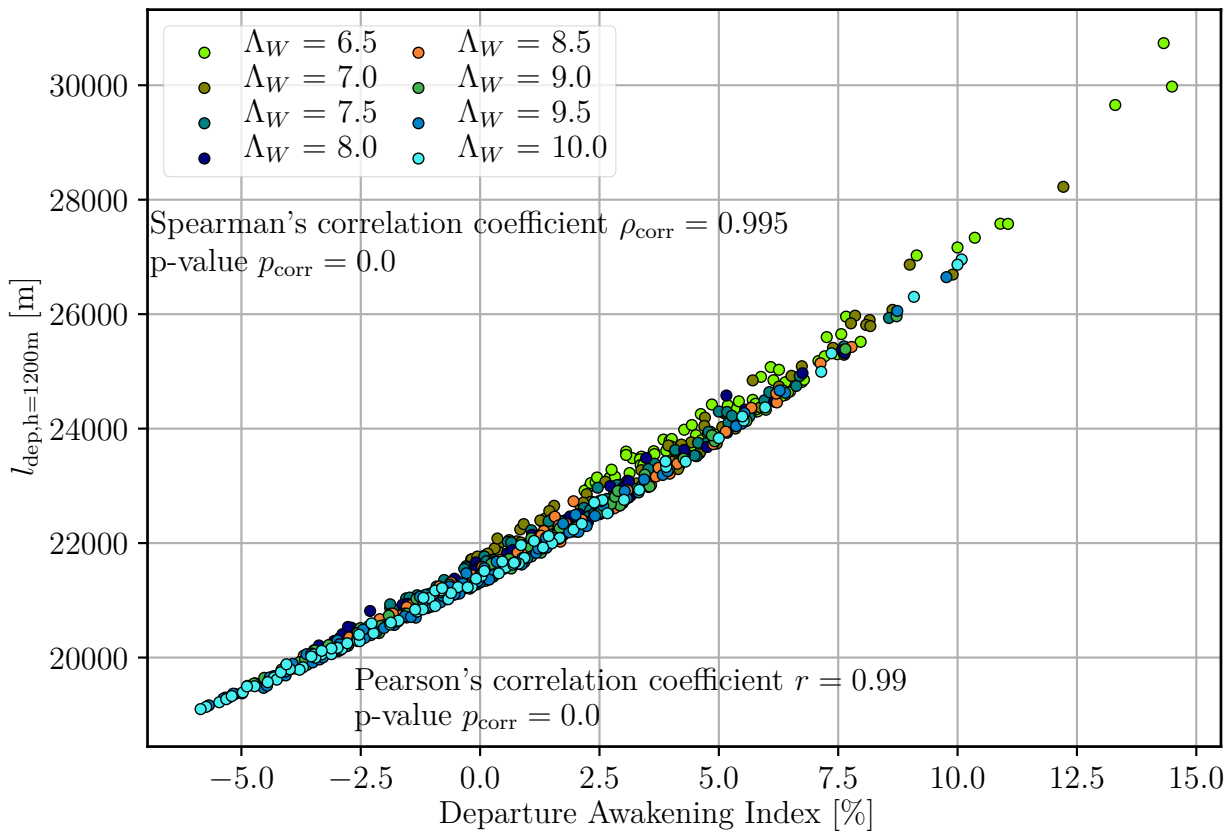


**Figure A.6.1.4:** Distance until a height of 1200 m is reached over the Departure Awakening Index of the basic airplane. The Pearson's correlation coefficient is about  $r = 0.99$ .

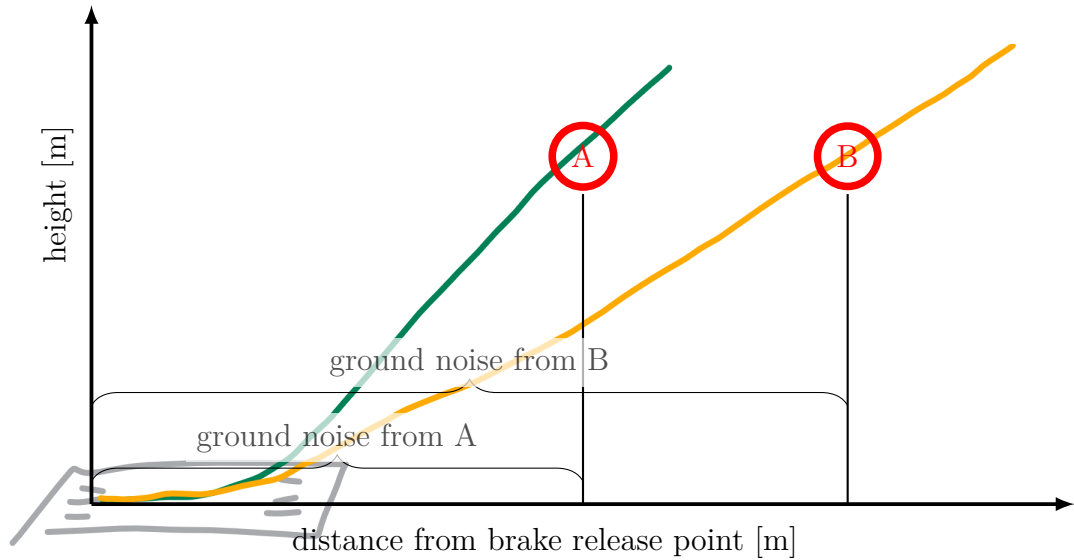


**Figure A.6.1.5:** Sketch explaining why a steep averaged climb response lowers the ground noise. It is assumed, that the noise emissions at location A and B are almost the same. Hence, the ground noise caused by location A and louder pollutes the ground over a shorter distance than the ground noise caused by location B and louder. Louder on ground would be all locations between brake release and the locations A and B, respectively. For this explanation, directivity effects have been neglected. However, they have been considered in the simulations.

## Approach Situation

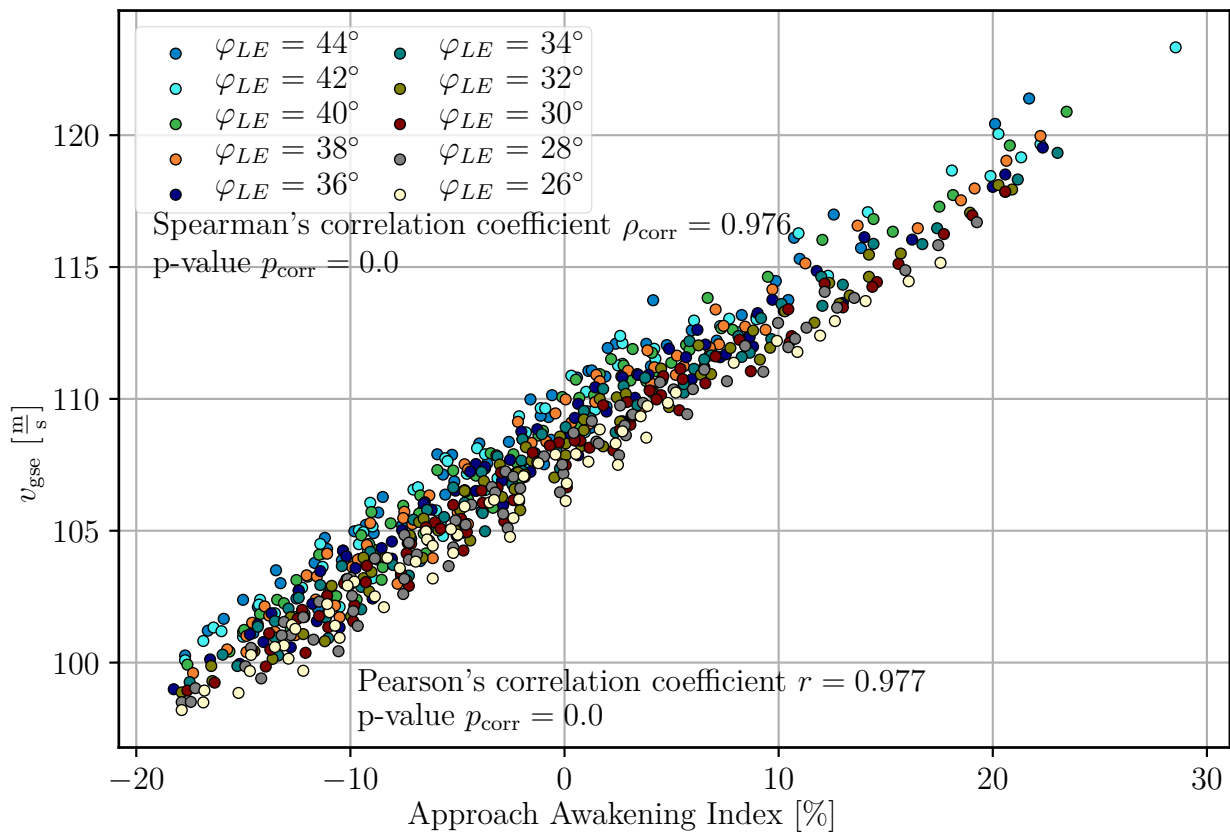


**Figure A.6.2.6:** Velocity at the end of the cruise configuration segment ( $v_{\text{gse}}$ ) over the Approach Awakening Index ( $\text{AWI}_{\text{app}}$ ) of the basic airplane.

Effects of Planform Parameters on the Awakening Index

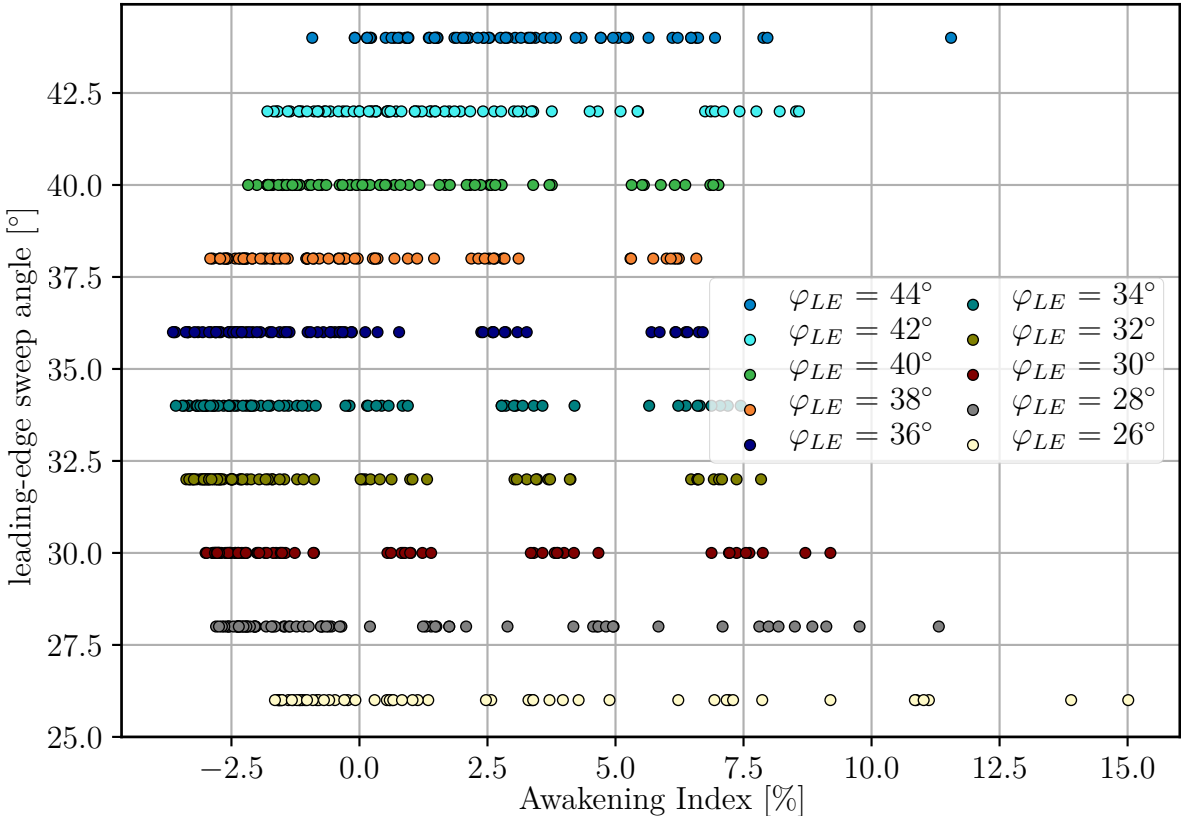
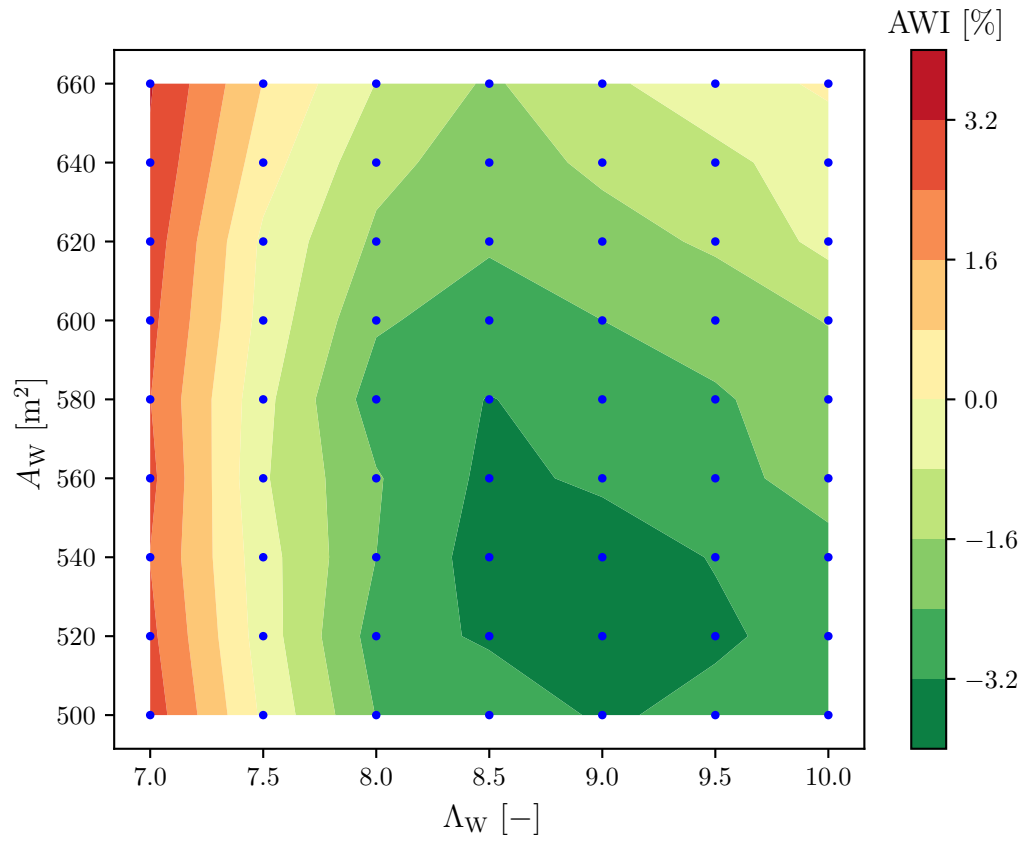
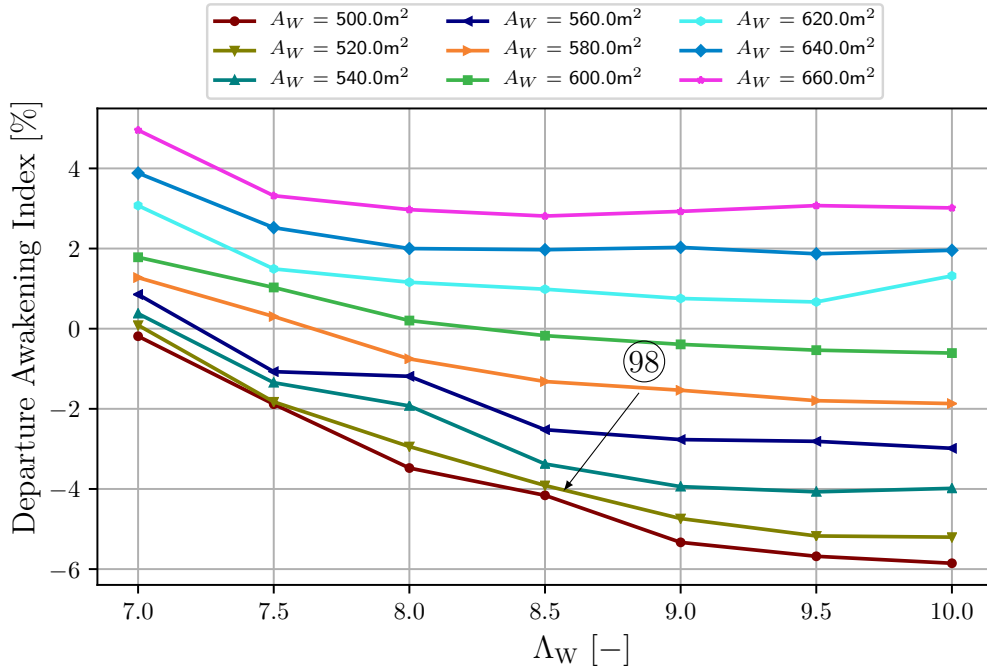


Figure A.6.3.7: Leading-edge sweep angle ( $\varphi_{LE}$ ) and Overall Awakening Index (AWI) for the various airplane designs of the basic airplane study.



**Figure A.6.3.8:** Overall Awakening Index over the aspect ratio and for all the wing areas for the leading-edge sweep angle  $\varphi_{LE} = 36^\circ$ . The same data as a line plot is plotted in Figure 6.4.



**Figure A.6.3.9:** Departure Awakening Index ( $AWI_{dep}$ ) over the aspect ratio for  $\varphi_{LE} = 36^\circ$  and all the wing areas ( $A_W$ ).

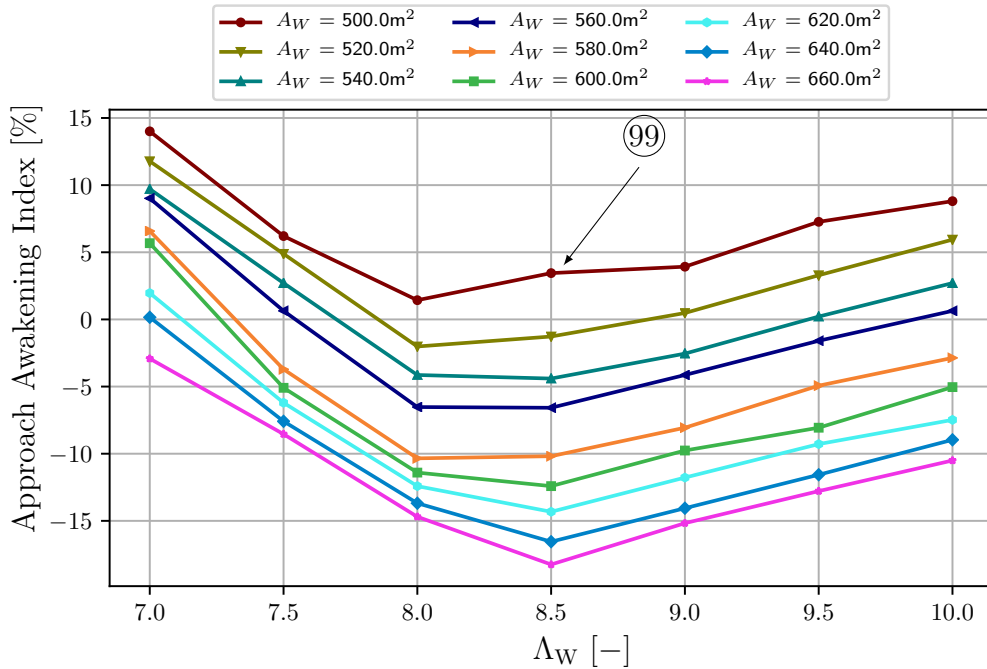


**Figure A.6.3.10:** Approach Awakening Index ( $AWI_{app}$ ) over the aspect ratio for  $\varphi_{LE} = 36^\circ$  and all the wing areas.

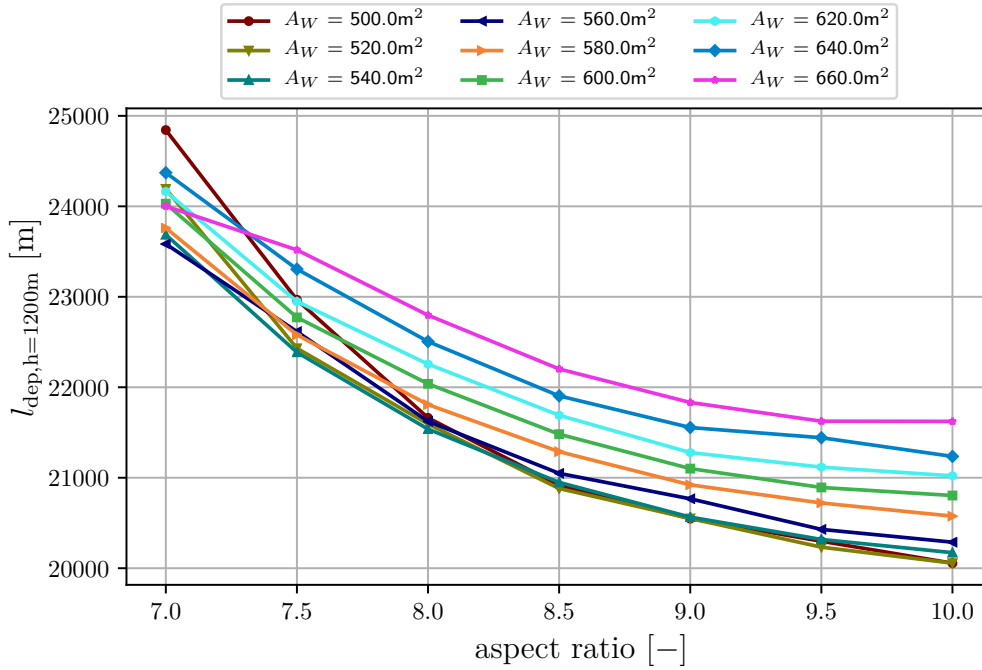


**Figure A.6.3.11:** The ground track length up to a flight height of 1200 m ( $l_{\text{dep},h=1200\text{m}}$ ) over the aspect ratio for all the wing areas ( $A_W$ ) at a leading-edge sweep angle  $\varphi_{\text{LE}} = 28^\circ$  for the basic airplane study.

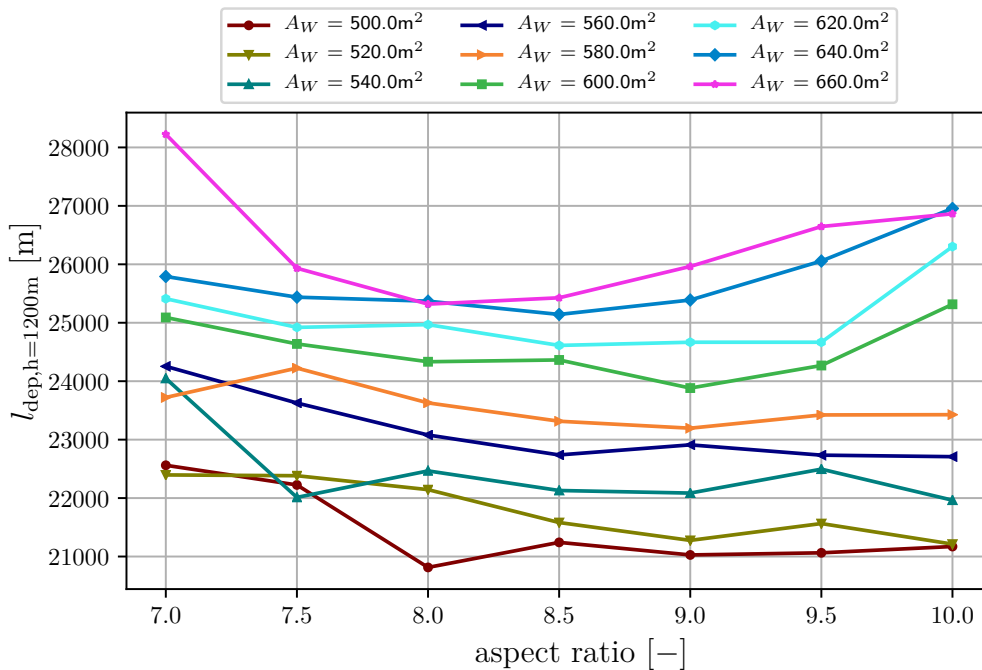


**Figure A.6.3.12:** The ground track length up to a flight height of 1200 m ( $l_{\text{dep},h=1200\text{m}}$ ) over the aspect ratio for all the wing areas ( $A_W$ ) at a leading-edge sweep angle of  $\varphi_{\text{LE}} = 44^\circ$  for the basic airplane study.

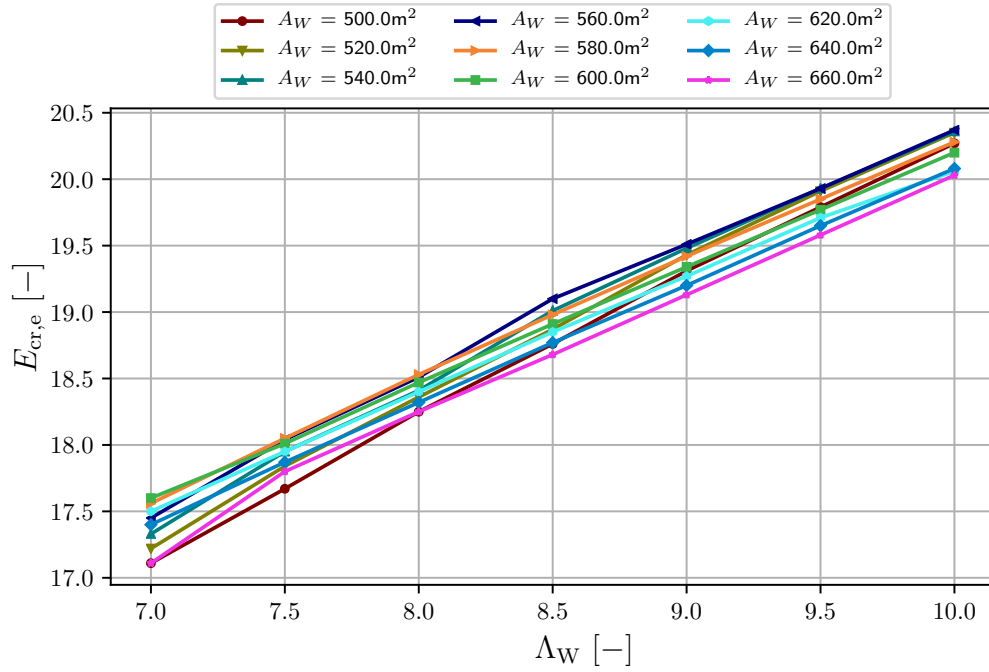


**Figure A.6.3.13:** Glide ratio in cruise configuration ( $E_{cr,e}$ ) at the end of cruise flight over the aspect ratio for all the wing areas for  $\varphi_{LE} = 36^\circ$  for the basic airplane study.

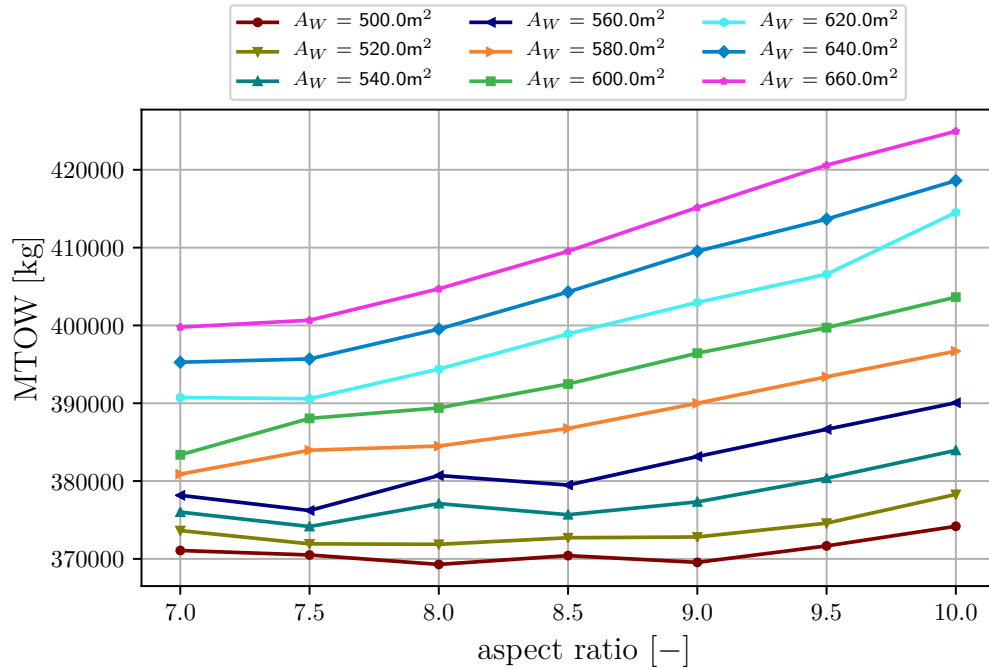


**Figure A.6.3.14:** Maximum takeoff weight (MTOW) over the aspect ratio for all the wing areas for  $\varphi_{LE} = 36^\circ$  for the basic airplane study. Payload and design range have been held constant for the whole study.

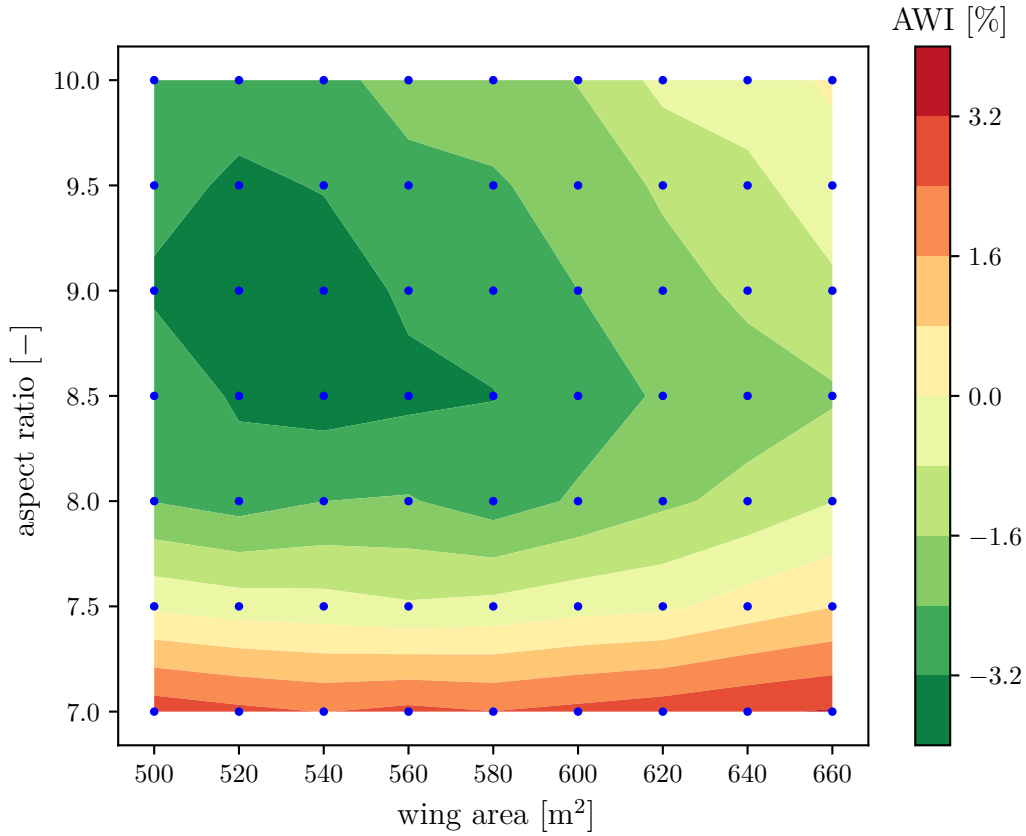


**Figure A.6.3.15:** Awakening Index (AWI) over the wing area and over the aspect ratios for  $\varphi_{LE} = 36^\circ$ . The same data as a line plot is plotted in Figure 6.7.

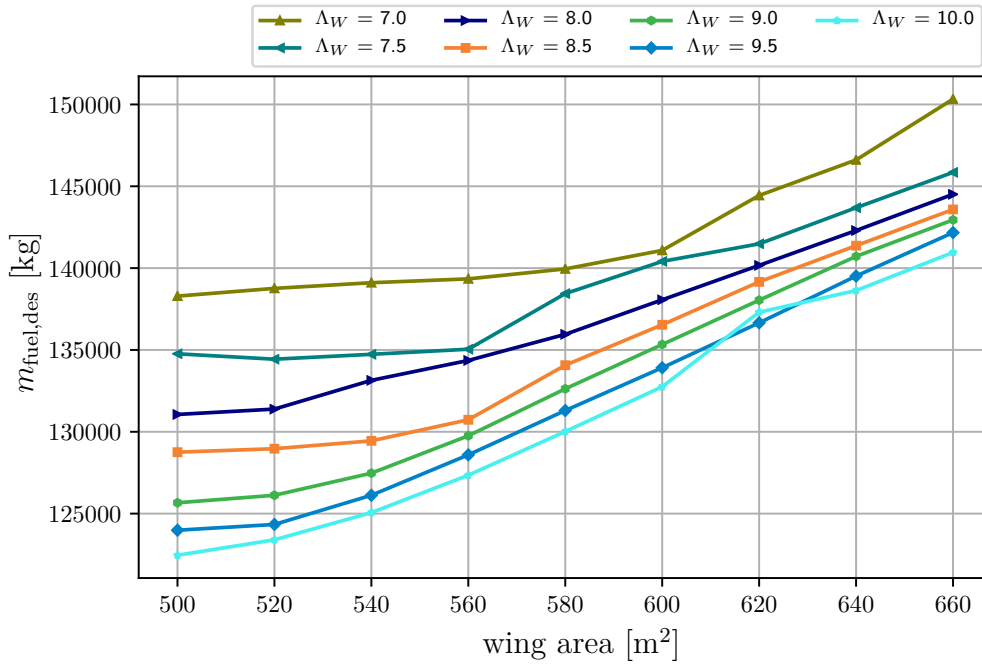


**Figure A.6.3.16:** Trip fuel mass for design mission ( $m_{fuel,des}$ ) over the wing area for  $\varphi_{LE} = 36^\circ$  for selected aspect ratios ( $\Lambda_W$ ).

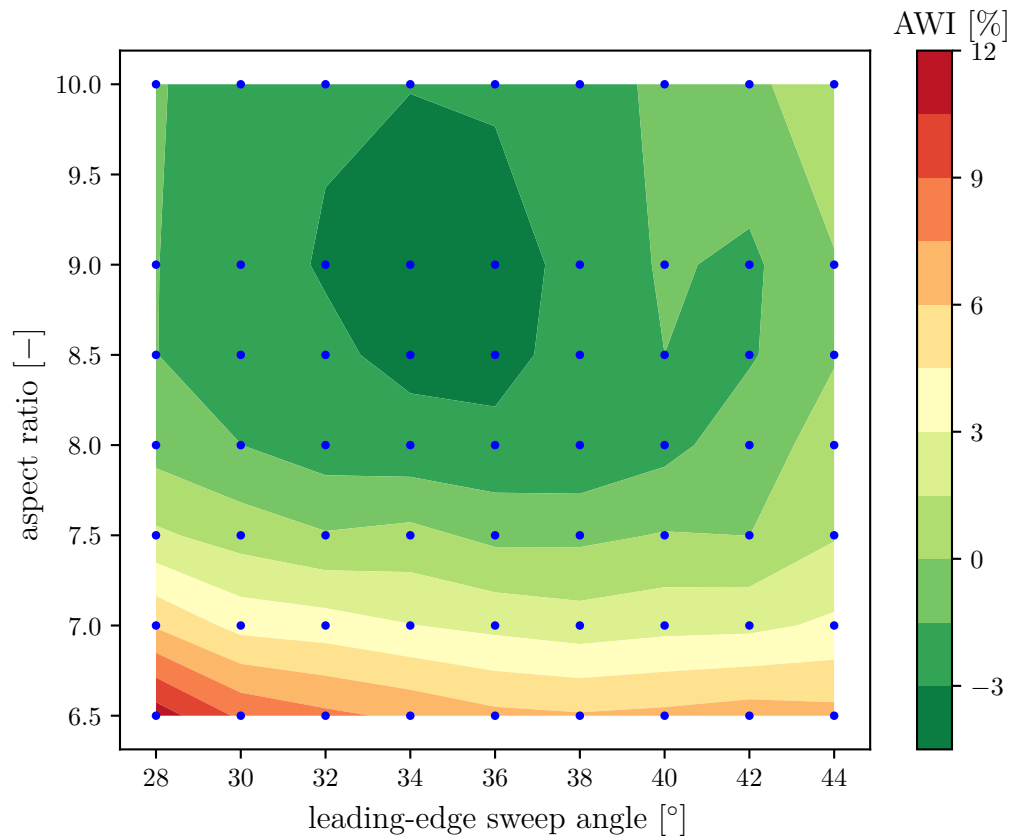


**Figure A.6.3.17:** Awakening Index over the leading-edge sweep angle ( $\varphi_{LE}$ ) for all the aspect ratios at a wing area  $A_W = 520 \text{ m}^2$ . The same data as a line plot is plotted in Figure 6.10.

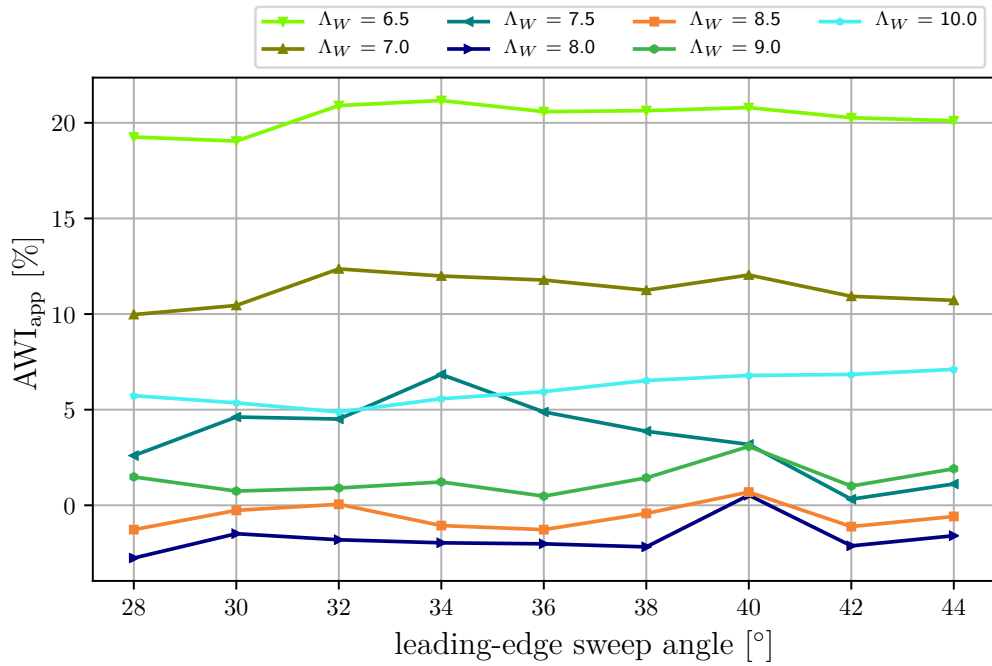


**Figure A.6.3.18:** Approach Awakening Index over the leading-edge sweep angle for  $A_W = 520 \text{ m}^2$  for all the aspect ratios.

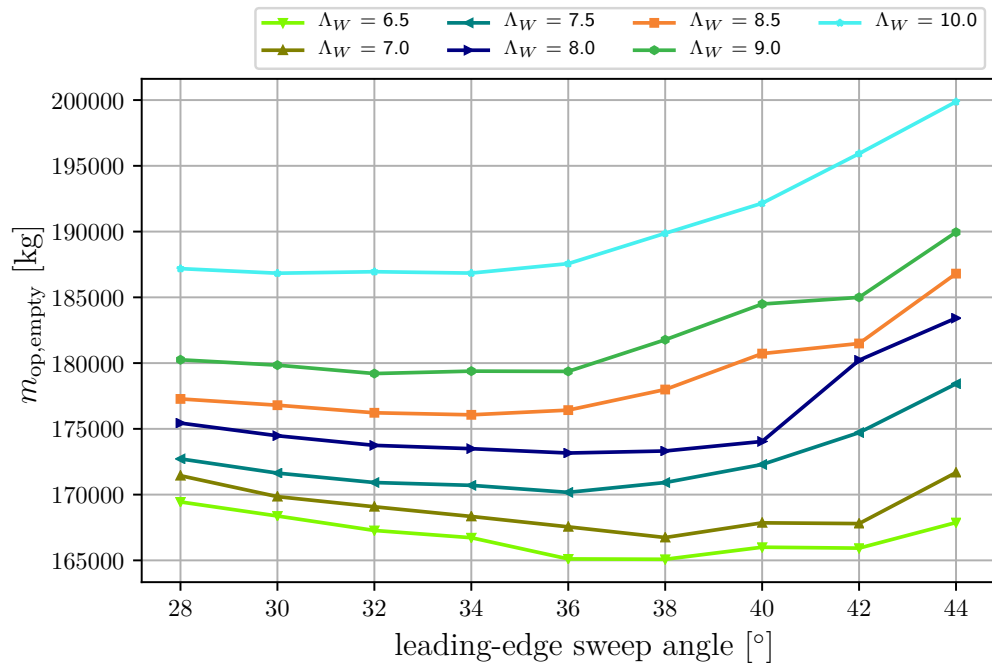


**Figure A.6.3.19:** Operating empty weight ( $m_{\text{op,empty}}$ ) over the leading-edge sweep angle for  $A_W = 520 \text{ m}^2$  for all the aspect ratios.

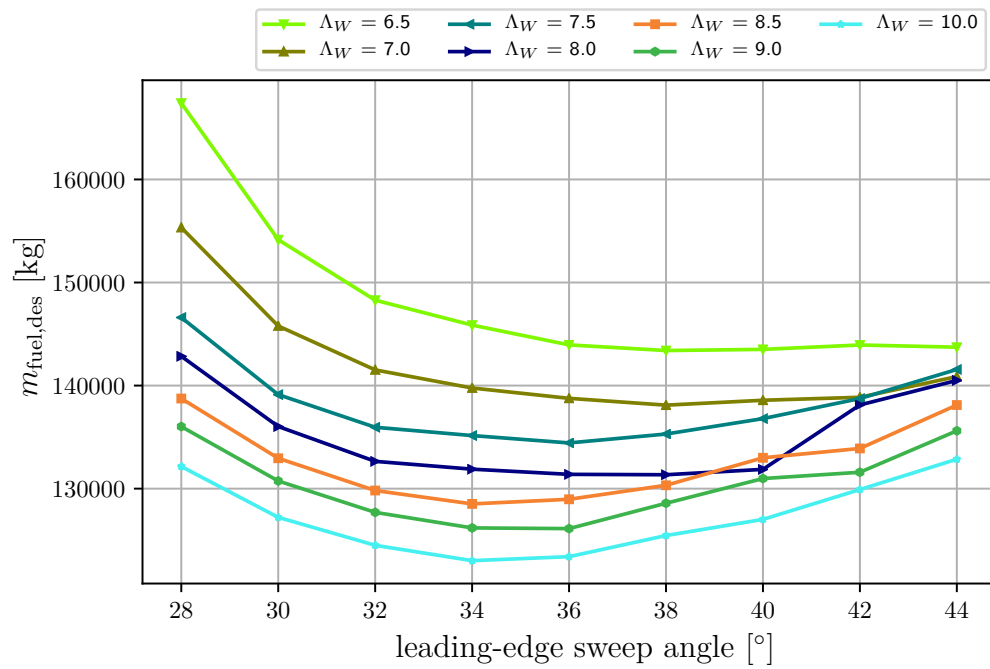


**Figure A.6.3.20:** Trip fuel mass for design mission ( $m_{\text{fuel,des}}$ ) over the leading-edge sweep angle for  $A_W = 520 \text{ m}^2$  for all the aspect ratios.

## Airplane Selection

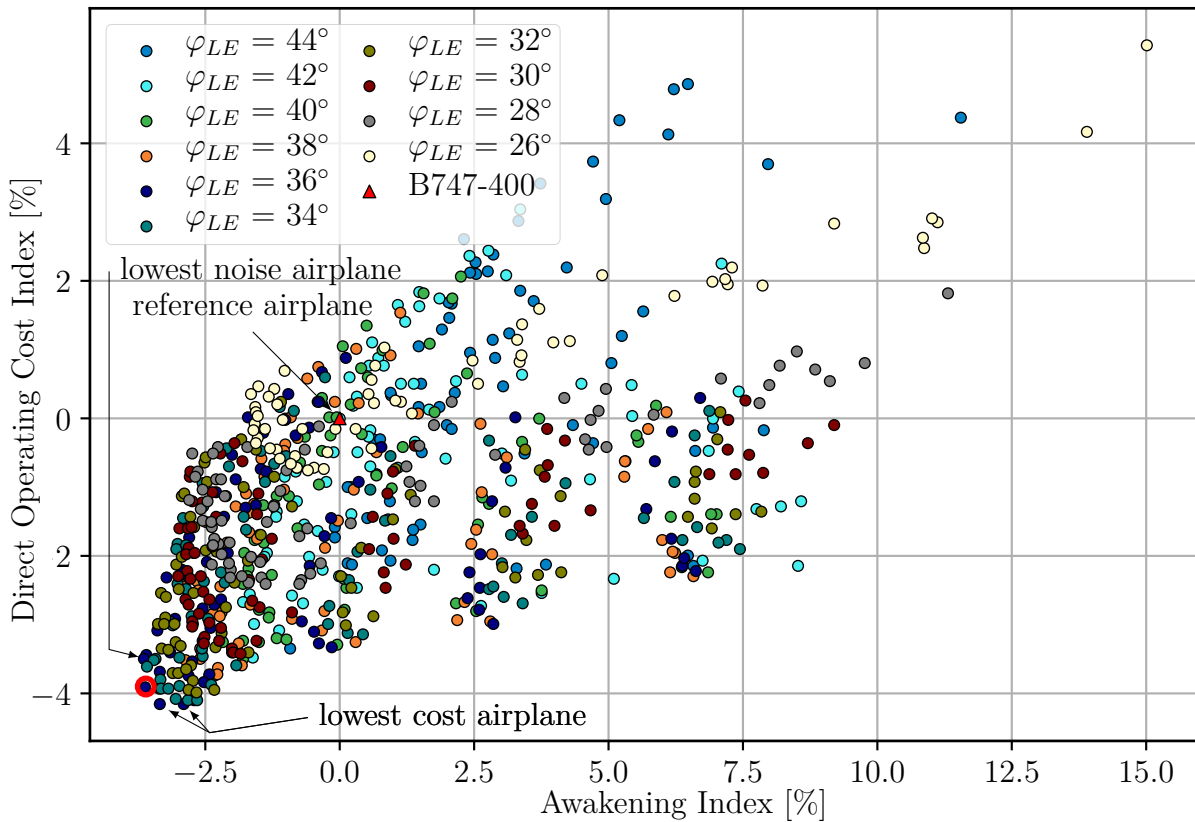


**Figure A.6.4.21:** Direct Operating Cost Index (DOCI) and Awakening Index (AWI) for the **basic airplane** study. The color denotes for the leading-edge sweep angle ( $\varphi_{LE}$ ). The red circle marks the selected optimum, that exhibits  $\varphi_{LE} = 36^\circ$ ,  $A_W = 520 \text{ m}^2$ , and  $\Lambda_W = 9.0$ . The same airplanes, though distinguished by color according to their aspect ratio and wing area, are shown in Figures 6.13 and A.6.4.22, respectively.

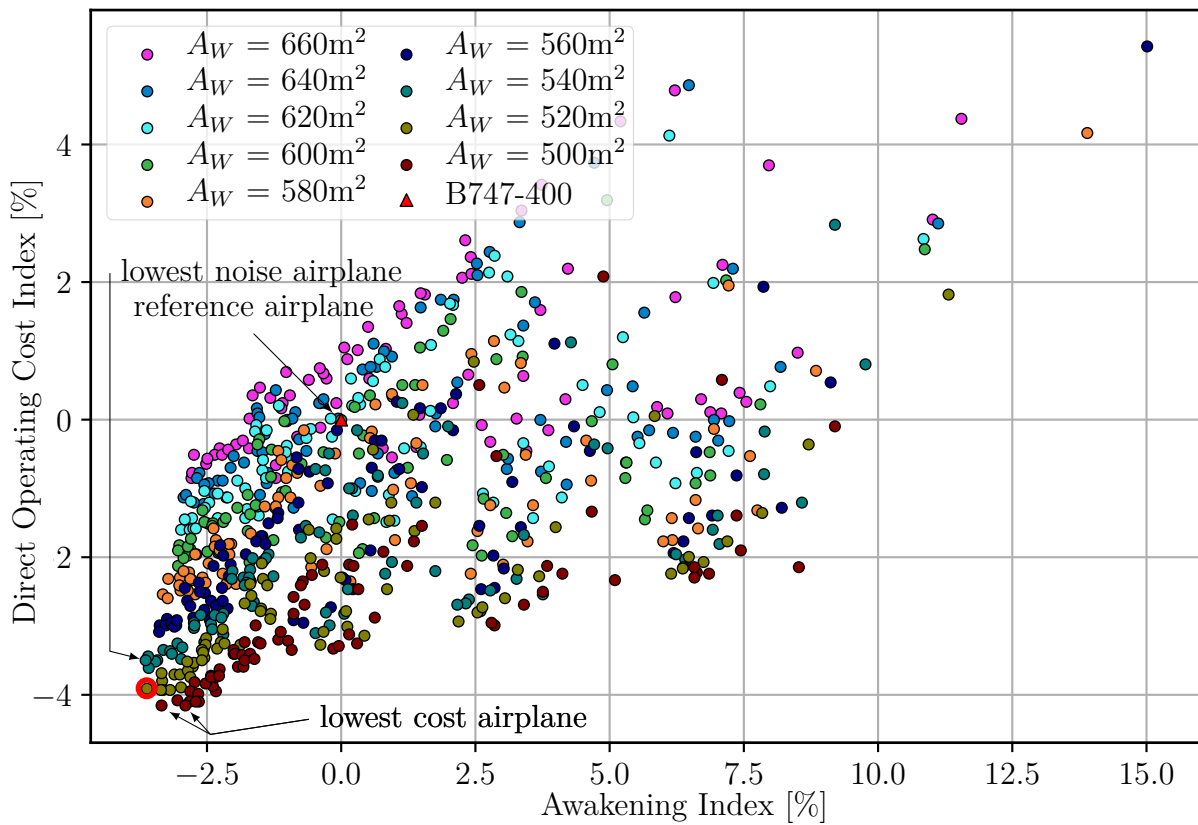


**Figure A.6.4.22:** Direct Operating Cost Index (DOCI) and Awakening Index (AWI) for the **basic airplane** study. The color denotes the wing area ( $A_W$ ). The red circle marks the selected optimum, that exhibits  $\varphi_{LE} = 36^\circ$ ,  $A_W = 520\text{m}^2$ , and  $\Lambda_W = 9.0$ . The same data colored by aspect ratio and leading-edge sweep has been depicted in Figures 6.13 and A.6.4.21.

### Dominating Airframe Noise Sources

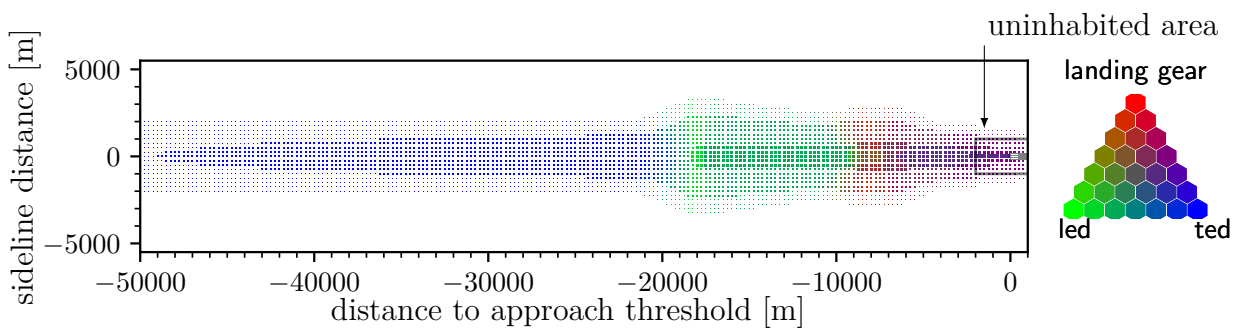


**Figure A.6.5.23:** Dominating airframe noise sources during approach of the selected **basic airplane** and, hence, prior to mounting low noise technologies. The same data, but showing relevant approach noise sources, has been depicted in Figure 6.16.

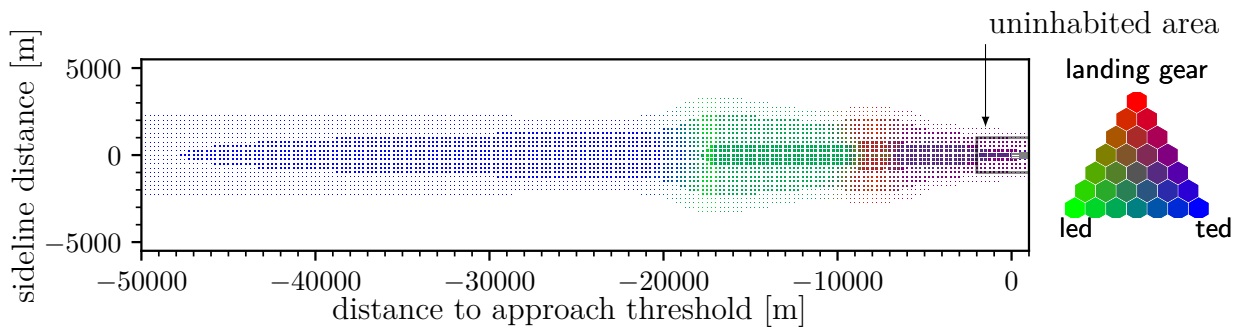


**Figure A.6.6.24:** Dominating airframe noise sources during approach of the **reference airplane**. The same data, but showing relevant approach noise sources, has been depicted in Figure 6.20.

## Chapter 7

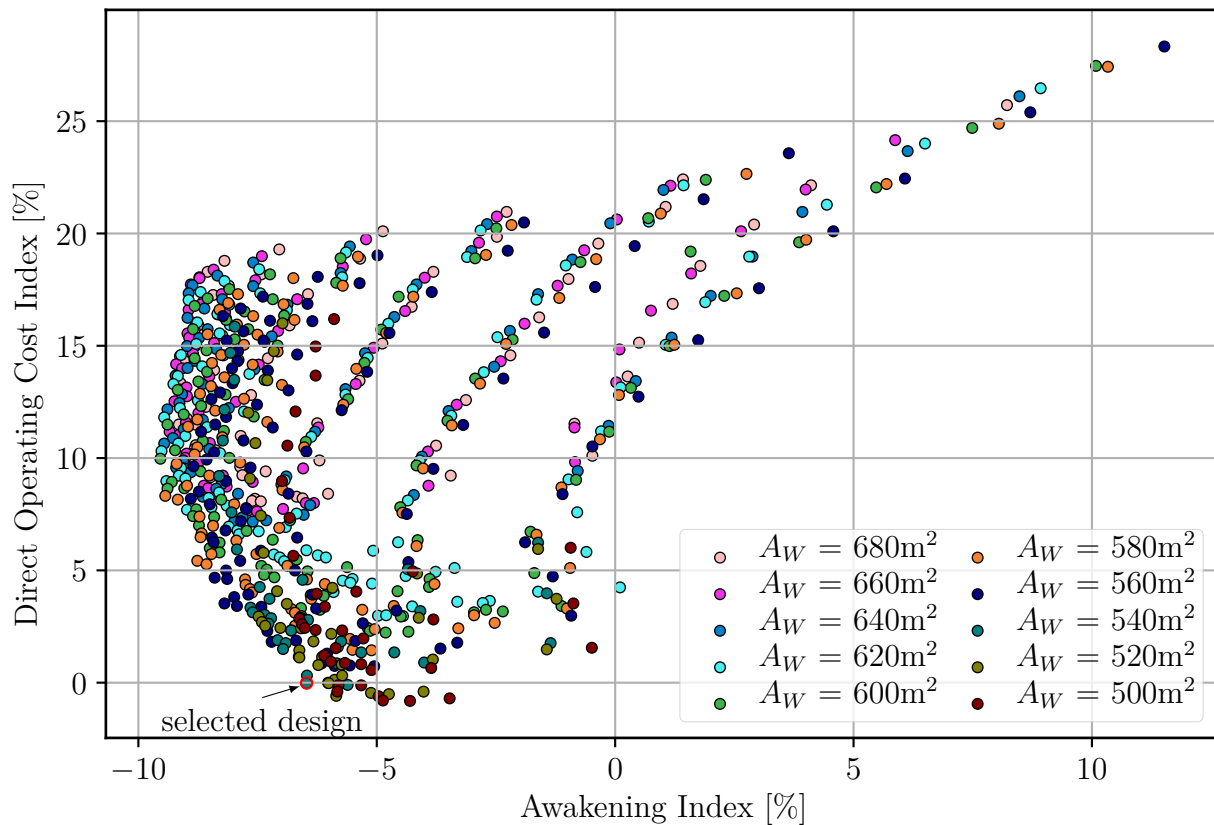


**Figure A.7.1.25:** Direct Operating Cost Index (DOCI) over Awakening Index (AWI) of the **engine-over-wing airplane** study. Each point corresponds to one airplane design, and shows its Direct Operating Cost Index and Awakening Index. The color denotes the wing area ( $A_W$ ). The same airplanes, though distinguished by color according to their aspect ratio and leading-edge sweep angle, are shown in Figures 7.4 and A.7.1.26, respectively.

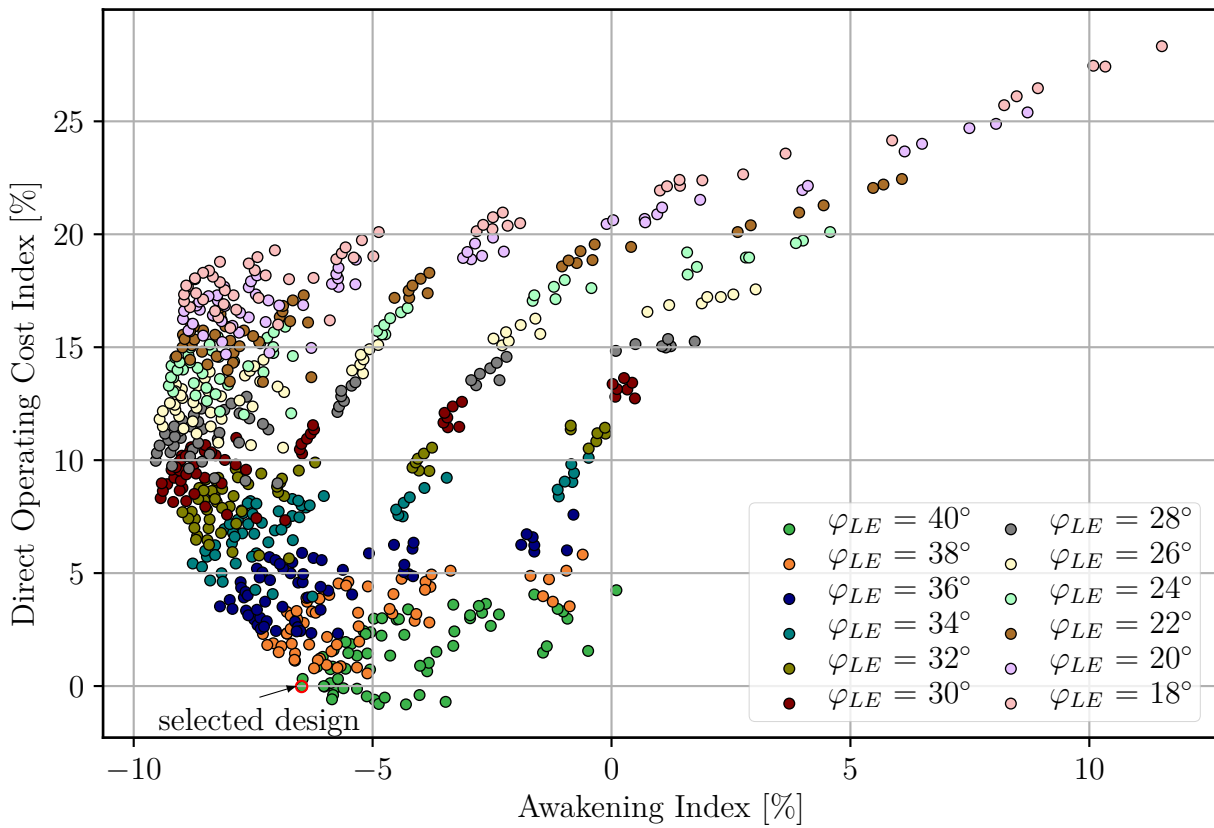


**Figure A.7.1.26:** Direct Operating Cost Index (DOCI) over Awakening Index (AWI) of the **engine-over-wing airplane** study. Each point corresponds to one airplane design, and shows its Direct Operating Cost Index and Awakening Index. The color denotes for the leading-edge sweep angle ( $\varphi_{LE}$ ). The same airplanes colored by the aspect ratio and wing area have been shown in Figures 7.4 and A.7.1.25, respectively.

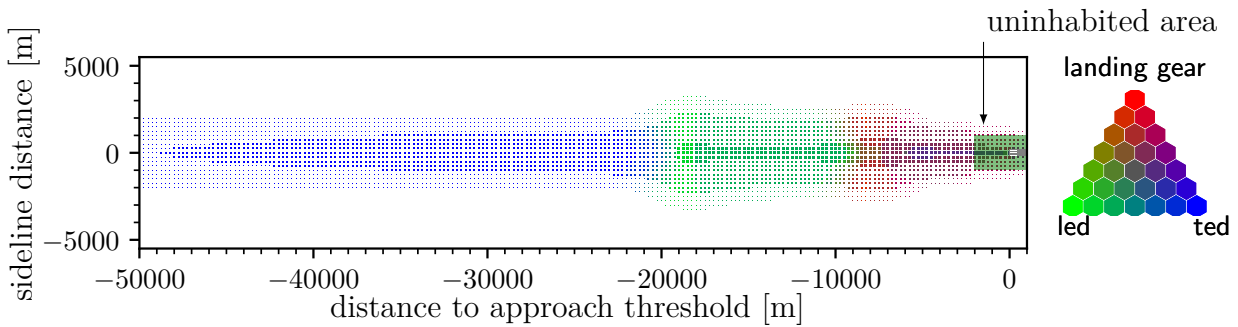


**Figure A.7.1.27:** Dominating airframe sound sources and the awakening probability of the **engine-over-wing airplane** during approach. The same figure showing all relevant sound sources during approach has been depicted in Figure 7.8.

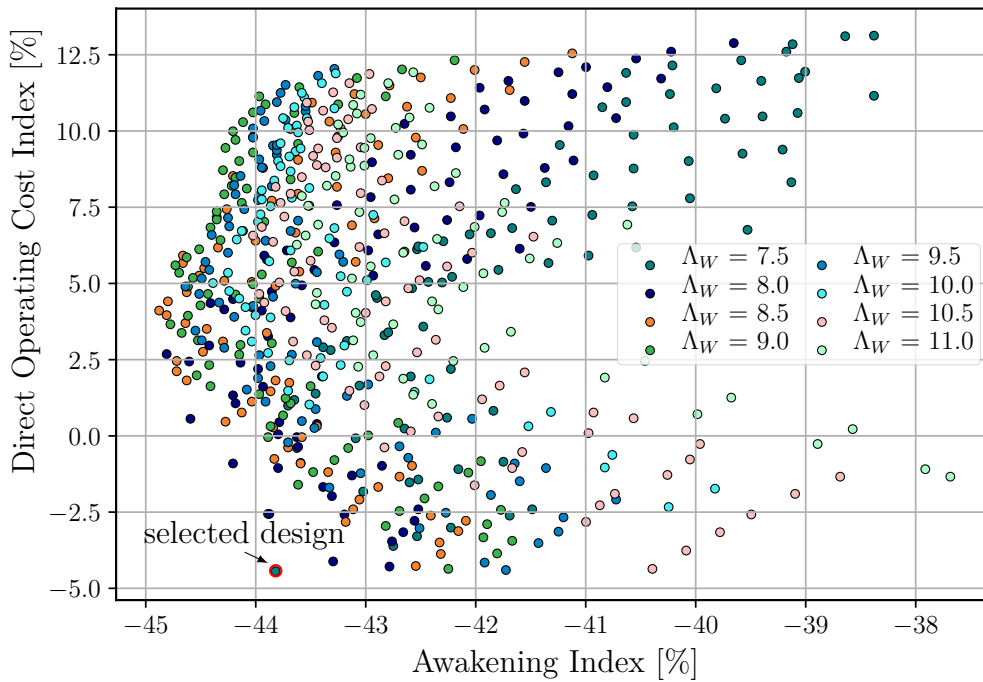


**Figure A.7.2.28:** Direct Operating Cost Index over Awakening Index of the **new-engine-option airplane**. Each point corresponds to one airplane design, and shows its Direct Operating Cost Index and causing Awakening Index. The color displays the aspect ratio ( $\Lambda_W$ ), as it has been the design parameter with the highest correlation coefficient. The same airplanes, though distinguished by color according to their wing area and leading-edge sweep angle, are shown in Figures A.7.2.29 and A.7.2.30, respectively.

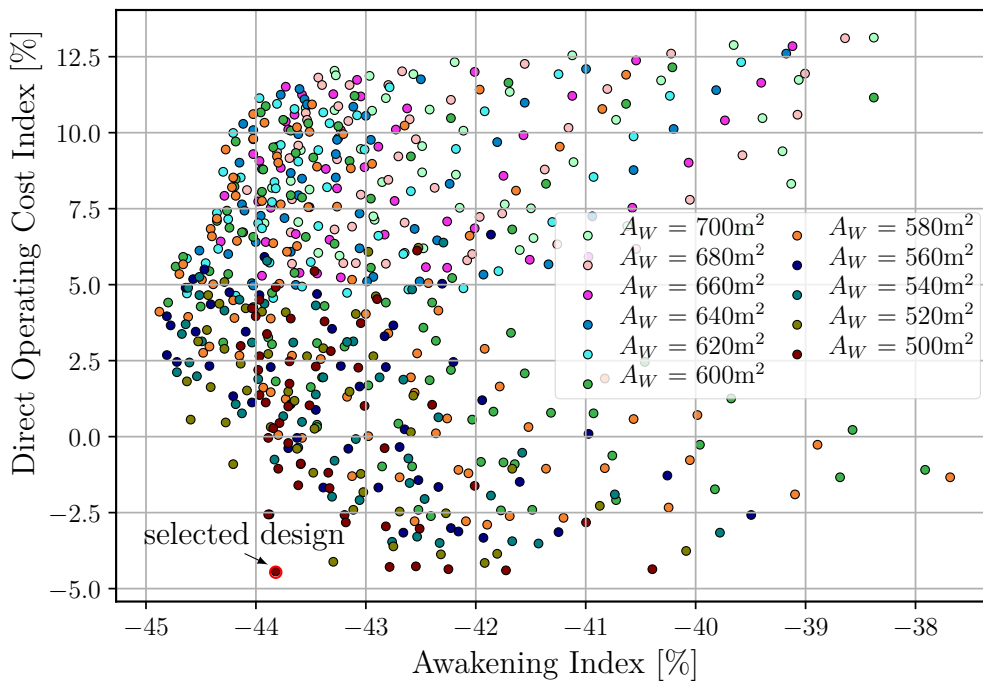


**Figure A.7.2.29:** Direct Operating Cost Index (DOCI) over Awakening Index (AWI) of the **new-engine-option airplane** study. Each point corresponds to one airplane design, and shows its Direct Operating Cost Index and Awakening Index. The color denotes the wing area ( $A_W$ ). The same airplanes, though distinguished by color according to their aspect ratio and leading-edge sweep angle, are shown in Figures A.7.2.28 and A.7.2.30, respectively.

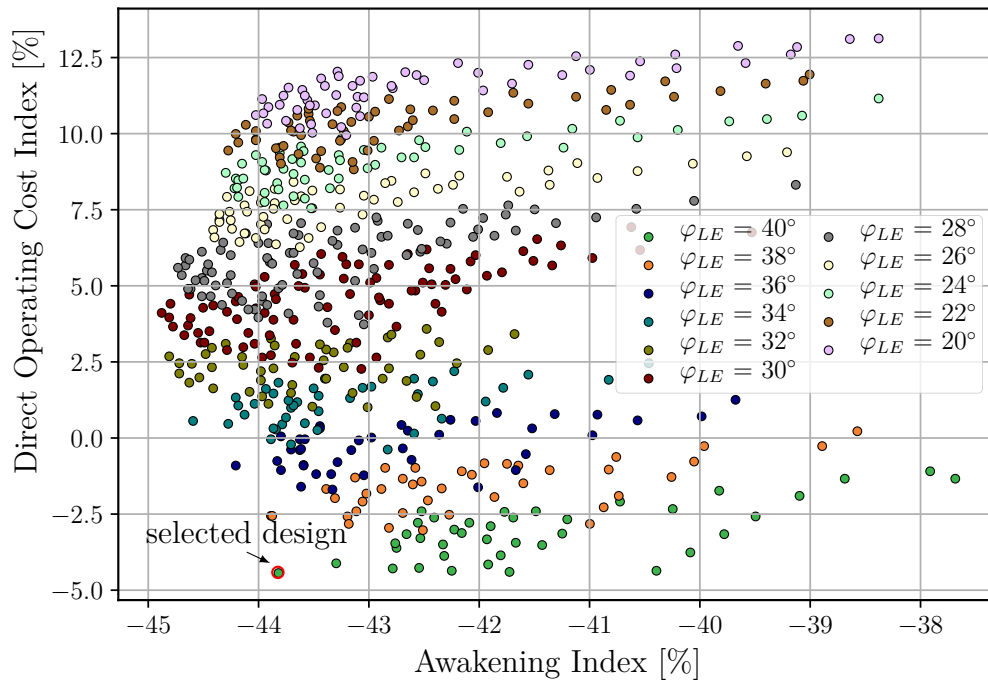


**Figure A.7.2.30:** Direct Operating Cost Index (DOCI) over Awakening Index (AWI) of the **new-engine-option airplane** study. Each point corresponds to one airplane design, and shows its Direct Operating Cost Index and Awakening Index. The color denotes for the leading-edge sweep angle ( $\varphi_{LE}$ ). The same airplanes colored by the aspect ratio and wing area have been shown in Figures A.7.2.28 and A.7.2.29, respectively.

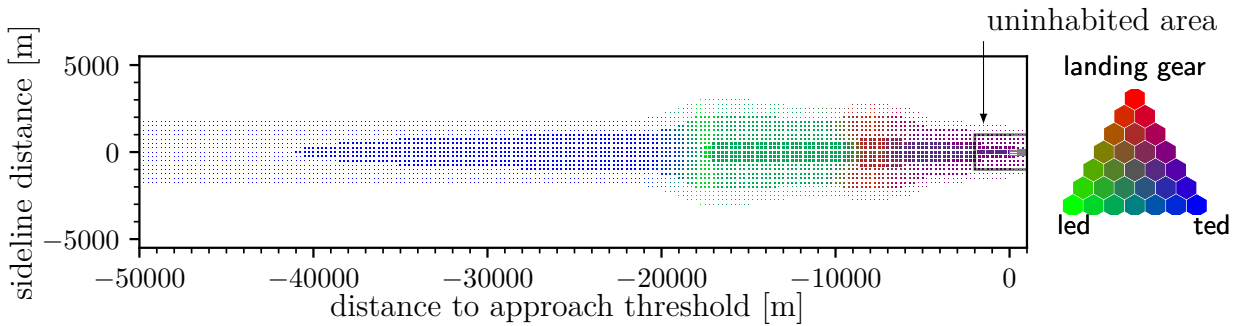


**Figure A.7.2.31:** Dominating airframe noise sources of the **new-engine-option airplane** during approach. Figure 7.13 shows the same approach and its corresponding awakening reactions colored by the noise sources relevant during approach.

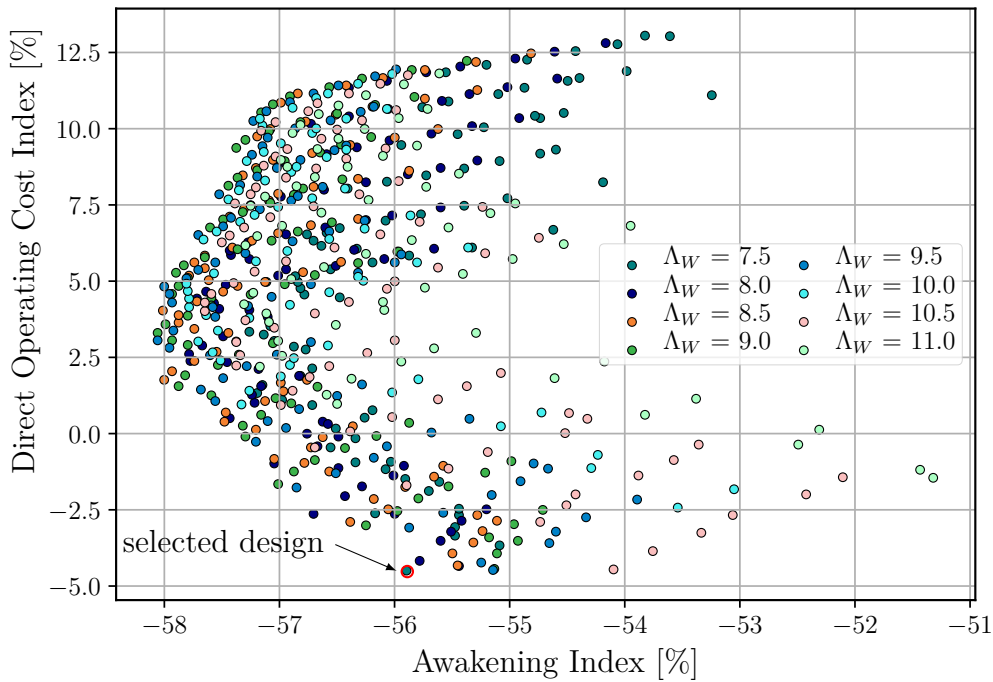


**Figure A.7.3.32:** Direct Operating Cost Index over Awakening Index of the **low-noise-wing airplane**. Each point corresponds to one airplane design, and shows its Direct Operating Cost Index and causing Awakening Index. The color displays the aspect ratio ( $\Lambda_W$ ), as it has been the design parameter with the highest correlation coefficient. The same airplanes, though distinguished by color according to their wing area and leading-edge sweep angle, are shown in Figures A.7.3.33 and A.7.3.34, respectively.

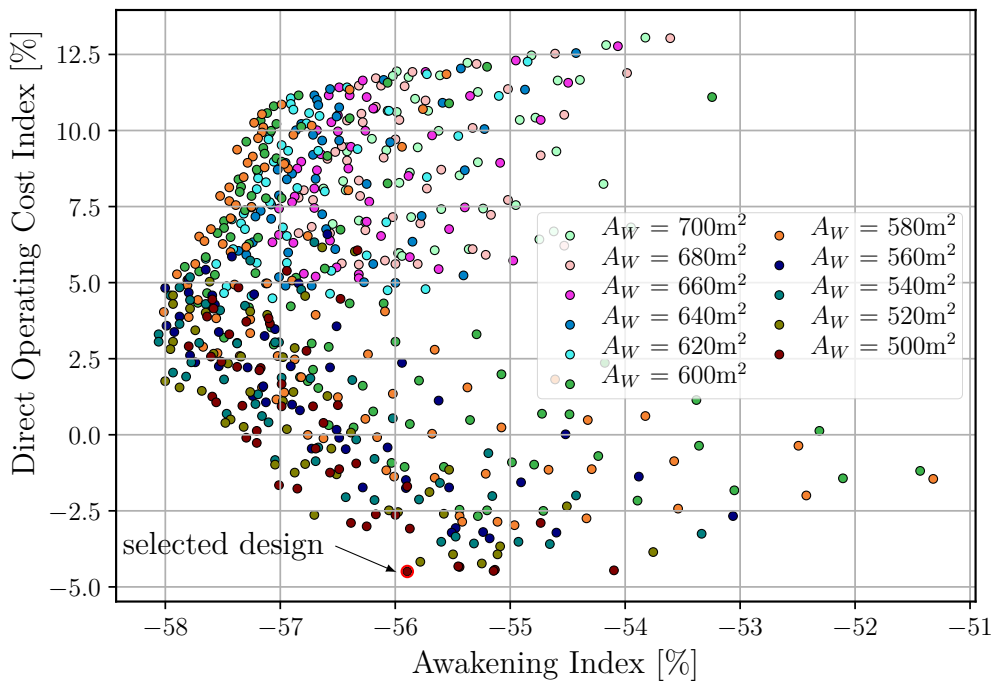


**Figure A.7.3.33:** Direct Operating Cost Index over Awakening Index of the **low-noise-wing airplane** study. Each point corresponds to one airplane design, and shows its Direct Operating Cost Index and Awakening Index. The color denotes the wing area ( $A_W$ ). The same airplanes, though distinguished by color according to their aspect ratio and leading-edge sweep angle, are shown in Figures A.7.3.32 and A.7.3.34, respectively.

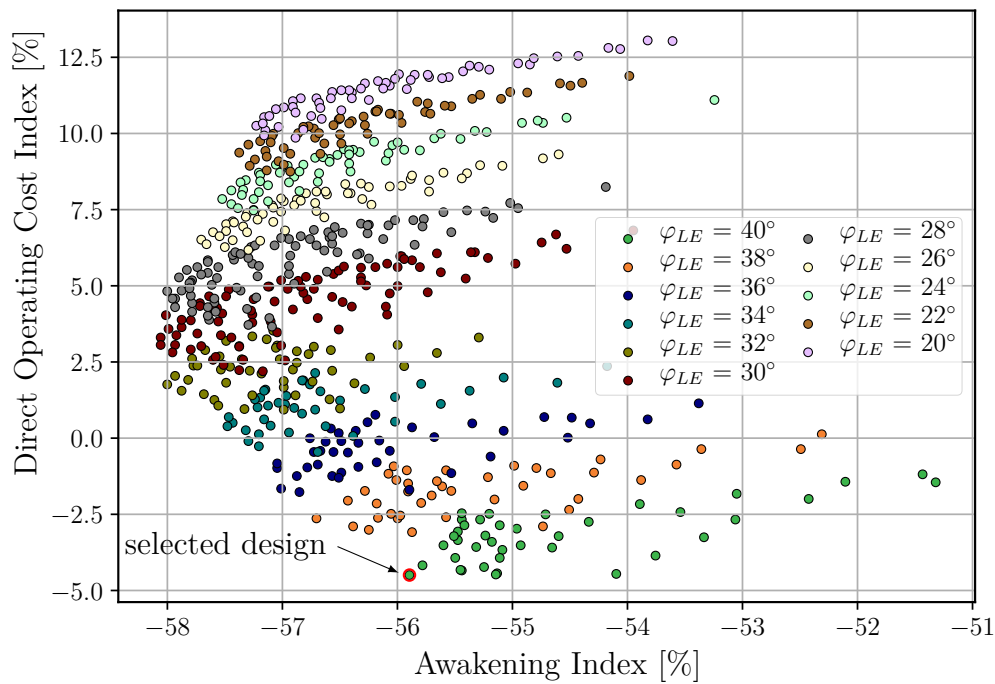


**Figure A.7.3.34:** Direct Operating Cost Index (DOCI) over Awakening Index (AWI) of the **low-noise-wing airplane** study. Each point corresponds to one airplane design, and shows its Direct Operating Cost Index and Awakening Index. The color denotes for the leading-edge sweep angle ( $\varphi_{LE}$ ). The same airplanes colored by the aspect ratio and wing area have been shown in Figures A.7.3.32 and A.7.3.33, respectively.

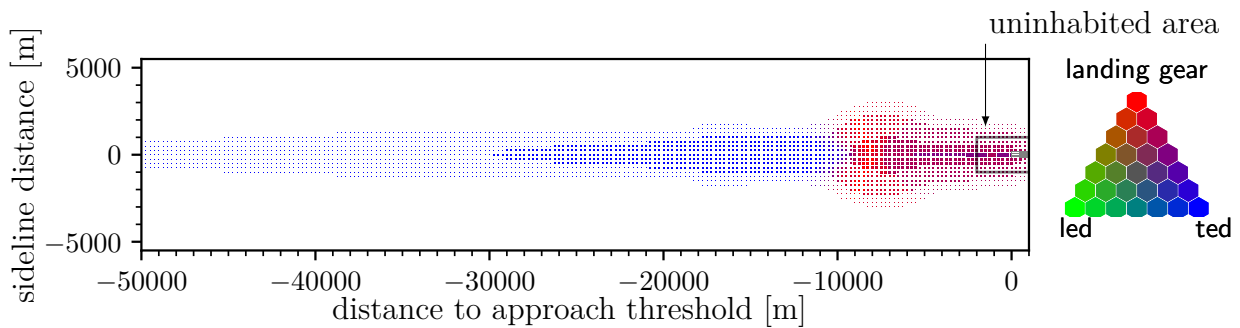


**Figure A.7.3.35:** Dominating airframe noise sources of the **low-noise-wing airplane** during approach. Figure 7.19 shows the same approach and its corresponding awakening reactions colored by the noise sources relevant during approach.

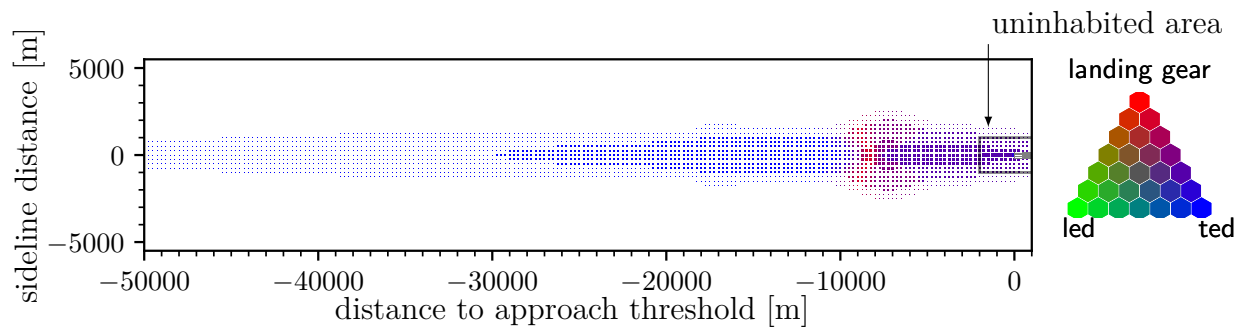


**Figure A.7.4.36:** Dominating airframe noise sources of the **landing-gear-fairing airplane** during approach. Figure 7.23 shows the same approach and its corresponding awakening reactions colored by the noise sources relevant during approach.



## B | Error Estimation

### B.1 Error Estimation: Single Sound Source Compared with Four Sound Sources

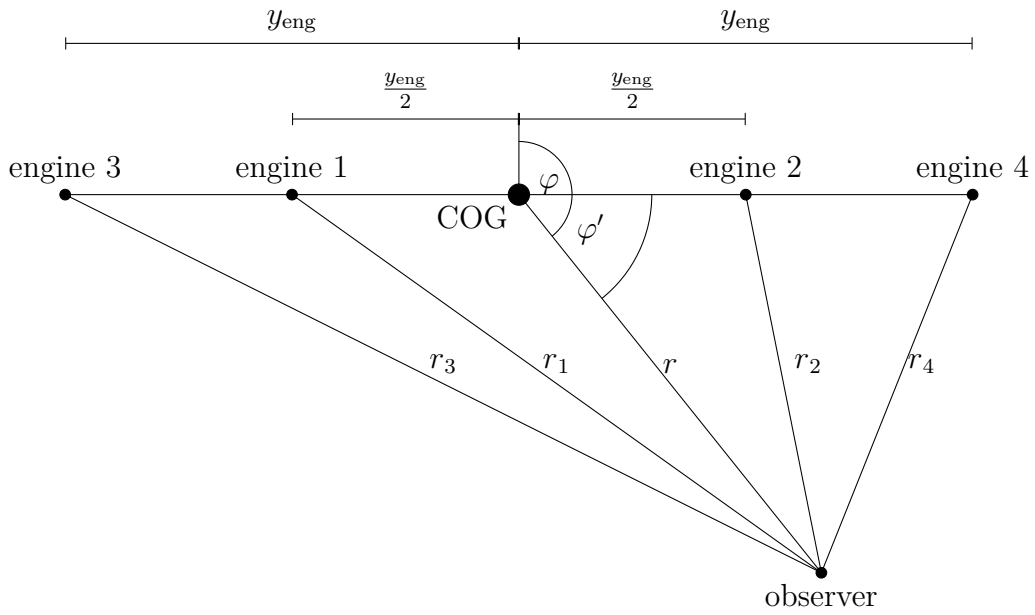


**Figure B.1.0.1:** Observer location relative to the airplane's COG and engine locations. Front view.

The sound pressure level by four point sources is calculated as described in the following.

$$\varphi' = \varphi - \frac{\pi}{2} \quad (\text{B.1})$$

The distance between each engine point source to the observer is calculated by the following equations.

$$r_1 = 0.25y_{eng}^2 + r - 0.5y_{eng}r \cos(\pi - \varphi') \quad (\text{B.2})$$

$$r_2 = 0.25y_{eng}^2 + r - 0.5y_{eng}r \cos(\varphi') \quad (\text{B.3})$$

$$r_3 = y_{eng}^2 + r - y_{eng}r \cos(\pi - \varphi') \quad (\text{B.4})$$

$$r_4 = y_{eng}^2 + r - y_{eng}r \cos(\varphi') \quad (\text{B.5})$$

This can be made dimensionless and re-written by

$$r' = \frac{r}{y_{\text{eng}}} \quad (\text{B.6})$$

$$\sin(\varphi) = \cos(\varphi') \quad (\text{B.7})$$

From this, Eq. (B.8) follows.

$$\frac{I_{1234}}{I_{\text{ref}}} = \frac{I_{12}}{I_{\text{ref}}} + \frac{I_{34}}{I_{\text{ref}}} = \frac{0.5(r'^4 + r^2)}{r'^4 + 1 + r'^2(2 - \sin^2(\varphi))} + \frac{0.5(r'^4 + 0.25r^2)}{r'^4 + 0.0625 + 0.25r'^2(2 - \sin^2(\varphi))} \quad (\text{B.8})$$

Equation (B.8) is the sound intensity at the observer relative to the sound intensity of four engines placed in the center of gravity of the airplane. This relation is printed in Figure B.1.0.2. Note that only geometric attenuation for a spherical wave has been considered, and atmospheric attenuation has been neglected.

The spanwise engine distance from the center is about  $y_{\text{eng}} = 21$  m at the considered Boeing B747-400. At 100 m height the error is about 0.1 dB and less. The higher the airplane, the lower the error. At very low heights, for example the distance from left to right outboard engine, the error is below 0.6 dB.

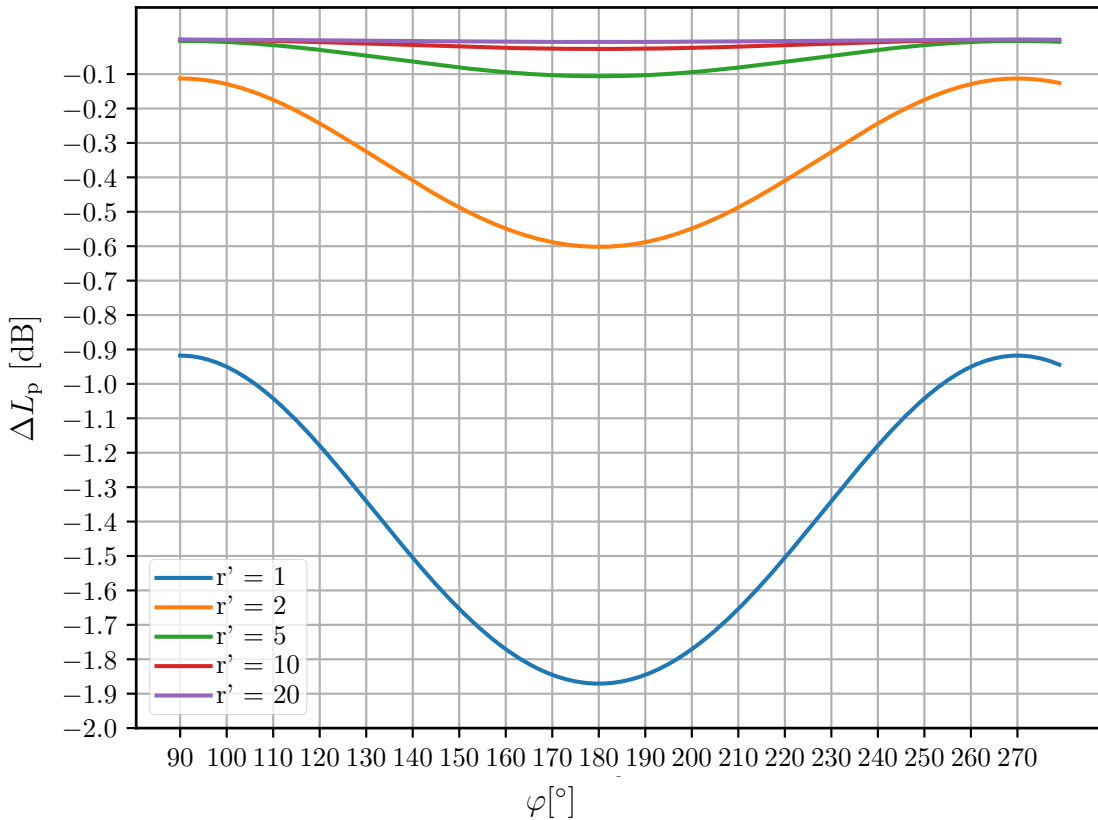


**Figure B.1.0.2:** Estimated noise prediction error due to considering the engine location in the airplane's COG

# C | Additional Data and Information Describing the Airplane Designs

## C.1 Center of Gravity of the B747-400

Landing gear strut loads are given by Airport planning manual [13].

| strut max. load (static) | max forw COG | max aft COG |
|--------------------------|--------------|-------------|
| front landing gear       | 31200 kg     | 25000 kg    |
| main landing gear        | 91200 kg     | 92750 kg    |

The four main gear struts are averaged in their position. As the struts have a longitudinal distance of 3.07 m, this means the wing mounted main gears were fictitiously moved 1.535 m to the back and the fuselage mounted landing gears are fictitiously moved 1.535 m to the front. This results in a fictitious distance of 25.605 m between the front and main landing gear struts. A moment equilibrium results in the following max. forward and max aft center of gravity positions for maximum taxi weight.

| reference weight | max. forw | max. aft |
|------------------|-----------|----------|
| max. taxi weight | 31.337 m  | 31.738 m |

## C.2 Data of All Airplanes

**Table C.1:** Airplane data of this thesis' concepts.

| Airplane<br>Variable                                  | ref     | basic               | eow                | neo                 | lnw                 | lgf                 |
|---|---------|---------------------|--------------------|---------------------|---------------------|---------------------|
| I.e. sweep [°]  | 42      | 36                  |                    | 40                  |                     |                     |
| Wing area [m <sup>2</sup> ]<br>(Δ to ref [%])         | 561.9   | 520.0<br>( -7.46)   | 540.0<br>( -3.90)  | 500.0<br>(-11.02)   |                     |                     |
| Aspect ratio [-]<br>(Δ to ref [%])                    | 7.179   | 9.000<br>( 25.37)   | 9.500<br>( 32.33)  | 7.5<br>( 4.47)      |                     |                     |
| Max. aircraft length [m]<br>(Δ to ref [%])            | 70.79   | 70.74<br>( -0.07)   | 70.86<br>( 0.10)   | 70.71<br>( -0.11)   |                     |                     |
| Span [m]<br>(Δ to ref [%])                            | 64.89   | 69.74<br>( 7.47)    | 72.92<br>( 12.37)  | 62.63<br>( -3.48)   |                     |                     |
| Max. aircraft height [m]<br>(Δ to ref [%])            | 19.94   | 19.80<br>( -0.70)   | 20.06<br>( 0.60)   | 19.82<br>( -0.60)   |                     |                     |
| Design range [km]                                     | 10602   |                     |                    |                     |                     |                     |
| Cruise Mach [-]<br>(Δ to ref [%])                     | 0.850   |                     | 0.841<br>( -1.06)  | 0.833<br>( -2.04)   |                     |                     |
| Cruise altitude [ft]<br>(Δ to ref [%])                | 12.54   | 12.30<br>( -1.91)   | 12.43<br>( -0.88)  | 12.36<br>( -1.44)   |                     |                     |
| Engine  | CF6-80  |                     |                    | DKO20               |                     |                     |
| Bypass ratio [-]                                      | 5.1     |                     |                    | 12.0                |                     |                     |
| Static thrust [N]<br>(Δ to ref [%])                   | 1090120 |                     |                    | 933224<br>(-14.39)  |                     |                     |
| SFC in cruise [g/N/h]<br>(Δ to ref [%])               | 0.06075 | 0.061<br>( 0.84)    | 0.060<br>( -0.50)  | 0.05024<br>(-17.05) | 0.05025<br>(-17.04) | 0.05024<br>(-17.05) |
| Engine diameter [m]<br>(Δ to ref [%])                 | 2.692   |                     |                    | 3.000<br>( 11.44)   |                     |                     |
| Lift/Drag [-]<br>(Δ to ref [%])                       | 17.28   | 19.43<br>( 12.44)   | 18.27<br>( 5.73)   | 16.02<br>( -7.29)   | 16.01<br>( -7.35)   | 16.02<br>( -7.29)   |
| Max. lift coefficient [-]<br>(Δ to ref [%])           | 1.350   | 1.344<br>( -0.44)   | 1.395<br>( 3.33)   | 1.365<br>( 1.11)    |                     |                     |
| Max. takeoff weight [kg]<br>(Δ to ref [%])            | 390058  | 372815<br>( -4.42)  | 398848<br>( 2.25)  | 349170<br>(-10.48)  | 348560<br>(-10.64)  | 348802<br>(-10.58)  |
| Max. landing weight [kg]<br>(Δ to ref [%])            | 277557  | 274437<br>( -1.12)  | 288057<br>( 3.78)  | 255678<br>( -7.88)  | 255181<br>( -8.06)  | 255379<br>( -7.99)  |
| Operating empty weight [kg]<br>(Δ to ref [%])         | 178506  | 179369<br>( 0.48)   | 189484<br>( 6.15)  | 161989<br>( -9.25)  | 161524<br>( -9.51)  | 161709<br>( -9.41)  |
| Manufacturer empty mass [kg]<br>(Δ to ref [%])        | 162731  | 163806<br>( 0.66)   | 173846<br>( 6.83)  | 146396<br>(-10.04)  | 145930<br>(-10.32)  | 146116<br>(-10.21)  |
| Wing weight [kg]<br>(Δ to ref [%])                    | 43943   | 49570<br>( 12.80)   | 55330<br>( 25.91)  | 38245<br>(-12.97)   | 37826<br>(-13.92)   | 37842<br>(-13.88)   |
| Fuselage weight [kg]<br>(Δ to ref [%])                | 39341   | 38760<br>( -1.48)   | 38956<br>( -0.98)  | 37823<br>( -3.86)   | 37812<br>( -3.89)   | 37818<br>( -3.87)   |
| Fuel mass (design mission) [kg]<br>(Δ to ref [%])     | 128792  | 110989<br>(-13.82)  | 125103<br>( -2.86) | 105803<br>(-17.85)  | 105669<br>(-17.95)  | 105722<br>(-17.91)  |
| Landing speed [m/s]<br>(Δ to ref [%])                 | 68.65   | 70.89<br>( 3.26)    | 71.22<br>( 3.74)   | 69.71<br>( 1.54)    | 69.64<br>( 1.44)    | 69.67<br>( 1.49)    |
| Lift-off speed v <sub>2</sub> [m/s]<br>(Δ to ref [%]) | 82.62   | 84.52<br>( 2.30)    | 85.20<br>( 3.12)   | 82.83<br>( 0.25)    | 82.76<br>( 0.17)    | 82.78<br>( 0.19)    |
| DOC [EUR per seat km]<br>(Δ to ref [%])               | 0.05323 | 0.05115<br>( -3.91) | 0.053<br>( -0.02)  | 0.05087<br>( -4.43) | 0.05084<br>( -4.49) | 0.05085<br>( -4.47) |



**ISSN 1434-8454**

**ISRN DLR-FB--2021-23**